Studies of adhesives and metal contacts on silicon strip sensors for the ATLAS Inner Tracker

DISSERTATION

zur Erlangung des akademischen Grades

doctor rerum naturalium

(Dr. rer. nat.)

im Fach Physik

Spezialisierung: Experimentalphysik

eingereicht an der

Mathematisch-Naturwissenschaftlichen Fakultät

der Humboldt-Universität zu Berlin

von

M. Sc. Anne-Luise Poley

Präsidentin/Präsident der Humboldt-Universität zu Berlin
Prof. Dr.-Ing. Dr. Sabine Kunst

Dekanin/Dekan der Mathematisch-Naturwissenschaftlichen Fakultät
Prof. Dr. Elmar Kulke

Gutachter/innen:	1. Priv-Doz. Dr. Klaus Mönig
	2. Prof. Dr. Heiko Lacker
	3. Prof. Dr. Chris Parkes
Tag der mündlichen Prüfung:	12.04.2018

Abstract

This thesis presents studies investigating the use of adhesives on the active area of silicon strip sensors for the construction of silicon strip detector modules for the ATLAS Phase-II Upgrade. 60 ATLAS07 miniature sensors were tested using three UV cure glues in comparison with the current baseline glue (a non-conductive epoxy).

The impact of irradiation on the chemical composition of all adhesives under investigation was studied using three standard methods for chemical analysis: quadrupole time-of-flight mass spectroscopy, gel permeability chromatography and gas chromatography combined with mass spectrometry (GC-MS). GC-MS analyses of glue sample extracts before and after irradiation showed molecule cross-linking and broken chemical bonds to different extents and allowed to quantify the radiation hardness of the adhesives under investigation.

Probe station measurements were used to investigate electrical characteristics of sensors partially covered with adhesives in comparison with sensors without adhesives. Leakage current, bulk capacitance, inter-strip capacitance and surface resistance were measured before and after gluing, after irradiation and after temperature cycling. The presence of glue on the active sensor area was found to increase the sensor leakage current and inter-strip capacitance and frequently led to early sensor breakdowns. Temperature cycling and irradiations reduced adverse effects due to glue to a small noise difference between sensors with and without glue.

Charge collection efficiency measurements in a β-source setup were used to study the influence of adhesives on the silicon bulk. All sensors under investigation showed equivalent charge collection efficiencies for sensors with and without glue, as well as signal-to-noise ratios above the required minimum of ten for the foreseen bias voltage. Before irradiation, sensors with glue showed increased cluster sizes, which could be attributed to fluorescence effects inside the glue using testbeam measurements.

During testbeam studies, sensor strips were found to respond inhomogeneously in bond pad regions. Follow-up measurements confirmed that the presence of bond pads affects the electric field within a sensor and leads to additional charge being collected around bond pads. As a result of these findings, the sensor bond pad layout was modified in order to minimise reduced tracking resolution caused by shifted strip responses.

Zusammenfassung

In dieser Dissertationen werden Untersuchungen zur Verwendung von Klebstoffen auf der Oberfläche von Silizium-Streifen-Sensoren für die Konstruktion von Detektormodulen für das ATLAS Phase-II Upgrade vorgestellt. Drei UV-härtende Klebstoffe wurden im Vergleich zu dem derzeitigen Standard-Klebstoff (einem nicht-leitenden Epoxid) an 60 ATLAS07 Miniatur-Sensoren getestet.

Der Einfluss von Bestrahlung auf die chemische Zusammensetzung aller verwendeten Klebstoffe wurde unter Verwendung von Standardmethoden zur chemischen Analyse untersucht: Flugzeitmassenspektrometrie, Gel-Permeations-Chromatographie sowie Gaschromatographie in Kombination mit Massenspektrometrie (GC-MS). Mithilfe der GC-MS Analysen von Klebstoffproben-Extrakten vor und nach Bestrahlung wurden verschiedene Ausmaße von Molekülvernetzung und gelösten Molekülbindungen festgestellt und der Grad von Strahlenhärte aller untersuchten Klebstoffe quantifiziert.

Mithilfe einer Sensor-Probestation wurden die elektrischen Eigenschaften von teilweise mit Kleber bedeckten Sensoren im Vergleich mit unbeklebten Sensoren untersucht. Die Leckströme, Oberflächenwiderstände, Kapazitäten zur Sensor-Rückseite sowie Zwischen-Streifen-Kapazitäten der Sensoren wurden vor und nach Bekleben, Bestrahlung und Durchführung von Wärmezyklen gemessen. Im Vergleich zu Sensoren vor dem Bekleben zeigten mit Klebstoff bedeckte Sensoren einen erhöhten Leckstrom, erhöhte Zwischen-Streifen-Kapazitäten sowie Durchbrüche des Leckstroms bei niedrigeren angelegten Spannungen. Durch Wärmezyklen und Bestrahlung wurden nachteilige Effekte des Beklebens von Sensoren auf ein geringfügig erhöhtes Rauschen reduziert.

Messungen der Ladungssammlungseffizienz in einem β-Strahlungs-Teststand wurden verwendet um den Einfluss von aufgetragenen Klebstoffen auf das Silizium-Kristallgitter zu untersuchen. Alle getesteten Sensoren - mit und ohne aufgebrachtem Klebstoff - zeigten vergleichbare Ladungssammlungseffizienzen sowie Signal-Rausch-Verhältnisse oberhalb des geforderten Minimums von zehn bei der vorhergesehenen Verarmungsspannung. Während der Messungen wurde festgestellt, dass bei unbestrahlten Sensoren mit Klebung Signale über eine durchschnittlich größeren Anzahl von Sensorstreifen verschmiert wurde als bei Sensoren ohne Klebung. Messungen im Teststrahl zeigten, dass dieser Effekt durch Fluoreszenzeffekte innerhalb des Klebers verursacht wurde.

Untersuchungen von Sensoren in Teststrahlmessungen zeigten außerdem, dass Sensoren um die zum Drahtbonden verwendeten Aluminiumflächen ungleichmäßig Ladung sammelten. Weiterführende Messungen konnten bestätigen, dass durch die Aluminiumflächen und darunterliegende Dotierungen das elektrische Feld innerhalb des Sensors verändert und zusätzliche Ladung um die Drahtbond-Flächen gesammelt wurde. In Reaktion auf die gemessene Inhomogenität wurde die Gestaltung zukünftiger Sensoren modifiziert, sodass der nachteilige Einfluss von Drahtbond-Flächen auf die Spurrekonstruktion minimiert wurde.

Contents

List of Figures

List of Tables

1 Introduction

The High Luminosity Upgrade of the Large Hadron Collider (LHC) at CERN, scheduled during Long Shutdown 3 (2024 to 2026) will require the replacement of the ATLAS Inner Detector (ID) with the ATLAS Inner Tracker (ITk) as part of the ATLAS Phase-II Upgrade. Different from the current ATLAS ID, the ITk will be an all-silicon detector, designed to cope with the higher particle density and radiation levels at the future High Luminosity LHC.

The ITk will consist of a silicon pixel tracker at its core, surrounded by a silicon strip sensor tracker, called the strip tracker. With a total of 165 m^2 of silicon strip sensor area, arranged in four layers in the central region and six layers in the forward region, the ITk strip tracker will require the construction of 18,000 modules. For a good track and energy resolution, the material budget of the ITk has been reduced with respect to the Inner Detector by changing the overall detector layout and cooling concept.

Silicon strip sensor modules for the ITk were reduced in complexity compared to modules for the ID: where readout electronics of ID modules were attached to bridges mounted over silicon strip sensors, readout electronics on ITk modules are glued directly on to the active sensor area during module construction. Sensors need to be stored in dry, clean environments before module assembly in order to avoid surface contaminations which can reduce the sensor performance. Covering a large part of the active sensor area with glue can affect the sensor performance, in particular after additional stress on the sensor during operation in the detector, such as irradiation and and the mechanical stress resulting from cooling the module to temperatures of -35 °C.

Extensive test campaigns were conducted to evaluate the performance of silicon sensors with different sensor architectures and wafer types, including irradiations with different types of particles up to different fluence levels. However, all previous tests studied sensors with surfaces free from adhesives, thus investigating sensors under circumstances which will not be found in the detector.

This thesis presents investigations of silicon strip sensors as planned to be used in the ATLAS strip tracker to study the impact of gluing, as well as well locally modified architectures, on the sensor performance.

Chapter 2 describes the future ATLAS ITk strip tracker and the requirements to silicon strip sensors arising from working conditions in the future ATLAS ITk. Chapter 3 presents the sensors which were available for this study and the irradiation and temperature treatments chosen to simulate working conditions in the strip tracker. In order to evaluate sensors with glue after irradiation, it was important to understand the effect of irradiation on the chemical composition of the adhesives under investigation. The development of a method to study chemical changes in adhesives caused by irradiation is outlined in chapter 4.

The performance of sensors with glue was evaluated in three types of measurements: chapter 5 presents the impact of gluing on electrical characteristics of sensors, measured in a probe station,

to investigate the impact of gluing on the sensor noise. Chapters 6, 7 and 8 present performance studies of sensors using a radioactive β-source setup and an electron particle beam, respectively, investigating charge collection efficiencies and the impact of gluing on the tracking performance.

Chapter 9 presents an additional deviation of the assumed ideal silicon strip sensor and its effect on the sensor performance: Wire bond pads, required for the connection of readout electronics channels to silicon sensor strips. Bond pads lead to locally modified sensor architectures which change the charge collecting area of individual sensor strips and thus affect charge collection.

Chapter 10 summarises the findings and outlines possible future studies.

2 The ATLAS Phase-II Upgrade

2.1 The Large Hadron Collider

The Large Hadron Collider (LHC) at CERN [7] is a synchrotron with a circumference of 27 km. Situated 100 m below the surface, it consists of superconducting magnets, cooled down to 1.9 K using liquid helium, to circulate two beams of either protons, lead or xenon ions at energies $\mathcal{O}$(TeV). The beams can be brought to collision at intersection points in four experimental caverns containing the four major experiments: Alice [8], ATLAS [1], CMS [9] and LHCb [10].

The LHC has been operated at different beam energies and instantaneous luminosities to be increased in steps during three runs:

1. Run 1:
   From late 2010 to 2012, the LHC was operated at a beam energy of 7 TeV (8 TeV in 2012) and an instantaneous luminosity being scaled up to $\mathcal{L} = 7.5 \cdot 10^{33}\,\mathrm{cm}^{-2}\mathrm{s}^{-1}$ (75 % nominal design luminosity). At the end of Run 1, an integrated luminosity of $\int \mathcal{L}dt = 30\,\mathrm{fb}^{-1}$ had been reached.

2. Run 2:
   From 2015 to 2018, data was collected at a beam energy of 13 TeV in 2015-2016, while the instantaneous luminosity was scaled up to nominal design luminosity ($\mathcal{L} = 1 \cdot 10^{34}\,\mathrm{cm}^{-2}\mathrm{s}^{-1}$). For data taking in 2018, the beam energy is foreseen to be increased to 14 TeV. At the end of Run 3, the total integrated luminosity is foreseen to have reached $\int \mathcal{L}dt = 150\,\mathrm{fb}^{-1}$

3. Run 3:
   From 2021 to 2023, data is planned to be taken at a beam energy of 14 TeV, while the instantaneous luminosity will be increased to $\mathcal{L} = 2 \cdot 10^{34}\,\mathrm{cm}^{-2}\mathrm{s}^{-1}$, so that a total integrated luminosity of $300\,\mathrm{fb}^{-1}$ will be reached by the end of data taking in 2023.

After Run 3, during Long Shutdown 3 (foreseen from 2024 to 2026), a major upgrade of the LHC will allow operation at an instantaneous luminosity of up to $\mathcal{L} = 7.5 \cdot 10^{34}\,\mathrm{cm}^{-2}\mathrm{s}^{-1}$ as the High Luminosity LHC.

2.1.1 The High Luminosity LHC

During the operation of the LHC, an extensive physics programme as been dedicated to both standard model processes, increasing the measurement precision of known processes [11] as well as confirming predictions [12], and searches for new phenomena, resulting in the discovery of the Higgs boson in 2012 [13] as well as limits on processes beyond the standard model [14].

In order to explore the full discovery potential of the LHC, the High-Luminosity Upgrade is planned to increase the instantaneous luminosity, allowing to accumulate an integrated

luminosity of $3000\,\mathrm{fb}^{-1}$. This increase of the integrated luminosity by a factor of ten will allow to study rare processes with a low cross-section currently limited by statists, such as e.g. at ATLAS:

- Higgs self-coupling
  After the discovery of the Higgs, measurements of the Higgs self-coupling allow a reconstruction of the Higgs potential and subsequently a better understanding of the impact of the Higgs mechanism on electroweak symmetry breaking. The trilinear self coupling constant λ_{HHH} can be studied in Higgs pair production, which has a theoretical cross-section of 40.8 fb, depending on the value of λ_{HHH} [15], corresponding to about 120,000 Higgs pair events. Due to the low production cross-section, the most interesting decay channels would be channels with either a high branching ratio ($H \to b\bar{b}b\bar{b}$ with 33 % and $H \to b\bar{b}W^+W^-$ with 25 % branching ratio) or a clean signature ($H \to b\bar{b}\gamma\gamma$, with a branching ratio of 0.26 %). The decay $H \to b\bar{b}W^+W^-$ has a signal-to-noise ratio of 10^{-5} [16], which was found to be too low to constrain λ_{HHH}. Searches for $H \to b\bar{b}\gamma\gamma$ and $H \to b\bar{b}b\bar{b}$ are expected to allow constraints on λ_{HHH} for $-0.9 < \lambda_{HHH}/\lambda_{SM} < 7.7$ and $0.2 < \lambda_{HHH}/\lambda_{SM} < 7.0$ ($-3.5 < \lambda_{HHH}/\lambda_{SM} < 11$ if systematics remain the same as for 2016 analysis), respectively [2] (all estimates at 95 % confidence level for $3000\,\mathrm{fb}^{-1}$).

- Flavour-changing neutral currents (FCNC)
  In FCNC, top quarks decay directly into up-type quarks (u or c) and a boson (γ, Z or H). While the process is highly suppressed in the standard model with branching ratios $< 10^{-12}$, several standard model extensions (such as quark-singlet models, a two-Higgs doublet or the minimal supersymmetric model) increase FCNC branching ratios to up to 10^{-4} [17]. Even in the absence of measured branching ratios for FCNC, improved experimental limits can constrain models predicting enhanced branching ratios. FCNC searches with 7 and 8 TeV data at the LHC have found an upper limit of $< 7 \cdot 10^{-4}$ for $t \to qZ$ (where $q = u, c$) [18]. The foreseen limits for $t \to qZ$ and $t \to q\gamma$ to be observed after the end of run 3, 10^{-3} and 10^{-4} with $300\,\mathrm{fb}^{-1}$, are expected to be improved to 10^{-4} and 10^{-5} with $3000\,\mathrm{fb}^{-1}$ at the 95 % confidence level [17].

- $t\bar{t}$ resonances and Z'
  Several standard model extensions predict the existence of new particles with a mass $\mathcal{O}$(TeV), which are expected to decay primarily into top quark pairs [2]. Searches for top quark pair resonances thus provide a method to search for new physics and set limits on models such as topcolour-assisted technicolour [19], which predicts the existence of a leptophobic Z' boson that decays into top quark pairs with a large branching ratio of about 33 % [20]. Previous searches for Z' have excluded a mass range up to 2.0 TeV using $3.2\,\mathrm{fb}^{-1}$ at $\sqrt{s} = 13\,\mathrm{TeV}$ and 95 % confidence level [21]. The High-Luminosity LHC is expected to increase this mass range up to 4 TeV (assuming $3000\,\mathrm{fb}^{-1}$ at $\sqrt{s} = 14\,\mathrm{TeV}$) [17].

An increase of the instantaneous luminosity from $1 \cdot 10^{34}\,\mathrm{cm}^{-2}\mathrm{s}^{-1}$ to $7.5 \cdot 10^{34}\,\mathrm{cm}^{-2}\mathrm{s}^{-1}$ leads to an expected increase of the average number of inelastic proton-proton interactions $< \mu >$ from about 23 to about 200 [2]. The increase in particle interactions (called pile-up) results

in increasing numbers of particle vertices and radiation levels and thus requires the LHC experiments to upgrade each detector to cope with the more challenging environment.

This thesis was based on silicon sensor and module designs for the ATLAS Phase-II Upgrade and is thus focused on the ATLAS detector.

2.2 The ATLAS Detector

The ATLAS detector is a cylindrical, multi-purpose particle physics detector with a length of 44 m and a diameter of 25 m (see figure 2.1). ATLAS follows the typical multi-layer design of

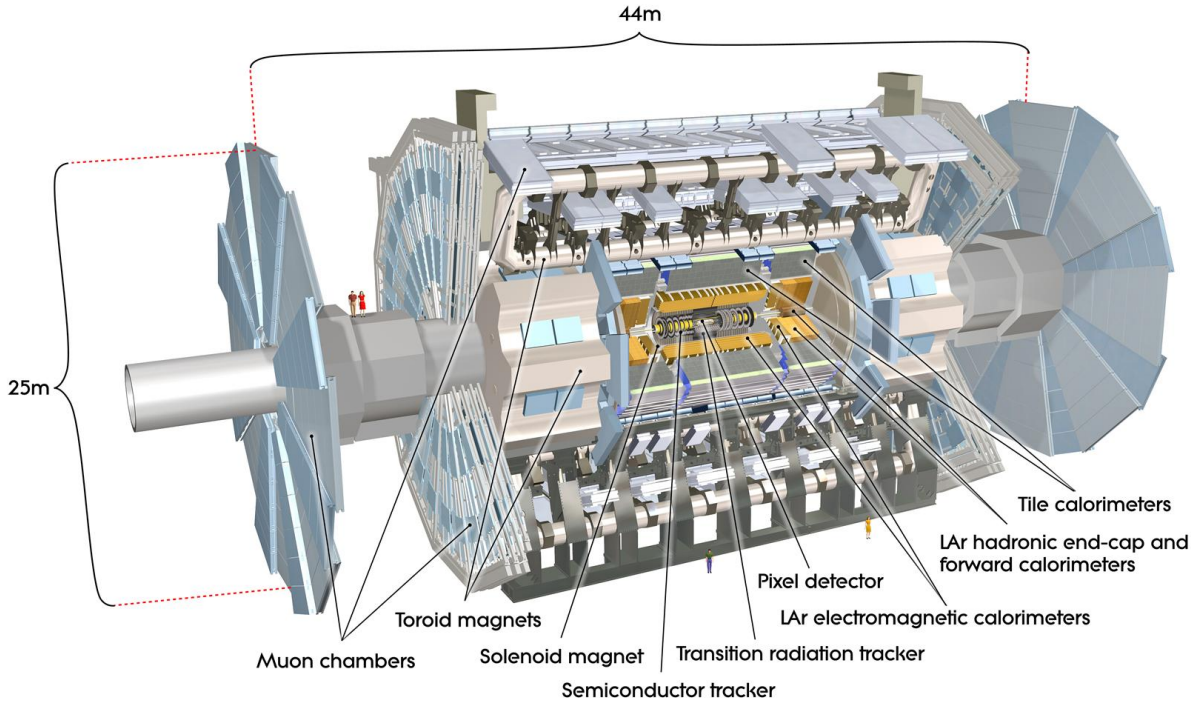

Figure 2.1: The ATLAS detector and its major sub-systems from [1]

particle physics detectors: at the centre of the detector, a tracking system identifies the traces of charged particles. The ATLAS Inner Detector [22], [4] consists of a silicon pixel detector, an silicon strip detector (called SemiConductor Tracker (SCT)) and a transition radiation tracker. Outside the Inner Detector, a liquid argon calorimeter [23] and a tile calorimeter [24] measure energy depositions of e^+, e^- and γ, and hadrons, respectively. The outermost layers of the ATLAS detector consist of the muon spectrometer [25], which tracks muons leaving the detector volume. Two separate magnet systems [26] are contained within the detector volume: a central solenoid with a mean field strength of 2 T surrounding the Inner Detector and a toroidal magnet surrounding the calorimeters with mean field strengths of 0.5 T (barrel) and 1 T (end-cap) [1].

A trigger system of several stages of hardware and software triggers [27], [28] reduces the data taking rate from a bunch crossing rate of 40 MHz to the maximum storage rate of about 100 Hz.

Adapting the ATLAS detector to the increasing instantaneous luminosity and beam energy of the LHC requires the extension, upgrade or replacement of several detector sub-systems.

2.2.1 The ATLAS Upgrade

Matching the LHC schedule, the ATLAS detector is planned to be upgraded in three phases during Long Shutdown phases between LHC runs:

- Phase-0 Upgrade (2013-2015)
  The Phase-0 Upgrade included a new beam pipe, upgraded shielding, repairs, maintenance and consolidations of detector sub-systems as well as several upgrades of the tracking system: new pixel services, a new cooling system, a diamond beam monitor and a new insertable pixel layer mounted directly on the beam pipe [29]

- Phase-I Upgrade [30] (2019-2020)
  Among smaller upgrades and maintenance work, the ATLAS Phase-I Upgrade involves four major projects:
  - New Muon Small Wheels [31]
    The luminosity increase beyond $1 \cdot 10^{34}\,\mathrm{cm}^{-2}\mathrm{s}^{-1}$ will lead to a degradation of the tracking efficiency and resolution in the forward muon wheels. Installing New Muon Small Wheels will improve both tracking and triggering performance for instantaneous luminosities up to the High Luminosity LHC.
  - The Fast Track Trigger [32]
    The higher instantaneous luminosity of the LHC will lead to an increased detector activity and increased rate of hardware triggers being sent to the software-based trigger system. In order to reduce the event rate sent to the software-based trigger system, a track trigger system can distinguish between high-momentum particle tracks of interest and low-momentum tracks by performing a fast track fit of detector hits in the pixel and silicon sensor layers.
  - The Liquid Argon Calorimeter Phase-I Upgrade [33]
    In order to increase precision, trigger information from Liquid Argon Calorimeter layers will be read out using smaller towers: instead of combining cells to 0.1×0.1 ($\Delta\eta \times \Delta\phi$) towers, information from the front and middle layer will be read out from 0.025×0.1 cells. New LAr Trigger Digitizer Boards will be installed to provide the trigger information to upgraded trigger processors called Feature Extractors.
  - The TDAQ System Phase-I Upgrade [34]
    In order to maintain current triggering performance levels in a much higher luminosity environment without raising trigger thresholds, the Phase-I Upgrade of the TDAQ system will include additional information from calorimeters and New Small Muon Wheels to improve jet selection and fake trigger rejection. Upgrades of the Central Trigger Processor and the High-Level Trigger processing farm will allow to keep the

readout and processing of Level-1 trigger events at a rate of 100 kHz while performing a sufficient reduction to below 1 kHz of event recording.

- Phase-II Upgrade [5] (2024-2026)

  - Trigger updates [35]
    The trigger system of the ATLAS Detector is required to maintain its current performance at low thresholds for single electrons and muons despite the anticipated increase in pile-up, which requires increasing both the latency and maximum rate of the trigger system. The Phase-II Upgrade foresees the replacement of all front-end electronics in existing systems to fulfil these requirements for the L1 trigger. The addition of a Level-0 hardware based on muon and calorimeter system will provide trigger information with a latency $< 6\,\mu s$ and a rate of 1 MHz
  - Calorimeter upgrades [35]
    Due to radiation tolerance limits, increased trigger rates and reduced trigger latencies, the readout electronics of both calorimeters are planned to be upgraded. Information from the last layer of the hadronic calorimeter will be provided to the trigger system in order to reduce fake rates in muon triggers. A concern for the Liquid Argon Calorimeter is an over-heating and local boiling in the liquid argon due to large energy depositions. Plans to compensate for the effect and maintain the current performance of the Liquid Argon calorimeter foresee either the replacement of the forward calorimeter with a new calorimeter with improved cooling or the addition of a MiniFCAL in front of the forward calorimeter in order to reduce the incoming particle flux.
  - A High-Granularity Timing Detector [35]
    For the design of the ATLAS detector, the innermost region of the calorimeter end-cap was designed with coarser granularity than the rest of the calorimeter, as physics simulations predicted the region to be unsuitable for precision physics. After the High Luminosity Upgrade, this region is expected to show a significantly degraded performance due to the expected pile-up increase. Equipping this region with a finely segmented detector with precision timing $\mathcal{O}$(ps) would compensate the coarser calorimeter granularity by providing additional information required to identify and reject energy clusters produced from pile-up in that region.
  - Muon System [35]
    For the Phase-II Upgrade, improvements of the muon system focus mainly on the performance of the muon trigger system: trigger electronics are planned to be upgraded in both barrel and end-caps, trigger chambers in the forward region will be replaced and new detectors will be added to the muon barrel region.
  - Replacement of the Inner Detector with the Inner Tracker
    The Inner Detector will have reached the end of its lifetime at the end of Run 3 and will be replaced with the Inner Tracker (ITk). The construction and installation ATLAS tracking system is the most significant improvement of the ATLAS detector

in the Phase-II Upgrade and will be presented separately in the next section.

2.2.2 The ATLAS Inner Tracker

The Inner Detector of the ATLAS detector was designed to be operated over a period of 10 years at a constant instantaneous luminosity of $1 \cdot 10^{34}\,\mathrm{cm}^{-2}\mathrm{s}^{-1}$ and is not suitable for the more challenging environment of the High Luminosity LHC in several aspects [2]:

- Radiation damages
  The current pixel and strip detectors in the Inner Detector were designed to withstand fluences corresponding to an integrated luminosity of $400\,\mathrm{fb}^{-1}$ and $750\,\mathrm{fb}^{-1}$, respectively. While these limits allow an efficient operation of the Inner Detector up to the end of Run 3, higher limits will lead to increased sensor leakage currents exceeding the capacities of both power supplies and cooling capacities.

- Bandwidth
  A limited bandwidth between the front-end electronics, in both pixel and strip detector, and read-out driver buffering links leads to a bandwidth saturation and subsequent readout inefficiencies at an instantaneous luminosity of $3 \cdot 10^{34}\,\mathrm{cm}^{-2}\mathrm{s}^{-1}$ (about 40 % of the intended HL-LHC luminosity).

- Occupancy
  The increased number of proton-proton interactions per bunch crossing and resulting higher track density will lead to higher occupancies in the Inner Detector (100 % in the transition radiation tracker). These occupancy levels affect the efficiencies of pattern recognition and track finding and lead to higher rates of fake tracks. In order to compensate the higher track density, a finer granularity is required to reduce detector occupancy.

The deficits of the current Inner Detector required the design and construction of a new tracker rather than an upgrade of the old one.

The future ATLAS Inner Tracker (ITk) was designed for an operation in the High Luminosity LHC ($\sqrt{s} = 14\,\mathrm{TeV}$, $\mathcal{L} = 7.5 \cdot 10^{34}\,\mathrm{cm}^{-2}\mathrm{s}^{-1}$) meeting the tracking requirements defined by the intended physics programme (see section 2.1.1).

The ITk will be an all-silicon detector consisting of an (inner) pixel detector and an (outer) strip detector (see figure 2.2). The envelope of the ITk is defined by the solenoid magnet and thus restricted to the size of the current Inner Detector. Compared to the Inner Detector, both pixel and strip detector in the ITk will cover larger ranges of radius and pseudo-rapidity, translating into a larger total area of silicon sensors in the detector (see table 2.1). Since the studies presented in this thesis were concerned with silicon sensors used in the ITk strip detector, its focus is on silicon strip sensors and detector modules.

The ITk strip detector barrel and end-caps are composed of mostly identical sub-structures called staves (barrel) and petals (end-cap). While each of the six discs in an end-cap consists of 32 petals (384 in total), the number of staves in a barrel layer depends on its radius and increases towards outer radii (with 28 staves at $r = 405\,\mathrm{mm}$ and 72 staves at $r = 1000\,\mathrm{mm}$), with a total number of 392 staves. Petals and staves consist of a sandwich of carbon fibre face

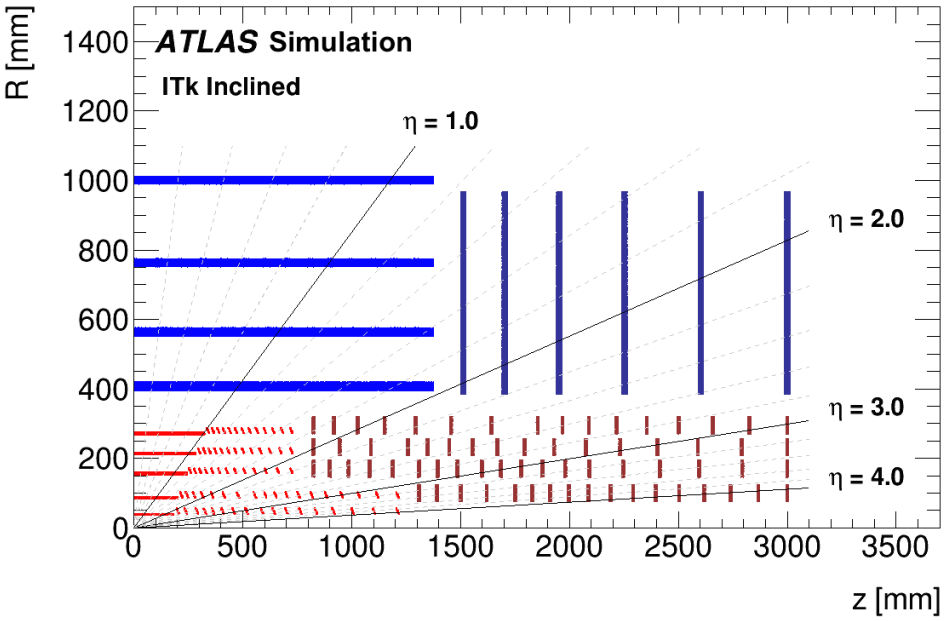

Figure 2.2: The layout of the future ATLAS ITk (from [2]): quarter of the cross-section along the beam pipe. Layers of the ITk strip detector (blue) are represented accurately, the layout of the pixel detector (red) had not been fixed at the time of this publication.

		Inner Detector		Inner Tracker	
		barrel	end-cap	barrel	end-cap
pixel detector	$\|z\|$ range, [m]	< 0.4	0.5 - 0.7	$< 0.7(0.8)/< 1.2(1.3)$	0.8 - 3.0
	radius range, [mm]	51 - 123	89 - 150	39 - 271	80 - $\approx$ 320
	silicon area, [m^2]	1.4	0.7	5.1	3.1
	number of layers	3	3	5	varying
strip detector	$\|z\|$ range, [m]	< 0.7	0.9 - 2.7	< 1.4	1.5 - 3.0
	radius range, [mm]	299 - 514	275 - 560	405 - 1000	385 - $\approx$ 980
	silicon area, [m^2]	34.4	26.7	105	60
	number of layers	4	9	4	6

Table 2.1: Comparison of the of the pixel and strip detectors in the ATLAS Inner Detector and Inner Tracker as detailed in [4], [5], [1] and [2]

sheets with bus tapes and carbon fibre honeycomb filling for mechanical stability. Carbon foam surrounding embedded titanium pipe with liquid CO_2 ensure a good thermal contact to modules glued directly to the face sheet. Each petal side is planned to be populated with 9 end-cap modules with different geometries, each stave side is planned to support 14 barrel modules with either short sensor strips (inner two layers) or long sensor strips (outer two layers), requiring about 11,000 barrel modules and 7,000 end-cap modules [2].

While silicon strip detector modules in the ITk vary in sensor shape and electrical components depending on their position in the ITk, their structure is the same throughout the detector. A general overview is presented below.

2.2.3 Silicon Strip Detector Modules

Comparing silicon strip detector modules from the ID (see figure 2.3) and ITk (see figure 2.4), modules built for the ID can be seen to show a more complex structure. In the ID, silicon

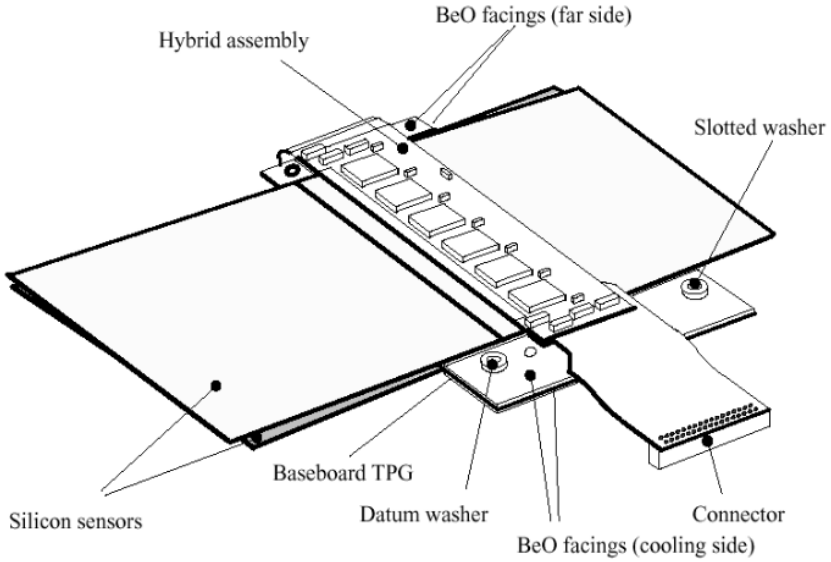

Figure 2.3: Layout of a silicon strip detector module in the Inner Detector (from [3]): silicon sensors are glued on to both sides of a baseboard with an attached heat spreader for cooling. Hybrids with readout chips form bridges over the sensor surfaces.

sensors were glued on to both sides of a base board that provided mechanical support as well as thermal conductivity through attached heat spreaders. Hybrids with glued on readout chips were mounted over each sensor surface without a direct contact between sensor and hybrid as "an effort [had been] made to avoid gluing to the active surface, given the uncertainties associated with long term ageing and radiation effects" [4]. Cooling was provided to modules by connecting the beryllium facings of the module to heat sinks soldered to cooling pipes on the global support structure. Modules were held on a support structure by PEEK clips to the beryllium module facings [3].

In contrast, the planned layout of silicon strip detector modules for the ITk (see figure 2.4) does not contain mechanical support or cooling structures. Different from the ID, detector modules are not connected directly to a global support structure, but mounted on local support structures (petals/staves), which are then attached to a global support structure. Local support structures consist of carbon fibre structures with an embedded cooling loop and provide both mechanical support and cooling for detector modules which are glued on to both sides of the local support structures. Detector modules for the ITk therefore consist only of a single silicon

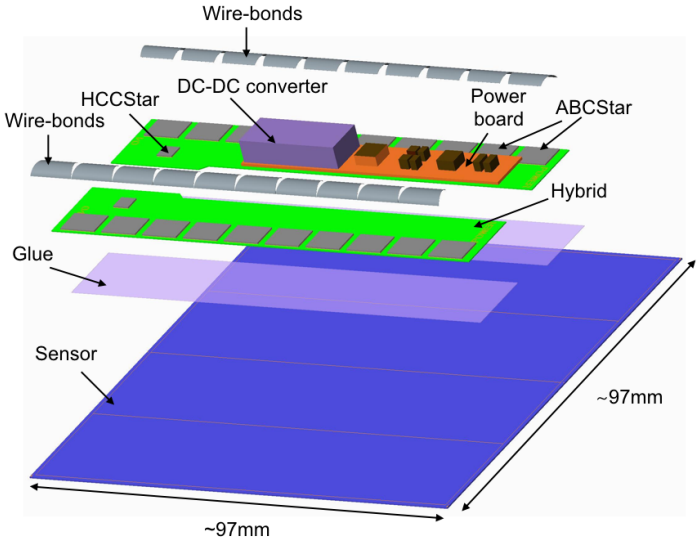

Figure 2.4: Layout of a silicon strip detector module for the Inner Tracker (from [2]): A module consists only of a sensor and the electronics required to read it out, which are glued directly on to the sensor.

sensor with all electronics required for the operation of the module glued directly on to the sensor surface. Depending on the module type (short/long strip in the barrel region, ring 0 to 5 in the end-cap region), a module has one or two hybrids with seven (ring 3) to twelve (ring 2) readout chips (called ABCStar), one or two hybrid control chips (called HCCStar) and one or no power boards. Power boards, among other functions, contain electronics converting and controlling high voltage supplied to the sensor, monitoring environmental conditions, providing trigger information and reading out data from the HCCStar to transmit it to readout electronics for a whole local support structure [2].

Silicon sensor strips are connected to the front-end channels of an ABCStar readout chip by aluminium wire bonds attached to dedicated aluminium wire bond pads on each sensor strip. All subsequent signal connections in the readout chain are also made using wire bond connections.

Hybrids and power boards are attached to the sensor by gluing directly on to the active sensor area using a non-conductive, two-component adhesive: Epolite FH-5313 [2]. Since the

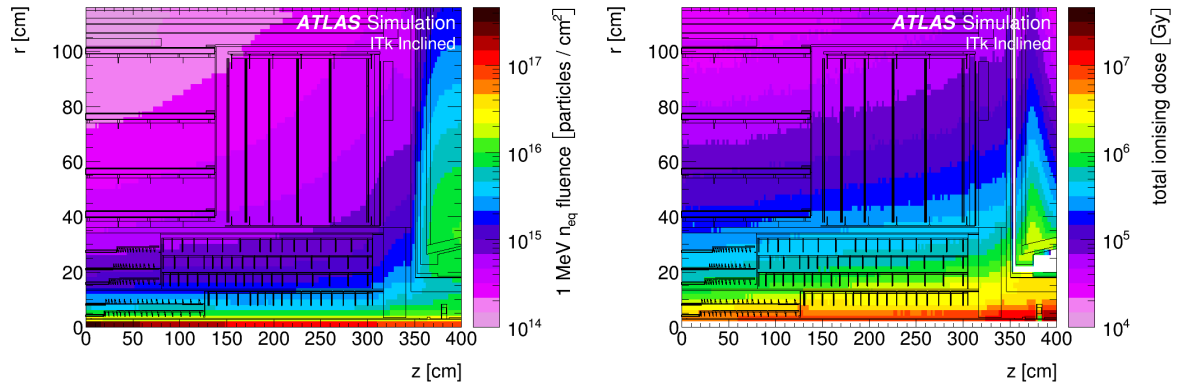

(a) Expected total fluence in the ITk strip tracker, from [2]

(b) Expected total dose in the ITk strip tracker, from [2]

Figure 2.5: Total fluence and dose expected in the ITk including a safety factor of 1.5, from [2].

active components on both hybrids and power boards are cooled by the cooling loop inside the local support structure, the adhesive does not only provide mechanical support, but also the cooling contact to the active components.

After gluing directly to the sensor had been avoided for the construction of the Inner Detector, the impact of gluing to the sensor surface had to be studied in detail specifically for the sensors used in the ITk strip detector.

2.2.3.1 Environmental Conditions for Silicon Strip Sensors in the future ATLAS Strip Tracker

For sufficiently efficient tracking as required by the ATLAS physics programme, signal collection with a signal-to-noise-ratio ≥ 10 is needed [2] in silicon strip modules throughout the operation time of the ATLAS detector after the Phase-II Upgrade.

Due to the high instantaneous luminosity in the High Luminosity LHC and the resulting high number of interactions per bunch crossing (see section 2.2.2), detector modules are expected to experience high levels of irradiation. After reaching an integrated luminosity of $\int \mathcal{L}_{\text{inst}} dt = 3000\,\text{fb}^{-1}$, fluence levels in the strip tracker are expected (including a safety factor of 1.5) to reach $1.2 \cdot 10^{15}\,\text{n}_{\text{eq}}/\text{cm}^2$ in the end-cap ($8.1 \cdot 10^{14}\,\text{n}_{\text{eq}}/\text{cm}^2$ in the barrel) and doses of up to 50.4 MRad (35.7 MRad in the barrel) [2]. Figures 2.5a and 2.5b show the simulated fluence and dose in the ITk strip tracker accumulated after an integrated luminosity of $\int \mathcal{L}_{\text{inst}} dt = 3000\,\text{fb}^{-1}$. ATLAS silicon strip sensors were found to require a bias voltage of up to -700 V to be fully depleted after having been irradiated to $1 \cdot 10^{15}\,\text{n}_{\text{eq}}/\text{cm}^2$ [36]. In order to keep the sensor leakage current as low as possible, sensors are cooled using bi-phase CO_2 at a temperature of $-35\,°\text{C}$ circulating inside the local support structure to which modules are mounted.

While being cooled from below, sensors are heated by chips on the hybrid (HCCStar and ABCStar) and power board (mainly the bPOL12V, former upFeast). Depending on the number of these chips on a module and their distance to the underlying cooling loop, FEA simulations

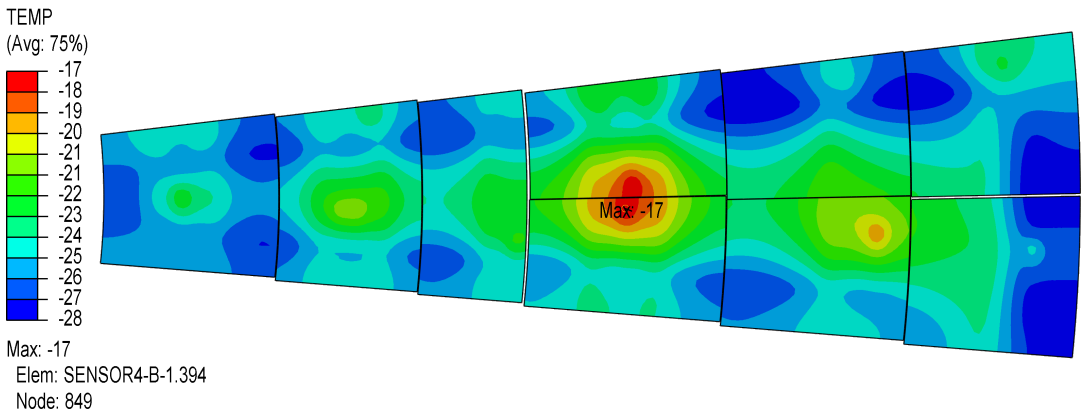

Figure 2.6: FEA temperature simulation of a petal in the strip tracker after 3000 fb^{-1}, from [2]. Due to the position of the power board on Ring 3 between cooling tubes, its bPOL12V chip is expected to become the the hottest area on the petal, leading to a temperate difference of 10 °C on R3 modules.

have shown sensors develop temperature differences of up to 10 °C between the hottest and coolest areas of a sensor (see figure 2.6). Sensors are required to be able to operate in a working temperature range from −30 °C to +20 °C, plus an additional safety margin towards higher temperatures (an interlock system is foreseen to deactivate the power supply to a module if its temperature exceeds +40 °C).

During operation, the ITk will be flushed with nitrogen to keep the humidity low enough to avoid condensation on cooled sensors.

2.3 Silicon Strip Sensors for the ATLAS ITk

Sensors for the ATLAS ITk strip tracker vary in shape and size depending on their position in the detector (see table 2.2), but have the same overall sensor design and architecture. It should be noted that while the ATLAS17 layout for sensors to be used in the ITk differs from the layout of ATLAS07 sensors used for the measurements presented here, the overall sensor layout has not been changed. The description of the sensor layout presented here will thus focus on ATLAS07 sensors as they are more relevant for this study.

ATLAS07 sensors were cut from 150 mm wafers with p^- bulk material and have a thickness of 320 µm with an aluminised backplane for HV contact. The sensor area consists of an active area collecting charges and an inactive area of dead material acting as a buffer between the dicing edges and the active area. The inactive area is used to apply marks to the sensor (see figure 2.7):

- precision markers for module assembly
- name of the sensor type
- wafer specifications

Position	Sensor type	Number of strip rows	Channels per sensor	Pitch [µm]
Barrel	short-strip	4	5128	75.5
Barrel	long-strip	2	2564	75.5
End-cap	R0	4	4360	73.5 - 84.0
End-cap	R1	4	5640	69.0 - 81.0
End-cap	R2	2	3076	73.5 - 84.0
End-cap	R3	4	3592	70.6 - 83.5
End-cap	R4	2	2052	73.4 - 83.9
End-cap	R5	2	2308	74.8 - 83.6

Table 2.2: Sensor types in the ATLAS ITk strip tracker (from [2]): due to the conical shape of end-cap sensors, the strip pitch varies in the inner and outer sensor regions. Sensors with four rows of strips have two hybrids glued to each sensor.

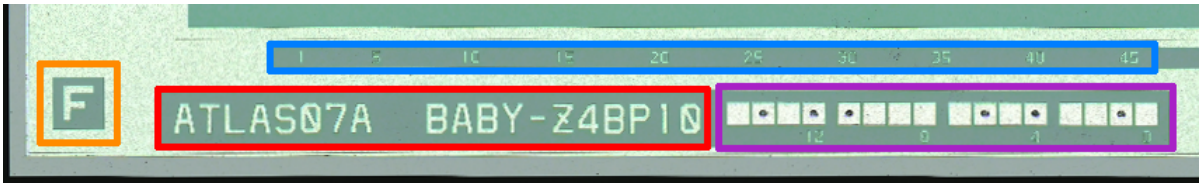

Figure 2.7: Corner of an ATLAS07 mini sensor with marks on the inactive area: precision marks for module assembly (orange), sensor type (red) and wafer specifications (violet) and numbers of the sensor strips (blue).

- strip numbers

The active area of the sensor is surrounded by three rings (see figure 2.8), which are situated on top of implant rings contacted by vias:

1. the outermost ring (active edge), connected to a p-doped implant ring defines the sensor volume and prevents the diced edges of the sensor from developing a high electric field
2. the floating guard ring, connected to an n-doped implant ring, shapes the field in the active sensor area and minimises edge effects
3. the bias ring, also connected to an n-doped implant ring, acts as an additional guard ring to ensure a homogeneous field for all sensor strips. Each sensor strip is connected to the bias ring via bias resistors, ensuring that all strips have a homogeneous potential.

The active sensor area is divided in two or four rows of strips arranged with equidistant pitches (1282 strips with a pitch of 74.5 µm on ATLAS07 barrel sensors). Each sensor strip consists of the following layers:

- an n-doped implant in the p^- silicon bulk
- a silicon oxide coupling capacity layer over the bulk with implants

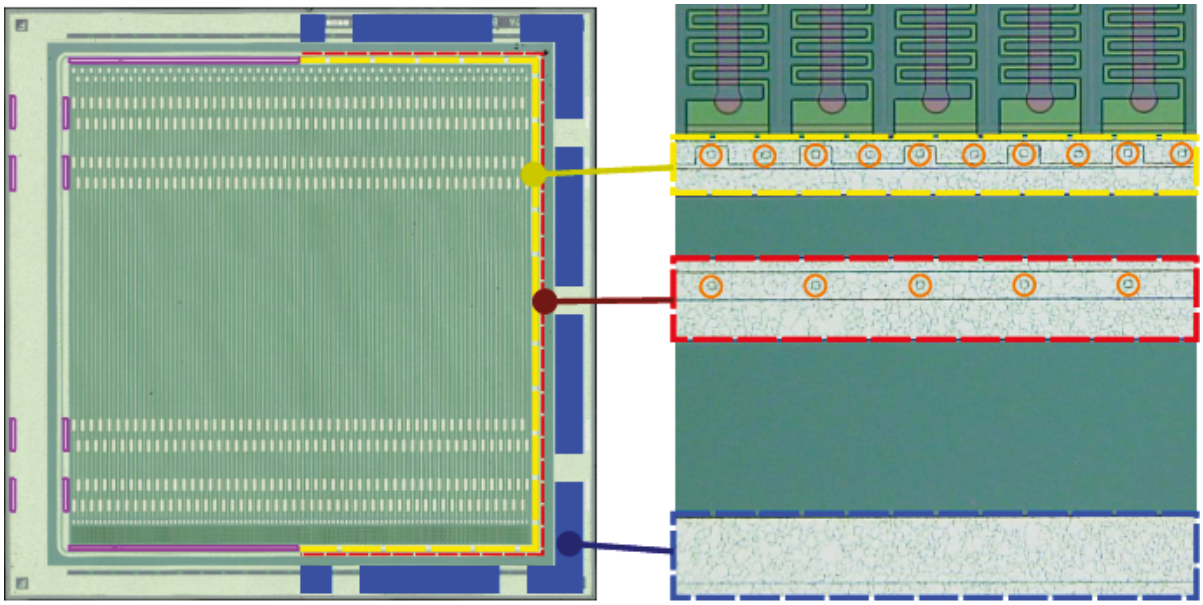

Figure 2.8: Protective rings around the active area of ATLAS strip sensors: The active edge (blue) contacts an underlying p-doped implant ring, the guard ring (red) and bias ring (yellow) are connected to n-doped implant rings by vias (orange) through vias in a silicon oxide layer grown over the sensor bulk. While most of the sensor surface is covered by an additional passivation layer of silicon oxide, openings in the passivation layer (violet) allow to contact the ring and underlying implant directly, e.g. for grounding.

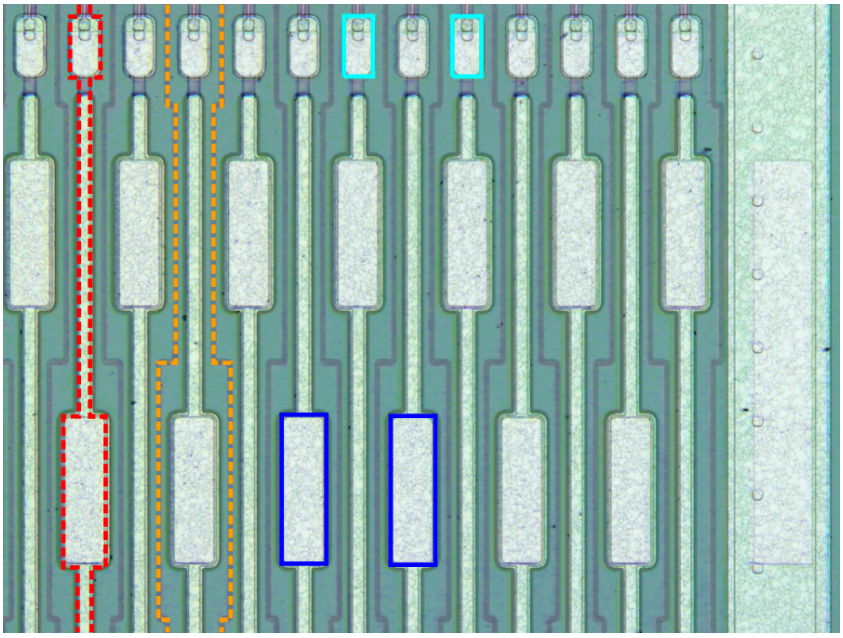

Figure 2.9: Architecture of a silicon sensor strip: n-doped strip implants (dashed red line) are electrically separated by p-doped implants (dashed orange line). Each strip has AC pads (solid blue line) where the passivation layer is opened to the underlying aluminium pad and DC pads (solid cyan line) where, in addition to the opened passivation layer, a vias through the coupling capacity layer provides a direct contact to the strip implant.

- an aluminium strip situated over the implant coupling capacitively to the implant
- an additional silicon oxide passivation layer with openings to contact the aluminium layer below to read out strips

Between adjacent sensor strips, p-doped implants (called p-stops) are added to the bulk to ensure isolation between strips after irradiation. Each sensor strip has openings through the first and second silicon oxide layer (see figure 2.9):

- AC pads (openings in the passivation layer) which allow a contact to the aluminium layer on top of each strip implant. These pads are used both for tests of sensor characteristics and to accommodate wire bonds connecting sensor strips and ASIC readout channels, which require a wider aluminium area and a wider implant below.
- DC pads (openings in the passivation layer on top of vias through the coupling capacity layer) which provide a direct contact to the underlying implant. These pads are used exclusively for test of the sensor performance and, while also requiring a wider aluminium layer and implant, are thus smaller than AC pads.

Sensor strip implantss are not directly connected to the bias ring implant in order to protect the sensor against large input signals, e.g. from beam splashes in the detector [37]. For ATLAS

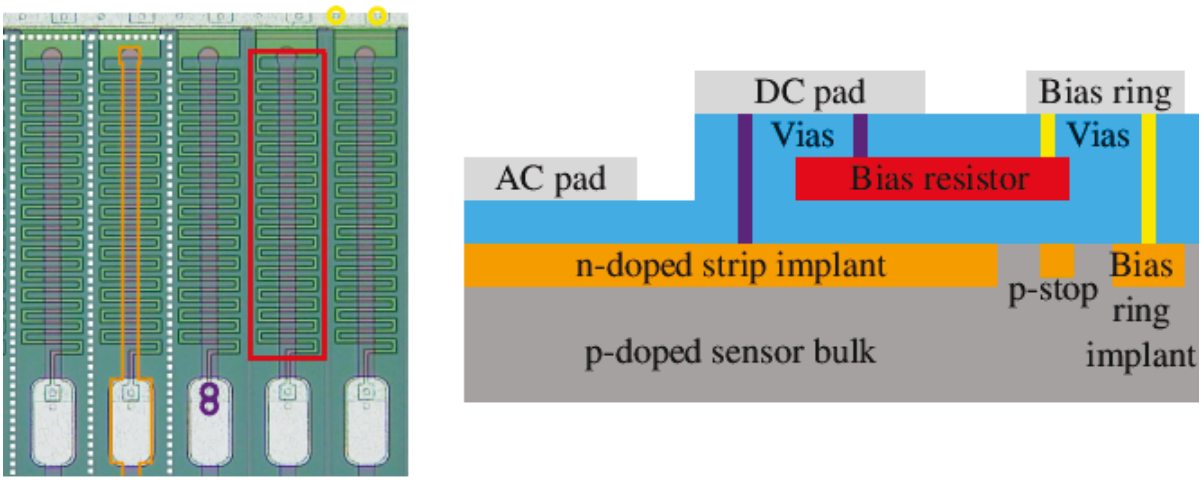

Figure 2.10: Connection of individual sensor strips to the bias ring: DC pads of sensor strips, connected to the strip implant (orange) by vias (yellow), are brought to contact with the bias ring, connected to the bias ring implant by vias (violet), using a high resistivity polysilicon structure (red) called bias resistor. Strips are electrically separated by p-doped implants (white), which are arranged both between sensor strips and between strip implants and bias ring.

sensors, this punch-through protection is achieved by disconnecting the implants from bias ring and sensor strips and connecting them via a high-resistivity structure of polysilicon (see figure 2.10).

During irradiation, positive charges accumulate in the coupling capacity silicon oxide layer, which attracts electrons and leads to a short-circuit between strip implants. In order to repel accumulating electrons, two strategies were used for ATLAS07 sensors (see section 3.1:

- p-spray, which describes a shallow p-doping over the whole surface of the sensor bulk between n-doped strip implants
- p-stops, meaning p.doped implant lines arranged between sensor strips and bias ring as well as between adjacent strip implants (see figure 2.10)

Both methods (separately and combined) were used on ATLAS07 sensors.

2.3.1 Electrical Specifications of Silicon Strip Sensors for the ITk

Sensors need to be designed to provide the required signal-to-noise ratio of ≥ 10 before and after irradiation. While the charge that can be collected from a sensor with a thickness of 320 µm is fixed (see section 6.1.1), the noise Q depends on the electrical characteristics of the sensor [38]:

$$Q = \sqrt{Q^2_{\text{leakage current}} + Q^2_{\text{parallel resistance}} + Q^2_{\text{series resistance}} + Q^2_{\text{load capacitance}}} \tag{2.1}$$

where the different contributions lead to the following requirements to the sensor:

- $Q_{\text{leakage current}}$ increases with increasing leakage current and thus requires a low leakage current.
- $Q_{\text{parallel resistance}}$ depends on the resistance between sensor strip and bias ring (called bias resistance), decreases with increasing bias resistance and thus requires a high bias resistance.
- $Q_{\text{series resistance}}$ depends on the resistances inside the strip implant and aluminium layer, increases with increasing metal strip resistance and thus requires a low resistance.
- $Q_{\text{load capacitance}}$ is comprised of the capacitance between adjacent sensor strips (inter-strip capacitance) and the capacitance between sensor strip and backplane (backplane capacitance). The load capacitance increases with increasing capacitance and is usually the most significant contribution to the overall noise [38].

ATLAS07 sensors were thus required to fulfil the following criteria [39]:

- inter-strip capacitance of about 0.8 pF/cm
- backplane capacitance of about 0.27 pF/cm
- bias resistance of about 1.5 MΩ

It should be mentioned that for sensors to be used in the ATLAS ITk, the specifications were expanded [2] to include:

- bulk resistance $\geq 3\,\text{k}\Omega\text{cm}$
- full depletion voltage $< 330\,\text{V}$
- bias resistance 1-2 MΩ
- inter-strip resistance $\geq 10\times$ $\text{R}_{\text{bias resistance}}$ (measured at 300 V and 23 °C
- inter-strip capacitance $\leq 1\,\text{pF/cm}$ (measured at 300 V and 100 kHz)
- breakdown voltage $\geq 700\,\text{V}$
- leakage current $\leq 0.1\,\mu\text{A}$ (measured at -700 V and room temperature)

With additional specifications for the sensor performance after irradiation up to $1.2{\cdot}10^{15}\,\text{n}_{\text{eq}}/\text{cm}^2$ and 50 MRad:

- inter-strip resistance $\geq 10\times$ $\text{R}_{\text{bias resistance}}$ (measured at 400 V and 23 °C
- breakdown voltage must be larger than the lower of either $\geq 700\,\text{V}$ or $V_{\text{full depletion}} + 50\,\text{V}$
- collected charge ≥ 7500 electrons per minimally ionising particle at 500 V

Where applicable, these specifications were used for comparison with the sensor measurements performed for this study

2.3.2 Sensor Handling during Module Construction

During the module production phase, sensors and modules not in use will be stored in a low-humidity clean-room environment in electrostatic discharge-proof containers in order to minimise performance decreasing influences. Throughout the module construction process, sensors are handled in a series of steps potentially damaging to the sensor:

- Application of vacuum
  Several module construction steps, such as gluing, wire bonding and probing, require flattening the sensor by applying vacuum to the sensor backside. Without vacuum application, sensors were found to have an intrinsic bend leading to a height difference of e.g. 60 µm measured for R0 sensors (specifications allow up to 200 µm [40]). Applying vacuum to flatten the sensor exerts mechanical stress on the sensor (about 7 MPa for an R0 sensor). Compared to the stress required to break a sensor from bending (measured to be about 25 MPa in case of an R0 sensor [41]), applying vacuum is thus a considerable stress for the sensor.

- Gluing
  Glue is applied to both sides of a silicon strip sensor: readout electronics are glued on to the sensor surface using a two-component epoxy glued (Epolite FH-5313) and the connection between modules and local support structures is made using a silicon gel (SE 4445), baseline selection in 2017. SE 4445 was chosen for its high thermal conductivity to provide a good cooling contact to the sensor, and for its low modulus which ensured stress from thermal expansion or contraction between sensor and support structure would be absorbed by the glue layer rather than the sensor. This glue connection is thus a small contributor to stress on a sensor. The glue foreseen to be used on the sensor surface has a higher modulus (see section 3.4.1), which makes it less yielding under mechanical stress. During gluing, glue is applied to a vacuum-flattened sensor and cures in that position, holding the sensor in a flattened position against its intrinsic bend and thus effectively applying stress on the sensor.

- Wire bonding
  In order to attach wire bonds to the bond pads of a sensor, a bond wedge applies ultrasonic power to a bond wire before pressing down on it with a bond force of about 20 cN. Bond wedges used to wire bond ITk strip detector modules have small footprints of down to $(51 \times 76\,\mu m^2)$, making the locally applied stress on the sensor during wire bonding as high as 52 MPa. While during normal wire bonding, the force is absorbed by the bond wire and the sensor is supported by a jig, overhanging sensor edges could be damaged in case of wire bonding problems.

- High Voltage contact
  Each sensor is biased by high voltage applied to its backplane. At the time of writing, the baseline method for producing a high voltage connection to the sensor backplane was the attachment of an aluminium tab using a bond wedge without an inserted bond wire. The process of attaching a high voltage connection is thus comparable to the process of wire

bonding performed on the backplane of the sensor. It should be noted that a wedge with a larger footprint (called a waffle wedge) is foreseen to be used for that bonding step.

- Transport
  Sensor testing and module construction sites are distributed over various countries, requiring the shipment of both sensors and modules. Test shipments with prototype transport boxes registered maximum short-time accelerations of up to 25 g, which can lead to movements of the sensor or module against its holding structure.

Several steps in the production of detector modules could potentially damage a sensor or worsen its performance. Repeated quality controls along the process ensure that significant changes are detected and the overall sensor performance is within acceptable operational parameters.

While most of the module construction steps exert mechanical stress on the sensor, gluing affects the sensor in several ways due to its direct contact with the sensor surface: it can interact chemically with the sensor, cause mechanical stress during curing and due to temperature changes and affect the electrical characteristics on the sensor surface.

This thesis is thus focused on investigating effects on the sensor performance from gluing to the sensor surface.

3 Sensors and Treatments

3.1 ATLAS07 Miniature Sensors

The intended studies required a large number of silicon studies with comparable characteristics and sensor architectures as similar as possible to the ATLAS silicon strip sensors to be used in the future ATLAS ITk. ATLAS07 miniature sensors, available from ATLAS silicon sensor prototyping in 2007 [39], were found to have sensor architectures sufficiently close to future ATLAS silicon strip sensors to allow for a translation of the results to future ATLAS ITk sensors. Figure 3.1 shows an ATLAS07 Wafer layout: for each ATLAS07 sensor, 24 miniature sensors were positioned around the sensor.

Since one aim of the original sensor prototyping run was to investigate different sensor architectures and wafer characteristics, ATLAS07 miniature sensors present a range of possible combinations of:

- float zone material
  float zone type 1 (FZ1) is a higher-quality wafer material with a higher resistivity $\approx 6.7\,\mathrm{k\Omega cm}$, compared to the lower-quality wafer material float zone type 2 (FZ2), with a lower resistivity $\approx 6.2\,\mathrm{k\Omega cm}$ [42], but significantly lower costs.

- sensor architectures
  different realisations of the intended sensor type were tried in order to compare their impact on the sensor behaviour (see figure 3.2)
  - BZ1: no p-stop implants between standard strip implants (16 µm)
  - BZ2: double p-stop implants between standard strip implants
  - BZ3: standard p-stop and strip implants (16 µm with 22 µm aluminium top layer)
  - BZ4A-BZ4D: standard p-stop and strip implants with different punch-through-protection realisations
  - BZ5: wider strip implants (22 µm) and narrower aluminium top layer (16 µm) and standard p-stops
  - BZ6: wider strip pitch between p-stop and strip implants (100 µm instead of 74.5 µm)

- p-spray
  the electrical insulation between the n-type strip implants can be obtained by using p-type implants (see section 2.3) between strip implants, which are included in most of the sensor architectures under investigation, or by using p-spray on the wafer surface. As a consequence, while individual miniature sensors have architectures with or without p-stops, all sensors on a wafer have p-spray, if applied.

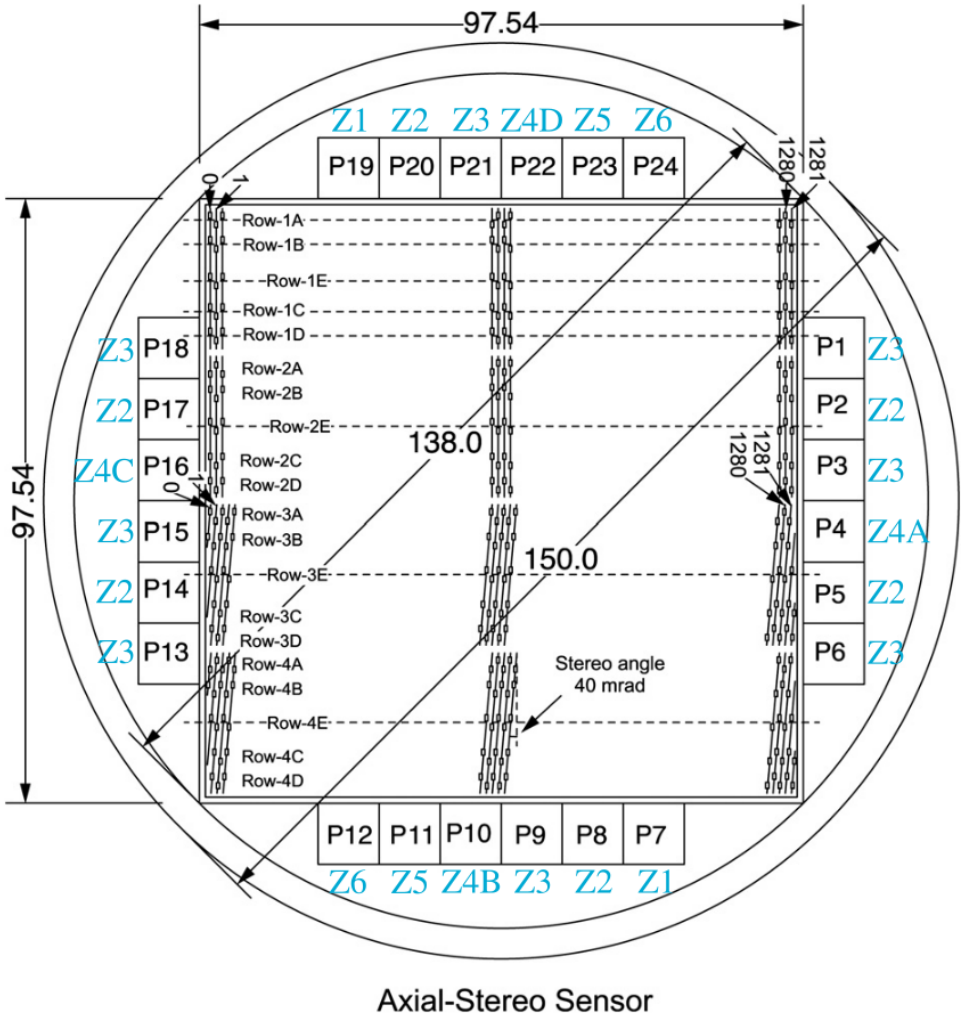

Figure 3.1: Wafer layout for ATLAS07 silicon strip sensors: one barrel sensor $97.54 \times 97.54\,\mathrm{cm}^2$ in the centre of the 6 inch wafer leaves room around its edges for 24 $1 \times 1\,\mathrm{cm}^2$ miniature sensors with different sensor architectures (types Z1 to Z6). The blue notes indicate the sensor architecture corresponding to each miniature sensor position on the wafer mask.

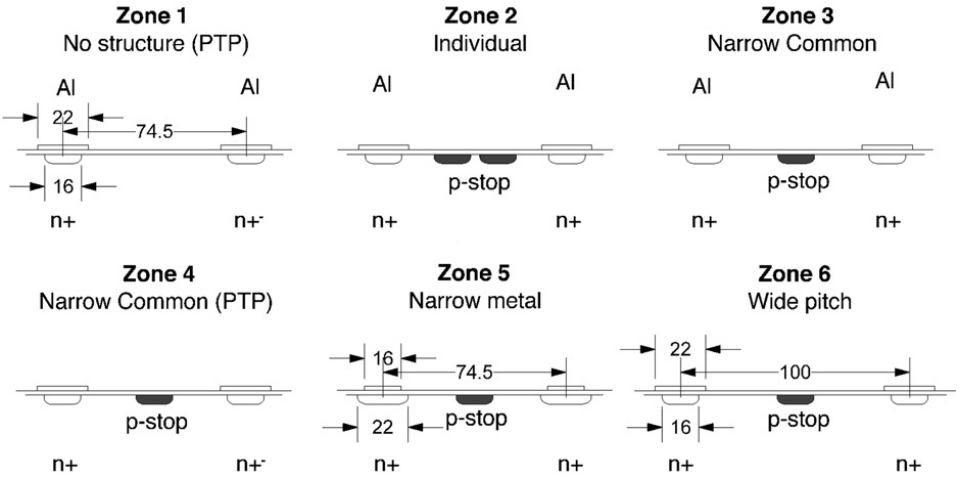

Figure 3.2: Sensor architectures for miniature sensors realised on ATLAS07 silicon sensor wafers. Starting from the standard sensor layout Z3 (strip implants with a width of 16 µm and a 22 µm aluminium top layer, arranged at a strip pitch of 74.5 µm and separated by a single p-stop implant), each of the architectures shows the variation of one aspect. Z1 has no p-stop implants, Z2 double p-stop implants, Z5 has wider strip implants and narrower aluminium top layers, Z6 has a larger strip pitch and Z4A-D have different punch-through protection structures.

Since the prototype testing had occurred several years before these studies, only a limited number of miniature sensors with different combinations of sensor architecture and wafer characteristics were available. Table 3.1 lists the properties of the 58 miniature sensors used in these studies.

3.2 Gluing

In the ATLAS ITk, hybrids holding readout chips as well as power boards are going to be glued directly onto the silicon sensor surface (see section 2.2.3. The glue foreseen to be used for the construction of all silicon strip sensor modules is Epolite FH-5313, a two-component, non-conductive epoxy glue that was chosen to replace [43] Araldite 2011, which was used in the ATLAS SemiConductor Tracker [44].

Epolite FH-5313 has several disadvantages for the mass-production of silicon strip sensor modules, most importantly a long curing time of 12 hrs and availability from only one vendor. In parallel to investigating the impact of gluing a hybrid onto a sensor with Epolite FH-5313, more glues were chosen both in order to investigate the behaviour of silicon strip sensors after gluing and study possible alternatives to Epolite FH-5313 to glue hybrids onto sensors.

The glues selected for comparison were three types of UV glue which had been studied as replacements for the silver epoxy glue used between readout chips and hybrid [45]:

- DYMAX 3013 [46], a very low viscosity UV cure glue (viscosity 0.2 Pa · s)
- DYMAX 6-621 [47], a low viscosity UV cure glue (viscosity 0.8 Pa · s)

Float zone	type 1		type 2	
p-spray	yes	no	yes	no
BZ1	-	-	-	-
BZ2	3	-	1	3
BZ3	5	-	1	5
BZ4A	1	3	1	3
BZ4B	2	2	-	3
BZ4C	1	2	-	3
BZ4D	3	2	1	3
BZ5	-	-	2	3
BZ6	4	-	2	1

Table 3.1: ATLAS07 miniature sensors available for sensor studies listed in categories of wafer characteristics (float zone material and p-spray) and sensor architecture (BZ1 to BZ6). Since only limited numbers of miniature sensors with the same characteristics were available, groups of sensors with sufficiently similar behaviour had to be found.

- Loctite 3525 [48], a viscous UV cure glue (viscosity 9.5-21 $\mathrm{Pa} \cdot \mathrm{s}$)

All three glues had already been found to work in a temperature range including the operating temperature range in the ATLAS ITk, not to corrode aluminium or silicon and show sufficient radiation hardness [49] and were thus considered to be good candidates to glue hybrids onto sensors. Since a previous study had found irradiation to be able to cause glue joints to become brittle and crumble, radiation hardness was found to be a major criterion for the selection of glue candidates. Sufficiently radiation hard glues were thus considered to be reasonable candidates.

UV cure glues of different viscosities around the viscosity of Epolite FH-5313 [50] ($3.6\,\mathrm{Pa} \cdot \mathrm{s}$) were chosen in order to compare the impact of glue accidentally spilling outside of the intended glue area and covering parts of the sensor bias ring.

Previous studies investigating hybrid on sensor gluing ([43] and [51] had found that one effect of gluing onto a sensor can be a significantly lowered breakthrough voltage. In order to avoid conducting further studies with a glue that reduced the breakthrough voltage, first gluing tests were performed by applying 2.5 µl of glue on the centre of the sensor (see figure 3.3a) and measuring the leakage current afterwards (measurement described in section 5.3.1). For each UV cure glue, two miniature sensors were prepared with only a glue dot in the centre of the sensor.

More detailed studies were conducted with sensor glue joints as similar as possible to module construction by gluing pieces of FR4 covered with solder resist (similar to the bottom side of a hybrid) onto the sensors. The FR4 was chosen to be 1 mm, thicker than a hybrid used in module production (thickness 270 µm). The thicker material approximated the reinforcing effect of ASICs glued onto a hybrid and offered the possibility to perform shear tests by moving a shear tester wedge against the FR4. Each FR4 piece had a size of $3 \times 7\,\mathrm{mm}^2$ to cover the full sensor width while leaving half of each strip empty, so that some of the aluminium pads on the

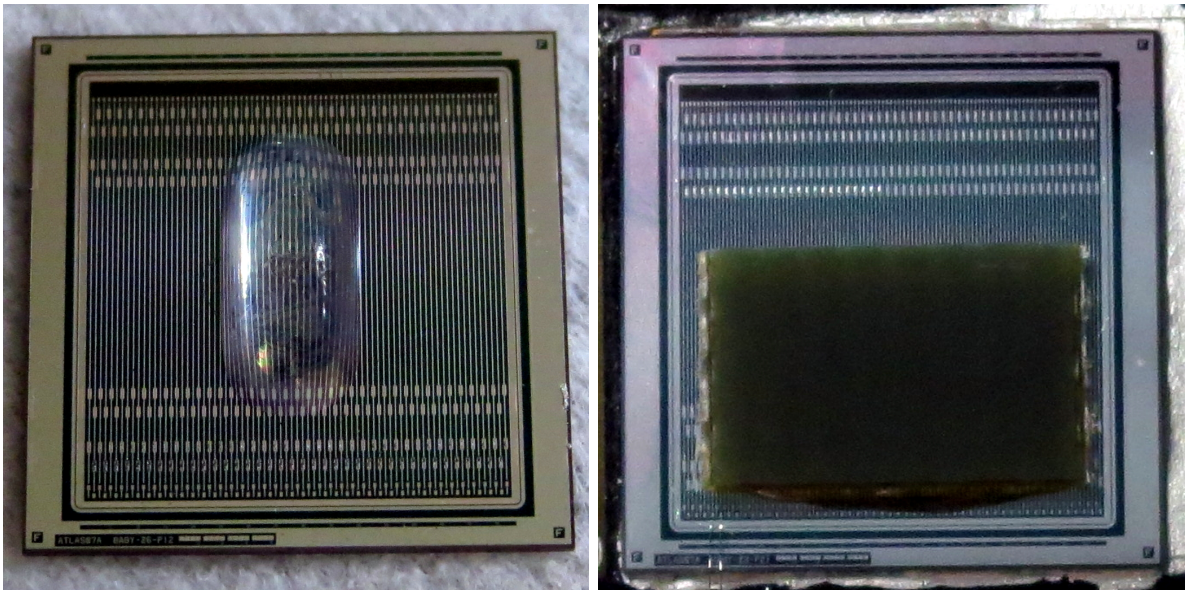

(a) ATLAS07 miniature sensor with 2.5 µl DYMAX 6-621 glue

(b) ATLAS07 miniature sensor with 2.5 µl Loctite 3525 and FR4

Figure 3.3: Examples of ATLAS07 miniature sensors with glue samples on the surface of the active area

sensor could still be contacted. Figure 3.3b shows an example of a miniature sensor with glue and FR4.

2.5 µl of a glue were dispensed per miniature sensor, so that a glue coverage of 75-90 % below the $3 \times 7\,\mathrm{mm}^2$ FR4 piece would lead to a glue thickness of 130 to 160 µm, similar to the glue layer in a module. Glue was applied using a microliter pipette with a precision of about 5 % [52], which had been found to provide sufficient repeatability for dispensing the glues under investigation.

Afterwards the glue was cured by applying UV light from UV LEDs [53] for 10 min to ensure a fully cured glue layer.

3.3 Irradiations

3.3.1 Use of Silicon for Semiconductor Trackers

The use of silicon for tracking detectors relies on its semiconductor characteristics for signal generation (the process of charge generation and collection is described in section 6.1). Like all semiconductors, silicon has only few free charge carriers, because electrons in the valence band are separated from the conduction band by an energy gap $E_{gap} = 1.12\,\mathrm{eV}$ [38]. The Fermi energy E_F, where half of the available levels is occupied, lies halfway between valence band and conduction band (see figure 3.4a)

By doping the silicon, i.e. intentionally adding atoms of different elements, additional energy

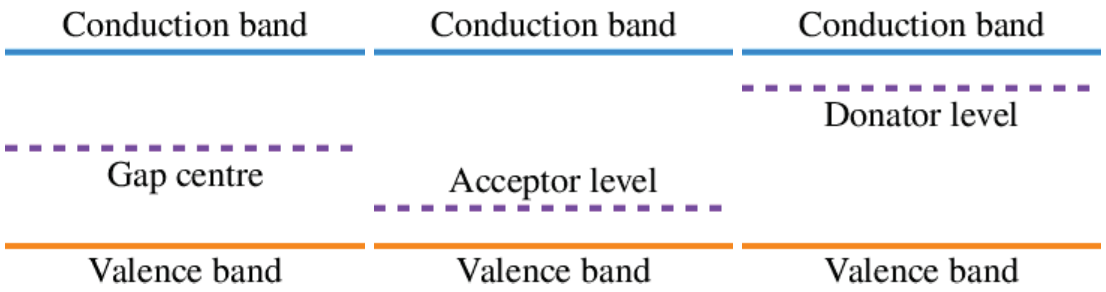

(a) Energy levels in a semiconductor without doping

(b) Energy levels in a semiconductor with n-doping

(c) Energy levels in a semiconductor with p-doping

Figure 3.4: Energy levels in a semiconductor material with and without doping. Adding a p/n doping material leads to an additional donator/acceptor level between conduction and valence band.

levels can be introduced: by adding atoms of elements from the fifth main group, e.g. phosphor, which have an additional electron compared to silicon atoms, which have four electrons to form covalence bonds, free electrons are added to the silicon grid, i.e. donator levels (see figure 3.4b). Correspondingly, adding atoms from elements in the third main group, e.g. boron, which are missing an electron compared to the surrounding silicon atoms, introduces new donor levels (see figure 3.4c). In each case, the introduction of new energy levels shifts the fermi energy towards these levels. By combining positively doped silicon (here: bulk material) and negatively doped silicon (here: sensor strip implants), a pn-junction is created. The differences in Fermi energies in differently doped energies lead to the free charge carriers in each component to move: electrons move to the lower fermi energy level created by the additional acceptor state and holes move to the higher fermi energy level created by the additional donator state. Once a thermal equilibrium is reached, the fermi energy level in both doping regions is identical and an electrical potential barrier separates electrons and holes, leading to an area depleted of all free charge carriers between both doping regions.

This depleted area, which can be increased by applying reverse bias voltage, allows silicon sensors to be used for particle tracking: the number of electron-hole-pairs created by a charged particle in silicon ($\mathcal{O}(10^4)$) is significantly smaller than the number of free charge carriers in a comparable volume of silicon ($\mathcal{O}(10^9)$). Only the operation of silicon as a reverse biased pn-junction allows to deplete a sensor of free charge carriers sufficiently to detect signals created by charged particle tracks.

Irradiation of silicon strip sensors has different effects on silicon, of which some can result in additional acceptor or donator energy levels being introduced (see section 3.3.2). These effects can both reduce the signal collected in a sensor (see section 6.1) and increase the sensor noise (see section 5.1), worsening the overall sensor performance significantly. In combination with a glue layer added to the sensor surface, irradiation could lead to additional sensor effects caused by a combination of chemical and radiation effects.

Since one of the major challenges in the development of detectors is the high radiation environment of LHC experiments (see below), irradiation studies were considered a priority for

the investigation of sensors that had been glued.

3.3.2 Radiation Damages in Silicon

Irradiation affects silicon sensors by causing mainly two types of effects [38]:

- bulk damage (displacement of atoms in the sensor bulk)
- surface defects (ionisation in insulator layers and formation of interface defects)

The type of radiation damage and its effects on the sensor performance depend on the the type of radiation as well as the type of silicon in use.

The bulk damage from different types of radiation can be estimated using the Non Ionizing Energy Loss (NIEL) hypothesis, which allows to calculate the displacement damage $D(E)$ as [38]:

$$D(E) = \sum_i \sigma_i(E_{\text{kin}}) \int_0^{E_{\text{R, max}}} f_i(E_{\text{kin}}, E_{\text{R}}) P(E_{\text{R}}) dE_{\text{R}}, \tag{3.1}$$

where

- $P(E_{\text{R}})$ is the Lindhard partition function [54] describing the fraction of a particle's energy going into the displacement of silicon atoms
- $f_i(E_{\text{kin}}, E_{\text{R}})$ is the probability that a collision with a particle with the energy E_{kin} will occur and lead to the transfer of a recoil energy E_{R}
- $\sigma_i(E_{\text{kin}})$ is the probability of the process
- $E_{\text{R, max}}$ is the maximum energy that can be transferred

In order to compare radiation damages from different types of radiation, the standard of the neutron equivalent fluence $\text{n}_{\text{eq}}/\text{cm}^2$, corresponding to the displacement damage of $1\,\text{MeV}/\text{cm}^2 = \Phi_{\text{eq}}$, is used. Radiation damages can thus be scaled with respect to the radiation damage of 1 MeV neutrons using the hardness factor κ:

$$\kappa = \frac{\Phi_{\text{eq}}}{\Phi}, \tag{3.2}$$

where Φ_{eq} is the radiation damage of a flux of particles with a certain energy expressed as the equivalent of 1 MeV neutrons.

Figure 3.5 shows an overview of the displacement energies of different particles.

Particles traversing silicon interact with the atoms in the bulk lattice via strong and electromagnetic force and displace individual atoms (point defects), creating vacancies and interstitials as well as complex defects (clusters) consisting of combined atom displacements and impurities (see figure 3.6). Defects can move through the silicon bulk and connect to other defects, forming complex defect clusters. Depending on the type and energy of a particle interacting with silicon, different bulk damages occur predominantly: charged particles produce Frenkel pairs and local

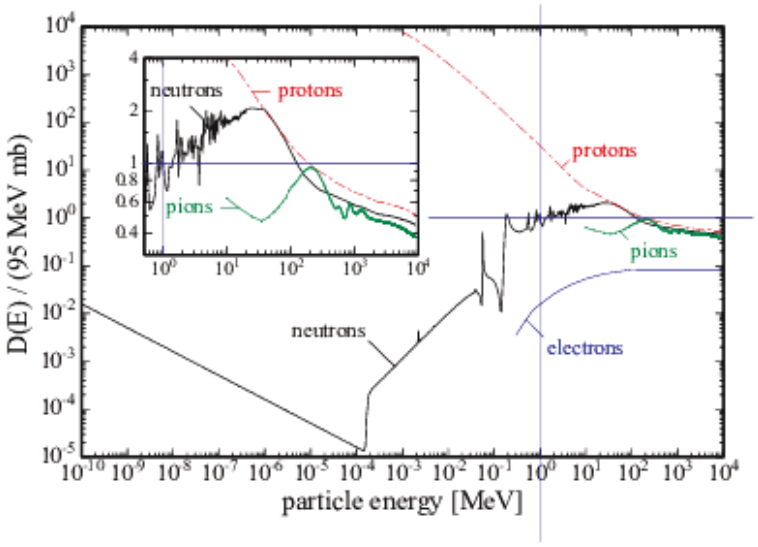

Figure 3.5: Displacement damages for different particles relative to the neutron equivalent fluence Φ_{eq} [55]

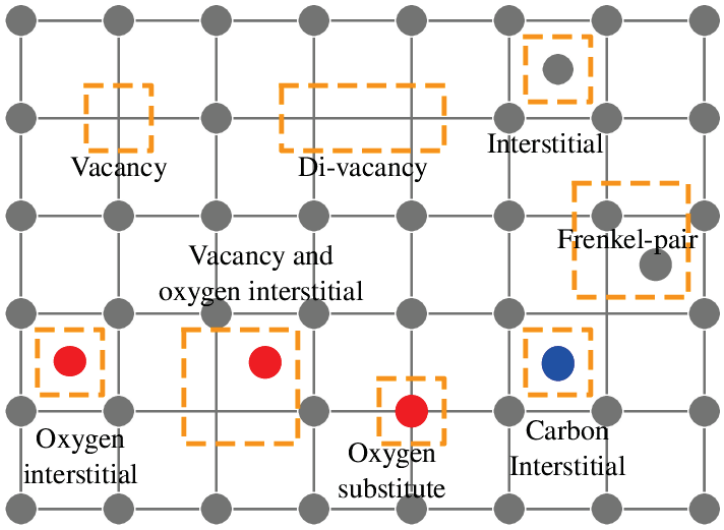

Figure 3.6: Examples of bulk damages in a silicon lattice: individual silicon atoms are displaced, leading to vacancies or interstitials, which can form more complex damages. Impurities, such as oxygen and carbon, can cause similar effects in the lattice.

defects, whereas neutrons and other strongly interacting particles can produce long cluster defects, from [56].

Defects in the silicon bulk correspond to new energy levels as they can act as donors or acceptors. As such, they affect the macroscopic behaviour of a sensor:

- Leakage current
  Defects with energy levels in the centre between conduction and valence band lead to the production of electron-hole-pairs and thus increase the leakage current. This type of defect is produced constantly during irradiation, hence the corresponding leakage current increase has been found to increase approximately linearly with fluence [38].

- Depletion voltage
  The depletion voltage, at which a sensor is fully depleted of free charge carriers (see section 5.3.1), depends on the space charge concentration inside the sensor volume. Additional acceptor states close to the valence band as well as donor states close to the conduction band lead to an increase in space charge, which leads to an increased depletion voltage. Highly irradiated sensors thus require bias voltage much higher than unirradiated sensors. It should be mentioned that irradiation decreases the dependence of a sensor's bulk capacitance on the applied bias voltage (see section 5.3.2) and thus the bulk capacitance can not be used for the determination of the full depletion voltage any more.

- Charge trapping
  Certain bulk defects in silicon can trap charges and thus impede charge collection in the sensor. At high irradiation levels ($1 \cdot 10^{15}\,\mathrm{n_{eq}/cm^2}$ and above), frequent trapping can reduce the effective lifetimes of charges beyond the time required to traverse the full sensor volume. If the effective lifetime does not allow charge carriers to reach the top of a sensor, the full charge can not be collected any more and the charge collection efficiency is reduced [38].

It should be mentioned that some types of bulk defects, e.g. Frenkel pairs, can be healed by exposing sensors to elevated temperatures for a defined amount of time (e.g. 60 °C [57]), called beneficial annealing. If irradiated sensors continue to be exposed to elevated temperatures over a longer period of time, reverse annealing occurs, which leads an increase in acceptor levels and thus increases the sensor depletion voltage. Both types of annealing can be prevented by storing sensors at temperatures below 0 °C. While beneficial annealing could improve the performance of sensors after irradiation, a continuous storage at temperatures below 0 °C could not be guaranteed in these studies due to the various treatments and tests sensors were subjected to afterwards. The sensors irradiated for this study were thus not annealed beyond unavoidable temperature increases during tests.

Surface damages are predominantly caused by ionisation effects, where several effects contribute to positive charges accumulating at the interface region between silicon and silicon oxide [38]:

- the lattice mismatch between silicon oxide and silicon leads to a high concentration of defects

- in the oxide layer, the mobility of electrons is much larger than the mobility of holes ($\mu_{\text{electrons}} = 20\,\text{cm}^2/\text{Vs}$ and $\mu_{\text{holes}} = 2 \cdot 10^{-5}\,\text{cm}^2/\text{Vs}$), leading to a separation of electrons and holes
- a high trap density at the interface region leads to an accumulation of holes

A static layer of positive charges attracts electrons from the bulk, which accumulate at the interface region and lead to an increased inter-strip capacitance and decreased inter-strip resistance. For ATLAS sensors, this effect is counteracted by positively doped implants between sensor strip implants and applying p-spray to the sensor surface.

Depending on the interface region between adhesive and sensor surface, adhesives could contribute to both surface and bulk defects: depending on the molecular structure inside the glue, electrostatic effects such as partial charges can affect the accumulation of charges in the interface area and thus contribute to surface effects. Additionally, chemical effects could lead to individual atoms being disconnected from glue molecules and drifting into the silicon bulk, contributing to impurities and interstitial atoms.

It was thus considered important to perform irradiations leading to both bulk and surface damages with glue applied to the sensor surface in order to study different types of effects.

3.3.3 Irradiations Approximating Radiation Levels in the Future ATLAS Strip Tracker

The radiation environment in the ATLAS strip tracker will consist of a mix of particles and energies which can not be provided by an irradiation facility. In order to study the effects of irradiation on sensors with glue, sensors were thus irradiated to comparable levels of fluence and ionising dose using the available facilities.

Radiation levels in the future strip tracker were simulated to reach $1.2 \cdot 10^{15}\,\text{n}_{\text{eq}}/\text{cm}^2$ and 50.4 MRad at $3000\,\text{fb}^{-1}$ (see section 2.2.3.1), which includes a safety factor of 1.5. Since this safety factor accounts for changes in the detector layout and uncertainties in the simulation, an additional safety factor of 1.5 was included to allow for run times increasing to up to $4000\,\text{fb}^{-1}$, leading to a total fluence of $2 \cdot 10^{15}\,\text{n}_{\text{eq}}/\text{cm}^2$ and ionising dose of 75.6 MRad.

Three irradiation facilities were available at the time irradiations were performed:

- the "Karlsruhe Kompakt Zyklotron" (KAZ) at Karlsruhe Institute of Technology (KIT), providing protons with an average energy of 23 MeV (hardness factor $\kappa = 2.05$ [58])
- a linear accelerator at the Los Alamos Neutron Science Center (LANSCE), providing protons with an average energy of 800 MeV (hardness factor $\kappa = 0.71$ [59])
- TRIGA-Mark-III at the Jožef Stefan Institute (JSI), providing thermal neutrons (hardness factor $\kappa = 0.9$ [60])

Table 3.2 summarises the differences in particle flux and deposited energy for each of the irradiation types. Comparing doses corresponding to the intended fluence of $2 \cdot 10^{15}\,\text{n}_{\text{eq}}/\text{cm}^2$, it was found that an irradiation with 800 MeV protons leads to a total ionising dose most comparable to the dose expected in the strip tracker. Irradiations with 23 MeV protons and

	Irradiation facility		
	KIT (23 MeV protons)	LANSCE (800 MeV protons)	JSI thermal neutrons
Fluence	$2 \cdot 10^{15}\,\mathrm{n_{eq}/cm^2}$	$2 \cdot 10^{15}\,\mathrm{n_{eq}/cm^2}$	$2 \cdot 10^{15}\,\mathrm{n_{eq}/cm^2}$
Hardness factor κ	2.05	0.71	0.9
Particle flux	$0.98 \cdot 10^{15}\,\mathrm{cm^{-2}}$	$2.81 \cdot 10^{15}\,\mathrm{cm^{-2}}$	$2.22 \cdot 10^{15}\,\mathrm{cm^{-2}}$
Stopping power	42.26 MeV $\mathrm{cm^2/g}$	4.44 MeV $\mathrm{cm^2/g}$	-
Energy deposition per particle	1.35 MeV	0.14 MeV	-
Total deposited energy	211.4 J	64.1 J	-
Total ionising dose	283 MRad	86 MRad	2 MRad [60]

Table 3.2: Fluence and corresponding ionising dose at different irradiation facilities

thermal neutrons lead to much higher or lower ionising doses, respectively. It would therefore have been preferable to conduct irradiations mainly with 800 MeV in order to reach both the intended dose and fluence.

However, there were two additional aspects to consider for the choice of an irradiation facility:

- Cooling
  Chemical reactions in glue caused by irradiations can be expected to be temperature dependent [61]. In order to investigate the impact of irradiation on sensors with glue under realistic conditions, being able to cool down the samples during irradiation was considered an important requirement. Irradiation facilities at JSI and LANSCE do not provide active cooling during irradiations and samples can heat up during irradiation, whereas KIT does provide cooling down to -20 °C.

- Activatability
  Irradiations performed for an earlier study showed that sensors irradiated using 800 MeV protons and glue samples irradiated with thermal neutrons were highly active after irradiation. These samples required long time periods before the activity had decreased sufficiently to perform further sensor tests and treatments. Irradiations with 23 MeV protons had not led to similar levels of activation and were thus considered preferable.

Taking all aspects into account, KIT was chosen to be used for baseline irradiations with additional irradiations at LANSCE and JSI. Due to a limited number of available sensors, it was not possible to have similar sets of sensors irradiated at each facility.

Four sets of sensors were sent to be irradiated:

- Sensors to be irradiated only
  Ten sensors from the same wafer (FZ2, without p-spray) were sent to be irradiated. Each glue under investigation was applied to two miniature sensors, two were left blank. Additionally, two of the sensors showed a high leakage current before treatments and were thus complemented by two more sensors from a different wafer (FZ2, without p-spray).

- Sensors to be irradiated and temperature cycled afterwards
  A set of ten sensors from the same wafer (FZ1, with p-spray) was chosen for these tests and each glue under investigation was applied to two sensors. One sensor showed an early breakdown and was thus replaced. Due to a lack of sensors from FZ1 sensors with p-spray at this point, it had to be replaced with a sensor from a FZ1 wafer without p-spray.

- Sensors irradiated at LANSCE
  Only limited numbers of sensors from the same wafer were available at this point, reducing the number of samples for this irradiation to four (FZ1 wafer, no p-spray). Two of these sensors were left blank, two were glued with DYMAX 6-621.

- Sensors irradiated at JSI
  Similar to the selection of sensors for irradiation at LANSCE, only four sufficiently similar sensors were available for this study (FZ2 wafer, p-spray). Two of the sensors were left blank for reference, two were glued with Loctite 3525.

While sensors with different architectures had to be used due to limited availability, sensors with significantly different geometries (BZ1 without p-stops and BZ6 with larger strip pitches) were excluded from these studies.

3.4 Temperature Cycles

Environmental temperatures affect glue joints in different ways:

- working temperature range
  if the environmental temperature exceeds the working temperature range, particularly glass transition temperature or melting point, chemical connections between glue molecules and connected materials can fail, leading to a weakened or failing glue joint

- mechanical stress induced by temperature changes
  glue joints connecting materials with different coefficients of thermal expansion experience mechanical stress during temperature changes when materials expand or contract to different extents. Repeated temperature changes of glue joints can thus lead to repeated bending and relaxing of the involved materials, leading to a weakened glue joint over time.

- ageing
  Chemical reactions in glue molecules can lead to the production of decay products, which can react with and degrade the connected materials or fumigate and react with e.g. the silicon sensor surface. Ageing processes can be sped up by increased temperatures, allowing to simulate the end-of-life performance after a short time period at higher temperatures.

While all adhesives under investigation are known to have a working temperature range sufficient for the ATLAS ITk [49], both the impact of repeated mechanical stresses following temperature changes and possible chemical reactions of the glues with the sensor surface were important subjects of investigation.

Sensor samples were not available in sufficiently large quantities of similar sensor types to study both effects separately. As a compromise, a thermal cycling procedure was used which combined both aspects of temperature tests.

3.4.1 Temperature Changes

In silicon strip sensor modules, the glue layer under investigation connects silicon sensors and circuit boards consisting of layers of polyimide (34 %), adhesive (11 %), copper (34 %) and solder resist (21 %) [62], percentages by mass. For the samples used in this study, FR4 pieces were glued onto silicon miniature sensors.

Table 3.3 summarises the material characteristics relevant to estimate the stress induced by temperature changes.

	Modulus of elasticity, GPa	Coefficient of thermal expansion, µm/(m·°C)	Poisson's ratio	Density, g/cm^3
Silicon	131	3	0.24	2.33
Epolite Ⓡ FH-5313 [50]	2.3$^{(*)}$	94	0.4$^{(**)}$	1.17
Loctite Ⓡ 3525 [48]	0.175	97	0.4$^{(**)}$	1.08
DYMAX Ⓡ 6-621 [47]	0.73	n.s.	0.4$^{(**)}$	1.08
DYMAX Ⓡ 3013 [46]	0.35	n.s.	0.4$^{(**)}$	1.04-1.07
FR4 [63]	21-24	11-15	0.12-0.14	1.8-1.9
Polyimide [64]	2.5	20	0.34	1.42
Adhesive	n.s.	n.s.	0.4$^{(**)}$	n.s.
Copper	117	17	0.35	8.92
Solder resist	n.s.	n.s.	0.38 [65]	n.s.

$^{(*)}$ No information was available for the modulus of elasticity of Epolite FH 5313, it was thus estimated from the information in [66].
$^{(**)}$ Information about the Poisson's ratio was not provided for any of the adhesives under investigation and was thus assumed to be similar to the average value for epoxy glues [67]

Table 3.3: Modulus of elasticity, coefficient of thermal expansion and density for adhesives and hybrid materials. Entries n.s. indicate information not provided by the manufacturer.

A hybrid consists of several layers of materials with different characteristics, where no information is provided about the thermal or mechanical characteristics of the used solder resist or adhesive. A coarse estimate for the properties of a hybrid was attempted making the approximations that the hybrid consisted only of copper and kapton. Since thermal expansion and contraction are unrestricted perpendicular to the sensor surface and exert mechanical stress only when occurring parallel to it, its cross-section was approximated to have both materials homogeneously distributed.

These simplifications allowed to calculate the hybrid CTE as [68]:

$$\alpha_{\text{hybrid}} = \frac{\alpha_{\text{copper}} \cdot \frac{f_{\text{copper}} \cdot E_{\text{copper}}}{\rho_{\text{copper}}} + \alpha_{\text{polyimide}} \cdot \frac{f_{\text{polyimide}} \cdot E_{\text{polyimide}}}{\rho_{\text{polyimide}}}}{\frac{f_{\text{copper}} \cdot E_{\text{copper}}}{\rho_{\text{copper}}} + \frac{f_{\text{polyimide}} \cdot E_{\text{polyimide}}}{\rho_{\text{polyimide}}}}, \tag{3.3}$$

where α is the coefficient of thermal expansion, f is the volume fraction, E is the modulus of elasticity and ρ is the density of a material. The CTE of a hybrid was thus estimated to be about 17.1 µm/(m $\cdot^{\circ}$ C).

Using the same assumptions as above, the hybrid's modulus of elasticity was estimated as [69]:

$$E_{\text{hybrid}} = f_{\text{copper}} \cdot E_{\text{copper}} + f_{\text{polyimide}} \cdot E_{\text{polyimide}}, \tag{3.4}$$

where E is the modulus of elasticity and f is the volume fraction. The modulus of elasticity was coarsely estimated to be 41 GPa.

For a joint of different materials, the stresses induced by temperature changes can be estimated from the joint geometry and individual material properties (described in [70]).

In order to understand the stresses occurring in a glue layer connecting two materials, both connections were treated as two individual connections of two materials each: a connection of glue and sensor and a connection of glue and FR4.

In a given material with a linear coefficient of thermal expansion α, a temperature change ΔT causes a strain ϵ:

$$\epsilon = \alpha \cdot \Delta T \tag{3.5}$$

For isotropic materials, this strain occurs equally in all directions:

$$\epsilon_x = \epsilon_y = \epsilon_z \tag{3.6}$$

If a material is constrained and its expansion is blocked, the occurring strain results in stress σ in the material:

$$\sigma = \epsilon \cdot E, \tag{3.7}$$

where E is the modulus of elasticity of that material.

Since the material is effectively compressed in the constraint direction, it will try to expand perpendicular to the constraint:

$$\epsilon_{\perp} = -\nu \cdot \frac{\epsilon}{E}, \tag{3.8}$$

where ν is the material's Poisson's ratio.

For a joint of materials connected over an area A oriented in x and y, both materials can expand in z-direction without causing stress. Assuming the involved materials 1 and 2 are isotropic, they expand equally in x and y, so that the stresses σ in both directions can be assumed to be identical:

$$\sigma_{1,x} = \sigma_{1,y} = \sigma_1, \sigma_{2,x} = \sigma_{2,y} = \sigma_2 \tag{3.9}$$

In both x and y-direction, the forces F acting on materials 1 and 2 can be assumed to be in equilibrium:

$$F_{1,x} = -F_{2,x}, F_{1,y} = -F_{2,y} \tag{3.10}$$

Since the stress in an area A is calculated from

$$\sigma = \frac{F}{A}, \tag{3.11}$$

equation 3.10 becomes

$$\sigma_{1,x/y} \cdot A_{1,x/y} + \sigma_{2,x/y} \cdot A_{2,x/y} = 0, \tag{3.12}$$

where $A_{1/2,x/y}$ are the cross-sections of materials 1 and 2 in the yz/xz-plane. Since the glue layer forms a strong connection with the other material, the strains in both layers can be assumed to be identical:

$$\epsilon_x = \epsilon_y = \epsilon_1 = \epsilon_2 = \epsilon \tag{3.13}$$

Summing up all contributions to thermal expansion (equations 3.5, 3.7 and 3.8), the occurring strain can be calculated as:

$$\epsilon = \alpha \cdot \Delta T + \frac{\sigma}{E} - \nu \cdot \frac{\sigma}{E} \tag{3.14}$$

Using equations 3.12 and 3.13, the stresses can be calculated, too:

$$\sigma_{1/2} = \frac{\Delta T \cdot E_{2/1} \cdot (\alpha_{2/1} - \alpha_{1/2})}{\frac{E_{2/1}}{E_{1/2}} \cdot (1 - \nu_{1/2}) + \frac{A_{1/2}}{A_{2/1}} \cdot (1 - \nu_{2/1})} \tag{3.15}$$

The dimensions of the involved materials were approximated:

- the size of the FR4 pieces glued onto miniature sensors ($3 \times 7\,\mathrm{mm}^2$), with a sensor thickness of 320 µm and a glue layer thickness of 145 µm 3.2
- the size of a glue area in a gluing stencil [71] with an area increase corresponding to a thickness decrease during gluing [62]: $1.56 \times 16.25\,\mathrm{mm}^2$, assuming the same areas covered on both hybrid and sensor
- for the calculation of stresses from two-material joints at a time, the assumed glue thickness was divided by two

Module glue joints are made under cleanroom conditions at temperatures of about 20 °C. During operation, sensors are cooled down to -20 °C, corresponding to a temperature change of -40 °C, which was also used for the calculations.

Table 3.4 summarises the calculated stresses for different glue joints. The results calculated from theoretical behaviour show that the stresses expected to occur in the miniature sensors used for these studies are comparable to the stresses occurring in actual detector modules. The stresses in miniatures were found to be slightly higher than those in detector modules, making their thermal cycling a reasonable approximation of a full detector module. It should be mentioned that for several of the glues, parameters were unknown (e.g. Poisson's ratio or coefficient of thermal expansion) and had to be guessed based on typical glue parameters.

The stresses from both the silicon sensor and the hybrid/FR4 were found to exert approximately the same stresses on the glue, so that the stress can be assumed to be approximately homogeneous throughout a glue layer. Because all glues have higher coefficients of thermal expansion than the other materials involved and thus contract more when being cooled, the

		Stresses in glue layers, [MPa]			
		DYMAX 3013	DYMAX 6-621	LOCTITE 3525	Epolite FH-5313
Modules	hybrid-glue	1.9	3.9	0.9	11.6
	glue-sensor	2.2	4.6	1.1	13.9
Samples	FR4-glue	2.0	4.1	1.0	12.3
	glue-sensor	2.2	4.6	1.1	13.9
	glue strength	18 MPa	20 MPa	24 MPa	55 MPa

Table 3.4: Approximate stresses in glue layers for modules and miniature sensors constructed for glue tests. Glue properties were estimated from standard glue values, were not provided in data sheets. All stresses were found to be below the strength of the individual glues, i.e. not in danger of damaging the glue layer.

stress exerted on them corresponds to a pulling stress. The calculated stresses in all glue layers are much lower than their respective strengths, so that a temperature change of -40 ℃ can be assumed not to damage the glue joint.

Epolite FH-5313 shows the largest stress due to its high modulus of elasticity. Additionally, repeating the calculation for stresses occurring in silicon, silicon connected to Epolite was found to have a higher stress (3 MPa, compressive) than the other glues (0.5-1 MPa), which could cause damages in the sensor, such as micro-cracks. While the glue connection can be assumed to stay intact during the temperature change, repeated temperature variations would be able to weaken the glue joint or damage the sensor. It was thus decided to study possible impacts on the sensor performance by performing 100 temperature cycles and studying the sensor performance afterwards.

Additionally, irradiation studies (see section 4.2) found that UV glues become less elastic by irradiation, i.e. their modulus increases. Similar to the behaviour of Epolite FH-5313, this change can be expected to increase the stress on the glue. No information about the modulus of elasticity of irradiated glues were available, the effect was thus studied directly by irradiating sensors before thermal cycling and investigating their performance afterwards. These studies were performed in addition to the sensors which were only thermally cycled.

3.4.2 Ageing

In the future ATLAS detector, silicon strip sensor modules will be operated at -20 ℃ for about 10 yrs, with periods of an estimated two months per year at room temperature. According to a general rule for chemical processes, such as the ageing of glue, the speed of a chemical reaction is increased two to four times if the temperature is increased by 10 ℃ [72]. The speed increase factor, called Q_{10} factor, is reaction specific and unknown for the adhesives under investigation. For an assessment of the required ageing time, Q_{10} factors of 2 and 4 were used as a lower and upper estimate, respectively.

The ageing process is faster for higher temperatures, hence the maximum cycling temperature

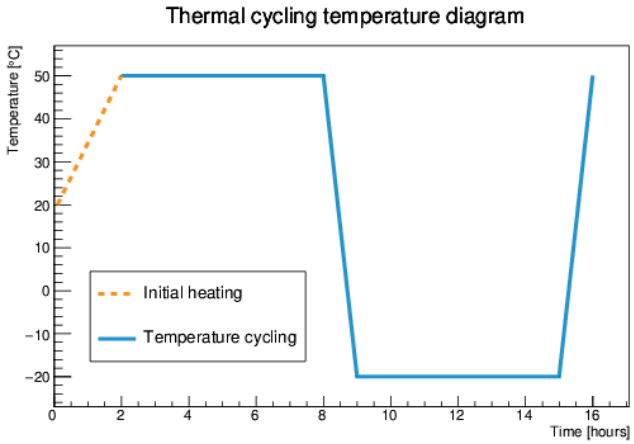

Figure 3.7: Climate diagram for the cycling of miniature sensors with glue samples: after an initial heating period, the temperature cycles (temperature extrema held for six hours each with transition times of 1 hour each) were performed 100 times.

was chosen to be as high as possible without affecting any of the involved materials beyond accelerating the normal ageing behaviour. A maximum temperature of +50 °C used, which is slightly higher than the lowest glass transition temperature of the involved glues (43 °C for Loctite 3525), which was considered not to have a negative impact. For comparability, the same maximum cycling temperature was used for all miniature sensors. Table 3.5 summarises the required ageing times at 50 °C to investigate the ageing behaviour of sensor module glue joints. Following the procedure of previous temperature cycling procedures [49], a total of 600 hours at

		Accelerated ageing at +50 °C		
	Time	Time for $Q_{10} = 2$	Time for $Q_{10} = 3$	Time $Q_{10} = 4$
Operation at -20 °C	220 months	52 days	3 days	0.4 days

Table 3.5: Time required for the simulated ageing over ten years of operation cooled down to -20 °C, assuming different temperature acceleration factors.

50 °C were scheduled, corresponding to 220 months at -20 °C for a Q_{10} factor of 2.2.

3.4.3 Performed Cycles

Following the requirements outlined in the previous sections, the temperature was cycled between -20 and +50 °C. A transition time of one hour was chosen in accordance with the limits of the climate chamber in use [73]. Temperature extremes were held for six hours each, allowing a sufficient ageing of the components. The corresponding climate diagram is shown in figure 3.7 100 temperature cycles were performed with the humidity level of the climate chamber below 15 %, where possible. Hence, each sensor was kept at -20 °C and +50 °C for 600 hours each.

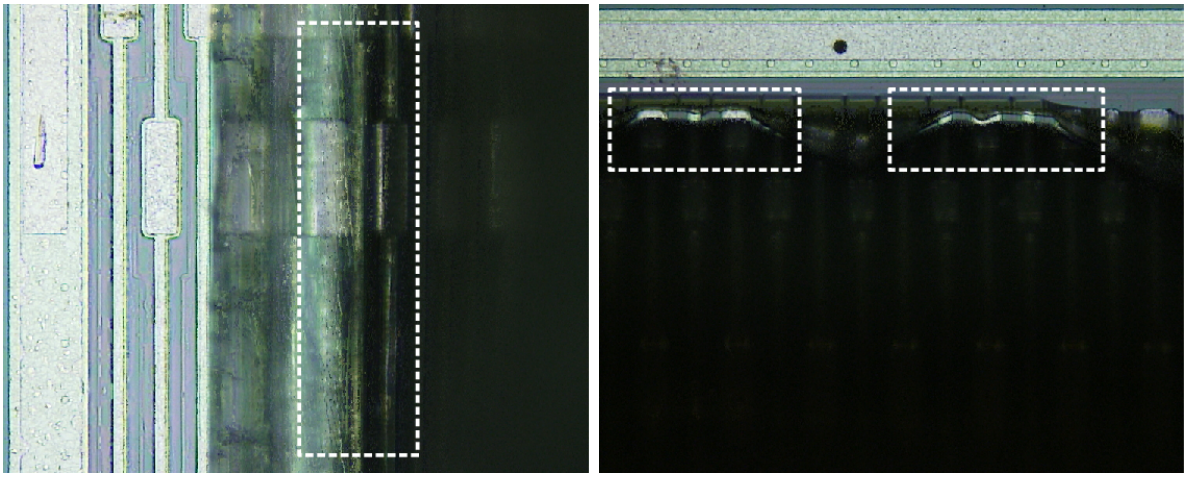

(a) fine cracks inside a glue layer (b) openings in a glue layer caused by cracks

Figure 3.8: Cracks inside DYMAX 3013 glue layers on sensors after temperature cycling (left) and temperature cycling after irradiation (right).

Under the assumption that the ageing of glue does not have a very low reaction rate with a Q_{10} factor below 2.2, 600 hours at +50 °C exceed the ageing expected for 220 months at -20 °C.

Irradiation in combination with temperature cycling was considered the most important part of the study, as it corresponded most closely to the final performance of sensors in the ATLAS Inner Tracker. Hence, the best quality sensors were chosen for this study: 10 float zone 1 type miniature sensors from the same wafer were used (see section 3.3.3).

In addition to the tests of irradiation and thermal cycling combined, another series of sensors was only temperature cycled, both in order to quantify the impact of thermal cycling directly and as a backup for sensors irreversibly damaged by irradiation and temperature cycling. Ten float zone type 2 miniature sensors from the same wafer were used for these studies, of which two were left blank and each of the four glues was used on two of the remaining sensors.

3.5 Observations after Treatments

All sensors were visually inspected after their respective treatments had been concluded using a Keyence laser microscope [74]. On several sensors, the glue layer showed cracks at the edge of the glue layer, either as a structure within the glue layer (see figure 3.8a) or as openings in the glue layer (see figure 3.8b). Table 3.6 summarises the sensors for which the effect was observed. While the small sample size does not allow to draw any reliable conclusions, several observations can be made: After separate proton irradiation and temperature cycling, only individual cases of damaged glue layers were observed. Sensor which were both irradiated and temperature cycled did show cracked glue layers for more than half of the samples, indicating that the glues were more susceptible to the stress from temperature cycling after irradiation. This effect was studied further in structure analyses of irradiated glues (see chapter 4.1). Additionally, cracks

	Adhesive on sensor			
	DYMAX 3013	DYMAX 6-621	Loctite 3525	Epolite FH-5313
Proton irradiation	1/2	0/2	0/4	0/2
Temperate cycling	1/2	1/2	0/2	0/2
Irradiation + cycling	1/2	2/2	1/2	1/2

Table 3.6: Sensors showing cracked glue layers after treatments. Cracks were found to occur most often after irradiation and temperature cycling. Glue on samples irradiated with thermal neutrons or 800 MeV protons did not show cracks in the glue layer.

in glue layers were observed more often for more fluid glues (DYMAX 3013 and DYMAX 6-621) than for more viscous glues (Loctite 3525 and Epolite FH-5313). This effect might depend on fluid glues spreading wider, leading to a thinner film and cracking more easily. But it should be noted that the effect could only be observed for glue emerging from under the FR4. If the glue area was covered under the FR4, which occurred more often for more viscous glues, no damages in the glue layer could be observed.

In conclusion, visual observations indicated that glues after irradiation and temperature cycling were most likely to show damages. An observed preference for more fluid glues to break more easily can not be unambiguously attributed to the glue viscosity alone.

4 Material Studies of Irradiation Effects on Adhesives

4.1 Irradiation studies

The main focus of the presented studies is the behaviour of silicon strip sensors under the combined stresses of gluing and irradiation or thermal cycling. Irradiation parameters were chosen to approximate the radiation damage in silicon. For all types of radiation, sensors were irradiated up to a fluence of $2 \cdot 10^{15}\,\mathrm{n_{eq}/cm^2}$ (see section 3.3), which, e.g. in case of proton irradiations, lead to an ionising dose much higher than expected in the ITk strip tracker.

In order to be able to attribute effects observed for irradiated sensors with glue to changes in the glue layer, the impact of irradiation on the adhesives under investigation was studied directly. Dedicated glue samples were prepared and irradiated for chemical analysis, so that molecular changes could be studied and possibly quantified.

In parallel to sensor irradiations, glue samples were irradiated under the same environmental conditions. Samples of all glues under investigation were arranged on a polyethylene plate, chosen for its low activatability after irradiation. Due to size constraints at the irradiation facilities in Los Alamos and JSI, glue samples were arranged on an area of $8 \times 8\,\mathrm{mm^2}$ (see figure 4.1). For each available type of radiation, glue samples were irradiated up to the equivalent of silicon fluences of 1, 2, 3 and $4 \cdot 10^{15}\,\mathrm{n_{eq}/cm^2}$, so that quantifiable changes could be tracked over a range of irradiation levels.

After all irradiations had been performed, the samples were found to be too active to perform any abrasive procedures. The samples were allowed a year, stored at -20 °C, for their activity to subside before doing any analysis. Table 4.1 shows an overview of the irradiated samples and their status. From the samples suitable for chemical analysis, glue samples irradiated in Los Alamos and at KIT up to 1 and $2 \cdot 10^{15}\,\mathrm{n_{eq}/cm^2}$ were chosen for further analysis. Since sensors were irradiated up to $2 \cdot 10^{15}\,\mathrm{n_{eq}/cm^2}$ as well, these fluences were found to be the most important to understand the glue radiation damage in the sensor samples. Both Epolite FH-5313 and the UV cure glues under investigation showed colour changes after irradiation, with the colour intensity increasing from light yellow to yellow-orange for the UV cure glues and dark orange-brown for Epolite FH-5313. Glues irradiated with 23 MeV protons showed much more intense colours than samples irradiated with 800 MeV.

Within the same glue, colour changes can be associated with chemical changes, i.e. a stronger colour change indicates that a chemical reaction producing a certain colour occurred more often. This comparison is only valid for samples of the same glue, as chemicals in different glues show colour changes at different rates. For samples of the same glue, differences can be understood by comparing the different types of irradiation using the hardness factor κ. The hardness factor quantifies the difference in radiation damage by non-ionising energy losses (NIEL) in

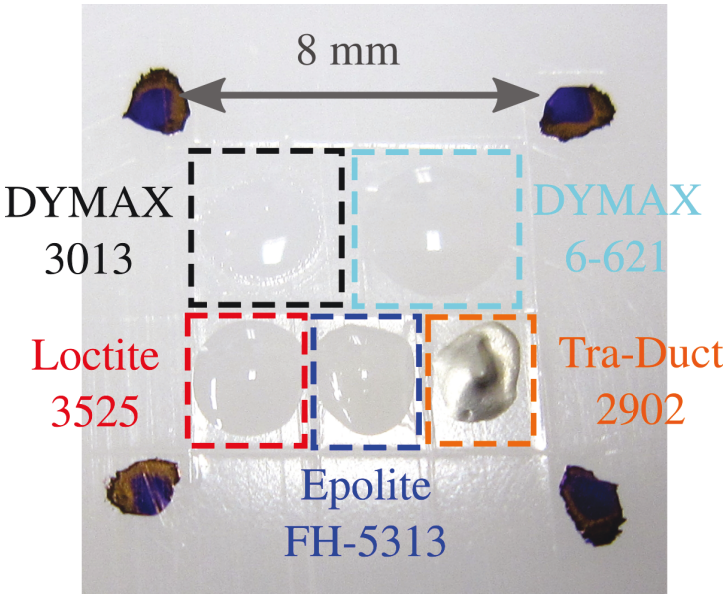

Figure 4.1: Polyethylene plate with samples of three UV cure glues as well as Epolite FH 5313 and a silver epoxy glue. Highly fluid glues (DYMAX 3013 and -621) were allocated larger areas in order to accommodate a sufficient volume. Corners of the glue sample area were marked to simplify alignment in the beam area.

	Irradiation facility		
	JSI (reactor neutrons)	KIT (23 MeV protons)	Los Alamos (800 MeV protons)
$1 \cdot 10^{15}\,n_{eq}/cm^2$	active	inactive	inactive
$2 \cdot 10^{15}\,n_{eq}/cm^2$	active	inactive	inactive
$3 \cdot 10^{15}\,n_{eq}/cm^2$	active	inactive	active
$4 \cdot 10^{15}\,n_{eq}/cm^2$	active	inactive	active

Table 4.1: Overview of irradiated samples and their activity status in September 2016. While all samples irradiated at KIT were suitable for chemical analysis, all neutron irradiated samples were too active to be analysed. The measured activities included both glue samples and polyethylene plate, making the absolute activity of only minor interest.

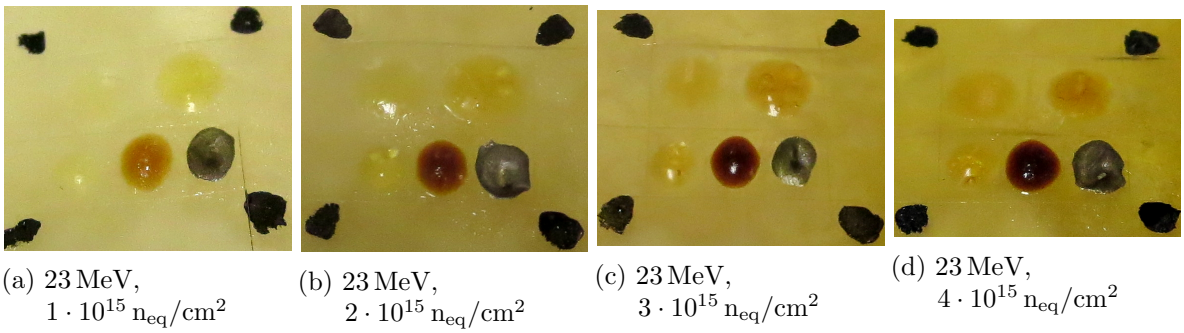

(a) 23 MeV, $1 \cdot 10^{15}$ n_{eq}/cm^2
(b) 23 MeV, $2 \cdot 10^{15}$ n_{eq}/cm^2
(c) 23 MeV, $3 \cdot 10^{15}$ n_{eq}/cm^2
(d) 23 MeV, $4 \cdot 10^{15}$ n_{eq}/cm^2

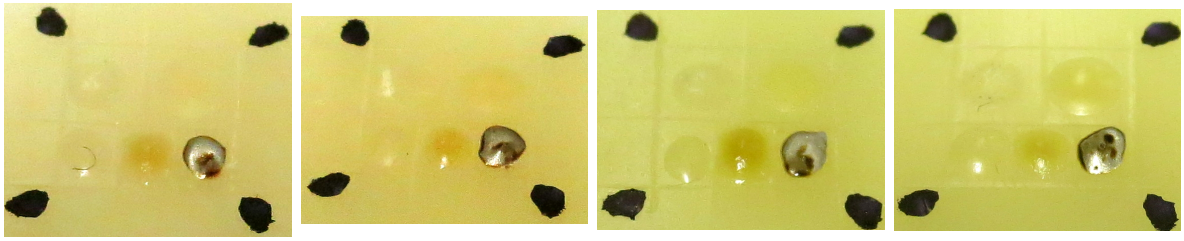

(e) 800 MeV, $1 \cdot 10^{15}$ n_{eq}/cm^2
(f) 800 MeV, $2 \cdot 10^{15}$ n_{eq}/cm^2
(g) 800 MeV, $3 \cdot 10^{15}$ n_{eq}/cm^2
(h) 800 MeV, $4 \cdot 10^{15}$ n_{eq}/cm^2

Figure 4.2: Glue samples on polyethylene after irradiations with 23 and 800 MeV up to different fluences. All UV glues samples, initially transparent, show colour changes with increasing fluences, with Epolite FH-5313 (bottom middle) showing the darkest colour after irradiation. Colour changes in samples irradiated with 23 MeV protons show much more significant colour changes than samples irradiated with 800 MeV protons.

silicon compared to the radiation damage by neutrons with an energy of 1 MeV. For KIT and Los Alamos, the hardness factors are 2.05[58] and 0.71[59], respectively, so that a fluence of $2 \cdot 10^{15}\,\mathrm{n_{eq}/cm^2}$ is reached by irradiation with $0.98 \cdot 10^{15}\,\mathrm{protons/cm^2}$ for a proton energy of 23 MeV or $2.82 \cdot 10^{15}\,\mathrm{protons/cm^2}$ for a proton energy of 800 MeV.

For an estimate of the energy deposition by irradiation, the stopping powers of protons were used. While no information was available about stopping powers of protons in the adhesives under investigation, these parameters were approximated by using stopping powers of common plastics (see figure 4.3) [75]. While the absolute stopping powers of plastics vary for different

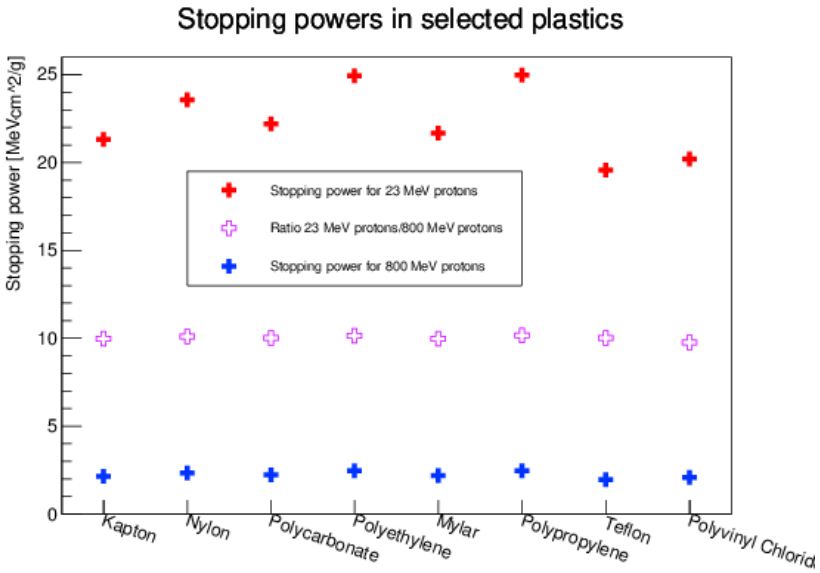

Figure 4.3: Stopping powers for 23 MeV and 800 MeV protons in different plastics. While the stopping powers show variations for different materials, the stopping power rations were found to be constant.

materials (around 20(2) $\mathrm{MeV \cdot cm^2/g}$ for 23(800) MeV protons), the ratio of stopping powers at both energies is constant at 10. Since adhesives are chemically similar to plastics, this ratio can be assumed to be similar in the glues under investigation.

Combining the difference in particle flux (about three times as many 800 MeV protons as 23 MeV protons) and stopping power (a factor of about ten), a fluence of $2 \cdot 10^{15}\,\mathrm{n_{eq}/cm^2}$ of 23 MeV protons deposits approximately about 10/3 times as much energy in the glue samples as a fluence of $2 \cdot 10^{15}\,\mathrm{n_{eq}/cm^2}$ from 800 MeV. Assuming that colour change correlates with deposited energy, a visual comparison of all samples matches this approximation: the colour changes of the sample irradiated up to $4 \cdot 10^{15}\,\mathrm{n_{eq}/cm^2}$ with 800 MeV protons are comparable to the sample irradiated up to $1 \cdot 10^{15}\,\mathrm{n_{eq}/cm^2}$ with 23 MeV protons.

Using an approximate glue dot radius of 2 mm, average glue thickness of about 100 µm and glue density of $1.1\,\mathrm{g/cm^3}$, an estimate for the ionising dose deposited in each glue sample could be made (see section 3.3.3). Without knowing the actual stopping power in glue, an average value was calculated using comparable polymers (2 MeV $\mathrm{cm^2/g}$ for 800 MeV protons, 22 MeV

cm^2/g for 23 MeV protons).

Using these values, $1 \cdot 10^{15}\,n_{eq}/cm^2$ of 23 MeV protons deposit about 1.7 MGy per glue sample, and about 0.5 MGy per glue sample from 800 MeV protons. While this dose is much higher than the dose expected in the ITk strip tracker (60 to 288 kGy in the end-cap and 46 to 218 kGy in the barrel [76]), it corresponds to the dose seen by glue layers on the studied sensor samples in order to reach sufficient fluences.

Reactor neutrons from JSI are known to have a hardness factor $\kappa = 0.9$ and an ionising dose of $1 \cdot 10^{14}\,n_{eq}/cm^2 = 100$ kRad [60], making the ionising dose in samples irradiated up to $2 \cdot 10^{15}\,n_{eq}/cm^2$ approximately 2 MRad, i.e. lower than the ionising dose expected in the ATLAS strip tracker.

Chemical covalence bonds in polymers have typical energies of $\mathcal{O}$(eV) (3.61 eV between carbon atoms, 4.28 eV between hydrogen and carbon atoms, 5.07 eV between chloride and carbon atoms [77]). Energies of all radiation types were sufficient to break these covalence bonds, which connect the molecules in a glue layer. The overall impact on the adhesive depends on its specific chemical structure: broken covalence bonds can result in disconnected polymer molecule fragments, weakening the glue layer, or to broken molecule chains reattaching themselves to different molecules, improving interconnectivity of the glue molecules and strengthening the glue layer [61]. The aim of the studies presented in this chapter was to investigate the specific impact of irradiation on different glues and, if possible, quantify the occurring radiation damage.

4.2 Feasibility Studies

In cooperation with the Infrapark Basel, different standard chemical analyses were tested in order to find a method that would allow a qualitative and, if possible, quantitative conclusion about the impact of irradiation on the glues under investigation.

For initial feasibility studies, two samples of DYMAX 6-621 with approximately 1 g each were prepared: both were cured with UV light for 1 min. One of the samples was then irradiated up to a fluence of $1 \cdot 10^{15}\,n_{eq}/cm^2$ with 23 MeV protons.

Three methods of structure analysis were investigated:

- quadrupole time-of-flight mass spectrometry
- size-exclusion chromatography
- gas chromatography - mass spectrometry

Each of these methods required dissolving the glue sample in a solution, which could then be analysed. Since the molecular structure of the glue was unknown, different organic solvents were tested for usability:

- dimethylformamide
- chloroform
- hexane

- tetrahydrofuran
- fluorinated alkanes
- fluorinated alcohols

It was found that while different solvents were able to dissolve the unirradiated glue sample, none of the samples were able to fully dissolve the irradiated sample. This discrepancy indicates that irradiation did not lead to a weakening of the chemical connections, but caused a higher level of interconnectivity between the glue molecules (called cross-linking), corresponding to a stronger glue joint.

Instead of fully dissolving the samples, tetrahydrofuran extracts were produced instead, where

1. the samples were cooled down with liquid nitrogen and crushed in a mortar
2. 2 mg of glue are added to 10 ml of hydrofurane
3. the solution is heated to 40 °C for 30 min and then left over night at 25 °C

The resulting extract was used for further analysis. Hence, the results shown below indicate changes of glue molecules present in the extract and do not present the full spectrum of molecules in glue after curing.

4.2.1 Quadrupole Time-of-Flight Mass Spectrometry

A first attempt to analyse the differences between glue before and after irradiation was made using time-of-flight mass spectrometry [78]. This method required the molecules in a solution to be ionised, so that they can be accelerated by voltage. The kinetic energy of each molecule can then be calculated as:

$$E_{\text{kin}} = U \cdot q, \tag{4.1}$$

where U is the accelerating voltage (here: 2 kV) and q is the charge of the molecule, usually ± 1 e. While all molecules can be assumed to have the same kinetic energy after acceleration, their velocities depend on their respective masses:

$$v_{\text{molecule}} = \sqrt{\frac{2 \cdot E_{\text{kin}}}{m_{\text{molecule}}}} \tag{4.2}$$

After passing the accelerating field, the ions pass through a quadrupole magnet which performs an initial selection of molecules in a defined mass window. By recording the numbers of collected molecules in short time bins, the spectrum of molecule weights per charge in a solution can be determined.

Figures 4.4a and 4.4b show the results as provided by the analysis software for extracts of irradiated and unirradiated DYMAX 6-621 in tetrahydrofuran. The spectra obtained from the quadrupole time-of-flight measurements show separate peaks rather than continuous distributions. This structure can be attributed to the readout time of the mass analyser: after ions of a specific weight have been registered by the readout system, molecules with a slightly

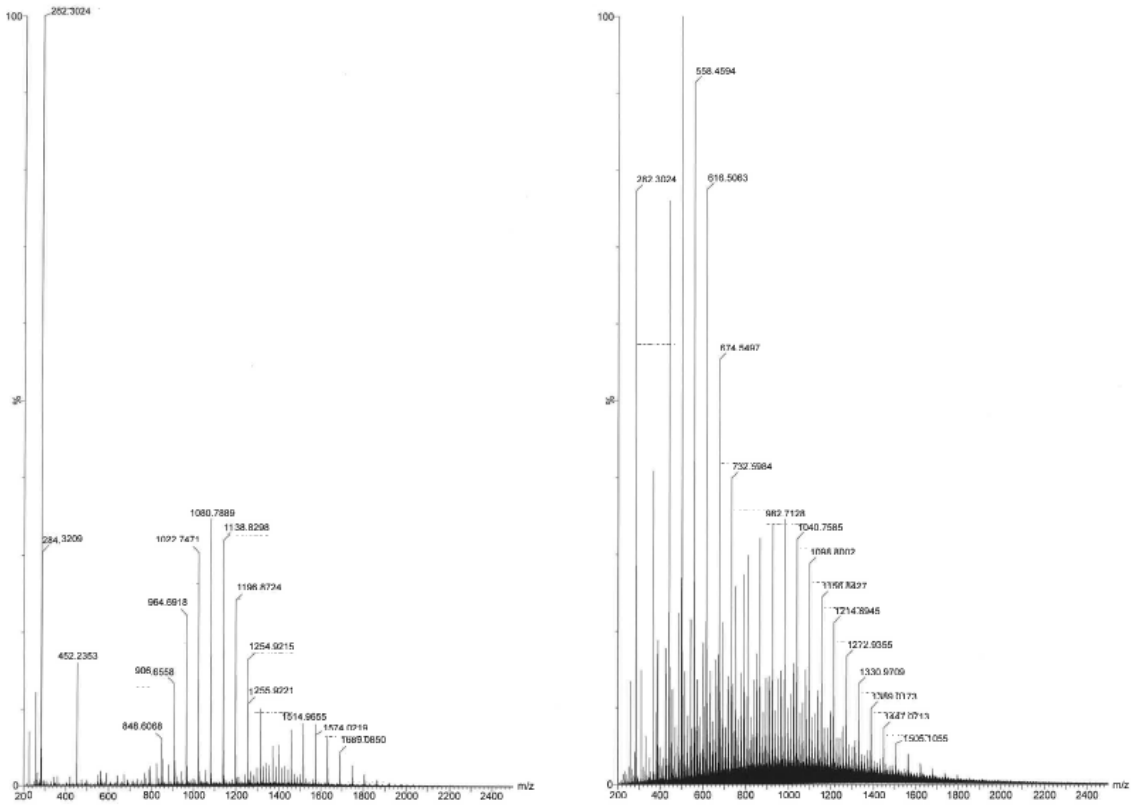

(a) Analysed solution: extract of unirradiated DY-MAX 6-621 in tetrahydrofuran

(b) Analysed solution: extract of irradiated DY-MAX 6-621 in tetrahydrofuran

Figure 4.4: Mass/charge spectra obtained from quadrupole time-of-flight mass spectrometry analysis showing the intensity registered intensity for specific mass/charge combinations. The irradiated sample shows a larger spread of molecule weights up to higher retention times. Results of these measurements were provided only as plots, raw data was not available.

higher mass and retention time can not be read out until the downtime has passed, leading to a continuous spectrum being registered as a discrete distribution.

The results show qualitatively, that, in the irradiated glue sample, molecules with longer retention times (i.e. higher weights) were found than in the unirradiated glue sample. This observation supports the conclusions drawn from the solubility of both samples in organic solvents: irradiation seems to cause the formation of additional covalence bonds, leading to larger molecule clusters. This method allowed neither an identification of the molecules corresponding to individual peaks nor a quantification of their content. It was thus rejected as a method to further study radiation damages in the glues under investigation.

4.2.2 Gel Permeation Chromatography

Size-exclusion chromatography, such as gel permeation chromatography, is a standard method for the analysis of polymers [79]. Polymers are produced from short carbon-based molecules and can have a large range of resulting molecule chain lengths, which can be used as a quality criterion of the polymerisation process. While glue molecules do not follow the exact same process, they do form connections between molecules, effectively forming larger molecules comparable to polymers. For the investigation of irradiation effects on glue, the molecule size was considered a useful criterion to differentiate between the formation of new connections between molecules or broken connections causing smaller molecules.

Gel permeation chromatography is based on the observation that molecules of different sizes travel through gel at different velocities: small molecules get trapped in small pores, while larger molecules can move unobstructed. This mechanism can be used to divide molecules according to their size: a mixture of molecules is filled into a hollow tube (size exclusion column) that is filled with e.g. polymer beads with different pore sizes. Particles move through the column according to their size: the larger a molecule, the sooner it travels through the column. The pore sizes define the usability range of the column: insufficient small or large pore sizes lead to all very small or very large molecules passing through the column without differentiability.

The solution is collected after passing through the column (then called eluate), with the time passed since filling the column (retention time) corresponding to the molecule size. By monitoring the eluate continuously or in short time bins, the fraction of molecules with certain sizes can be evaluated. Figure 4.5 shows the results for an unirradiated sample of DYMAX 6-621, solved in tetrahydrofuran, in comparison with an irradiated sample, extract in tetrahydrofuran. The separate peaks for small molecule sizes indicated that some of the constituents of uncured glue were still present in the cured samples: if the molecules had formed covalence bonds with other molecules, a spectrum of molecule sizes would be visible. The irradiated glue sample showed smaller peaks than the unirradiated glue sample, suggesting that the curing process had continued during irradiation. Since the permeation process could not be calibrated for each glue constituent, the peaks could not be attributed to individual components.

For larger molecule sizes, i.e. connected molecules, the irradiated sample showed a higher fraction than the unirradiated sample, indicating that more connections had been formed by the polymers during irradiation. This result qualitatively supported the conclusions drawn from the solubility of both glue samples in organic solvents and quadrupole time-of-flight mass spectrometry: the irradiated sample seemed to have continued forming covalence bonds during

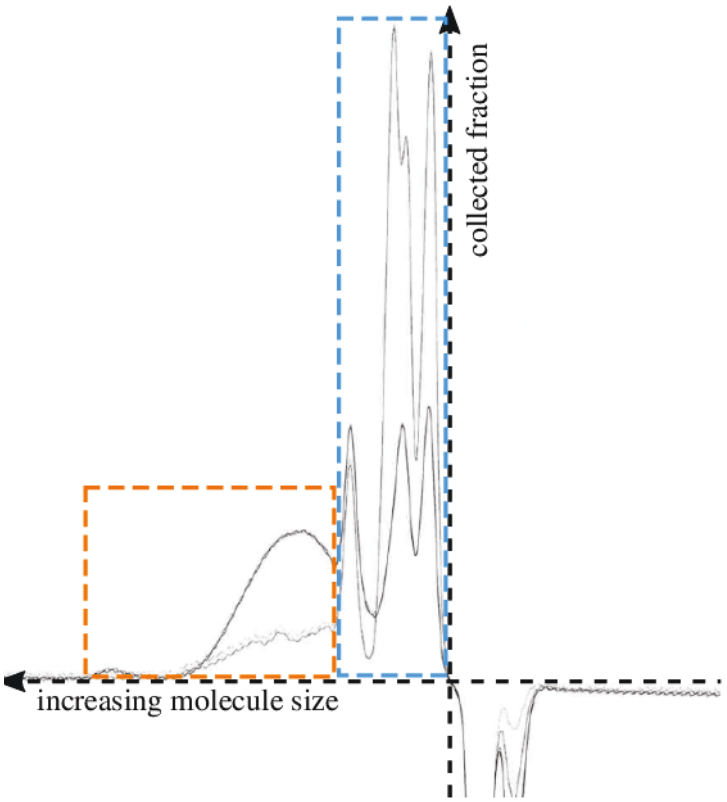

Figure 4.5: Results of a Size Exclusion Chromatography for an irradiated and an unirradiated sample of DYMAX 6-621 as provided by the testing facility (Infrapark Basel). From left to right, the molecule size decreases, i.e. the time required to pass the size exclusion column increases. The thick black line represents the irradiated glue sample, the thinner line the unirradiated glue sample. Two effects can be seen in the plot: for low molecule sizes (marked by the blue frame), separate peaks can be distinguished, with the unirradiated sample showing higher peaks than the irradiated sample. For higher molecule sizes (marked by the orange frame), a continuous spectrum of sizes can be seen, with the irradiated sample having a visibly larger content than the unirradiated sample. Results of these measurements were provided only as plots, raw data was not available.

irradiation and thus provided higher connectivity of individual modules.

It should be noted that no information was provided about the maximum molecule size:

- the molecule size exceeding the largest pores in use, resulting in an unobstructed path through the size exclusion column
- the molecule size too large to travel through the column at all

Quantitative results concerning the molecule sizes in irradiated in unirradiated samples were thus considered unreliable.

The method did, however, allow to draw qualitative conclusions about the impact of irradiation on DYMAX 6-621. It was thus considered to be a useful method to draw qualitative conclusions about the impact of radiation glue.

4.2.3 Gas Chromatography - Mass Spectrometry

As an alternative to the previous methods, which allowed to separate molecules according to size or molecular weight, gas chromatography in combination with mass spectrometry was investigated as possible technique to obtain quantifiable results.

This method combines selection by size (gas chromatography) and selection by mass (mass spectrometry), which allows to distinguish between molecules of similar sizes or masses that could not be separated by using size or mass exclusion spectrometry individually [80].

In a gas chromatograph, similar to gel permeation chromatography, the extract is transported through a column filled with size exclusion structures. The transport through the column is achieved by a gas flow, e.g. helium or hydrogen. Larger molecules travel faster through the column than smaller molecules, making the eluate sorted by molecule size.

The molecules are then captured, ionised and exposed to a magnetic field B, in which ionised particles are accelerated by Lorentz force F_L:

$$F_\mathrm{L} = Q \cdot (E + v \times B), \tag{4.3}$$

where E is the electrical field and Q and v are the charge and velocity of an ion. The magnetic field forces each ion on a circular path, where

$$\frac{m \cdot v^2}{r} = Q \cdot v \cdot B, \tag{4.4}$$

so that the radius of the particle track is given by:

$$r = \frac{v \cdot m}{B \cdot Q} \tag{4.5}$$

Inside the magnetic field, the ions can break into smaller molecules and their tracks separate according to mass and charge (and initial velocity, if no velocity filter is used) and thus allow the collection of information about the weight/charge of molecules in the eluate. For each retention time, i.e. molecule size passing through the gas chromatograph, a mass spectrometer image is created, allowing to identify specific molecules by comparing the constituents to known spectra.

These information can then be related to the known contents of the glues under investigation: since several of the chemicals contained in the adhesives are classified as hazardous, they are specified in the respective glue material safety data sheets (see table 4.2). For specific molecule compositions, mass spectrometry allows to identify organic structures of similar atomic contents and molecule sizes due to different spectra of molecule debris [81]. For the extract under investigation, a mixture of molecule fractions and combinations of different sizes and structures led to ambiguous GC-MS spectra (see below). The analysis was thus focused on molecules which were known to be glue constituents from their respected material safety data sheets. An analysis of tetrahydrofuran extracts of cured and irradiated DYMAX 6-621 in a gas chromatograph/mass spectrometer showed differences in the concentrations of Isobornyl acrylate some of its decay products (see figure 4.6):

- Isoborneol
- 2-Bornanone (camphor)
- Isobornyl formate

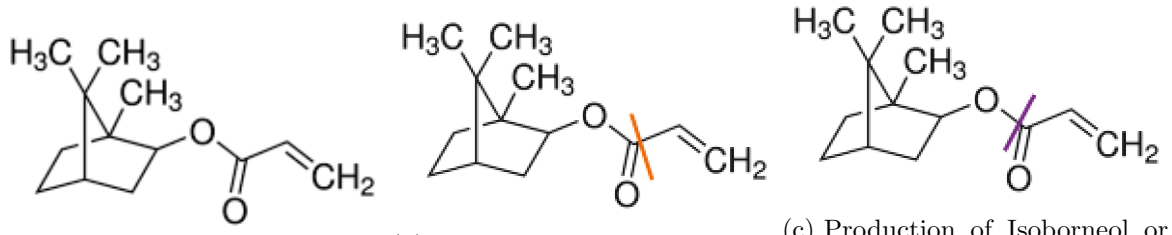

(a) Isobornyl acrylate molecule

(b) Production of Isobornyl formate from Isobornyl acrylate

(c) Production of Isoborneol or 2-Bornanone from Isobornyl acrylate

Figure 4.6: Major constituent of DYMAX 6-621 Isobornyl acrylate and possible decay products. Isobornyl acrylate consists of a carbon hexagon, where two carbon atoms on opposite corners are connected to another carbon atom. Additional carbon atoms with three hydrogen atoms are connected two the additional carbon atom as well as one of the corner atoms. A chain of additional oxygen and carbon atoms is connected to one of the hexagon carbon atoms, which connects to other molecules during the curing process. If the molecule breaks at the orange line, an Isobornyl formate molecule is created. If Isobornyl acrylate breaks at the violet line, the freed oxygen electron can either form a double covalence bond with the connected carbon atom, creating 2-Bornanone, or attach to a new hydrogen atom, creating Isoborneol.

Both uncured glue molecules (Isobornyl acrylate) and its decay products were not connected to other glue molecules, making them easier to extract by a solvent. Figure 4.7 shows the results from an initial gas chromatograph/mass spectrometer analysis of cured and irradiated DYMAX 6-621. It was found that the two glue samples showed significant differences for several molecules:

Content	Epolite FH-5313 resin [85](r) + hardener [86](h)	DYMAX 3013 [82]	DYMAX 6-621 [83]	Loctite 3525 [84]
70-100 %	Epoxy resin (r)			
30-75 %	Higher ethyleneamines (h)			
30-60 %				Polyurethane Methacrylate Resin
25-50 %		Isobornyl acrylate, Urethane Acrylate	Isobornyl acrylate, Urethane (Meth)Acrylate Oligomer, 2-Hydroxyethyl methacrylate	
15-55 %	Pentaethylenehexamine mixture (h)			
15-25 %		N,N-Dimethyl-acrylamide		
10-30 %	Butanediol diglycidyl ether (r)			2-Hydroxyethyl methacrylate, High boiling methacrylate
5-10 %				Acrylate monomer
2-25 %	Tetraethylenepentamine mixture (h)			
1-5 %	Allyl glycidyl ether (r)	Photo initiator, Silane Coupling agent	Acrylic acid, t-Butyl Perbenzoate, Photo initiator, Maleic acid, Epoxy resin	Hydroxyalkyl methacrylate, Acrylic acid, Photo initiator, Substituted silane
< 2 %	Triethylenetetramine mixture (h)			
0.1-1 %				Methacrylic acid, Ethylene glycol

Table 4.2: Components of all adhesives under investigation as specified in their material safety data sheets ("hazardous components"). Percentages for Epolite FH-5313 refer to the resin (r) or hardener (h), not the combined mixture. Knowledge about the individual components allowed the identification of peaks in chemical analyses.

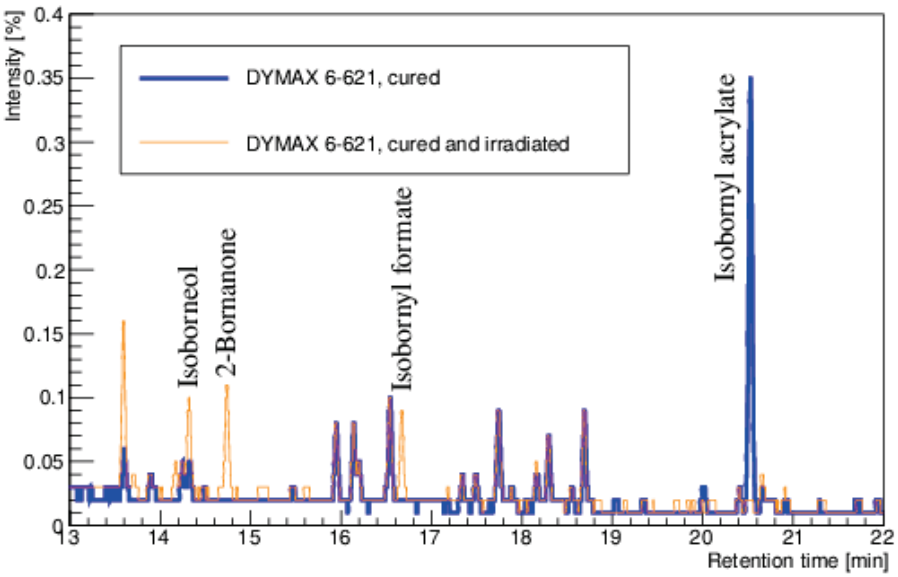

Figure 4.7: Gas chromatograph/mass spectrometer spectra for a cured and an irradiated sample of DYMAX 6-621, in the retention time range for the chemical under investigation (Isobornyl acrylate) and some of its decay products. While the spectra of cured and irradiated glue agree very well for large parts of the retention time range, the cured sample shows significantly higher amounts of uncured glue, while the irradiated sample shows peaks of decay products which are not present in the cured glue sample.

- Isobornyl acrylate
  While the sample of cured DYMAX 6-621 showed a high concentration of this molecule (i.e. uncured glue), the irradiated sample showed only a negligible contribution. After irradiation, all uncured glue had connected to other molecules, i.e. cured.

- Isobornyl acrylate decay products
  The cured glue sample showed a small contribution of Isoborneol, but no other decay products of Isobornyl acrylate. After irradiation, the contribution of Isoborneol had increased and contributions from other decay products (2-Bornanone and Isobornyl formate) appeared.

The results suggest that irradiation had two effects on the glue under investigation: uncured glue was cured and some of the glue molecules decayed into smaller molecules. Since the individual contributions could be quantified (see table 4.3), this method allowed a quantification of the impact of irradiation on glue. This method was thus chosen to investigate the impact of

	Material contributions, [a.u.]	
	cured sample	irradiated sample
Isobornyl acrylate	164.4	0.9
Isoborneol	1.0	3.0
2-Bornanone	0.0	5.1
Isobornyl formate	0.0	2.9

Table 4.3: Contributions of uncured glue (Isobornyl acrylate) and decayed glue molecules in a cured and an irradiated sample (23 MeV up to $2 \cdot 10^{15}\,\mathrm{n_{eq}/cm^2}$) of DYMAX 6-621. Contributions were calculated by integrating each contributions' intensity over the corresponding retention time range. The irradiated sample showed a smaller contribution of uncured glue and higher contributions of decay products than the cured sample.

irradiation on the glues under investigation.

4.3 Results of GC-MS Analysis

Each peak in the gas chromatography spectrum (see figure 4.9) corresponds to an associated spectrum in the mass spectrometer. Large organic molecules, which usually break while traversing the spectrometer, can be identified by comparing entries in the mass spectrometer to a database containing standard organic molecules. For small molecules of similar sizes, which traverse a gas chromatograph after similar amounts of time, their spectra are too similar to allow discrimination with sufficient certainty.

The glue samples irradiated for these studies were chosen to be smaller than the samples analysed in the feasibility study in order to allow the irradiation of multiple glue samples using a small beam diameter. The smaller sample size was found to lead to spectra, where only a

low number of peaks could be unambiguously identified and most peaks did not allow a precise identification (see figure 4.8). Instead of identifying individual molecule components, the spectra patterns were analysed.

Comparing the gas chromatography spectrum results for irradiated and unirradiated glue, three patterns were found (see figures 4.9):

- intensity increase by irradiation (see figure 4.9a):
  Peaks observed in some or all of the irradiated samples had not been observed in the cured sample or had shown a lower intensity in the cured sample.

- no intensity changes between cured and irradiated samples (see figure 4.9b):
  Matching intensities found in cured and irradiated samples were interpreted as irradiation having no visible effect on the chemical structure of a glue.

- intensity reduction by irradiation (see figure 4.9c):
  If peaks observed in a sample of cured glue showed a lower intensity or disappeared after irradiation, they represented molecules which were solvable in a cured sample, but were dissolved to a smaller extent after irradiation.

Depending on the spectrum of a cured glue sample, the presence of peaks in irradiated glue samples was thus classified as intensity increase, intensity decrease or no change.

The glue spectra were analysed using a ROOT [87] macro searching for peaks in each GC-MS spectrum. The first derivative of each spectrum was used to find peaks by requiring:

- a deviation of $\pm 0.05\,\%$ between two neighbour data points

- for points over a length of at least 0.03 min (11 data points)

- with at least four points with the first derivative $\geq 0.05\,\%$ and at least four points with first derivate $\leq -0.05\,\%$

in order to ensure that only peaks in at least one of the spectra measured for each glue were considered and statistical fluctuations were ignored. Positions of peaks were searched and assigned individually for each glue.

Entries in the circumference of peaks in the spectrum corresponded to more than 100,000 counts in the gas chromatograph, making uncertainties from statistical fluctuations negligible. Uncertainties were thus estimated from systematic variations of the integral boundaries of each peak and calculating the resulting effect on its integrated area. Figures 4.10 to 4.13 show the gas chromatograph spectra for all glues together with the effects of irradiation on the integrated peak areas. Since this study was concerned with changes induced by radiation, all peaks found for irradiated samples were compared to peaks at the same positions for the unirradiated reference sample.

In order to compare radiation induced composition changes for different glues, all occurring changes were added up: for each glue and GC-MS spectrum after irradiation, the changes of integrated peak areas were added up separately for decreasing peak areas and increasing peak areas. Since sums of increasing and decreasing peak areas compensate each other, changes

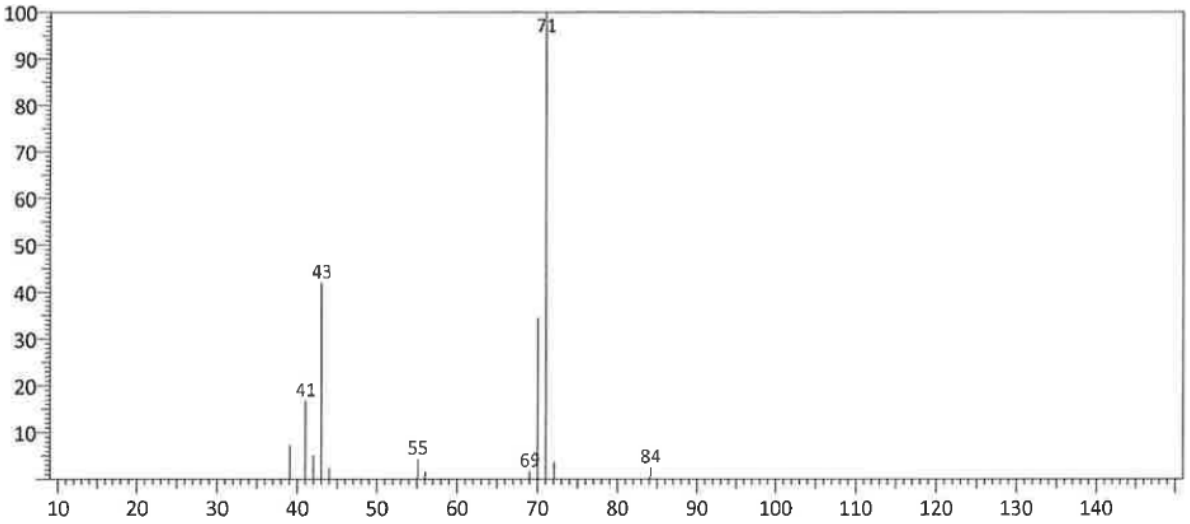

(a) Observed entries in mass spectrometer associated to peak in gas chromatograph

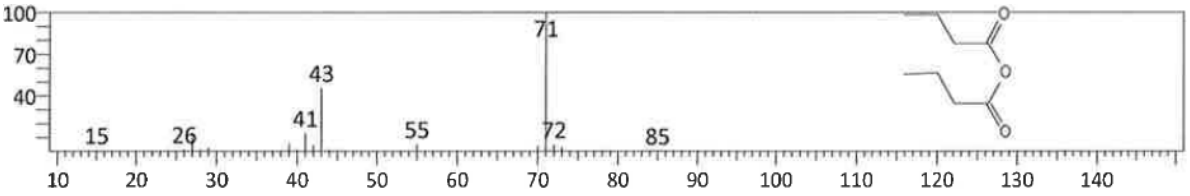

(b) Suggested match: Butanoic acid, anhydride

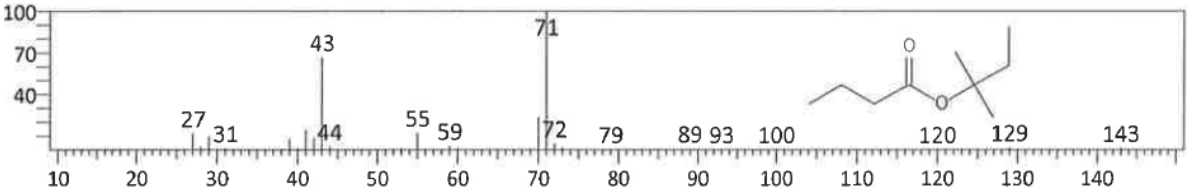

(c) Suggested match: Butyric acid, neopentylester

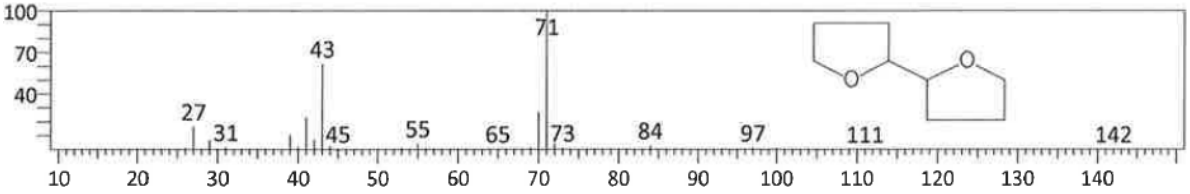

(d) Suggested match: 2,2'-Bifuran, octahydro-

Figure 4.8: Mass spectrometer entries associated with peak at retention time 13.78 min in gas chromatography spectrum of DYMAX 3013, irradiated with 800 MeV protons up to $1 \cdot 10^{15}\,\mathrm{n_{eq}/cm^2}$ and suggested matches from database. All pictures from Infrapark chemical analysis report.

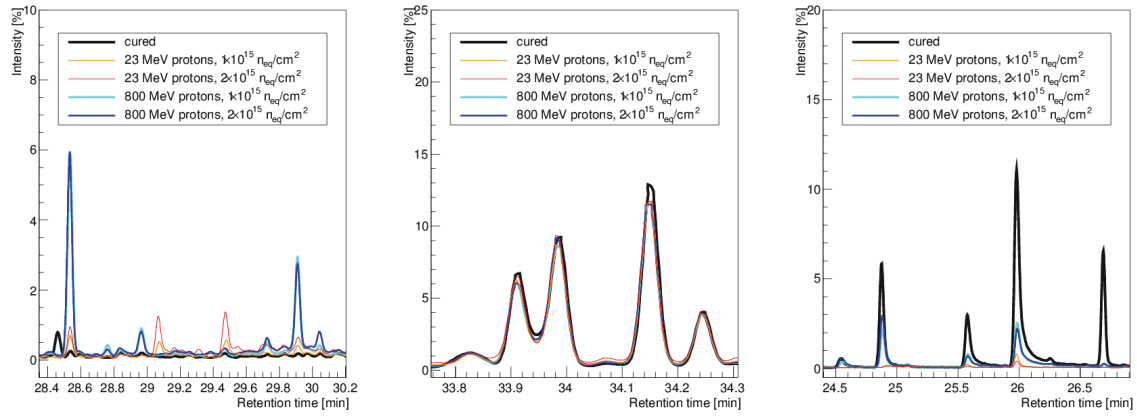

(a) Picture detail of GC-MS spectra for DYMAX 6-621: irradiated sample spectra show peaks with higher intensities than cured sample

(b) Picture detail of GC-MS spectra for Epolite FH-5313: spectra of cured and irradiated samples show overlapping peak intensities

(c) Picture detail of GC-MS spectra for DYMAX 3013: irradiated sample spectra show peaks with lower intensities than cured sample

Figure 4.9: Patterns observed in the comparison of GC-MS spectra for cured and irradiated glue samples

in individual contributions were considered more meaningful than the overall integrated area. Figure 4.14 shows the results for all glues under investigation in comparison. Different patterns can be observed for the different glues under investigation:

- Epolite FH-5313
  While Epolite FH-5313 shows the largest integrated peak area before irradiation, the spectra of irradiated samples show the smallest changes (relative to the unirradiated sample). An area increase occurred to a smaller extent than an area decrease, making the overall integrated peak areas after irradiation smaller than for the unirradiated sample. Changes were found to be small with respect to the original peak area.

- DYMAX 3013
  For DYMAX 3013, almost no increasing peak areas were found after irradiation. Decreasing peak areas added up to an almost 100 % reduction of the peak area of the sample with the highest irradiation with respect to the unirradiated sample.

- DYMAX 6-621
  Similar to DYMAX 3013, DYMAX 6-621 showed a decrease of the original integrated peak areas by almost 100 %. Different from DYMAX 3013, this glue did show visibly increasing peak areas as well. Since increases occurred to a smaller extent than decreasing peak areas, the overall integrated peak area was found to decrease. Lower doses were found to lead to a larger peak area increase than larger doses (discussion below).

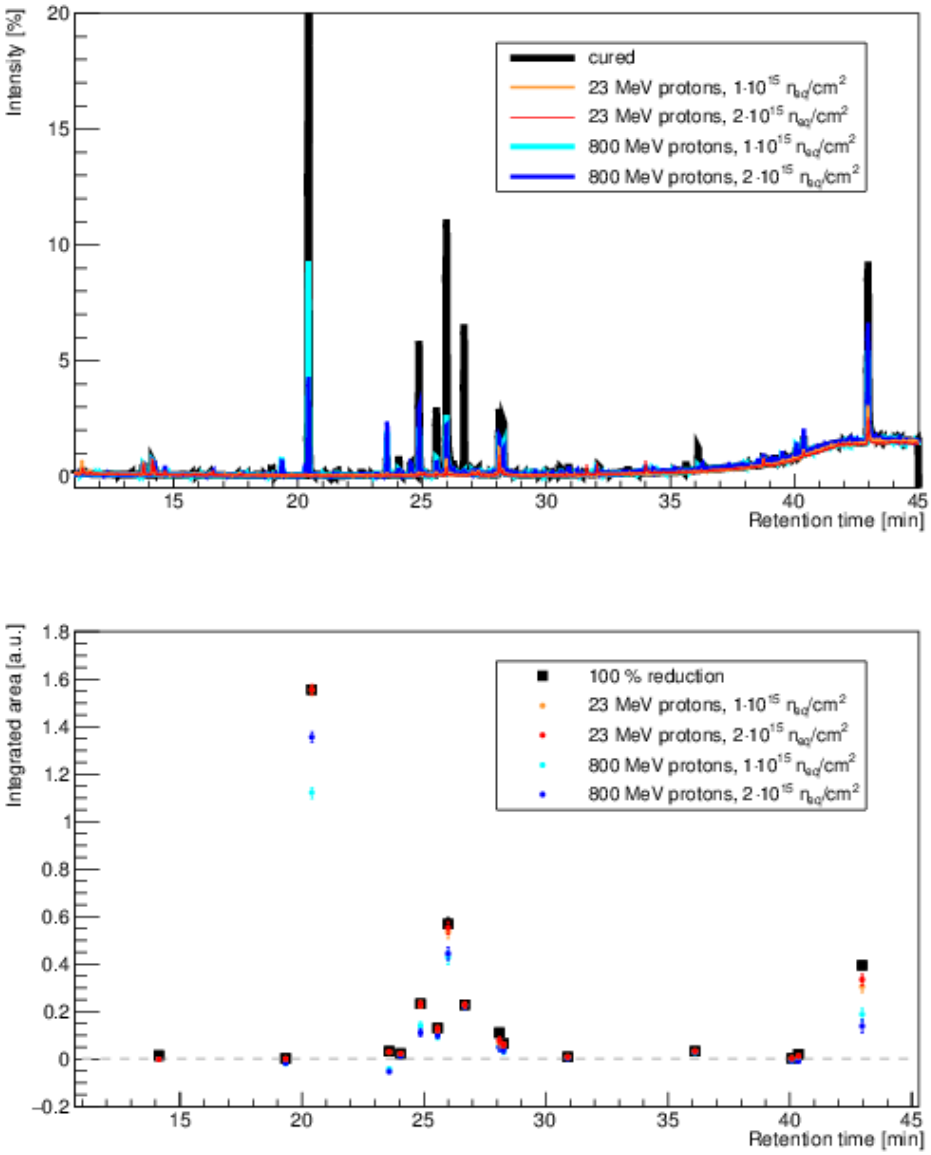

Figure 4.10: GC-MS spectra of DYMAX 3013 before and after irradiation. Each GC-MS spectrum shows the number of molecules passing through a gas chromatograph over time (retention time), with smaller molecules traversing the chromatograph faster than larger molecules. Each peak corresponds to a large concentration of molecules of the same or similar chemical composition or size. Bottom plots show the integrated areas of all peaks in a spectrum in comparison with the spectrum of the unirradiated sample (black). Markers > 0 represent peaks whose intensity decreased with irradiation, while markers < 0 represent peaks whose intensity increased after irradiation. DYMAX 3013 shows several peaks present in the unirradiated sample whose intensity was significantly reduced by irradiation. A high increase in peak intensity was found for only one position.

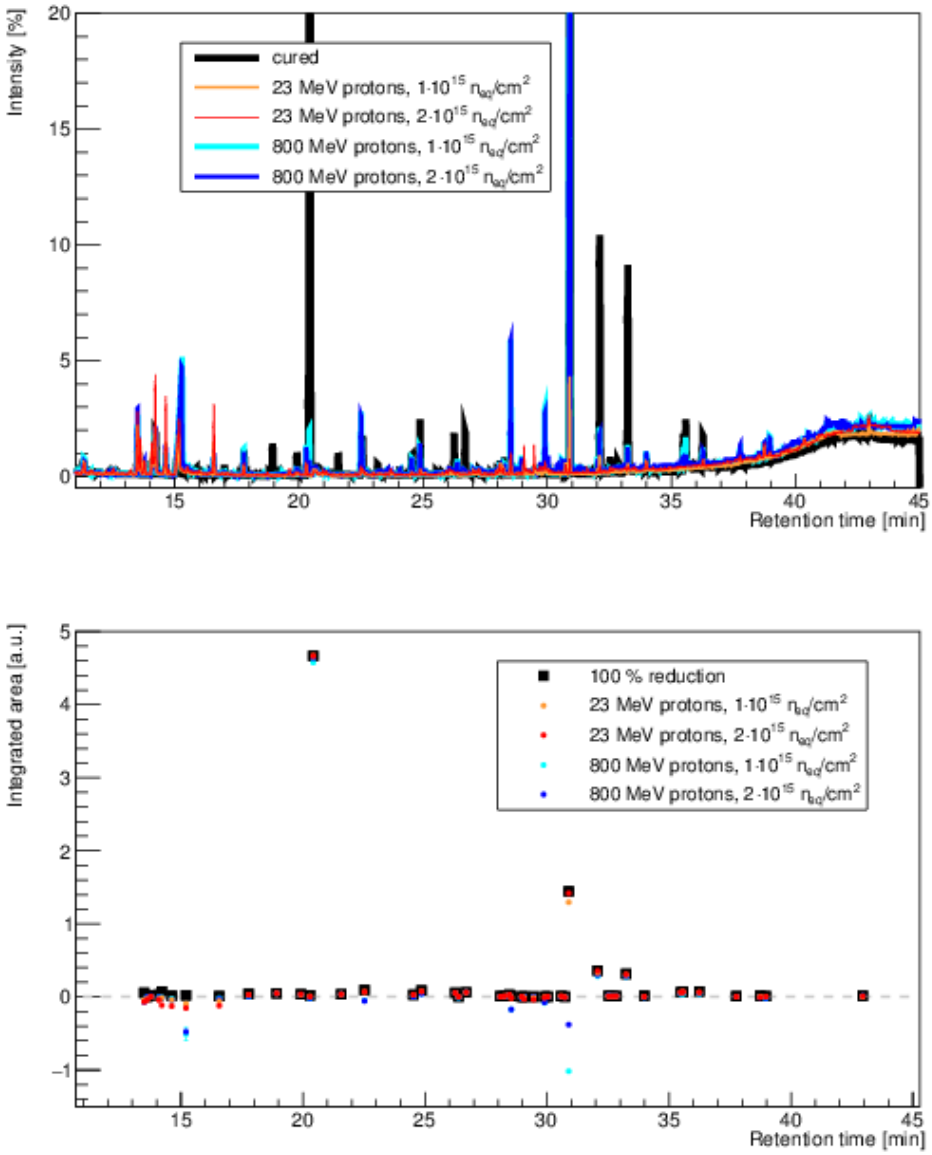

Figure 4.11: GC-MS spectra of DYMAX 6-621 before and after irradiation. Each GC-MS spectrum shows the number of molecules passing through a gas chromatograph over time (retention time), with smaller molecules traversing the chromatograph faster than larger molecules. Each peak corresponds to a large concentration of molecules of the same or similar chemical composition or size. Bottom plots show the integrated areas of all peaks in a spectrum in comparison with the spectrum of the unirradiated sample (black). Markers > 0 represent peaks whose intensity decreased with irradiation, while markers < 0 represent peaks whose intensity increased after irradiation. DYMAX 6-621 shows several peaks present in the unirradiated sample whose intensity was significantly reduced by irradiation as well as increasing peak intensities for low retention times.

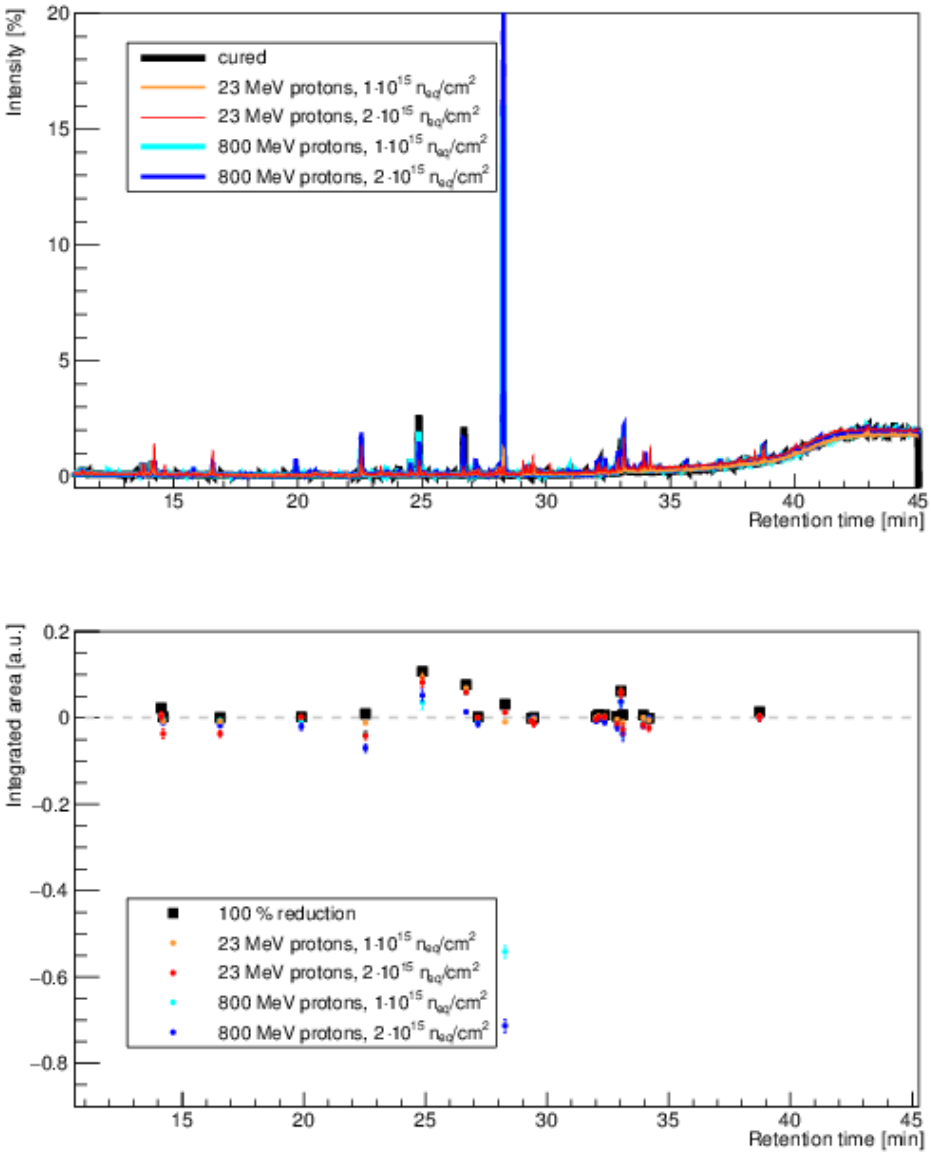

Figure 4.12: GC-MS spectra of Loctite 3525 before and after irradiation. Each GC-MS spectrum shows the number of molecules passing through a gas chromatograph over time (retention time), with smaller molecules traversing the chromatograph faster than larger molecules. Each peak corresponds to a large concentration of molecules of the same or similar chemical composition or size. Bottom plots show the integrated areas of all peaks in a spectrum in comparison with the spectrum of the unirradiated sample (black). Markers > 0 represent peaks whose intensity decreased with irradiation, while markers < 0 represent peaks whose intensity increased after irradiation. Loctite 3525 shows mainly peak intensity increases and only minor peak intensity decreases.

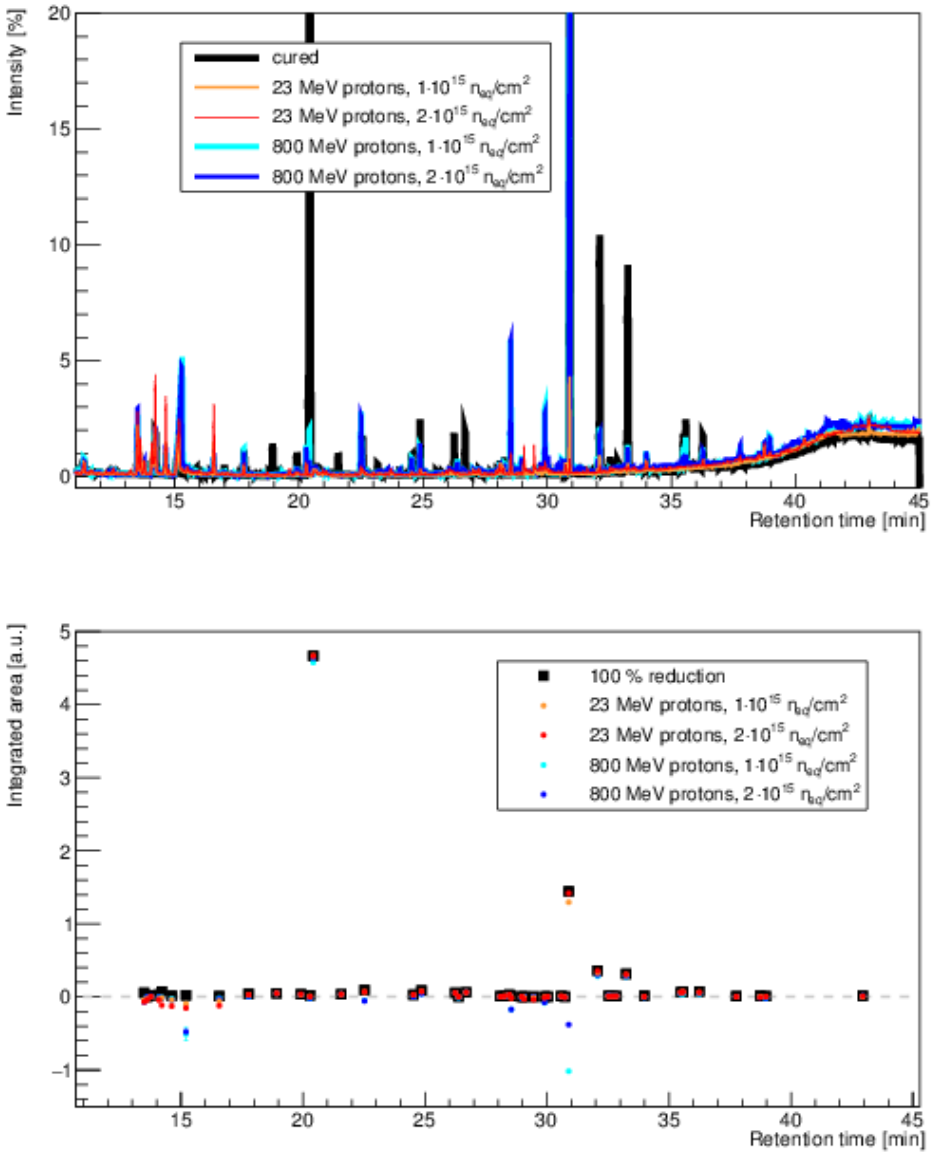

Figure 4.13: GC-MS spectra of Epolite FH-5313 before and after irradiation. Each GC-MS spectrum shows the number of molecules passing through a gas chromatograph over time (retention time), with smaller molecules traversing the chromatograph faster than larger molecules. Each peak corresponds to a large concentration of molecules of the same or similar chemical composition or size. Bottom plots show the integrated areas of all peaks in a spectrum in comparison with the spectrum of the unirradiated sample (black). Markers > 0 represent peaks whose intensity decreased with irradiation, while markers < 0 represent peaks whose intensity increased after irradiation. Epolite FH-5313 shows multiple peaks overlapping before and after irradiation, with only isolated peak intensities increasing or decreasing.

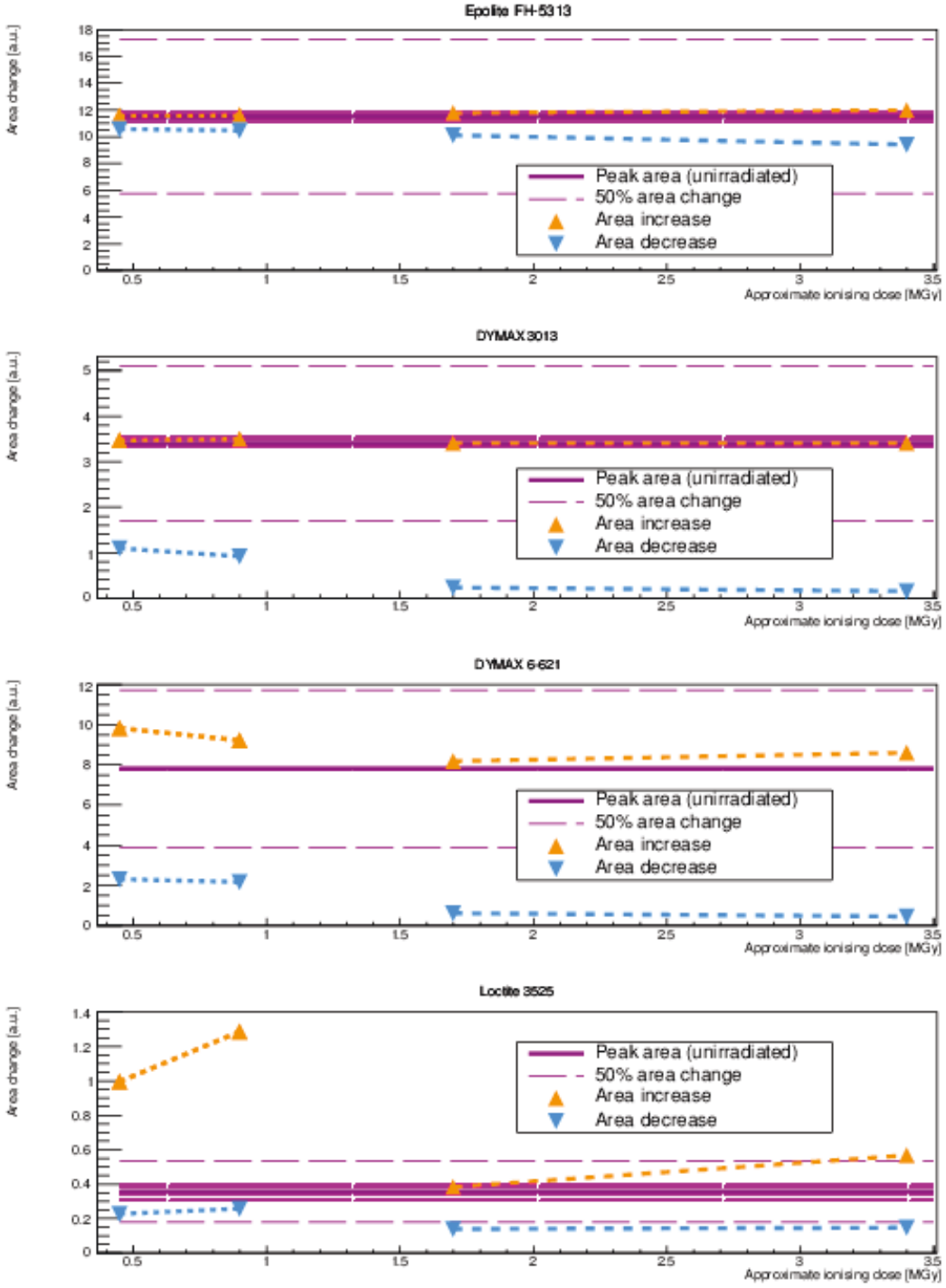

Figure 4.14: Changes in integrated areas of GC-MS spectra peaks before irradiation (violet line) with $3\,\sigma$-uncertainty range and after irradiation with 800 MeV protons (doses 0.6 MGy and 1.2 MGy) and 23 MeV protons (doses 1.1 MGy and 2.2 MGy). Decreased and increased peak areas do not represent absolute peak areas, but show the summed up changes, separated by increasing and decreasing peak areas, with respect to unirradiated samples. Uncertainties were calculated from varying peak integration areas.

- Loctite 3525
  Loctite 3525 was found to have the smallest integrated peak areas of the glues under investigation, leading to small changes by irradiation being large when compared to the original integrated area. This glue was found to show both increasing and decreasing peak areas to a similar extent for the highest irradiation doses, but showed significantly higher peak areas for lower ionising doses (discussion below).

Using the calculated area changes, split into area increases and decreases, allows to compare the changes occurring in different glues after irradiations.

However, taking into account the results from the feasibility study, where a larger sample size allowed the identification of individual components, area increase and decrease may be related to different effects (see subsection 4.2.3):

- a peak in the sample of a cured sample that decreased after irradiation was identified as one of the components of uncured glue. The intensity reduction after irradiation implied that this component had connected to other molecules after irradiation, reducing its solubility and thus the intensity of the associated peak, i.e. continued curing of the glue or the formation of stronger connections to other molecules (cross-linking). Reduced intensities of large peaks after irradiation were thus interpreted as molecules connecting to other molecules, either through the normal curing process or via cross-linking.

- peaks occurring in a sample after irradiation that had not been observed in the cured sample were identified as molecule groups that had been connected to one of the glue constituents. The occurrence of molecule parts detached from originally larger molecules were attributed to chemical bonds broken by irradiation. Since theses molecules had not been present in the cured sample, their appearance in the irradiated sample was attributed to radiation damage, i.e. molecules being broken up by irradiation.

While a peak area increase was thus assumed to reflect actual radiation damage, decreasing peak areas were considered to be potentially beneficial, matching previous observations that, for some glues, irradiation can improve a glue connection [45]. An interpretation of increasing peak areas as radiation damages would explain the observation made e.g. for Loctite 3525, where a lower dose led to larger peak area increases than higher doses. Taking into account the higher particle energy (800 MeV), a larger area increase can be attributed to chemical bonds that could be broken by higher energy particles, but not the lower energy 23 MeV protons despite their higher dose (see table 4.4). Dividing changes induced by irradiation into potentially beneficial and destructive radiation damages, Epolite FH-5313 and DYMAX 3013 were considered to show the best performance after irradiation. Loctite 3525 showed larger relative increases despite its absolute change being comparably small.

The method was found to allow a good understanding of chemical changes occurring in glues and thus a good criterion for their radiation hardness.

4.4 Conclusions of Chemical Analyses

Comparing samples of cured and uncured glue showed different changes:

Chemical bond	Energy, [eV]
O-O	1.51
C-C	3.61
C-O	3.71
C-H	4.28
O-H	4.80
O=O	5.16
C=C	6.36
C=O	7.72

Table 4.4: Energy in different covalence bonds occurring in common organic molecules, from [88].

- Colour change
  All of the four glues considered to be used on the sensor surface showed colour changes from initially transparent or light yellow to darker shades of yellow up to orange and brown (in case of Epolite FH-5313). As later discovered in chemical analyses, colour change does not correlate with chemical change and is thus not a reliable indicator: the intense colour change of Epolite FH-5313 after irradiation (see figure 4.2) did not correspond to large discrepancies in the GC-MS spectra of cured and irradiated glue samples (see figure 4.13).

- Brittleness
  Before irradiation, the glues under investigation showed a moderate level of elasticity, indicating a low modulus of elasticity. After irradiation, several samples were found to be less elastic and more brittle, indicating that the modulus of elasticity had been increased by irradiation.

- Solubility
  Whereas cured glue samples were found to be solvable in several organic solvents, irradiated glue samples showed reduced solubility. Samples could not be fully dissolved any more.

Increased brittleness and decreased solubility indicate that glue molecules, which had previously been not or only weakly connected to other molecules, had formed stronger bonds with other molecules. Stronger bonds can occur both by a delayed curing process, where previously unconnected glue molecules connect to other molecules, or cross-linking, where already connected molecules form additional bonds to other molecules.

Gas chromatography - Mass spectrometry measurements confirmed the suspected effect: extracts of uncured glue samples showed peaks which were not - or to a lesser extent - observed in irradiated glue samples. The measurements were not suitable to distinguish between unconnected glue molecules being extracted and glue molecules, which had formed a connection to other molecules, which was then broken up by the solvent. But the observed solubility of cured glue suggests that molecules in irradiated glue had formed connections beyond curing, i.e. cross-linking, which led to the increased modulus. In addition to stronger connections between molecules, irradiation was also found to lead to new molecules. The small size of these molecules

(compared to uncured glue molecules) indicated that they were broken off from larger molecules by irradiation and were thus an indicator for radiation damage in glues.

While the appearance of unconnected glue molecules after irradiation is a good indicator for radiation damages, it should be noted that the opposite effect is not desirable either: cross-linking can lead to volume shrinkage, increased density and higher modulus. For glue on sensors, stress occurring by different coefficients of thermal expansion should be absorbed by the glue rather than the sensor, which requires the used glue to have a much lower modulus than the sensor. For applications where glues are chosen for their mechanical characteristics, cross-linking can affect the thermo-mechanical behaviour. A good performance in a high radiation environment can thus be related to glues showing neither post-curing/cross-linking nor molecules breaking during irradiation.

Using gas chromatography - mass spectrometry allowed to quantify both effects and thus allowed to judge the degree of change in all glues under investigation (see table 4.5). Comparing different effects, Epolite FH-5313 was found to change the least (among the glues under investigation) during irradiation. It should be noted that several glues showed indications of broken molecules only for higher energy irradiations. Given the high particle energies at the LHC $\gg 800\,\mathrm{MeV}$, the occurrence of molecules breaking at higher energies can not be excluded and statements made here are based only on irradiation energies up to 800 MeV.

Adhesive	Post-curing/ cross-linking	Breaking
Epolite FH-5313	$18 \pm 2\,\%$	$4 \pm 1\,\%$
DYMAX 3013	$96 \pm 2\,\%$	$2 \pm 1\,\%$
DYMAX 6-621	$94 \pm 1\,\%$	$26 \pm 1\,\%$
Loctite 3525	$61 \pm 5\,\%$	$259 \pm 10\,\%$

Table 4.5: Radiation induced effects for different adhesives calculated based on areas of peaks in gas chromatography - mass spectrometry measurements. Post curing/cross linking refers to peak areas decreasing during irradiation, breaking refers to increasing peak areas. Percentages are calculated based on the peak areas measured using cured glue samples.

Using gas chromatography - mass spectrometry on samples of cured and uncured glues was thus found suitable to study chemical changes in glues caused by irradiation.

5 Studies of Electrical Sensor Characteristics

5.1 Sensor Characteristics under Investigation

An understanding of the performance of a sensor can be gained from its electrical characteristics, which determine the noise of a sensor and thus affect its signal-to-noise ratio (SNR). Applying glue to the surface of a sensor can potentially change its electrical properties. Hence, a comparison of the characteristics of sensors with different glues was considered a first step in the investigation of how the presence of glue on the surface of sensors affects their performance.

Glue on a sensor surface is expected to have to affect the characteristics of a sensor in two major ways:

- change of sensor surface properties due to mechanical stress exerted by curing glue and electrical characteristics of the cured adhesive
- worsened bulk characteristics due to chemical diffusion of glue atoms or molecules into the silicon

In order to assess either effect, the following sensor properties were monitored:

- Leakage current I_l (see section 5.3.1)
- Bulk capacitance C_b (see section 5.3.2)
- Inter-strip capacitance C_int (see section 5.3.3)
- A modified version of the inter-strip resistance R_int (see section 5.3.4)

Sensor characteristics were measured for blank sensors, after gluing and after sensor treatments.

Leakage current measurements before and after gluing, temperature cycling and irradiations were also published in [89].

For sensors irradiated with 800 MeV protons, inter-strip measurements on blank sensors and sensors with glue could not be performed due to the irradiation schedule, which did not permit the delay associated with full sensor measurements.

5.2 Probe Station Setup

All measurements were conducted in an automatic probe station PA200 [90] using probe needles. Sensors were individually placed on a cooling chuck, which was also used to apply high voltage to their backplanes, and held in position by vacuum (see figure 5.1). The sensor surface was contacted by either a needle on a wedge card, mounted on the chuck, or probe needles,

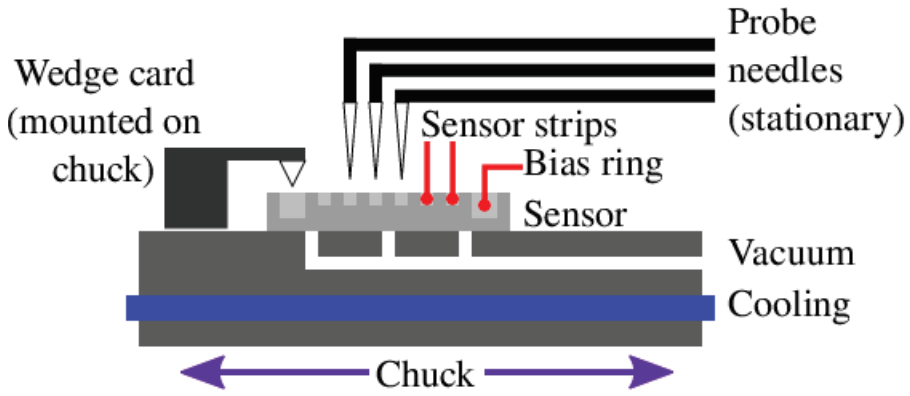

Figure 5.1: Probe station setup for silicon strip sensor measurements: a sensor was placed on a chuck that provided cooling, vacuum and a high voltage backplane contact. The sensor surface was contacted using a wedge card needle and probe station needles.

mounted on needle holders. Pre-programmed movements of the chuck allowed to measure the characteristics of individual sensor strips by moving the sensor with respect to the probe needles. The wedge card needle was used to have a continuous contact on the sensor surface despite movements of the chuck. A microscope was used for the positioning of both the wedge card needle and probe needles on the sensor.

Tests of non-irradiated sensors were conducted at a temperature of +20 °C, irradiated sensors were tested at a temperature of -20 °C. During measurement, the probe station was flushed with dry air to avoid condensation.

A patch panel was used to connect the chuck and needles to electric devices in use while keeping the sensor shielded from light inside the probe station.

The following devices were used for electric sensor measurements:

- a Keithley 6485 pico Ampere meter [6] for current measurements, measurement range up to 21 mA with an integration time of about 20 ms
- a Keithley 6487 voltage source [6] for applying small voltages, voltage range up to 500 V
- a Keithley 2410 voltage source [91] for applying high voltage, voltage range up to 1.1 kV
- an Agilent E4981A LCR meter [92] for capacitance measurements, measurement range up to 2 nF

All devices were steered and read out automatically using the Lab View-based software MeasureSoft [93]. A detailed description of the probe station setup and the Lab View programme used for its operation can be found in [94].

5.3 Measurements

5.3.1 Leakage Current

The sensor leakage current I_l, i.e. the current measured in a sensor when a reverse bias voltage is applied, is one of the defining characteristics of a silicon sensor. The leakage current is caused by electron-hole-pairs in the presence of an electric field and increases with the thickness of the charge depleted sensor volume. It can be calculated from [38]:

$$I_\mathrm{l} = \frac{1}{2} \cdot e \cdot \frac{n_\mathrm{i}}{\tau_\mathrm{L}} \cdot w \cdot A, \tag{5.1}$$

where e is the electron charge, n_i is the intrinsic carrier density, w is the thickness of the depleted sensor region (up to the sensor thickness for fully depleted sensors), A is the active sensor area and the free charge carrier lifetime τ_L can be calculated from

$$\tau_\mathrm{L} = \frac{1}{\sigma \cdot v_\mathrm{th} \cdot N_\mathrm{t}}, \tag{5.2}$$

where σ is the charge carrier cross section, v_th is the thermal velocity and N_t is the concentration of impurities/traps in the sensor. Since the leakage current depends on the impurity concentration, leakage current measurements were chosen to monitor possible chemical reactions of applied glue with the bulk.

The intrinsic carrier density n_i depends strongly on the temperature T:

$$n_\mathrm{i} \propto \exp\left(\frac{E_\mathrm{g}}{2 \cdot k_\mathrm{B} \cdot T}\right), \tag{5.3}$$

where E_g is the band gap of silicon at the measured temperature (1.12 eV at 300 K) and k_B is the Boltzmann constant. This relation allows to scale the leakage current measured at a specific temperature to different temperatures using:

$$I_\mathrm{l}(T) = I_\mathrm{l}(T_0) \cdot \left(\frac{T}{T_0}\right)^2 \cdot \exp\left(\frac{E_\mathrm{g}}{2k_\mathrm{B}} \cdot \left[\frac{1}{T} - \frac{1}{T_0}\right]\right), \tag{5.4}$$

where T_0 is a reference temperature.

For a standard unirradiated sensor, the thickness of the depleted sensor volume w increases with increasing bias voltage: $w \propto \sqrt{V}$ until the full sensor volume is depleted, i.e. up to the depletion voltage V_depl. Since $I_\mathrm{l} \propto w$ (see equation 5.1), the leakage current thus increases with increasing bias voltage $I_\mathrm{l} \propto \sqrt{V}$ up to V_depl.

Once the depletion voltage has been reached, i.e. the sensor has been fully depleted from free charge carriers, the leakage current only shows a small increase if the bias voltage increases further. When a sufficiently high bias voltage V_bd is reached, the leakage current can show a rapid increase due to an avalanche breakdown [38]. Both the depletion voltage V_depl, i.e. the operating bias voltage, and the breakdown voltage V_bd, i.e. the maximum operation voltage, are defining sensor characteristics which can usually be derived from the leakage current. The leakage current can thus be a good indicator of negative changes in the sensor performance,

e.g. higher depletion voltages and higher leakage current after irradiation or lower breakdown voltages after mechanical sensor damages.

However, most of the sensors under investigation did not show the sudden leakage current increase of a breakdown, but a gradually increasing slope of the leakage current (see figure 5.3), called a soft breakdown, which did not allow the identification of a specific breakdown voltage V_{bd}. While the leakage current can be used to identify the depletion voltage, the standard method of deriving the depletion voltage from bulk capacitance measurements was used (see section 5.3.2).

5.3.1.1 Setup for Leakage Current Measurements

The sensor leakage current I_{l} was measured by applying a reverse voltage to the sensor backside from a Keithley 2410 and contacting an opening in the bias ring with a probe needle (see figure 5.2). The resulting current was measured using a Keithley 6485 pico Ampere meter. During the measurement, the bias voltage was increased in steps of 1, 10 or 20 V, depending

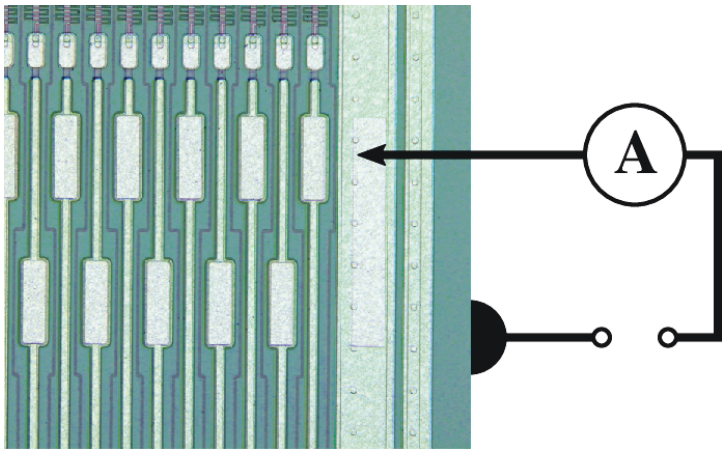

Figure 5.2: Schematic of a leakage current measurement setup: a reverse bias voltage was applied to the sensor backplane and the resulting current was measured using a probe needle contacting an opening in the bias ring.

on the voltage range (see table 5.1. For each applied bias voltage, the leakage current was

Voltage range		
Start [V]	End [V]	Step size [V]
0	-10	1
-10	-100	10
-100	-1000	20

Table 5.1: Reverse bias voltage steps for leakage current measurements

measured five times in time steps of 100 ms, of which the last three measurements were used to calculate an average leakage current. After each current measurement at a set voltage, a time delay of 1000 ms was set before starting a measurement at the subsequent voltage step. The process was interrupted automatically once a current of $9 \cdot 10^{-5}$ A was exceeded or manually once the current indicated a breakdown. After a measurement was finished, the bias voltage was ramped down to 0 V.

5.3.1.2 First Tests

Ideally the conditions during all sensor tests should be the same to ensure comparability. However, testing irradiated sensors required an operating temperature of -20 °C to reduce the leakage current. Cooling down sensors by approximately 40 K with respect to the ambient temperature has several disadvantages:

- due to the long cooling time, the time required for testing each sensor increased significantly
- as outlined in section 3.4.1, the different coefficients of thermal expansion of glue and silicon lead to mechanical stress in both the glue layer and the sensor. While mechanical stress in a sensor is known to affect its performance [95], the combined effects of possible chemical reactions and mechanical stress were considered difficult to distinguish.
- for measurements of multiple sensor strips, probe needles were found more likely to lose the contact to a sensor strip pad after a movement of the jig if the sensor had been cooled down. This observation was attributed to a contraction of the probe needles during contact with a cooled surface as well as the possibility of a small bending of the sensor after cooling.

Sensors were thus tested at a temperature of +20 °C, unless they had been irradiated.

Initial tests were performed for a float zone 2 miniature sensor, sensor architecture type 2 (see section 3.1), with 2.5 µl of Loctite 3525 on the surface. For leakage current measurements from bias voltages of 0 to -750 V, the sensor temperature was decreased from +20 to -20 °C in steps of 10 °C. The measured leakage currents were then compared to their theoretical predictions (see equation 5.4). For a temperature difference of 40 °C, the leakage current is expected to change by a factor of 39 [38]. The same measurements were performed for a blank miniature sensor with the same float zone material and sensor architecture for comparison. Results for both sensors are shown in figures 5.3a and 5.3b. Both sensors showed the expected leakage current increase with increasing temperature up to soft sensor breakdowns, where the leakage current increased more than expected from a temperature increase.

It was thus concluded that, especially for high voltages, the leakage current measurements for different temperatures do not match the theoretical predictions. Hence, comparisons of measurements at different temperatures are only valid up to the soft breakdown of a sensor.

5.3.2 Bulk Capacitance

A fully depleted sensor is free of charge carriers and can be modelled as a plate capacitor. The bulk capacitance C_b of a sensor can thus be calculated from the depth of the depletion layer

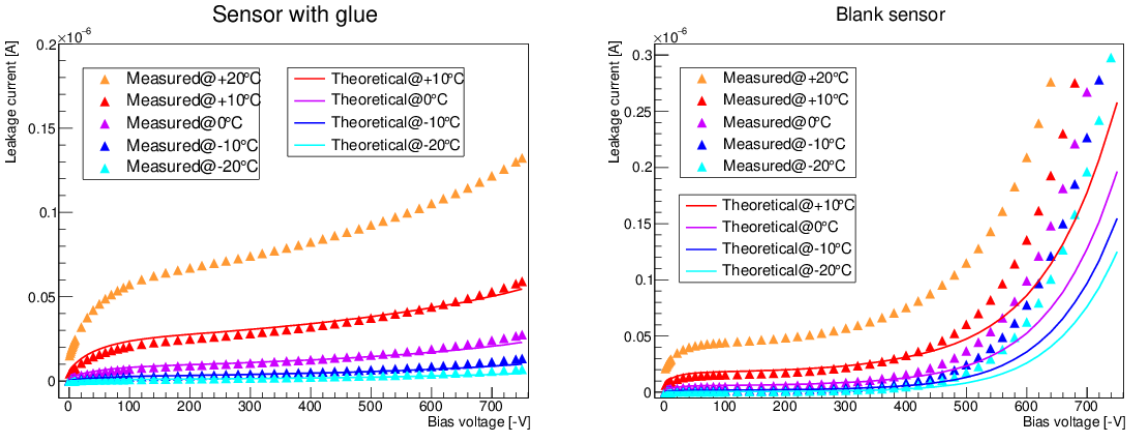

(a) Leakage current measurements for a miniature sensor with glue: the measured current was lower than the theoretical prediction for low bias voltages, but higher for large bias voltages.

(b) Leakage current measurements for a blank miniature sensor: the measured current agrees well with the theoretical prediction for low voltages, but was much higher for large bias voltages

Figure 5.3: Measurement of the leakage current dependency on the sensor temperature: the theoretical prediction approximates the measured current well up to voltages where soft breakdowns dominate the current and the standard temperature dependence does not apply

w [38]:

$$C_\mathrm{b} = \frac{\varepsilon}{w}, \tag{5.5}$$

where ε is the permeability of the bulk silicon. The depletion layer thickness can be calculated from:

$$w = \sqrt{2 \cdot \varepsilon \cdot \varrho \cdot \mu \cdot V}, \tag{5.6}$$

where ϱ is the silicon resistivity, μ is the mobility and V is the applied bias voltage.

For a fully depleted sensor, when the thickness of the depletion layer w equals the sensor thickness d, the depletion voltage V_depl becomes

$$V_\mathrm{depl} = \frac{d^2}{2 \cdot \varepsilon \cdot \varrho \cdot \mu} = \frac{e \cdot d^2 \cdot |N_\mathrm{eff}|}{2 \cdot \varepsilon}, \tag{5.7}$$

where e is the electron charge and $|N_\mathrm{eff}|$ is the effective charge carrier density.

Once depletion is reached, the bulk capacitance does not increase further with increasing bias voltage $V > V_\mathrm{depl}$:

$$C_b = \begin{cases} \sqrt{\frac{e \cdot \varepsilon \cdot |N_\mathrm{eff}|}{2 \cdot V}} & V \leq V_\mathrm{depl} \\ \frac{\varepsilon}{d} & V > V_\mathrm{depl} \end{cases}$$

Measuring the bulk capacitance as a function of the applied sensor bias voltage thus allows to identify the depletion voltage of a sensor (see section 5.3.2.2).

It should be noted that irradiation reduces the dependency of the capacitance on the applied bias voltage, so that determining the depletion voltage for irradiated sensors can require additional measurements.

5.3.2.1 Setup for Bulk Capacitance Measurements

The bulk capacitance of the sensor C_b is measured on openings in the bias ring as a function of the bias voltage applied to the sensor backplane. During the measurement, an LCR meter (an Agilent E4981A) measures the capacitance between sensor backplane and the sensor surface, and was thus exposed to the high voltage applied to the sensor. In order to protect the device from over voltage, an additional coupling box is used between the voltage source (a Keithley 2410) and the LCR meter. The coupling box is a high-pass filter [96] which separates direct current from alternating current in order to protect the LCR meter from direct current. Figure 5.4 shows the schematic setup of a bulk capacitance measurement. Before a measurement was

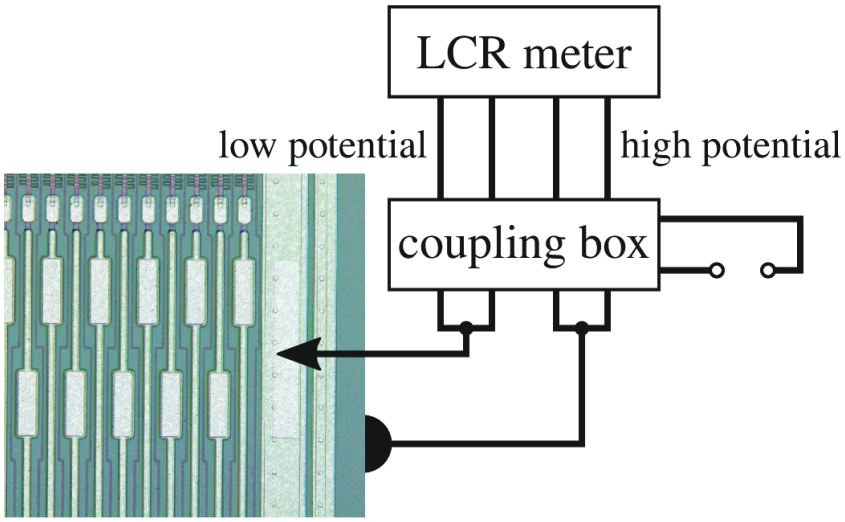

Figure 5.4: Schematic of a bulk capacitance measurement setup: a reverse bias voltage was applied to the sensor backplane and the bulk capacitance was measured on an opening in the bias ring using a probe needle. A coupling box between voltage source and LCR meter protected the LCR meter from over voltage.

started, an open correction was performed: the probe needle was lifted from the contact pad on the bias ring and the capacitance of the setup was corrected for. During the measurement, the same voltage steps, delays and interruption conditions as described in section 5.3.1.1 were used.

5.3.2.2 First Tests

The LCR meter in use allowed capacitance measurements at frequencies of 120 Hz, 1 kHz and 1 MHz [92]. While the bulk capacitance is independent of the sensor temperature, it can vary with the frequency used during the measurement (see figure 5.5). Initial tests were performed

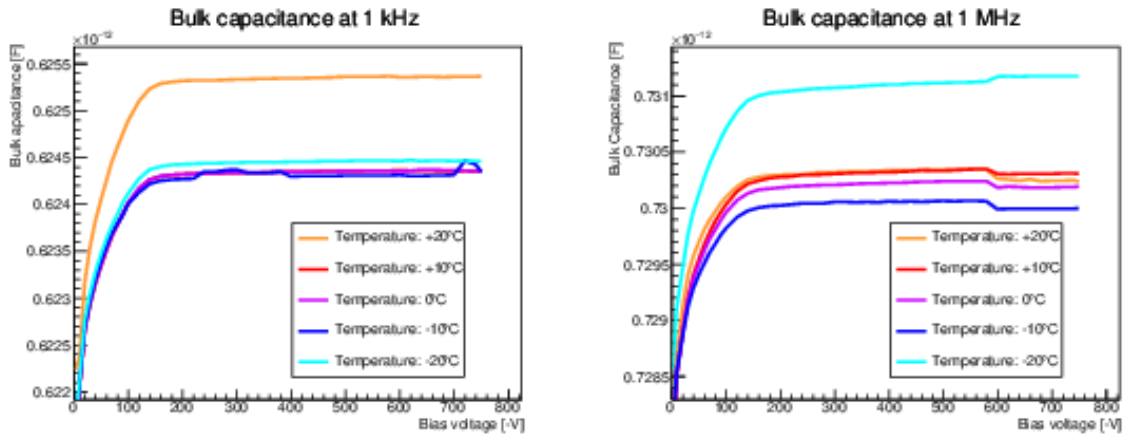

Figure 5.5: Bulk capacitance measurements of an ATLAS07 miniature sensor for different sensor temperatures and measurement frequencies. Measurements at different temperatures resulted in negligible bulk capacitance differences of 0.2 %, while using different frequencies changed the measured capacitance by 17 %.

with the same sensor used for leakage current measurements (see section 5.3.1.2) Measurements at different temperatures confirmed that the measured bulk capacitance is largely independent of the sensor temperature, but does depend on the applied frequency. For comparability with the inter-strip capacitance measurements (see section 5.3.3.1), the measurement frequency was chosen to be 1 MHz.

For an automated calculation of the depletion voltage V_{depl}, a fit of the inverse square of the bulk capacitance as a function of the applied bias voltage V was performed:

$$f(V) = 1/C_{\text{bulk}}^2 \tag{5.8}$$

Two separate linear fits are performed for the regions $V < V_{\text{depl}}$, where $1/C_{\text{bulk}}^2$ shows an approximately linear increase, and $V > V_{\text{depl}}$, where $1/C_{\text{bulk}}^2$ is constant. The depletion voltage V_{depl} is calculated from the intersection of both linear functions (see figure 5.6).

5.3.3 Inter-strip Capacitance

The capacitance between adjacent sensor strip AC pads C_{int} is a sensor design parameter that needs to balance three requirements:

- it needs to be sufficiently large for adjacent sensor strips to share charges, allowing to calculate a centre of the collected the charge, which improves the overall spatial resolution of a sensor (see section 6.6)

- it needs to be small enough with respect to the coupling capacitance between strip implant and AC pad for most of the charge to be transferred to the preamplifier

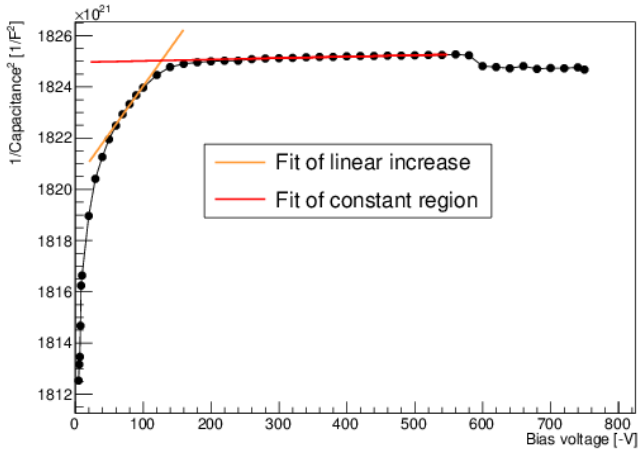

Figure 5.6: Calculation of the depletion voltage from separate linear fits of $1/C^2_{\text{bulk}}$ for bias voltages $V < V_{\text{depl}}$ and $V > V_{\text{depl}}$. The depletion voltage is situated at the intersection points of both linear fits.

- the capacitance between strips is a major contributor to the input noise of a module channel (in ABC130 barrel module prototypes, sensor strips were measured to contribute 1 pF/cm, of which 70 % are attributed to the inter-strip capacitance) and thus needs to be small.

A resulting standard choice for inter-strip capacitances is $\approx 1\,\text{pF/cm}$ [38] ($\approx 0.8\,\text{pF/cm}$ for ATLAS07 sensors [39].

The inter-strip capacitance, measured as a function of the applied bias voltage, is a good indicator of changes on the sensor surface and was thus chosen to monitor effects of glue on the sensor surface.

5.3.3.1 Setup for Inter-strip Capacitance Measurements

The capacitance between adjacent sensor strips C_{int} was measured by connecting a sensor strip contacted by a probe needle to the high potential of an Agilent E4981A LCR meter, while the two adjacent sensor strips were connected to the low potential entrance. The capacitance between the main sensor strip and its neighbours was measured while ramping up the reverse bias voltage applied to the sensor backplane from a Keithley 2410 voltage source. The bias ring was grounded via an opening using a wedge card needle. Figure 5.7 shows a schematic setup of the performed measurements. Prior to each sensor measurement, an open correction was performed for the LCR meter. During the measurement, the bias voltage was ramped up in steps listed in table 5.1.

In order to investigate the impact of gluing to the sensor surface, the inter-strip capacitance was not measured on individual sensor strips, but over a range of sensor strips. Automated measurements of multiple strips were done by using automatic jig positioning. After a sensor

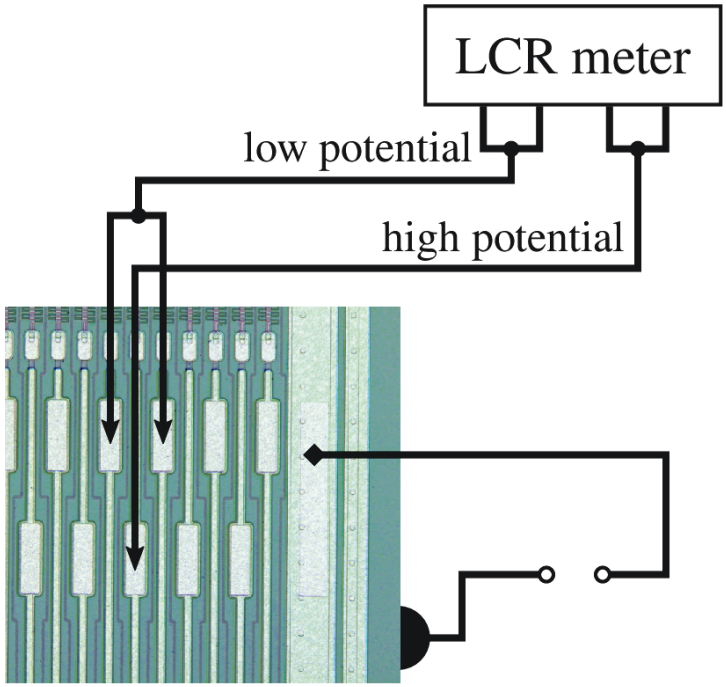

Figure 5.7: Schematic of an inter-strip capacitance measurement setup: a reverse bias voltage is applied to the sensor backplane and the capacitance between a sensor strip and its two neighbours is measured using an LCR meter. During the measurement, the bias ring is grounded using a wedge card needle.

had been placed on the jig, the programme's positioning system was aligned with the edges of the active sensor area using microscope imaging of the sensor. After performing an inter-strip capacitance measurement for the first sensor strip, the jig was automatically moved down to separate the sensor from the probe needles, moved perpendicular to the strip implant orientation by 149 µm (double strip pitch) and then up again to re-establish contact between the next strip and probe needles. During the movement, the positions of the probe needles were stationary, while the wedge card needle grounding the sensor moved with the sensor (see figure 5.8). Due

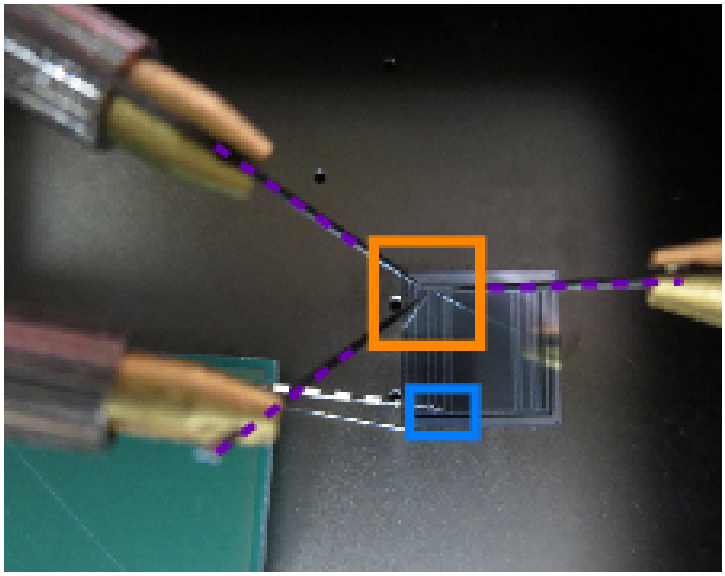

Figure 5.8: ATLAS07 miniature sensor in a probe station during an inter-strip capacitance measurement. The probe needle positions (indicated by dashed violet lines) on the sensor are stationary (orange box), while the wedge card needle (dashed white line) moves with the jig and its position on the sensor (blue box) does not change when the jig moves.

to the staggered layout of the sensor bond pads (see figure 5.7) and stationary probe needle positions, translation movements of the jig only allowed to contact every second sensor strip. Measurements were performed for sensor strips from the edge of the sensor to its centre in order to test different regions of the sensor. Hence, inter-strip capacitances were measured for 25 strips per sensor, i.e. one quarter of the sensor strips.

In accordance with measurements performed by the ATLAS ITk sensor group, inter-strip capacitance measurements were performed with a frequency of 1 MHz [36].

5.3.3.2 First Tests

Initial inter-strip capacitance measurements were performed for the same miniature sensor used for the measurements shown in sections 5.3.1.2 and 5.3.2.2, see figure 5.9. In accordance with standard measurements of ATLAS07 miniature sensors [36], inter-strip capacitance measure-

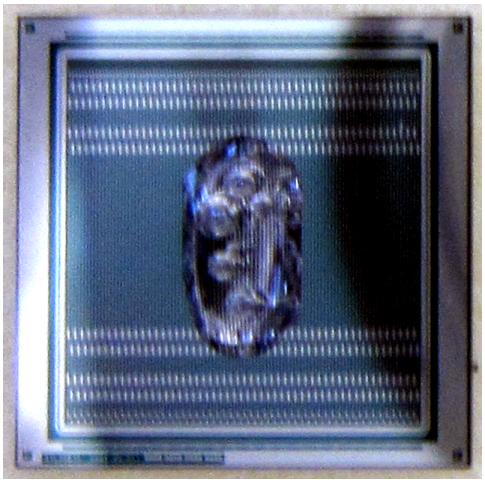

Figure 5.9: ATLAS07 miniature sensor (float zone 2, sensor architecture type 5) with glue (Loctite 3525) used for test measurements. Applying glue only to the centre of the sensor surface allowed to compare measurements for sensor strips with and without glue directly.

ments were conducted at a frequency of 1 MHz, which had been found to produce the most reliable results (see figure 5.10).

During full-sensor tests, measurements repeatedly showed steps in the measured capacitance. Steps usually reduced the measured capacitance by about 50 %, indicating that one of the two probe needles contacting the neighbouring strips lost contact. Particularly after the repeated measurements on the same AC pads required for a comparison of different measurement frequencies, the pad surfaces were found to become increasingly uneven (see figure 5.11). Since the automated measurements of multiple sensor strips relied on AC pads for each sensor strip being situated at the same height, scratches in the surfaces reduced the reliability of automatic probe needle contacts. The effect of one lost probe needle contact was investigated by performing two inter-strip capacitance measurements for the same sensor strips contacting only one or both neighbour strips 5.12. Losing the contact to one sensor strip was found to produce measurement curves with the same shape as curves measured with two contacted neighbour strips, but reduce the capacitance from $\approx 0.72\,\mathrm{pF}$ to $\approx 0.38\,\mathrm{pF}$, i.e. by about 50 %. Since lost probe needle contacts occurred mainly after repeated jig movements and for cooled sensors, an identification of low capacitances being caused by lost probe needle contacts was possible.

The inter-strip sensor capacitance should be independent of the sensor temperature [94], which would allow measurements of unirradiated sensors to be performed without cooling and still be comparable to later measurements of cooled sensors. Since the previously described problem of probe needles losing contact mainly occurred for cooled sensors, measurements at 20 °C were considered preferable over cold measurements. The temperature dependency of the inter-strip capacitance was thus investigated by testing at different temperatures (see figure 5.13). The inter-strip capacitance shown for each sensor strip is the measured value at the highest applied bias voltage. While the inter-strip capacitances measured at different

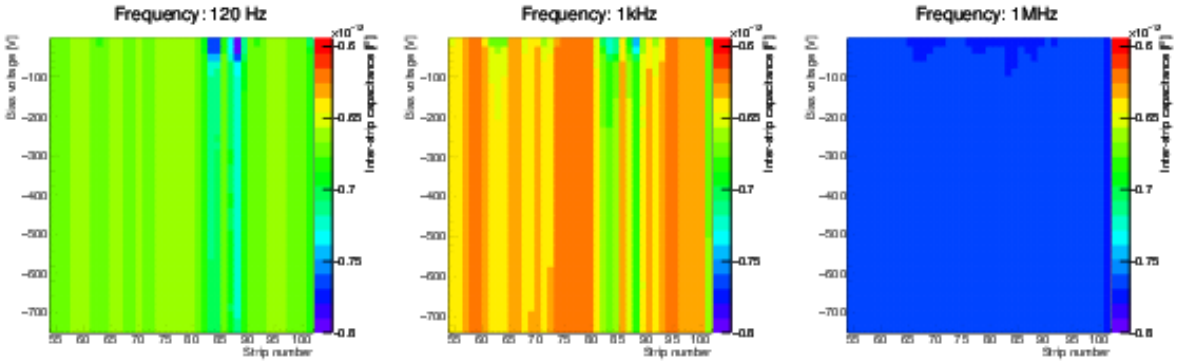

Figure 5.10: Inter-strip capacitance measurements measured for 25 sensor strips for an ATLAS07 miniature sensor using three different measurement frequencies. The highest available measurement frequency (1 MHz) was found to produce the most stable results.

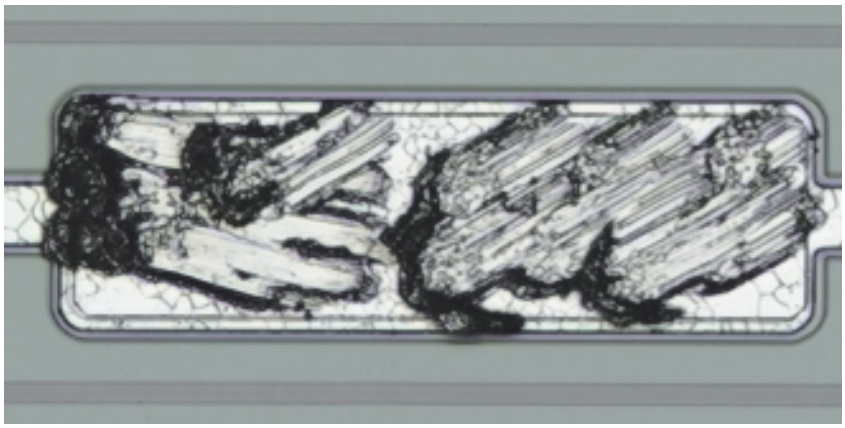

Figure 5.11: AC pads after multiple probe needle contacts: each measurement required to scratch the oxidised aluminium on the pad surface in order to establish an electrical contact, so that the pad surface accumulated scratch marks with each measurement.

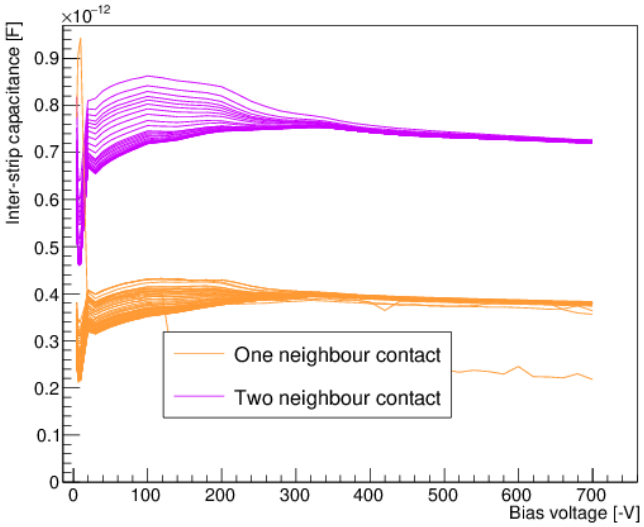

Figure 5.12: Inter-strip capacitance measurements for sensor strips with one or two neighbour strips being contacted by probe needles. Contacting only one neighbour strip reduced the measured capacitance by more than 50 % with respect to measurements where both neighbours were contacted.

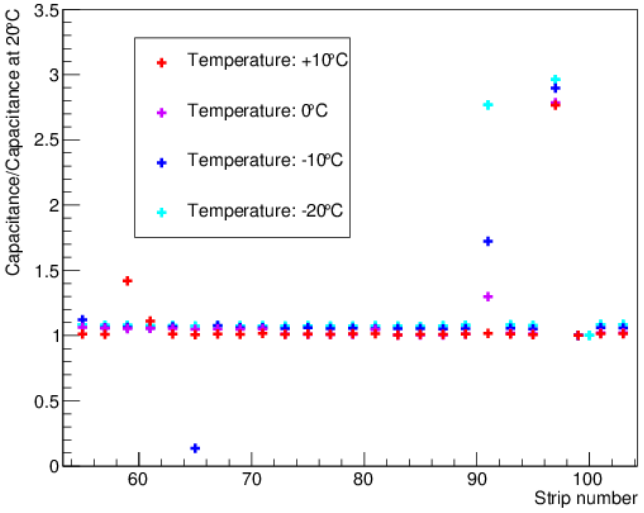

Figure 5.13: Inter-strip capacitances measured for 25 sensor strips at different temperatures, scaled with the inter-strip capacitances measured at 20 °C. Measurements at different temperatures were found to lead to small changes < 10 % for a temperature difference of 40 °C, except for individual outliers.

temperatures were found to show small discrepancies of up to 10 % for the largest temperature changes, they were considered to be acceptable. Individual, larger discrepancies were attributed to the corresponding strips showing defects after multiple previous measurements and probe needle contacts which might damage a sensor strip.

5.3.4 Inter-strip Resistance

The inter-strip resistance R_{int} is measured between two adjacent strip implants and can thus be used to judge the isolation of each individual strip. While the inter-strip resistance itself is not measured on the sensor surface, and is thus not strictly a surface measurement, it is sensitive to charges accumulated in the sensor oxide layer [38] and was thus considered to be a useful indicator of changes on the sensor surface.

5.3.4.1 Setup for Inter-strip Resistance Measurements

The resistance between adjacent strip implants was measured by applying a small voltage to a sensor strip (from a Keithley 6487 voltage source) and measuring the resulting current in the two adjacent sensor strips (using a a Keithley 6485 pico Ampere meter). The inter-strip resistance was calculated from the measured current increase and the applied voltage increase. These measurements were performed with fully depleted sensors or, in case of irradiated sensors with high depletion voltages, sensors with bias voltages as high as possible. High voltage was applied to the sensor backplane from a Keithley 2410 voltage source and the sensor bias ring was grounded by contacting an opening in the bias ring with a wedge card needle. Figure 5.14 shows a schematic setup of the performed measurements. Before each measurement, a short correction was performed: all three probe needles were brought in contact with the same sensor pad in order to bring them to the same potential. For each sensor strip under investigation, the applied voltage was ramped from -2.5 V to +2.5 V in steps of 0.25 V. A measurement was interrupted if the leakage current of the sensor exceeded $9 \cdot 10^{-5}$ A, i.e. in case of cooling system failure and subsequent leakage current increase.

As described in section 5.3.3.1, 25 strips per sensor were tested automatically using automated jig positioning.

5.3.4.2 First Tests

Initial tests were conducted using the previously studied sensor, operated over-depleted at (-200 V). Figure 5.15 shows an example measurement for the sensor. The measured inter-strip resistances of about 2.3 MΩ were found much smaller than the expected value $\mathcal{O}(\text{G}\Omega)$ [36]. The low resistance indicates that the measured current did not correspond to the current flowing between strip implants, but going through the bias resistor to the bias ring, thus corresponding to $2 \cdot R_{\text{bias}}$ (see figure 5.16).

The inter-strip resistance should be independent of the sensor temperature, which was investigated by conducting the same measurement repeatedly at different temperatures (see figure 5.17). Two of the five measurements showed large variations in the measured current, indicating a bad contact of the probe needle to the DC pad (see section 5.3.3.2). For measurements not

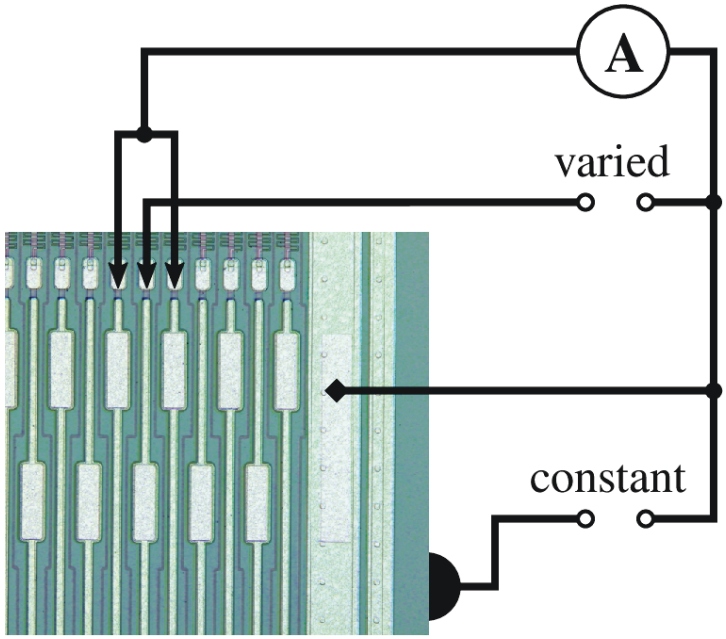

Figure 5.14: Schematic of an inter-strip resistance measurement: a reverse bias voltage is applied to the sensor backplane and the bias ring is grounded using a wedge card needle. The inter-strip resistance is measured by applying a mall voltage to a sensor strip and reading out the resulting current in the two adjacent sensor strips.

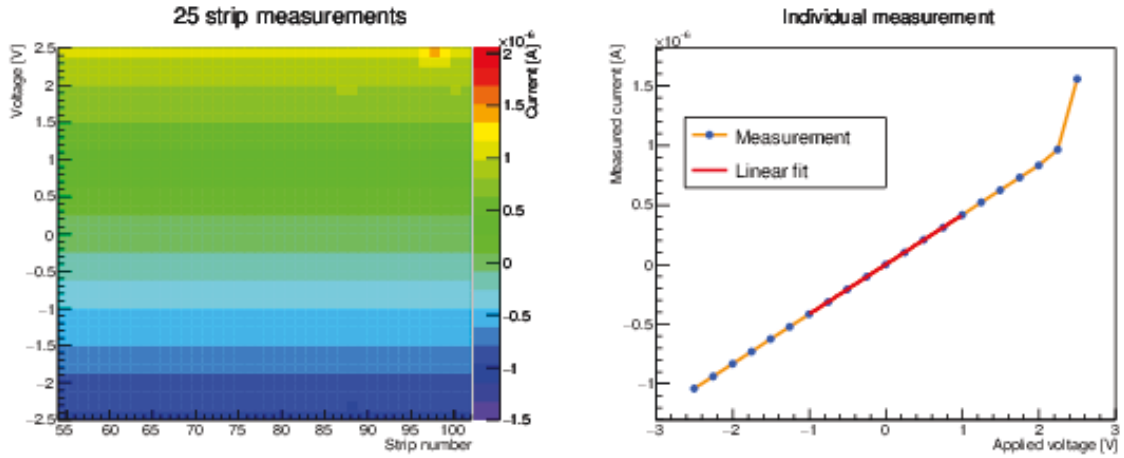

Figure 5.15: Example for inter-strip resistance measurements for 25 sensor strips. The measured currents were found to be mostly uniform across the sensor. For each sensor strip, the inter-strip resistance is determined by calculating the inverse of the fitted slope. In order to avoid deviating points at the beginning and end of a measurement, only the central measurement region -1 to +1 V was used for the fit.

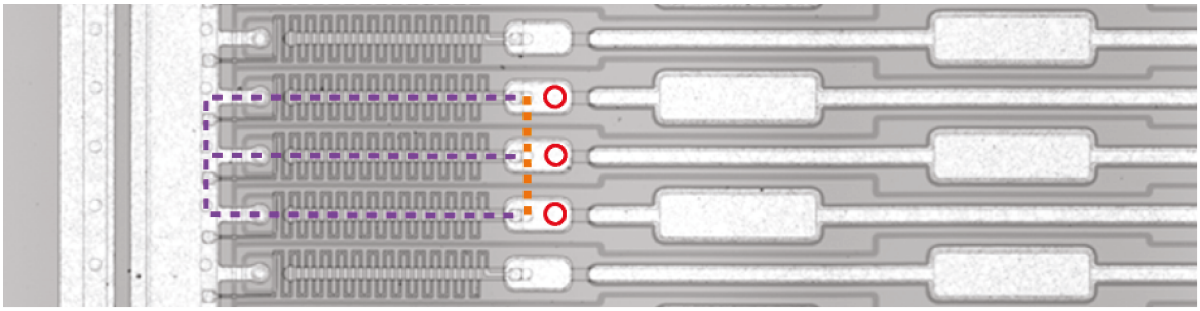

Figure 5.16: Measurement of the inter-strip resistance: if the inter-strip resistance is much higher than the bias resistance, the current measured on DC pads (red circles) goes through the bias resistor (violet lines) instead of the silicon bulk (orange line).

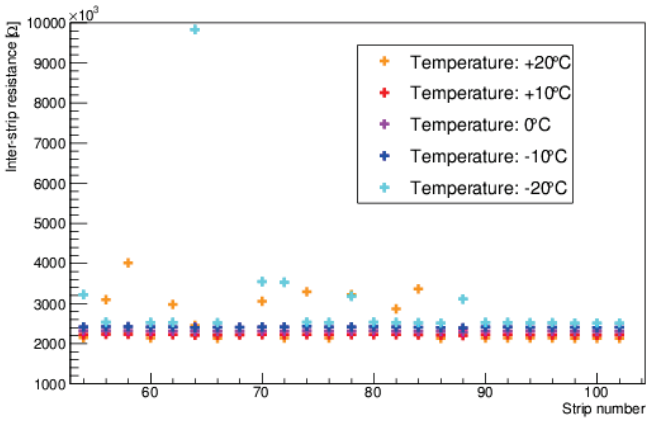

Figure 5.17: Inter-strip resistance measurements conducted at different sensor temperatures: the inter-strip resistance was found to increase by approximately 0.1 MΩ per 10 °C temperature decrease.

showing irregularities, the inter-strip resistance was found to increase by approximately 0.1 MΩ for a 10 °C temperature reduction. Since mechanical stress is known to affect the inter-strip resistance of a sensor [95], this increase can be attributed to mechanical stress in the sensor due to different coefficients of thermal expansion in glue and silicon.

Initial measurements showed that the inter-strip resistance was not affected by applying glue to the sensor surface and was thus not an effective variable to monitor to identify impacts of glue on the sensor performance. Additionally, the measurement was found to measure the bias resistance R_{bias} rather than the inter-strip resistance. Instead of contacting DC pads and measuring the current between strip implants, the same measurement was used to measure the surface current between adjacent strips by contacting AC pads.

5.3.5 Surface Resistance Measurements

The adhesives used on the surface of a sensor need to have a high electrical resistivity in order to maintain electrical insulation of individual sensor strips. For an estimate of the surface resistance of a strip on an ATLAS07 sensor, resistances for currents along different paths had to be considered (see figure 5.18). The overall surface resistance R_{surface} can be estimated as:

$$\frac{1}{R_{\text{surface}}} = \frac{1}{R_{\text{d;g}}} + \frac{1}{R_{\text{d;o}}} + \frac{1}{R_{\text{i;g/a}}} + \frac{1}{R_{\text{i;o/a}}}\frac{1}{R_{\text{i;g/o}}} + \frac{1}{R_{\text{c}}}, \tag{5.9}$$

where $R_{\text{d;g}}$ and $R_{\text{d;o}}$ describe the resistivity in glue and oxide; $R_{\text{i;g/a}}$, $R_{\text{i;o/a}}$ and $R_{\text{i;g/o}}$ are the resistances on the surfaces between glue and air, oxide and air and glue and oxide. R_{c} includes all paths for which the current has to overcome the coupling resistance R_{coupling} between AC pad and implant first:

$$R_{\text{c}} = 2 \cdot R_{\text{coupling}} + R_{\text{volume}}, \tag{5.10}$$

with R_{volume} summarising all paths for a current to continue from the implant:

$$\frac{1}{R_{\text{volume}}} = \frac{1}{R_{\text{c;s}}} + \frac{1}{R_{\text{c;i}}} + \frac{1}{R_{\text{c;}R_{\text{int}}}} + \frac{1}{R_{\text{c;}R_{\text{bias}}}}, \tag{5.11}$$

proceeding through the silicon bulk $R_{\text{c;s}}$, along the interface between silicon and silicon oxide $R_{\text{c;i}}$, via the bias resistor towards the bias ring $R_{\text{c;}R_{\text{bias}}}$ or directly to the neighbour implant $R_{\text{c;}R_{\text{int}}}$.

Silicon wafers used for ATLAS07 sensors are specified to have a resistivity of 6.7 kΩ·cm [39], which is lower than the standard resistivity of pure silicon of 64 kΩ·cm [97] due to doping. The silicon dioxide insulating the silicon bulk has a specific resistivity of $\geq 10^7$ kΩ·cm [98], whereas adhesives can have even higher specific resistivities, such as $7 \cdot 10^{14}$ kΩ·cm for Epolite FH-5313 [99]. Using these known characteristics, reasonable estimates can be made for the individual terms:

- $R_{\text{d;g}}$ can be calculated by approximating that half of a sensor strip is covered with a 120 µm glue layer. An average distance between sensor strip metal layers, taking into account the smaller distance between sensor strips in bond pad regions, was calculated to be 48.6 µm. Among the glues under investigation, a specific resistivity was only provided

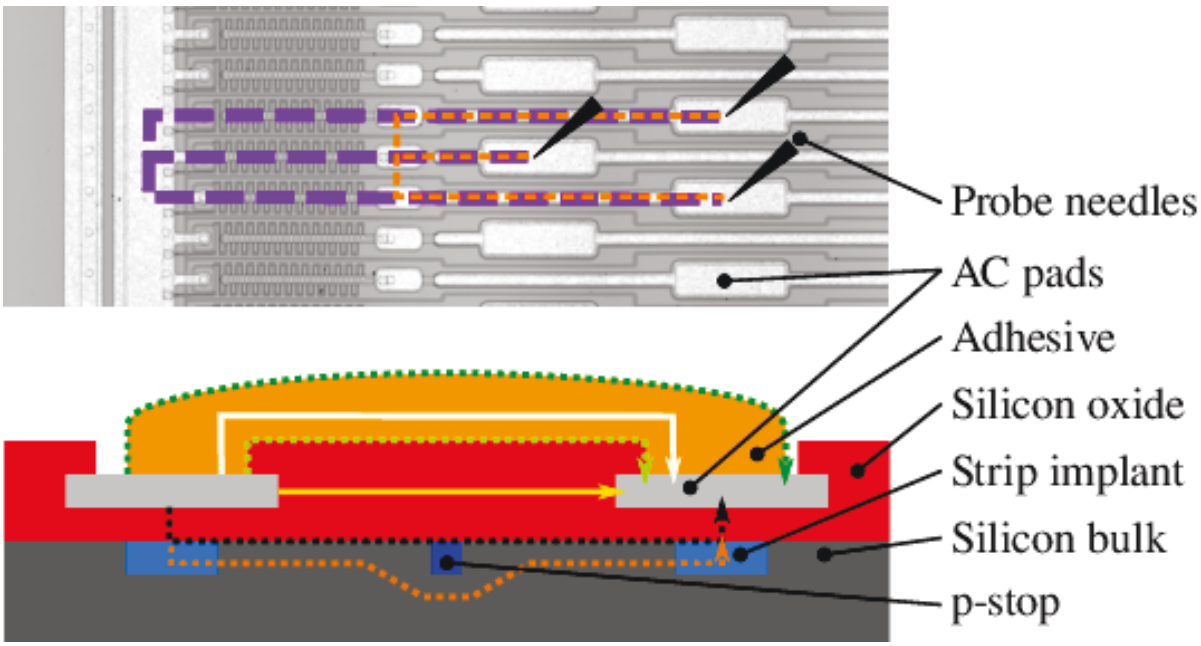

Figure 5.18: Contributions to surface currents between AC pads on an ATLAS07 sensor (not to scale): currents can potentially flow through the adhesive (white line) or the silicon oxide (yellow line) or along the interface layers along the silicon oxide layer (dashed light green line) or along the glue surface (dashed dark green line). Additional paths to be considered require to overcome the coupling resistance between AC pad and strip implant, which can lead to a current along the interface between silicon bulk and oxide (dashed black line), between strip implants (dashed orange line) or via the bias ring (dashed violet line).

for Epolite FH-5313, which was used for further calculations. $R_{\mathrm{d;g}}$ for sensors with glue is then calculated to be:

$$R = \frac{\text{resistivity} \cdot \text{length}}{\text{cross-section}} = 8 \cdot 10^{17}\,\Omega = 8 \cdot 10^{8}\,\mathrm{G}\Omega \tag{5.12}$$

- $R_{\mathrm{d;o}}$ requires an estimate for the thickness of the passivation layer, which is assumed here to be about 1 µm. Using the same average distance between neighbour sensor strips as before, the resistance can be calculated to be $R_{\mathrm{d;o}} = 6.9 \cdot 10^{3}\,\mathrm{G}\Omega$

- the coupling resistance R_{coupling}, which is required to calculate resistances where a current flows from the AC pad to the implant, can be estimated using their physical separation by an oxide layer with a cross-section corresponding to the overlapping areas of strip metal layer and implants (normal sensor strips and four bond pads). R_{coupling} can thus be estimated to be 3.5 GΩ.

- $R_{\mathrm{c;s}}$ requires the current to traverse 300 µm of silicon with a resistivity of 6.7 kΩ·cm. The resistance within the silicon bulk can be estimated to be $R_{\mathrm{c;s}} = 1.7\,\mathrm{k}\Omega$. It should be noted that the presence of p-stops affects the electric field within the sensor bulk and increases the effective resistance. $R_{\mathrm{c;s}} = 1.7\,\mathrm{k}\Omega$ should thus be considered a lower boundary.

- $R_{\mathrm{c};R_{\mathrm{bias}}}$ is the resulting current from $R_{\mathrm{bias}} = 1.5\,\mathrm{M}\Omega$ [39]

- $R_{\mathrm{c};R_{\mathrm{int}}}$ is the resistance for a current to go directly to a neighbour implant $R_{\mathrm{int}} = 10\,\mathrm{G}\Omega$ [36]

- $R_{\mathrm{c;i}}$ [100]. Since electron mobility $\propto$ electrical conductivity $\propto \frac{1}{\text{electrical resistance}}$, the resistance in the interface layer can be estimated as $13.4\,\mathrm{k}\Omega \cdot \mathrm{cm}$. Assuming an interface layer with a thickness of a few atomic layers $\approx 5\,\mathrm{nm}$, the resistance of the interface layer is calculated to be 0.2 GΩ.

- Other interface resistances $R_{\mathrm{i;o/a}}$, $R_{\mathrm{i;g/a}}$ and $R_{\mathrm{i;g/o}}$ can not easily be estimated, as they depend significantly on unknown parameters such as the thickness and surface resistivity of adhesives as well as the degree of contamination. A qualitative estimate will be made later with respect to the sensor-specific resistance.

These approximations for individual contributions to the overall resistance allow an estimate of the most likely path of a current between adjacent AC pads (see figure 5.19): R_{volume} (see equation 5.11) is dominated by the resistance in the silicon, making the overall resistance for a current through the coupling resistance $R_{\mathrm{c}} = 7\,\mathrm{G}\Omega$ (see equation 5.10). The overall resistance between two adjacent AC pads is thus approximately $\frac{1}{R_{\mathrm{surface}}} = \frac{1}{7\,\mathrm{G}\Omega}$. It should be noted that these calculations as well as the corresponding measurements concern only DC currents on the sensors surface. This estimate is only valid if the used sensor characteristics are valid (which will change e.g. after irradiation) and if the resistance in interface layers does not become lower than the coupling resistance. If a surface resistance is reduced significantly after gluing, it indicates an unwanted current along the interface layers between oxide layer and glue or over the glue surface.

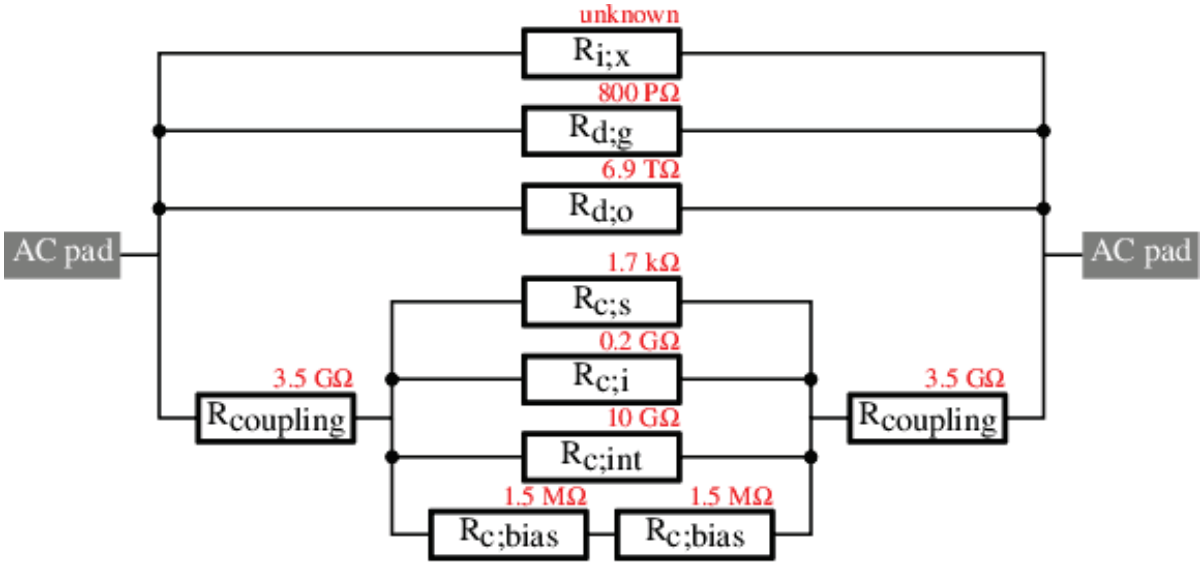

Figure 5.19: Resistances involved in surface resistance measurement corresponding to possible paths for a current to flow between two AC sensor pads (see figure 5.18) with estimated values. Resistances of interface layers $R_{i;x}$ involve too many unknown characteristics to make a reasonable estimate.

5.3.5.1 Measurement Setup

The surface resistance between adjacent sensor strips was measured by by applying a small voltage to a sensor strip (using a Keithley 6487 voltage source) while measuring the resulting current in both neighbour strips using a Keithley 6485 pico Ampere meter. By fitting the slope of the current change in dependence of the applied voltage, the surface resistivity between both sensor strips was calculated.

During the tests, sensors were biased up to full depletion or, in case of highly irradiated sensors, biased up to voltages as high as possible (-750 V for FZ2 sensors, -1000 V for FZ1 sensors). High voltage was applied via the sensor backplane using a Keithley 2410, while simultaneously using a wedge card contact to ground the bias ring. Figure 5.20 shows the schematic measurement setup. The measurements were performed analogue to the previously described inter-strip resistance measurements: 25 sensor strips were tested by ramping the applied voltage from -2.5 to 2.5 V in steps of 0.25 V and short corrections were performed before each measurement.

5.3.5.2 First Tests

An initial measurement was performed for the same sensor that had been previously used (FZ2 wafer with p-spray), tested over-depleted at -200 V. Figure 5.21 shows currents measured for 25 strips on the sensor. Different from resistivity measurements on the sensor DC pads, the current change is not symmetric for negative and positive applied voltage. This effect is most likely

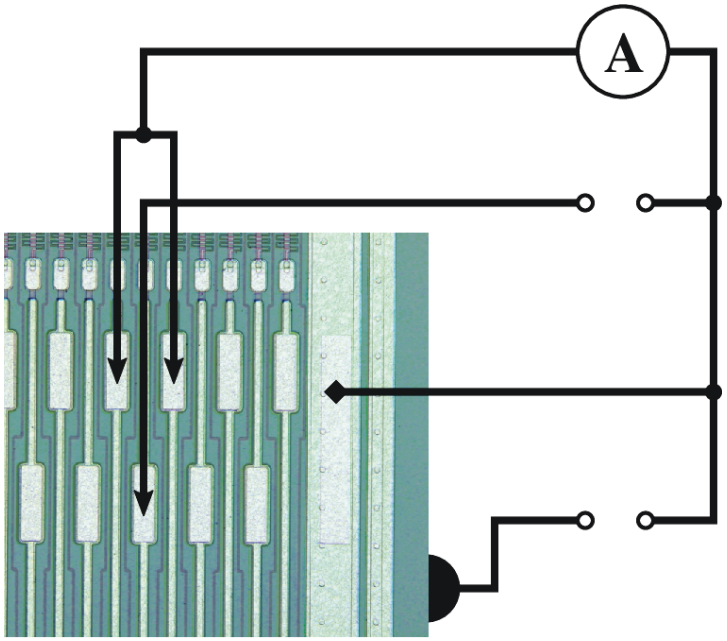

Figure 5.20: Schematic of a surface resistivity measurement between adjacent strips: a reverse bias voltage is applied to the sensor backplane and the bias ring is grounded using a wedge card needle. By varying the voltage applied to neighbour strips and measuring the resulting current in a sensor strip under investigation, the surface resistivity between the sensor strips was measured.

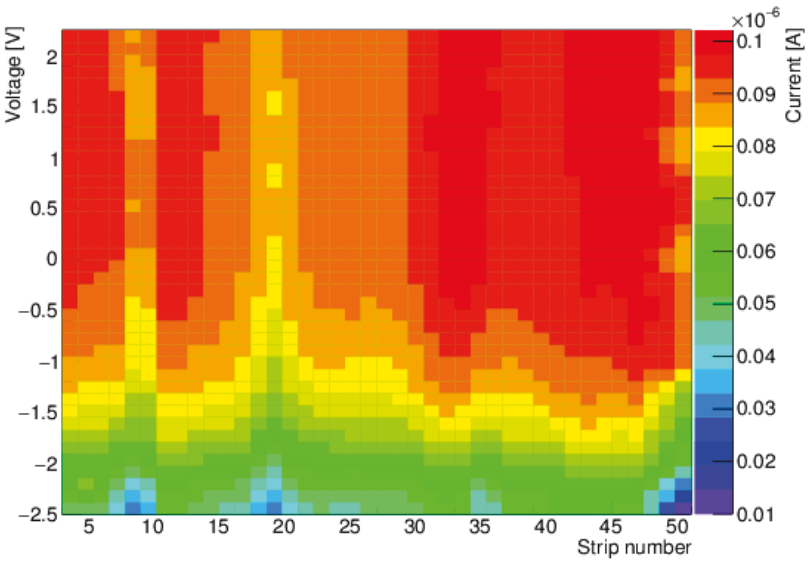

Figure 5.21: Surface current measurements for 25 strips on an ATLAS07 miniature sensor.

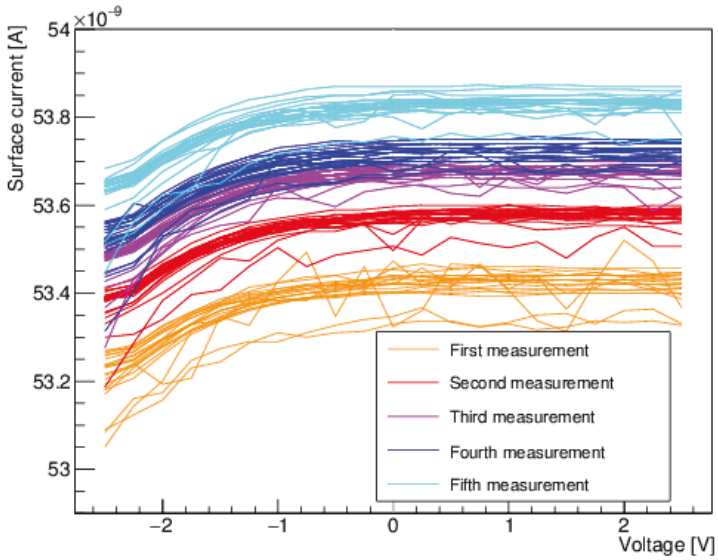

Figure 5.22: Repeated surface current measurements on 25 sensor strips of the same sensor. While the overall current differs between measurement repetitions, the slopes of individual measurements are reproducible.

caused by free charge carriers accumulating at the interface between silicon and silicon oxide which react differently if a negative or positive charge is applied, possibly due to the presence of p-spray.

Variations between measurements of individual strips were found to be larger than variations found between measurements on DC pads (see figure 5.15). Since this measurement directly depends on the electrical insulation and small contaminations, such as dust particles or fibres, can lead to a reduced surface resistance, larger variations between strips are expected for tests using AC pads. It was thus considered a good indicator for decreased electrical insulation between sensor strips caused by potential chemical interactions with glue. In order to test the reproducibility of surface current measurements, the test was repeated and the results of each individual measurement compared (see figure 5.22). While the overall surface current varied between measurements, the slopes of surface currents in individual strips were found comparable (see figure 5.23). As expected from the asymmetrical surface current curve, resistances calculated from applied voltages $\leq 0\,\mathrm{V}$ were smaller than resistances from voltages $\geq 0\,\mathrm{V}$. For all later calculations, the lower fit range (-2 to 0 V) was used as a worst case estimate. Strips at the edge of the sensor (up to about strip 25) show lower surface resistivities than strips in the centre of the sensor, which were covered with glue. This difference indicates that the surface resistance of the sensor is increased by glue.

The calculated resistances showed large fluctuations, which can be attributed to the measurement precision of the Ampere meter in use (see table 5.2). For large readout currents and large surface resistivities, current changes are small compared to the measurement precision of

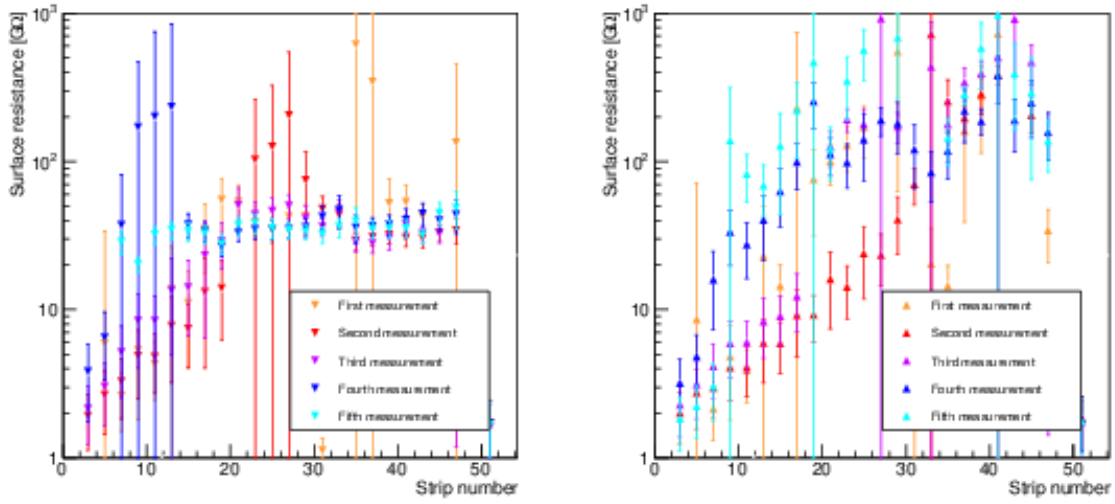

Figure 5.23: Surface resistivities measured repeatedly for 25 strips of a sensor. The plot shows fit results for applied voltages $\leq 0\,\mathrm{V}$ (downward pointing triangle) and $\geq 0\,\mathrm{V}$ (upward pointing triangle) are shown separately for comparison. Uncertainties are the uncertainties of the linear fit.

Range	Reading	RMS noise
2 nA	0.4 %	20 fA
20 nA	0.4 %	100 fA
200 nA	0.2 %	1 pA
2 µA	0.15 %	10 pA
20 µA	0.1 %	100 pA
200 µA	0.1 %	1 nA
2 mA	0.1 %	10 nA
20 mA	0.1 %	100 nA

Table 5.2: Measurement precision for the different ranges of a Keithley 6485 pico Ampere meter [6]

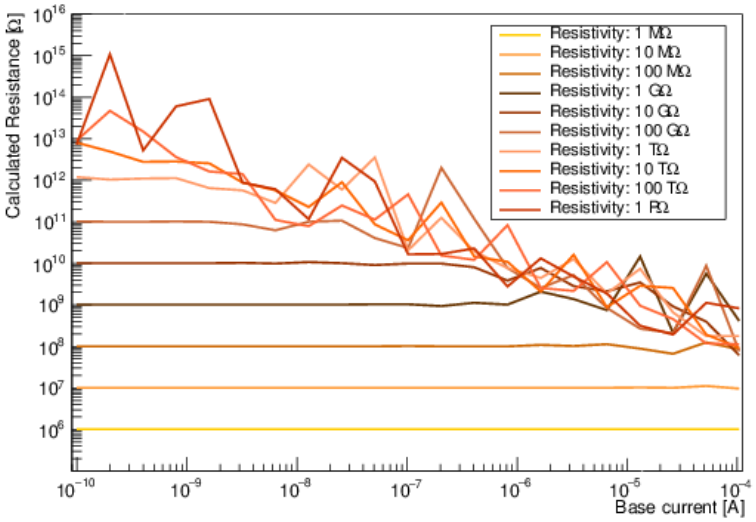

Figure 5.24: Surface resistances calculated from current changes modified by random numbers according to the measurement precision of the current range.

the pico Ampere meter. Figure 5.24 shows calculated surface resistivities for different sensor currents and surface resistivities. All reconstructed resistivities were artificially set to positive values to improve appearance. It was found that for large currents and large surface resistivities (mostly for $I \cdot R > 10^3\,\mathrm{V}$) fluctuations from the measurement dominate current changes from the applied voltage and lead to unreliable results. This measurement was thus considered more qualitative than quantitative: while it could not be trusted to determine the actual sensor surface resistance reliably due to a limited measurement precision, it could be trusted to identify a significantly reduced surface resistance by a chemical or mechanical damage.

Although high resistances above $10\,\mathrm{G\Omega}$ can not be considered reliable, measured strip resistances of 2-10 $\mathrm{G\Omega}$ match the estimation of $7\,\mathrm{G\Omega}$ well (see section 5.3.5).

5.4 Measurements on Blank Sensors Before Treatments

A limited number of miniature sensors was available for tests, which included different sensor architectures and wafer types (see table 3.1). Each treatment required ten sensors which were sufficiently similar to compare the impact of gluing. In order to select miniature sensors for each group, the electrical characteristics of all sensors were tested first. Sensors with architectures BZ1 (no p-stops) and BZ6 (wider strip pitch) were considered too different from the standard sensor layout (BZ3) for reasonable comparisons and were thus excluded from groups of comparable sensors.

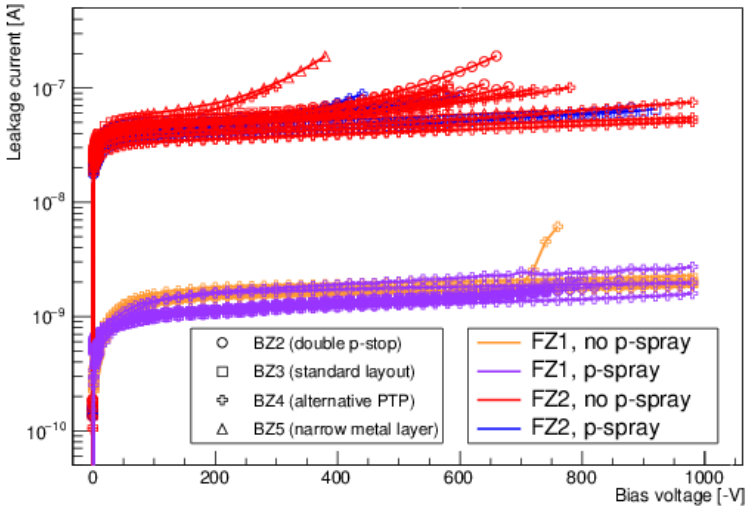

Figure 5.25: Leakage current measurements for miniature sensors used for later tests, with wafer type (colours) and sensor architecture (marker types) indicated. Leakage currents were measured up to -1000 V bias voltage or interrupted in case of an early breakdown. FZ1 sensors show consistently lower leakage currents than FZ2 sensors.

5.4.1 Leakage Current Measurements

Figure 5.25 shows leakage current measurements for all miniature sensors used for later tests. Leakage currents were found to differ significantly for FZ1 wafers and FZ2 wafers: the higher resistivity silicon used in FZ1 wafers led to a leakage current $\mathcal{O}(10^{-9}\,\mathrm{A})$ compared to $\mathcal{O}(10^{-8}\,\mathrm{A})$ for FZ2 sensors. Most of the FZ1 sensors showed the expected sensor behaviour of mostly constant current increase with voltage increase with a sharp increase once the breakdown voltage was exceeded. A large fraction of FZ2 sensors showed a soft breakdown, where the current did not show a constant increase with voltage, but an exponential current increase with voltage. Due to the exponential current increase, an actual breakdown voltage can not be defined, but for several sensors the effect occurred at bias voltages below -700 V (operating point in the ATLAS ITk).

No clear differences between sensors with different architectures or sensors with and without p-spray were observed in leakage current measurements.

5.4.2 Bulk Capacitance Measurements

Bulk capacitance measurements for all sensors under investigation are shown in figure 5.26. The use of a coupling box inserted between probe needles and LCR meter caused small steps in the measured bulk capacitance at 600 V. Bulk capacitance measurements did show dependences on the wafer type: sensors from an FZ2 wafer with p-spray showed a significantly earlier depletion

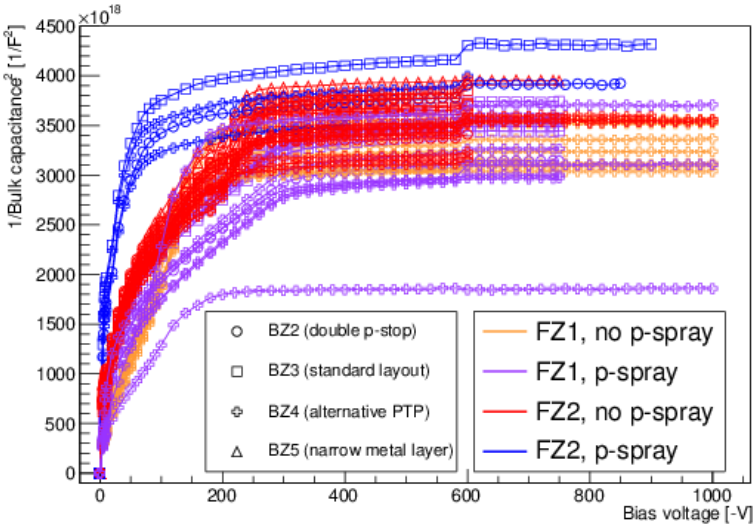

Figure 5.26: Bulk capacitance measurements for ATLAS07 miniature sensors with wafer type (colour) and sensor architecture (marker type) indicated. Bulk capacitances were measured up to the same bias voltage as used for the leakage current measurement of each sensor. Steps at a bias voltage of 600 V are caused by a coupling box inserted between probe needle and LCR meter.

(about 100 V) than other wafer types (about 250 V for FZ1 and FZ2 without p-spray, varying or FZ1 with p-spray). FZ1 sensors with p-spray showed a larger spread than FZ1 and FZ2 without p-spray. It should be noted that all miniature sensors with the wafer type FZ2 with p-spray as well as FZ1 without p-spray were from a single wafer. Due to the low statistics, findings can not be generalised for the wafer type, but can only be attributed to individual wafers.

Bulk capacitance measurements did not indicate any dependence of the capacitance or sensor depletion voltage on the sensor architecture, thus proving that the parallel plate capacitor model is adequate.

5.4.3 Surface Resistance Measurements

Figure 5.27 shows surface resistances measured for ATLAS07 sensors before treatment or gluing. Measurements were found to show large fluctuations both towards higher and lower resistances among strips on the same sensor. Due to the limited current measurement precision and high resistance, fluctuations are expected, especially for FZ2 sensors, which showed a higher current (see figure 5.24). However, since all FZ2 sensors with p-spray as well as all FZ1 sensors without p-spray were from a single wafer, the observation can not be generalised. Additionally, surface resistance measurements are susceptible to small changes of the sensor surface: scratches on the sensor surface or aluminium flakes from repeated probe needle contacts on AC pads (see figure 5.11) can spread metal over the surface. Metal flakes between AC pads and neighbour metal layers effectively reduce the distance between measurement points and can, if large enough,

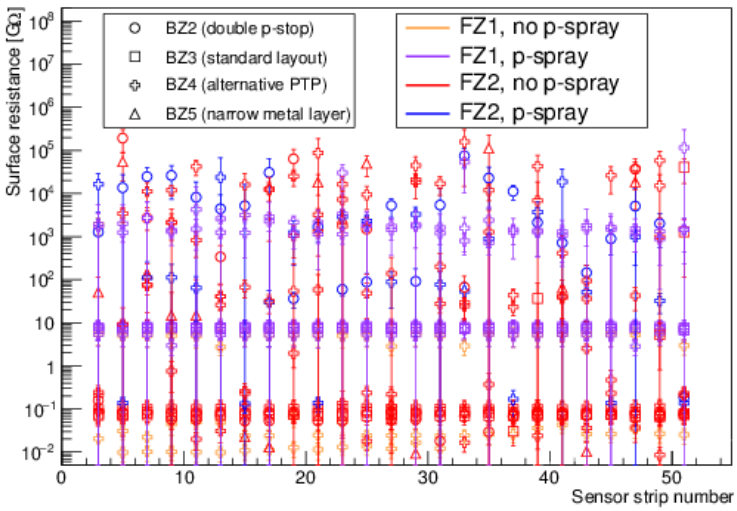

Figure 5.27: Surface resistances measured on 25 strips of ATLAS07 sensors with wafer type (colour) and sensor architecture (marker type) indicated. Surface resistances show a spread over several orders of magnitude. Uncertainties are uncertainties of the linear fit.

reduce the resistance for currents on top of the oxide layer.

Despite fluctuations, surface resistances showed a strong dependence on the wafer type: except for outliers, sensors without p-spray were found to have surface resistances $\mathcal{O}(10^{-2} - 10^{-1}\,\mathrm{G\Omega})$, whereas sensors from wafers with p-spray showed surface resistances $> 1\,\mathrm{G\Omega}$. This observation is expected, as p-spray is added to a sensor surface to reduce the mobility of free charge carriers. Additionally, comparing sensors from FZ1 and FZ2 type wafers with and without p-spray, sensors from FZ1 wafers were found to have lower surface resistances on average.

The measurements showed that surface resistances depend on whether p-spray has been added to a wafer. Sensors selected for the same treatment were thus chosen to have not only the same float zone material, but also to all have or not have p-spray applied.

5.4.4 Inter-strip Capacitance Measurements

Results of inter-strip capacitance measurements on ATLAS07 measurements are shown in figure 5.28. Sensors showed different ranges of inter-strip capacitance values: most sensors were measured to have the expected inter-strip capacitance of about 0.7 pF, i.e. about 0.88 pF/cm, (corresponding to the design value of $\approx 0.8\,\mathrm{pF/cm}$). Lower capacitance measurements can be attributed to one or two needles loosing contact with the neighbour AC pads (see section 5.3.3.2). Higher capacitance values were thought to be individual outliers, but were later discovered to be unreliable measurements (see section 5.5). Unfortunately, glue had been applied to the sensor surface at that point, and measurements on blank sensors could not be repeated.

Inter-strip capacitance measurements did not show any dependence on the wafer type or

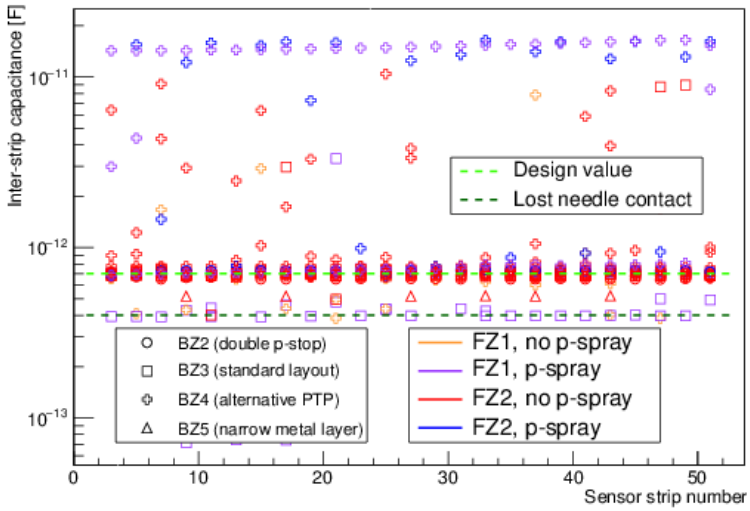

(a) Full capacitance range

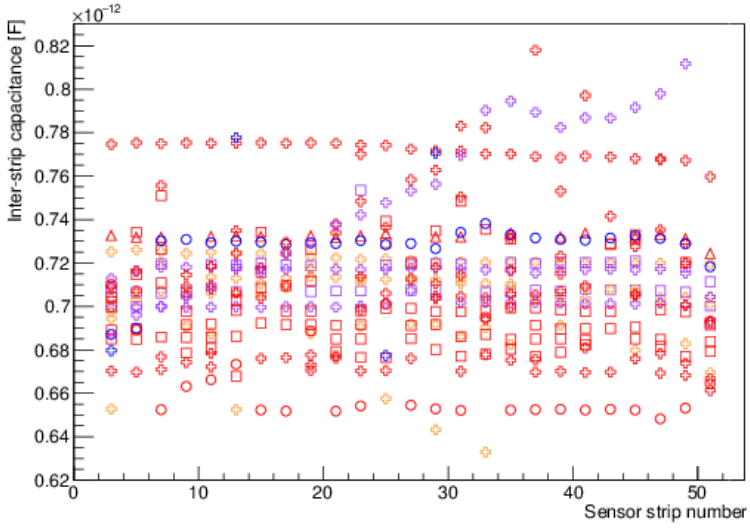

(b) Zoomed in capacitance range

Figure 5.28: Inter-strip capacitance measurements for ATLAS07 miniature sensors depending on wafer type (colour) and sensor architecture (marker type). The displayed point corresponds to the measured capacitance at the highest applied bias voltage. Inter-strip capacitances measured for most sensors agree with the design value, but individual measurements are lower (consistent with lost needle contacts) or significantly higher.

sensor architecture.

5.4.5 Results

Measurements on blank ATLAS07 sensors showed that the measured results depended on the wafer type, i.e. bulk material and presence of p-spray, but not on the sensor architecture:

- leakage current: depended on the bulk material
- bulk capacitance: depended on both bulk material and surface treatment (presence or absence of p-spray)
- surface resistance: depended on both bulk material and surface treatment
- inter-strip capacitance: did not show any dependence on the wafer type

Groups of sensors undergoing the same treatment were thus chosen to have the same wafer type and, if possible, be diced from the same wafer for comparability. Table 5.3 shows an overview of the sensors used for different treatments. Since only sensors with p-stops and similar

Treatment	Number of sensors	Wafer type		Wafers	Architectures
		Bulk	p-spray		
Irradiation (23 MeV protons)	12*	FZ2	no	148, 205*	2, 3, 4A-D, 5
Irradiation (23 MeV protons) + temperature cycling	10	FZ1	yes**	107, 52**	2, 3, 4A-D
Temperature cycling	10	FZ2	no	146, 150	2, 4A-D
Irradiation (800 MeV protons)	4	FZ1	no	72	4A-D
Irradiation (reactor neutrons)	4	FZ2	yes	154	2, 3, 4A-D

* Two sensors from a different wafer (FZ2, no p-spray) were added after two sensors showed an abnormally early breakdown

** After one sensor was found unsuitable during probe station test, it had to be replaced with the only available FZ1 sensor at the time, which did not have p-spray

Table 5.3: Sensor architectures, wafer types and wafers of ATLAS07 miniature sensors used for different treatments

strip-pitches were used (i.e. excluding BZ1 and BZ6 sensors), these requirements limited the numbers of sensors available for each treatment. Irradiations with protons were considered the most important one, as they combined a high ionising dose with bulk damages (see section 3.3.3) and were thus performed on sets of sensors allowing to test all glues under investigation. Only small sets of sensors with sufficiently similar wafer types were available for additional irradiations with reactor neutrons and 800 MeV protons, which allowed only a test of one glue in comparison with blank sensors.

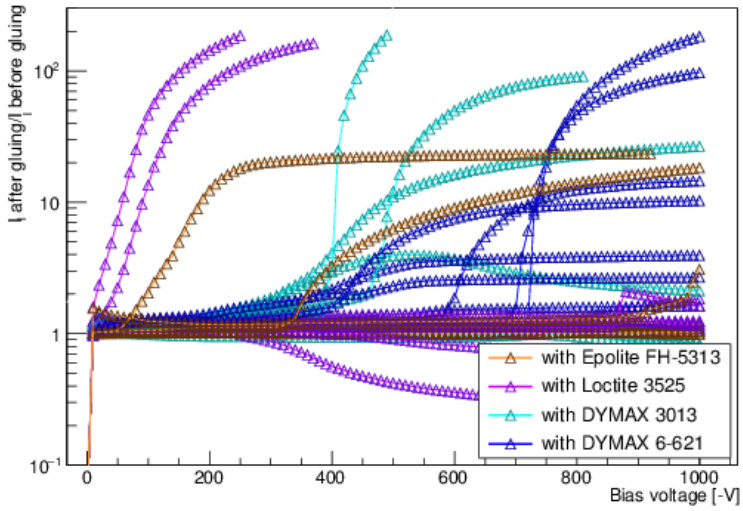

Figure 5.29: Ratios of sensor leakage currents before and after gluing: independent of the applied glue, most sensors show an increased leakage current after gluing.

5.5 Impact of Gluing on Sensor Characteristics

Applying glue to the surface of an ATLAS07 miniature sensor was found to increase the leakage current for most sensors (see figure 5.29). While the extent of the leakage current increase varied, an increase was observed for most sensors under investigation after gluing. In addition to changed leakage currents, several sensors showed earlier breakdowns after glue had been applied (see figure 5.30b). The effect was not observed for all sensors of a certain wafer type or glued with a particular glue, but occurred for individual sensors out of each group. Each glue led to several sensors showing an early breakdown, independent of whether they had shown an early or soft breakdown before (see figure 5.30a). Early breakdowns were found to be more likely to occur if glue had reached the bias ring of a sensor. This observation matches findings for a later version of the sensors (ATLAS12 sensors), where humidity was found to cause early breakdowns located in the bias ring [101]. The presence of glue, which contained a fraction of uncured glue (see section 4.3), on the bias ring, can be assumed to cause a similar effect. It should be mentioned that, while some sensors showed early breakdowns, all sensors fulfilled the ATLAS sensor specification of a leakage current $\leq 0.1\,\mu A$ at a bias voltage of -700 V, despite the observed leakage current increase after gluing.

Bulk capacitance measurements of sensors with glue did not show a decrease or increase compared to the capacitance before gluing (see figures 5.31a and 5.31b). The average value before and after gluing was found to be about 17 pF for the whole bulk, corresponding to 0.23 pF/cm, which is in good agreement with the design specification of about 0.27 pF/cm. One exception was found for two sensors (FZ1 without p-spray) with DYMAX 6-621 where, in both cases, applying glue increased the capacitance from 16.8 pF to 18.5 pF (see figure 5.32). The

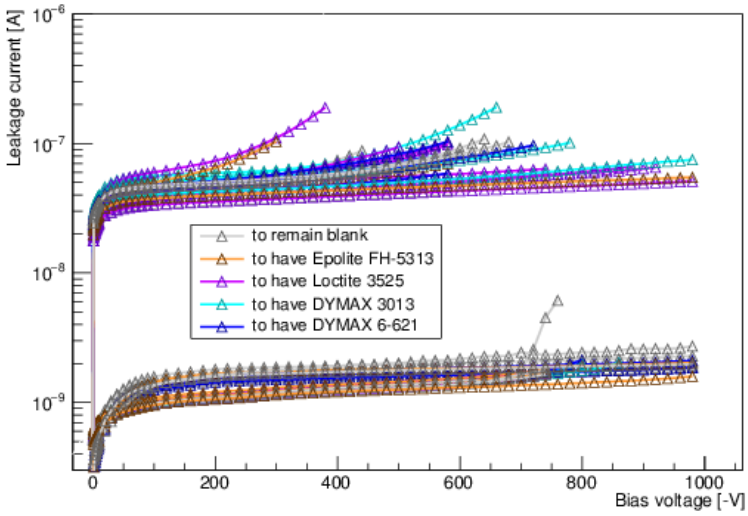

(a) Leakage currents of blank sensors

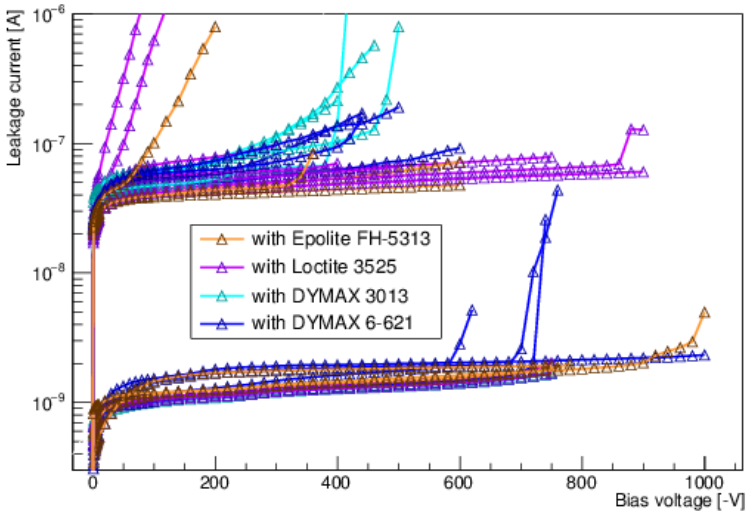

(b) Leakage currents of sensors with glue

Figure 5.30: Leakage currents of sensors before and after gluing: all sensors show an increased leakage current after glue has been applied. Each glue led to individual sensors showing an earlier breakdown than the blank sensor.

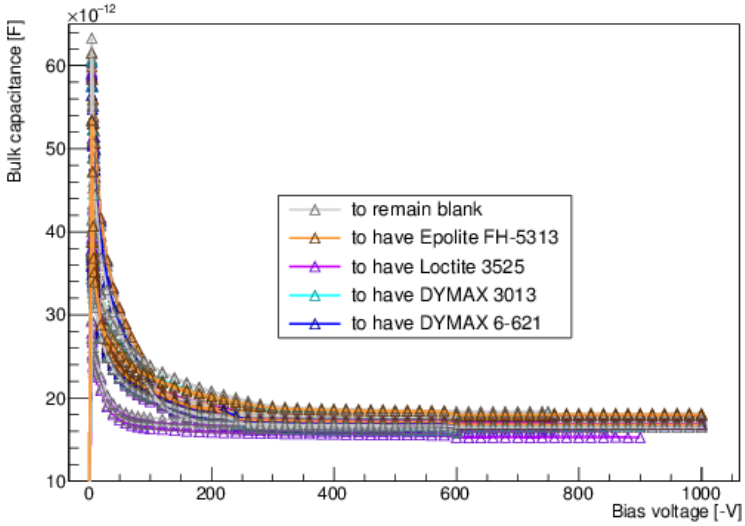

(a) Bulk capacitances of blank sensors

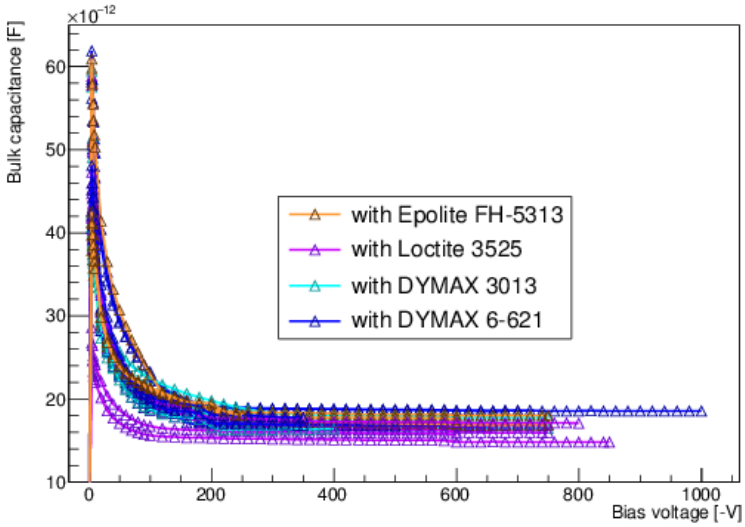

(b) Bulk capacitances of sensors with glue

Figure 5.31: Sensor bulk capacitances before and after gluing: Bulk capacitances did not show systematic decreases or increases after gluing.

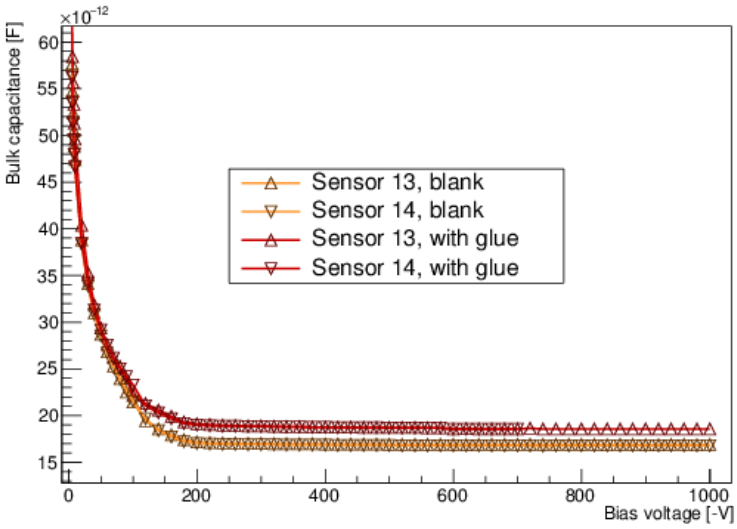

Figure 5.32: Bulk capacitance measurements of FZ1 sensors without p-spray: applying DYMAX 6-621 increased the bulk capacitance equally for both sensors.

same effect was not observed for other sensors with DYMAX 6-621, nor was it observed for a replacement sensor of the same wafer type. It thus needs to be assumed that this effect was specific to this wafer and can not be generalised.

Surface resistance measurements varied for sensors with FZ1 and FZ2 bulk material (see figure 5.33. The occurrence of high surface resistances in measurements of blank FZ1 sensors, but not FZ1 sensors after gluing, does not indicate a glue effect, but represents sensors which were later discovered to be damaged and thus had to be removed from the test group. They are thus not included in figures 5.33b and 5.33d. Independent of the applied glue, all FZ1 sensors showed the expected surface resistance of 1-10 GΩ after gluing. FZ2 sensors did not show a uniform behaviour throughout all sensors or glues, but trends: sensors with large fluctuations of surface resistances between strips continued to show large variations after gluing. Several sensors showed an increased surface resistance after gluing, comparable to the surface resistance of sensors with p-spray. This change, together with the lower surface resistance of sensors without p-spray, indicates that the measured surface current travels along the surface of the sensor bulk, and is hindered by p-spray. For glue to have a similar effect, it needs to chemically react with atoms with unpaired electrons, such as oxygen atoms in silicon oxide which are only connected to one silicon atom [102], or to seal gaps or cracks in the sensor surface. This is further supported by not only the surface resistance changing after gluing, but the absolute current being affected as well (see figures 5.34a and 5.34a). Average surface currents were calculated from the average currents at applied voltages at -1 V and +1 V. Similar to surface resistances, surface currents did not show the same systematic effect for all sensors, but a trend towards lower currents after glue had been applied, which also indicates reduced conductivity on the sensor surface. More clearly than surface resistance measurements, surface currents show

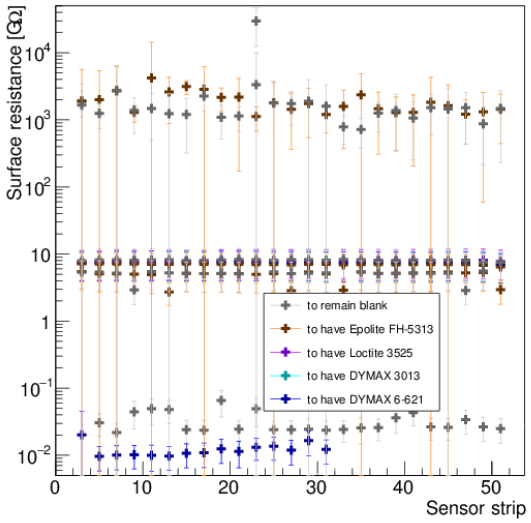

(a) Surface resistances of FZ1 sensors before gluing

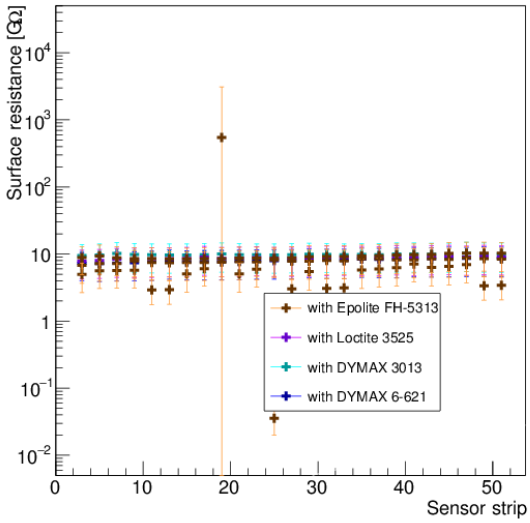

(b) Surface resistances of FZ1 sensors after gluing

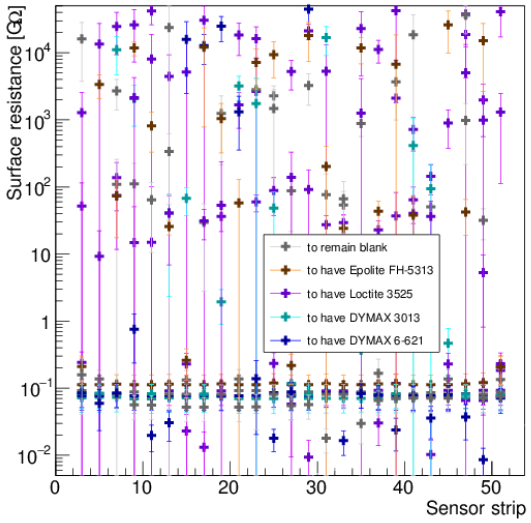

(c) Surface resistances of FZ2 sensors before gluing

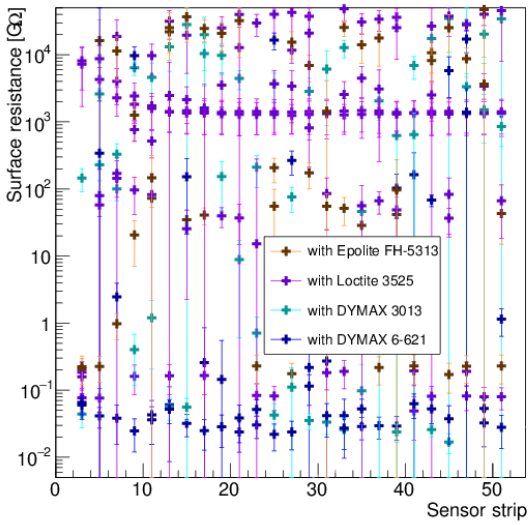

(d) Surface resistances of FZ2 sensors after gluing

Figure 5.33: Surface resistances of sensors before and after gluing, separated by sensor bulk material.

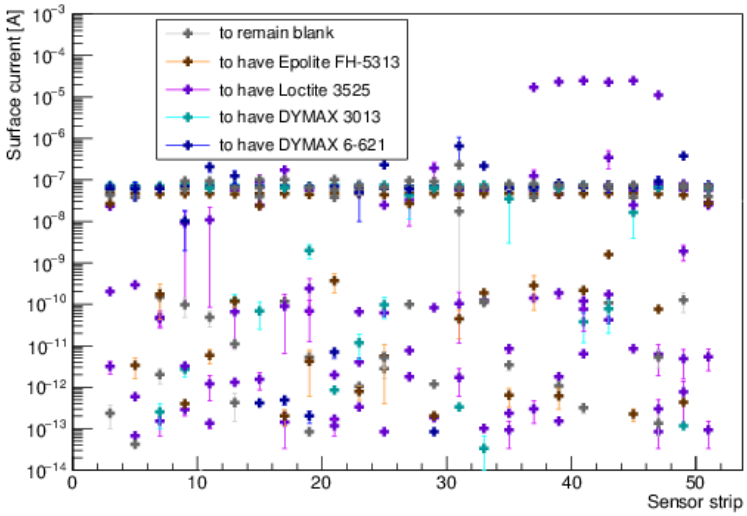

(a) Surface currents on blank FZ2 sensors

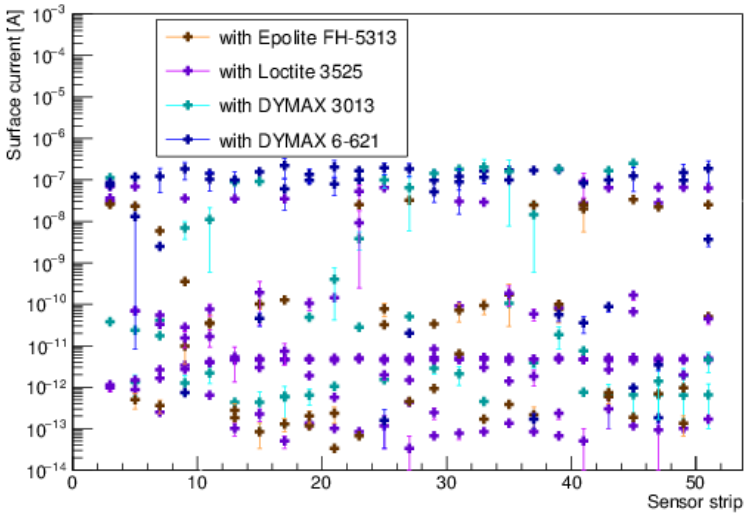

(b) Surface currents on FZ2 sensors with glue

Figure 5.34: Average surface currents of strips on ATLAS07 FZ2 sensors before and after gluing. For several sensors, applying glue can be seen to reduce surface currents. Uncertainties are calculated from the variations of current measurements at different voltages.

a dependence on the used glue: DYMAX 6-621 shows little improvement of the surface current after gluing, but sensors glued with Loctite 3525 show both increased surface resistance and reduced surface currents after gluing. Resistances and currents for sensor strips with DYMAX 3013 and Epolite FH-5313 fluctuated too much to derive any effects.

Inter-strip capacitances showed the most significant change after gluing (see figures 5.33a-5.33d). Inter-strip capacitances of sensors with glue were increased compared to sensors without glue to different extents:

- FZ1 sensors showed an increase by more than an order of magnitude after gluing (see figure 5.35b). Notably, some sensors glued with viscous glues (Epolite FH-5313 and Loctite 3525), show lower capacitances at the sensor edges. Since viscous glues do not spread over the sensor surface as much as less viscous glues (DYMAX 3013 and 6-621) do, edge strips were not covered with glue on several sensors. Locally lower capacitances at the sensor edges thus indicate that the increased capacitance is caused by glue covering sensor strips and not by an overall sensor effect.

- Most FZ2 sensors showed an inter-strip capacitance increase by up to a factor of 3 (see figure 5.35d), which matches expectations (see below).

- Several FZ2 sensors glued with Loctite 3525 showed the same inter-strip capacitance increase by more than an order of magnitude observed for FZ1 sensors.

Inter-strip capacitances of all sensors with glue were significantly higher than ATLAS07 sensor specifications ($\approx 0.8\,\mathrm{pF/cm}$).

It was later discovered that inter-strip capacitances of more than 10 pF are directly contradicted by noise measurements on modules built using full sensors. Sensor modules allow a direct measurement of the sensor noise increase by gluing, because readout electronics are glued onto one out of two sensor rows, leaving every second row blank. By comparing the noise of module channels connected to blank sensor strips and strips covered with glue, the combined impact of gluing on the sensor noise can be investigated. Since the noise contributed by each sensor strip is estimated to be $\approx 1\,\mathrm{pF/cm}$, of which 70 % are attributed to the inter-strip capacitance [2], this measurement allows an estimate of the inter-strip capacitance as well. Studies of modules using sensors with embedded pitch adapters [103], where inter-strip capacitances show large variations between sensor strips, support a strong correlation between inter-strip capacitance and readout channel noise [104].

Test results of ATLAS12 barrel modules constructed with Epolite showed a maximum input noise of 905 ENC (equivalent noise charge) on sensor strips with glue [105]. Measurements of input noises for different attached load capacitances show that a capacitance of 6.5 pF corresponds to an input noise of 1000 ENC, so that the measured capacitances of up to 17 pF should lead to a noise of up to 4000 ENC. Measured inter-strip capacitances of $\approx 10\,\mathrm{pF}$ are thus not supported by module measurements.

A TCAD simulation of a representative sensor cross-section in the bond pad region (see figure 5.36a) showed that adding a glue layer, i.e. a dielectric, to the surface of a sensor, increases the inter-strip capacitance by a factor of about 3 compared to a sensor without glue (see figure 5.36b. This simulation matches the observed inter-strip capacitance increase of

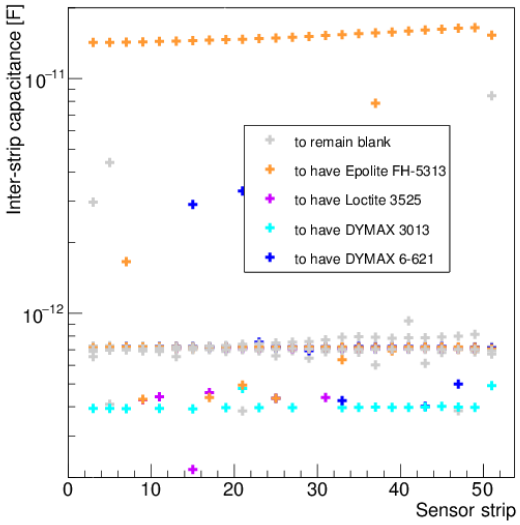

(a) Inter-strip capacitances of FZ1 sensors before gluing

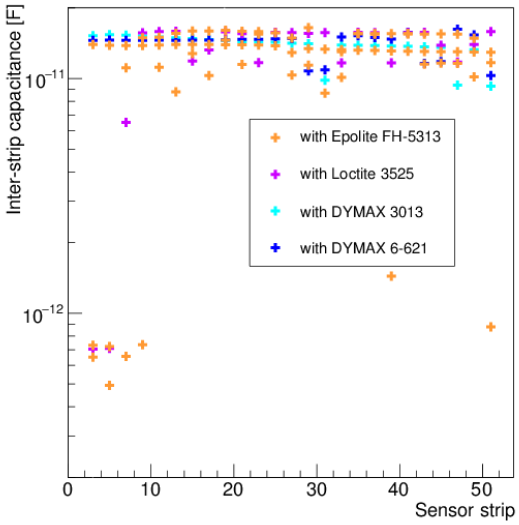

(b) Inter-strip-capacitances of FZ1 sensors after gluing

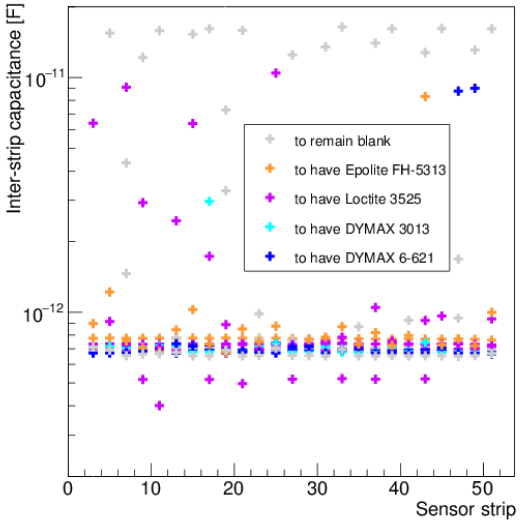

(c) Inter-strip capacitances of FZ2 sensors before gluing

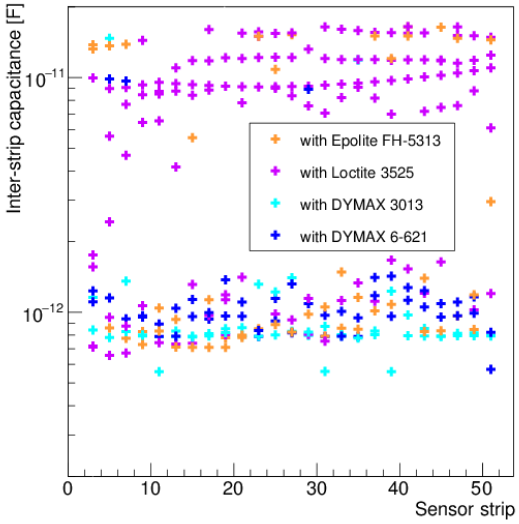

(d) Inter-strip capacitances of FZ2 sensors after gluing

Figure 5.35: Inter-strip capacitances for ATLAS07 miniature sensors before and after gluing: capacitances show large increases for different glues and wafer types.

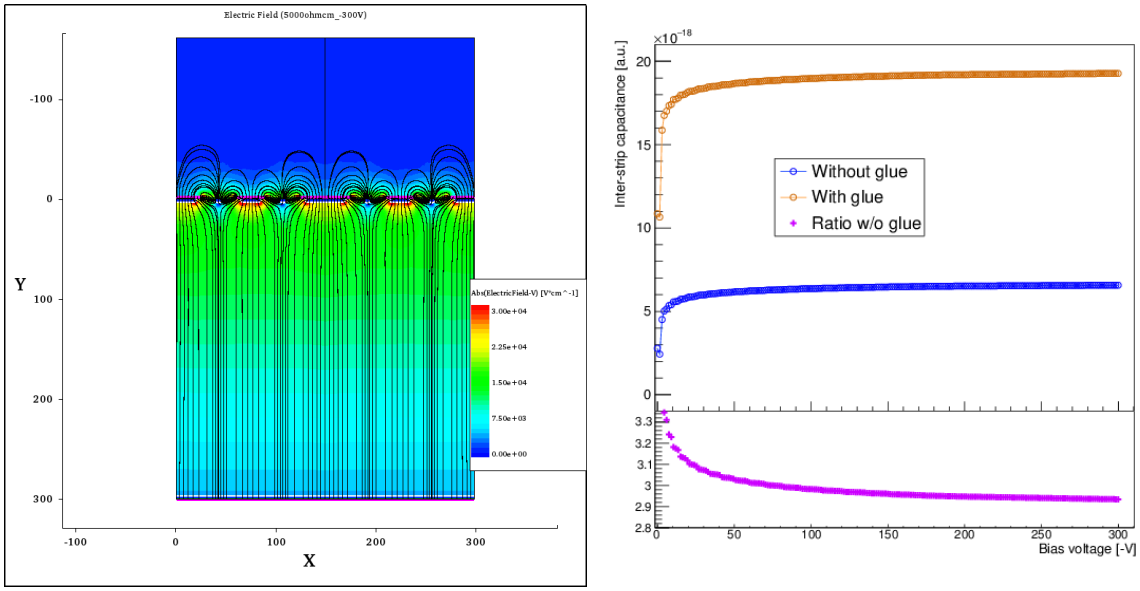

(a) 2D TCAD simulation of an ATLAS07 sensor bond pad region with a 120 µm glue layer

(b) Comparison of simulated inter-strip capacitances on sensors with and without glue

Figure 5.36: Simulated inter-strip capacitances of ATLAS07 sensors with and without glue. Adding glue to the sensor surface increases the capacitance measured between adjacent strips by a factor of 2.9 at depletion voltage.

most FZ2 sensors, which spreads over a range of 0.7 to 2.0 pF, corresponding to an increase of up to 2.9. Capacitances varying between strips on a sensor and different glues are expected due to different glue distributions and dielectric constants. Increases by up to about 2 pF are thus in good agreement with the simulation. All glues in that range showed similar inter-strip capacitance increases.

Larger inter-strip capacitances were contradicted by module noise measurements of large ATLAS sensors. Hence, high capacitances > 3 pF were thus considered to be indicative of an unsuitable measurement setup: the LCR-meter used for capacitance measurements was operated in the standard "series" mode. Depending on the range of the used capacitance and resistance (in this case inter-strip capacitance and resistance), using the standard "series" mode can lead to a wrong reconstruction of the capacitance [106]. This explanation is supported by all sensors with a notably high surface resistance after gluing (FZ1 sensors and FZ2 sensors glued with Loctite 3525) also showing an unreasonably high inter-strip capacitance.

When it was discovered that high inter-strip capacitance values > 3 pF were incompatible with module test results, the corresponding sensors had already been prepared for tests in a β-source setup and were glued onto printed circuit boards, which did not permit further probe station measurements.

Inter-strip capacitance results were thus only considered reliable up to values agreeing with the simulation and module test results.

5.6 Impact of Irradiation with 23 MeV Protons

Irradiations led to an increased leakage current in all sensors (see figure 5.37). All sensors

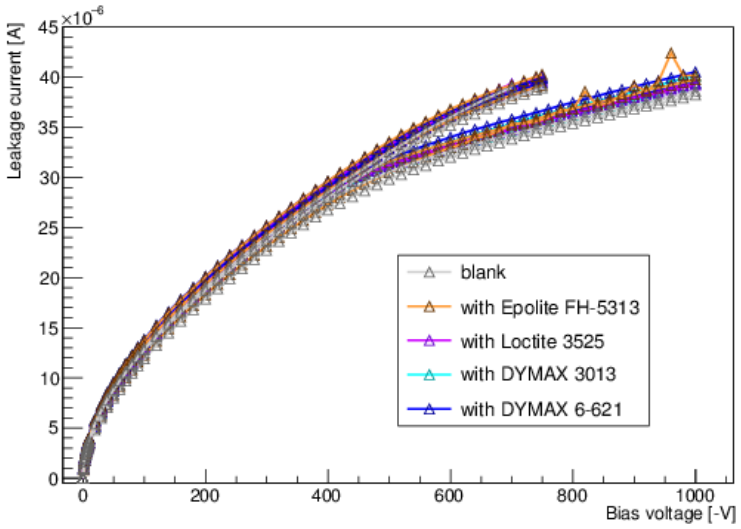

Figure 5.37: Leakage current measurements of ATLAS07 miniature sensors after irradiation with 23 MeV protons. FZ1 type sensors were tested up to bias voltages of -1000 V, FZ2 sensors up to -750 V as they showed a higher increase.

showed similar leakage currents up to bias voltages of about -400 V, after which sensors from FZ2 wafers showed higher currents than sensors from FZ1 wafers. Since n-in-p type sensors deplete from the sensor surface down to the backplane, this behaviour is expected, because for low bias voltages, the leakage current is dominated by the surface geometry, which is identical for both sensor types. For higher bias voltages, the higher resistivity of FZ1 sensors leads to a lower leakage current as observed in the measurement. No early breakdowns were observed for any of the sensors after irradiation - all sensors which had shown early breakdowns before or after gluing had improved after irradiation. All sensors fulfilled the sensor specification requirement of a breakdown voltage exceeding -700 V after irradiation. As observed before irradiation, sensors with glue showed a higher leakage current than blank irradiated sensors with a discrepancy of 3-10 %, depending on the sensor.

Bulk capacitance measurements did show differences for sensors from FZ1 and FZ2 sensors, but no dependence on the use of glue (see figures 5.38a and 5.38b).

Surface resistances were found to be significantly reduced after irradiation, with surface currents being increased accordingly (see figures 5.39a and 5.39b). After irradiation, surface resistances had decreased significantly to $< 10^{-3}$ GΩ. This change can be understood by considering changes in the silicon oxide layer during irradiation in the presence of oxygen: the high electrical resistivity of silicon oxide depends on an ideal grid, where each silicon atom is connected to four oxygen atoms and each oxygen atom is connected to two silicon atoms.

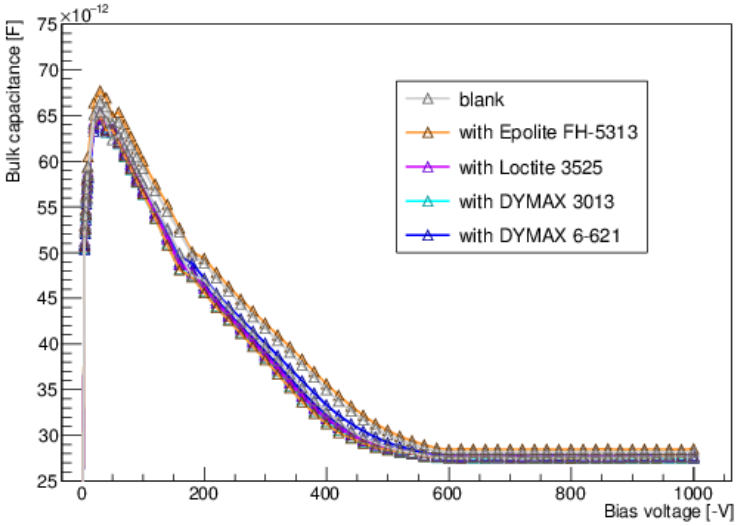

(a) Bulk capacitance measurements of ATLAS07 FZ1 sensors after irradiation with 23 MeV protons

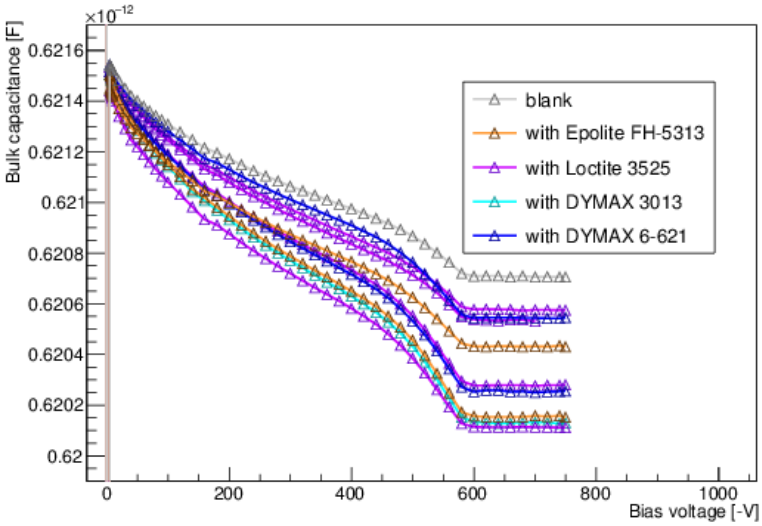

(b) Bulk capacitance measurements of ATLAS07 FZ2 sensors after irradiation with 23 MeV protons

Figure 5.38: Capacitances of ATLAS07 sensors after proton irradiation: FZ1 sensors showed a higher bulk capacitance than FZ2 sensors, but no dependence on the applied glue. The flattening at bias voltages of -600 V is caused by the use of a coupling box.

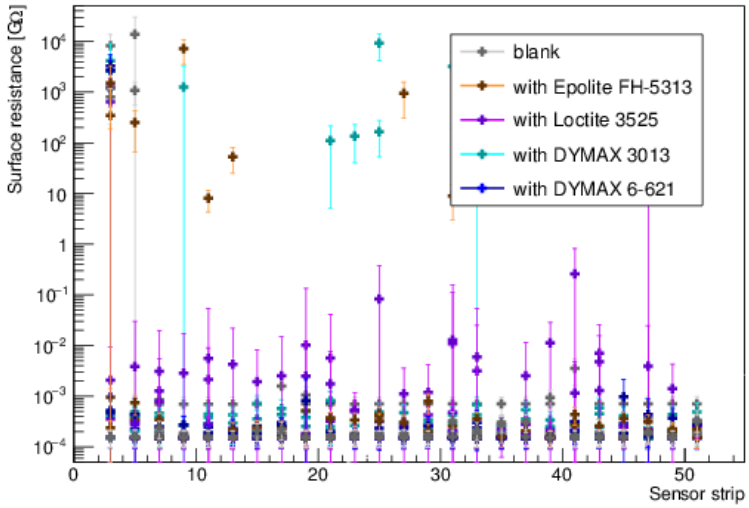

(a) Surface resistances of ATLAS07 miniature sensors after proton irradiation

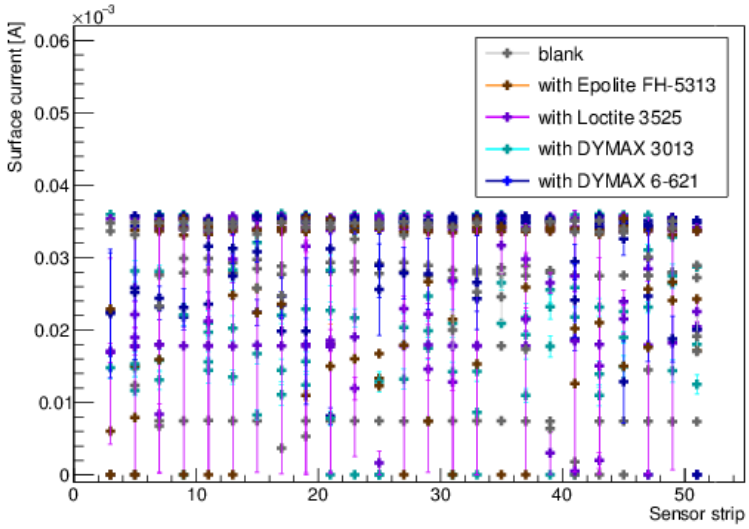

(b) Surface currents of ATLAS07 miniature sensors after proton irradiation

Figure 5.39: Surface current measurements of ATLAS07 miniature sensors after irradiation with 23 MeV protons. Sensors with glue show a tendency towards higher surface resistances and lower surface currents.

Oxygen atoms connected to only one silicon atom have unpaired electrons which act as electron donators and decrease the electrical resistivity of silicon oxide. The quality of silicon oxide grown on silicon sensors depends on the environmental temperature and oxygen concentration. During irradiations in the presence of oxygen, the existing silicon oxide layer can be damaged and connect to oxygen atoms in the air [107], leading to more imperfections in the silicon oxide layer and thus lowering its resistance. Miniature sensors which were partially covered with glue show a trend towards higher surface resistances than blank sensors after irradiation as well as lower surface currents. Since glue shields the sensor surface from oxygen in the atmosphere, the presence of glue on the sensor can be expected to mitigate the reaction of silicon oxide with oxygen, which matches the observations well.

Inter-strip capacitance measurements showed different results for FZ1 type sensors (with p-spray) and FZ2 type sensors (without p-spray), see figures 5.40a and 5.40b. FZ2 sensors without p-spray showed a high increase to 2.2-2.7 pF/2.8 pF (sensors with/without glue), which is caused by proton irradiation (see section 2.3): Irradiation leads to the accumulation of electrons near the surface of the sensor bulk, which causes a type inversion and acts as a conductive layer. While p-spray decreases the number of free electrons near the sensor surface and thus reduces the effective space charge density, p-stops create an electric field which interrupts the type-inverted layer. Both methods prevent the formation of a conductive channel between adjacent sensor strips, but affect the existence of free electrons differently. In the absence of p-spray, the existence of free charge carriers between strip and p-stop implants affects the electric field and thus increases inter-strip capacitance as observed in the measurements.

While glue led to increased inter-strip capacitances on unirradiated sensors, irradiated sensors with glue showed lower inter-strip capacitances than blank sensors. Glue in a sensor surface has a similar effect as p-spray on a smaller scale. Since glue is separated from the sensor bulk material and the conductive type-inversion layer by a silicon oxide, it can not interact directly with the sensor bulk. The observations thus indicate that glue accumulates charges and acts as a MOSFET gate. It should be noted that only FZ2 sensors without p-spray showed a high increase of inter-strip capacitance after irradiation: neither FZ1 sensors with p-spray (see figure 5.40a) nor FZ2 sensors with p-spray (see section 5.10) showed a similar increase. FZ1 sensors without p-spray (see section 5.9) did not show an increase either, as the higher resistivity FZ1 material mitigated the effects of a type-inversion layer. Similar to sensors before irradiation, sensors with glue showed a higher inter-strip capacitance than blank sensors after irradiation. The discrepancy decreased with irradiation to 1.3 pF for sensors with glue compared to 0.7-0.8 pF for blank sensors. The inter-strip capacitance of sensors with glue depends on the dielectric constant of glue and glue has been found to change with irradiation (see section 4.3). Irradiation can thus be assumed to reduce the dielectric constant of the glues under investigation

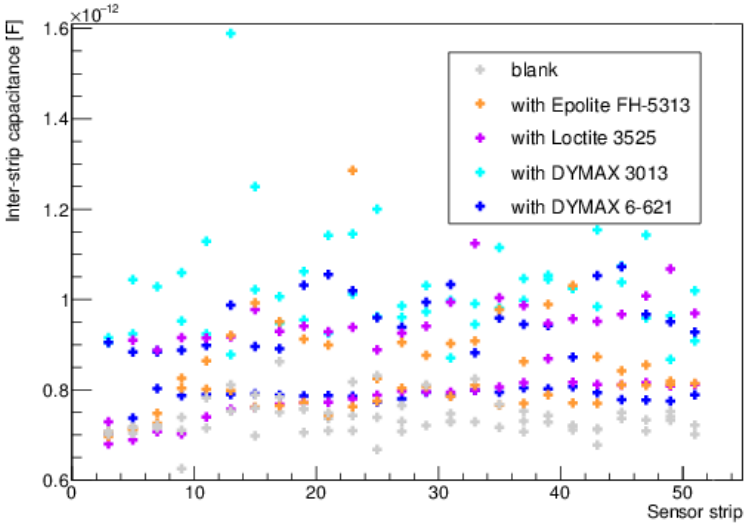

(a) Measurements of FZ1 type sensors with p-spray

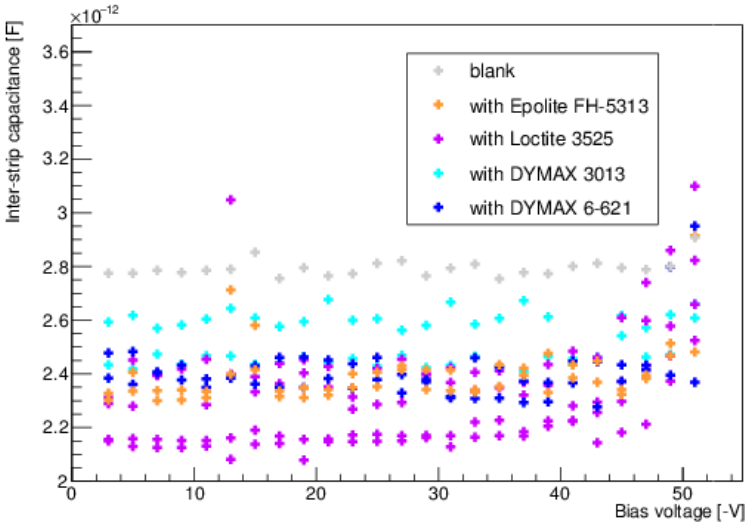

(b) Measurements of FZ2 type sensors without p-spray

Figure 5.40: Inter-strip capacitances of ATLAS07 sensors irradiated with 23 MeV protons: FZ1 sensors after irradiation showed similar capacitances as before irradiation, with glue leading to higher capacitances, whereas FZ2 sensors' capacitances had increased after irradiation, more for blank sensors than for sensors with glue.

5.7 Impact of Temperature Cycling on Sensor Characteristics

Only FZ2 type sensors (without p-spray) were temperature cycled directly after gluing. Since different glues did not show notable differences, plots for sensors after temperature cycling only differentiate between sensors with and without glue.

Figure 5.41 shows leakage current measurements of sensors after temperature cycling. After

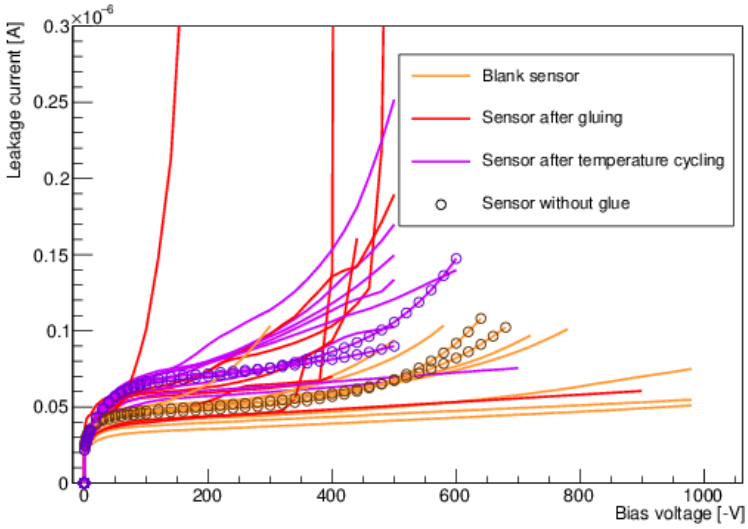

Figure 5.41: Leakage current measurements of ATLAS07 miniature sensors with and without glue before and after temperature cycling. Results for sensors with glue do not show any dependence on the used glue and are thus not differentiated. Blank sensors remaining blank are marked with circles.

temperature cycling, leakage currents of sensors both with and without glue had increased, with several sensors not fulfilling the ATLAS specification of a leakage current $< 0.1\,\mu A$ measured at -700 V any more. Since a large fraction of sensors showed soft breakdowns at different bias voltages before and after temperature cycling, leakage currents can not be compared directly. Using only leakage currents before breakdowns occurred, temperature cycling was found to increase currents by $\mathcal{O}(10^{-8}\,A)$ for every sensor, independent of whether it was blank or glued. In addition to an overall current increase, all but one sensor showed soft breakdowns after temperature cycling, with blank sensors behaving similar to sensors with glue. It should be noted that sensors showing early breakdowns after gluing had improved after temperature cycling and showed soft breakdowns. In previous studies, early breakdowns of silicon strip sensors after gluing have been shown to improve with glue curing [43] and temperature cycling [51]. Here, both irradiation and temperature cycling were found to improve early breakdowns: after irradiation, no sensor showed an early breakdown, whereas sensors after temperature cycling still showed soft breakdowns. Early breakdowns have been linked to curing before and glue is known to be not fully cured after nominal curing [108], but continues curing, especially when

exposed to increased temperatures or irradiation (see section 4.3). Early breakdowns can thus be attributed to the presence of uncured glue on the sensor surface, particularly in the vicinity of this bias ring.

Similar to leakage current, bulk capacitances showed an increase after temperature cycling, independent of the presence of glue on the sensor (see figure 5.42). Since the changes were

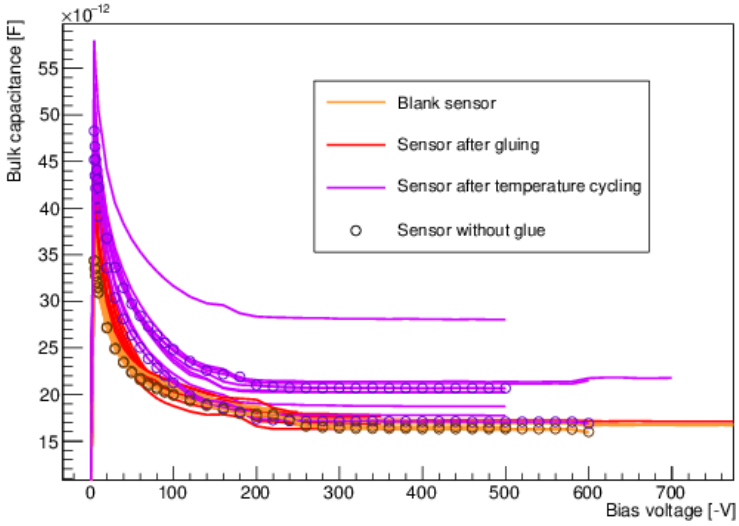

Figure 5.42: Bulk capacitance measurements of ATLAS07 miniatures sensors with and without glue after temperature cycling, in comparison with measurements of blank sensors and sensors after gluing. Since sensors glued with different adhesives did not show systematic differences, they are not differentiated in the plot. Blank sensors are marked with circle symbols.

observed both for blank sensors and sensors with glue, the effect can not be attributed to the presence of glue. The observed changes indicate that the strip implants were affected by the temperature changes: if strips were implanted with a sharp edge, temperature changes and prolonged times at elevated temperatures could lead to implanted atoms diffusing in the silicon grid [109]. The resulting larger implant depth and width would lead to both an increased leakage current and bulk capacitance and thus explain the observed effect.

Except for two sensors, which showed unreasonably high measurement results (see section 5.5), all inter-strip-capacitances were measured to be between 0.6 and 1.8 pF. Compared to sensors after gluing, temperature cycling reduced the average inter-strip capacitance (see figure 5.44). Comparing the average inter-strip capacitances of blank sensors (0.77 ± 0.03 pF), sensors after gluing (1.00 ± 0.33 pF) and after temperature cycling (0.77 ± 0.02 pF for sensors with glue, 0.71 ± 0.02 pF for blank sensors), temperature cycling can be seen to reduce the inter-strip capacitance. A small change in the inter-strip capacitance of blank sensors after temperature cycling matches the observed changes in leakage current and bulk capacitance. Similar to sensor measurements after gluing, glue on the sensor surface leads to a higher inter-strip capacitance

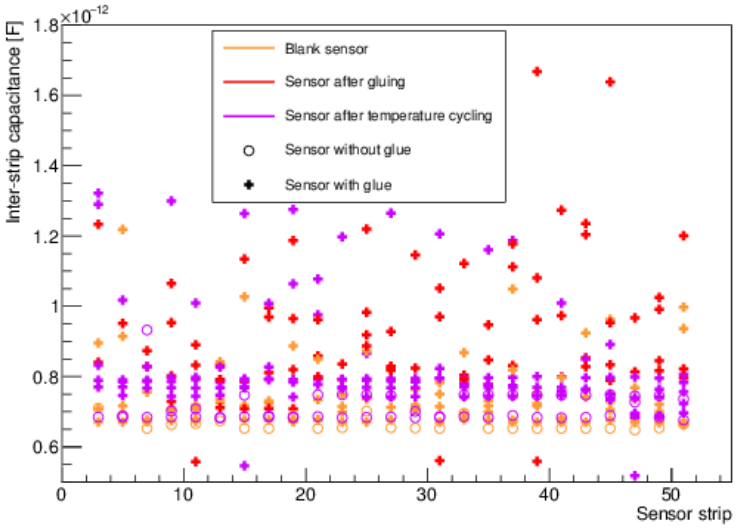

Figure 5.43: Inter-strip capacitances of blank and glued ATLAS07 sensors after temperature cycling. Blank sensors show lower inter-strip capacitances after temperature cycling than sensors with glue. Results from two sensors above 10 pF were excluded for visibility.

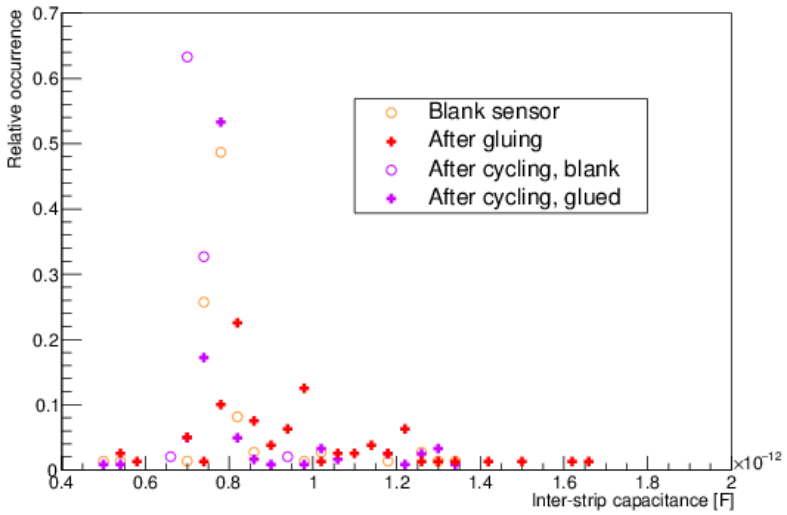

Figure 5.44: Inter-strip capacitances of ATLAS07 miniature sensors after gluing (red markers) and after temperature cycling. Values above 10 pF were excluded.

than observed for blank sensors. But compared to measurements after gluing, temperature cycling has decreased the observed inter-strip capacitance.

The increase of inter-strip capacitance in the presence of glue (see figure 5.36) depends on the permittivity of the glue. Since elevated temperatures lead to a continuation of the curing process in glue [108], the improved inter-strip capacitance can be understood as a side effect of fully cured glue: uncured glue molecules have groups of atoms designed to react with other molecules to form larger molecules (e.g. epoxy groups in epoxy glue). In uncured glue, these atoms are not connected to other molecules and thus have a higher reactivity than large molecules of interconnected glue. Since the permittivity of a material is associated with its polarisability, the presence of partially cured glue can be understood to cause a higher permittivity and thus a higher inter-strip capacitance than fully cured glue, as seen in the measurements. For a better understanding of the electrical differences of partially and fully cured glue, future measurements could investigate the permittivity of glue at different curing stages. It should be noted that, while inter-strip capacitances of sensors with glue exceeded the ATLAS07 specifications of about 0.8 pF/cm, sensors after temperature cycling fulfilled the criterion.

Surface resistances and currents show similar results for sensors with and without glue (see figures 5.45a and 5.45b). Different from surface resistances before temperature cycling, measurements after temperature cycling showed a small spread between $10^{-2} - 10^{-1}\,\mathrm{G\Omega}$ except for a few outliers. Similarly, surface currents of sensors after temperature cycling showed a small spread comparable to sensors before temperature cycling. The considerable increase in surface resistance and decrease in surface resistance seen on several sensors after gluing was not observed after temperature cycling. Additionally, the surface resistance on blank sensors showed a decrease before and after temperature cycling.

Due to different effects derived from sensor measurements, changes in surface resistances can not be attributed to a specific change with certainty. However, since the discrepancies, observed between sensors with and without glue in the previous measurement step, were not observed after temperature cycling, surface characteristics after temperature cycling can be assumed to be sensor dominated, not glue related.

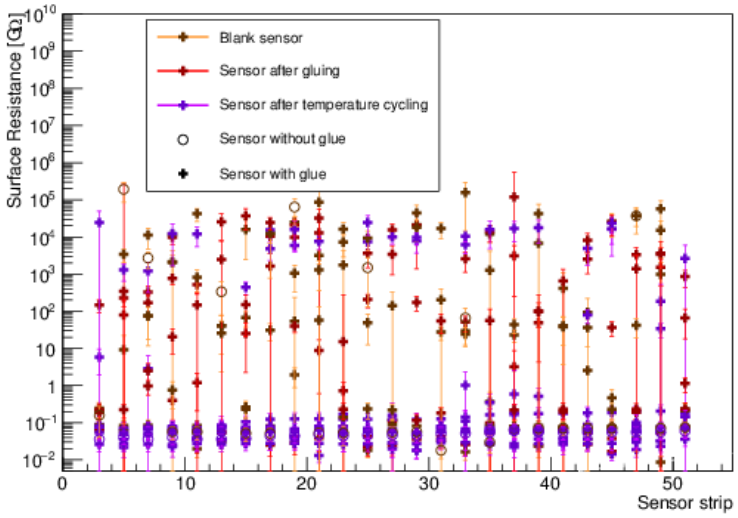

(a) Surface resistances after temperature cycling

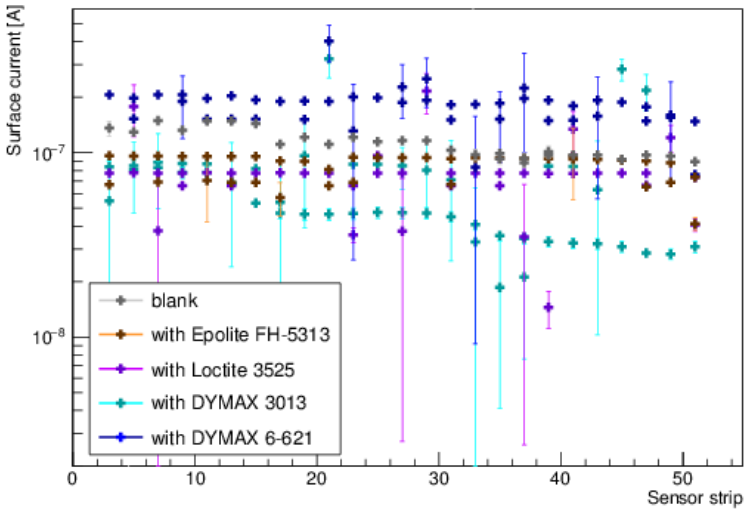

(b) Surface currents after temperature cycling

Figure 5.45: Surface measurements of ATLAS07 FZ2 miniature sensors after temperature cycling.

5.8 Impact of Temperature Cycling after Irradiation

Temperature cycling sensors after irradiation led to the expected leakage current improvement due to beneficial annealing (see figure 5.46, c.f. leakage currents after irradiation, figure 5.37). Previous leakage currents of $38 - 41 \cdot 10^{-6}$ µA were reduced to $16 - 18 \cdot 10^{-6}$ µA, measured at

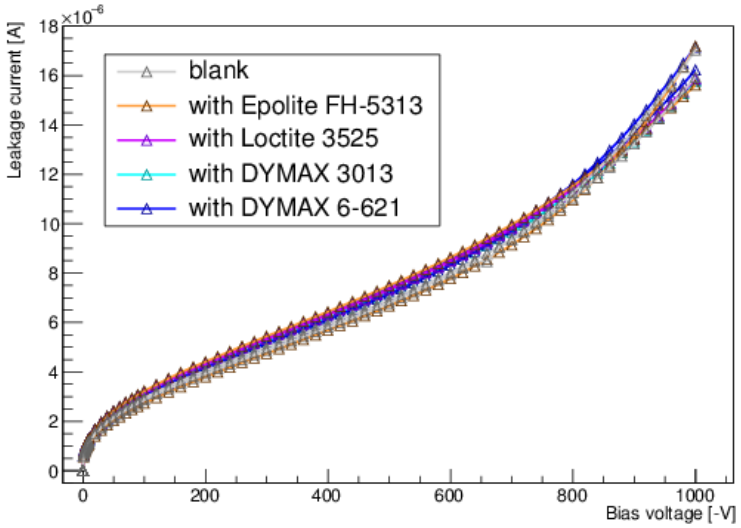

Figure 5.46: Leakage current measurements of ATLAS07 FZ1 type sensors after irradiation with 23 MeV protons and temperature cycling.

-1000 V bias voltage. All sensors were biased up to -1000 V without early breakdown and thus fulfilled the corresponding ATLAS07 requirement. Sensors with and without glue did not show differences in the measured leakage currents.

Bulk capacitance measurements (see figure 5.47) did not show any dependence on the presence or absence of glue. As expected for sensors after irradiation, the bulk capacitance is almost independent of the applied bias voltage. A flattening of the measured curves at -600 V is caused by the use of a coupling box, not an indication of depletion.

Inter-strip capacitances measured after temperature cycling and irradiation were found to be increased compared to the values measured after gluing and irradiation (see figure 5.48). While the increase of inter-strip capacitance after gluing can not be quantified due to questionably high results (see figure 5.35b), sensors after irradiation showed inter-strip capacitances similar to those of blank sensors before gluing (0.74 ± 0.01 pF/0.91 ± 0.01 pF for blank/glued sensors after irradiation compared to 0.71 ± 0.02 pF for blank sensors before irradiation). Different from FZ2 sensors without p-spray, irradiation of FZ1 sensors with p-spray showed only a small increase in inter-strip capacitance, with glued sensors showing a larger increase than blank sensors.

Temperature cycling after irradiation led to an increase comparable to that observed for FZ2 type sensors without p-spray: the inter-strip capacitance increased to 2.83 ± 0.01 pF/2.61 ± 0.01 pF for blank/glued sensors. Similar to FZ2 sensors without p-spray after irradiation, FZ1 sensors

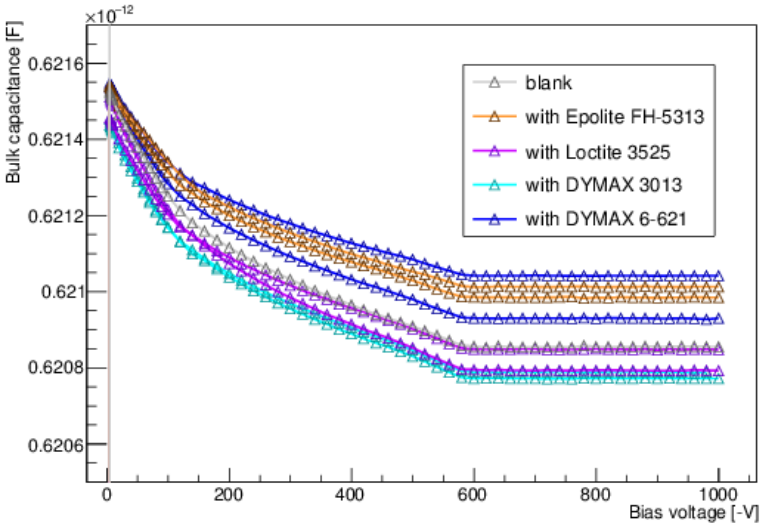

Figure 5.47: Bulk capacitances of ATLAS07 miniature sensors after irradiation and temperature cycling. Measurements of different sensors do not show any discrepancies for sensors with and without glue.

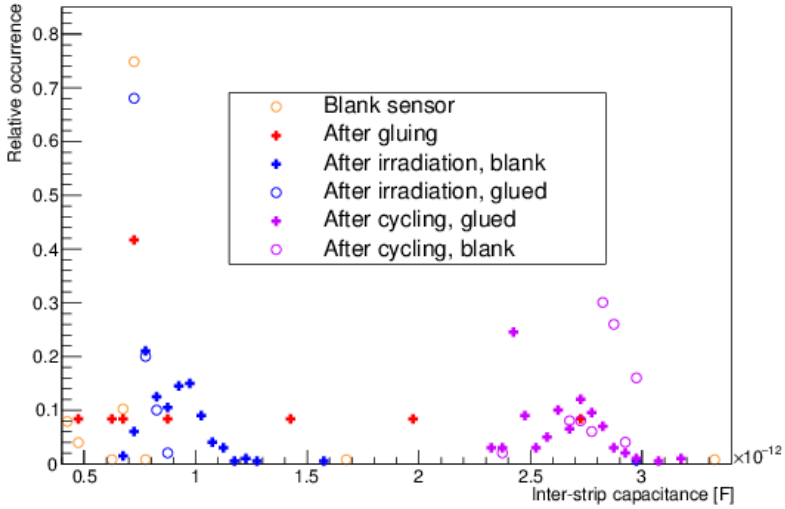

Figure 5.48: Inter-strip capacitances of ATLAS07 FZ1 type sensors measured before and after gluing, irradiation and temperature cycling. Temperature cycling after irradiation was found to increase the inter-strip capacitance. Inter-strip capacitances above 10 pF, which indicate a problem in the measurement setup, were excluded for better visibility.

with p-spray showed a tendency towards lower inter-strip capacitances for sensors with glue (see figure 5.49). As explained in section 3.3.2, radiation defects in silicon can diffuse through

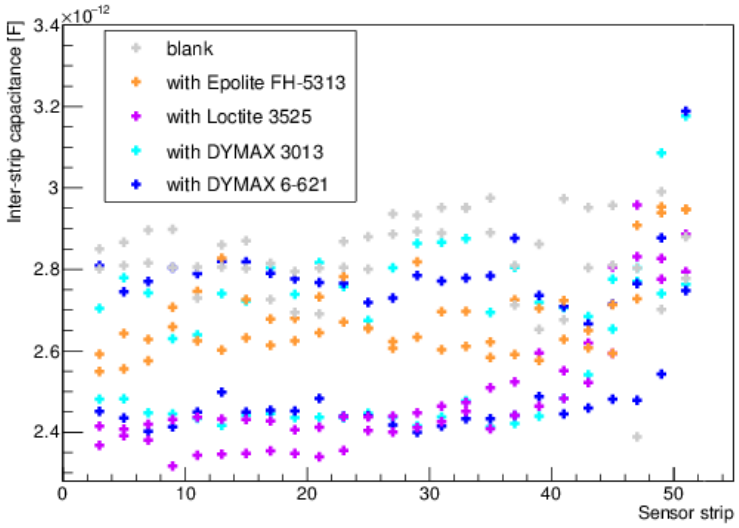

Figure 5.49: Inter-strip capacitances of ATLAS07 FZ1 type sensors measured after temperature cycling, following irradiation with 23 MeV protons.

the silicon lattice and accumulate in one area, e.g. - as indicated from the high inter-strip capacitance - the surface. While p-spray and p-stops in combination with the high resistivity FZ1 material compensated the accumulation of free charge carriers after irradiation, defect migration during high temperature phases increased the effect. A tendency towards lower inter-strip capacitances for sensors with glue indicates again that glues mitigate the increased capacitance from accumulated charges, e.g. by charging up during proton irradiation. A causation of the decrease by the actual presence of glue is again illustrated by several sensors with glue showing inter-strip capacitances converging towards results of blank sensors, as more viscous glues were not spread over strips at the sensor edge on each sensor.

Compared to surface currents $\mathcal{O}(10^{-5}\,\mathrm{A})$ after irradiation (see figure 5.39b), surface currents after temperature cycling were $\mathcal{O}(10^{-6}\,\mathrm{A})$ (see figure 5.50a). Surface resistances after irradiation were $\mathcal{O}(10^{-4}\,\mathrm{G\Omega})$ both before and after temperature cycling (see figure 5.50b). Since increased surface resistances after irradiation were attributed to an uncontrolled growth of silicon oxide in the presence of oxygen, a partial recovery of a resulting conductive oxide layer during temperature cycling can be expected. Surface currents and resistances did not show any dependence on the presence or absence of glue.

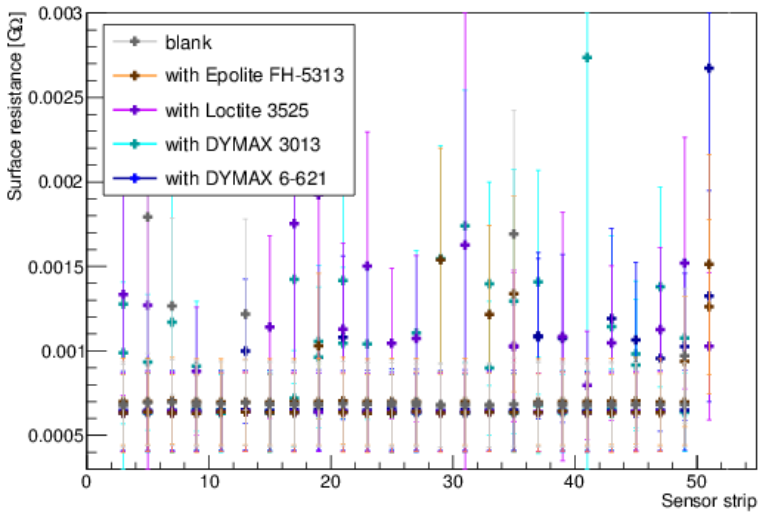

(a) Surface resistances after temperature cycling following irradiation

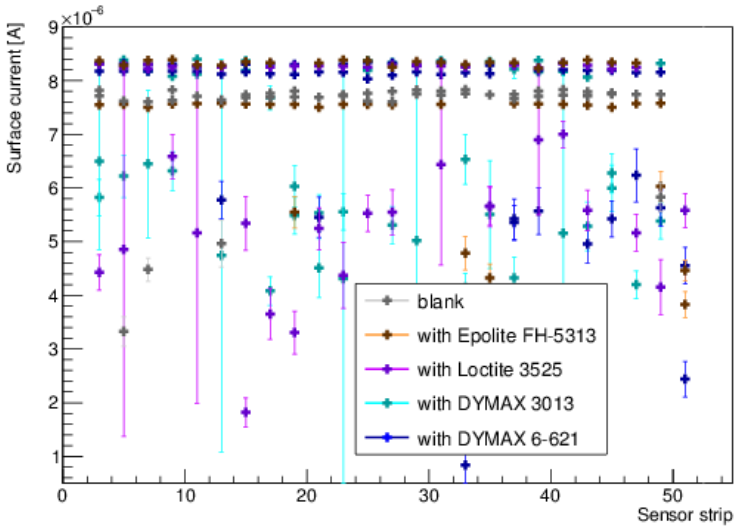

(b) Surface currents after temperature cycling following irradiation

Figure 5.50: Surface measurements on ATLAS07 FZ1 sensors after temperature cycling following an irradiation with 23 MeV protons. Sensors with and without glue show similar surface resistances and currents.

5.9 Impact of Irradiation with 800 MeV Protons

Leakage currents after irradiation with 800 MeV protons were found to be ≈ 90 µA (see figure 5.51) at a bias voltage of -1000 V. Sensors with and without glue did not show different leakage currents after irradiation and fulfilled the ATLAS specification of breakdown voltages beyond −700 V. Similar to leakage currents of sensor irradiations with 23 MeV protons, an

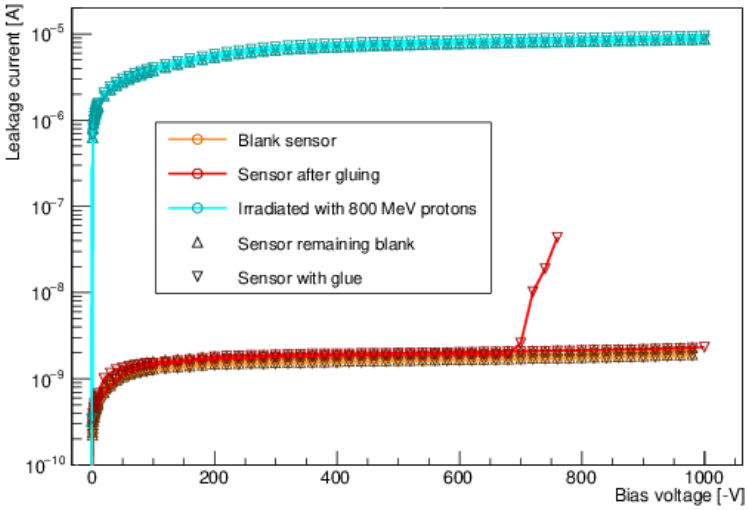

Figure 5.51: Leakage currents of ATLAS07 sensors with and without glue after irradiation with 800 MeV protons in comparison with leakage currents before irradiation.

early breakdown after gluing had disappeared after irradiation.

Bulk capacitances had increased after irradiation (see figure 5.52) and did not show any discrepancies for sensors with and without glue. Bulk capacitances for sensors irradiated with 800 MeV protons were found to behave the same as sensors irradiated with 23 MeV protons. A straightening of the curve at a bias voltage of -600 V is caused by the use of a coupling box and does not indicate depletion.

The sensors available for irradiation with 800 MeV protons were from a FZ1 wafer without p-spray. Inter-strip capacitances after irradiation (see figure 5.53) did not show the increase found for FZ2 type sensors without p-spray (see figure 5.40b), but values comparable to those of blank sensors as observed for FZ1 sensors with p-spray after irradiation (see figure 5.40a). Hence, the higher resistivity FZ1 material compensates for the absence of p-spray in preventing type inversion causing a higher inter-strip capacitance. Sensors with glue showed an inter-strip capacitance of about 0.8 pF, compared to about 0.7 pF for blank sensors. In the absence of a type-inverted bulk layer, glue does not have a beneficial effect, but acts as a dielectric and thus increases inter-strip capacitances.

Surface resistances and currents after irradiation with 800 MeV protons (see figure 5.54) were found to be similar to results after irradiation with 23 MeV protons 5.39a. Since the increase

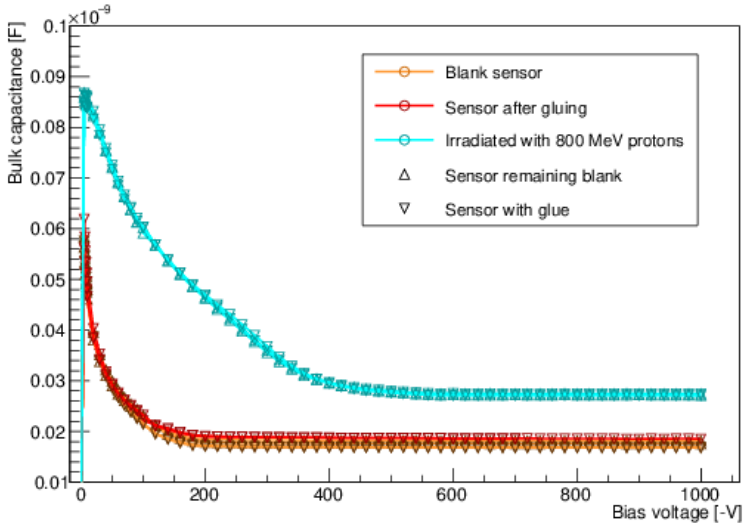

Figure 5.52: Bulk capacitances of ATLAS07 sensors after irradiation with 800 MeV protons in comparison with sensors before and after gluing.

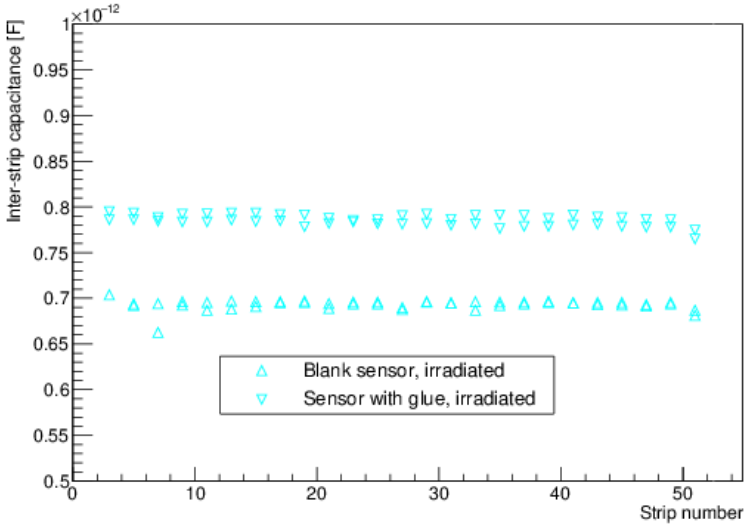

Figure 5.53: Inter-strip capacitances of ATLAS07 sensors after irradiation with 800 MeV protons: sensors with glue show higher inter-strip capacitances than blank sensors.

in both current and resistance after irradiation can be related to silicon oxide growth during irradiation, similar results are expected. No differences were observed between sensors with and

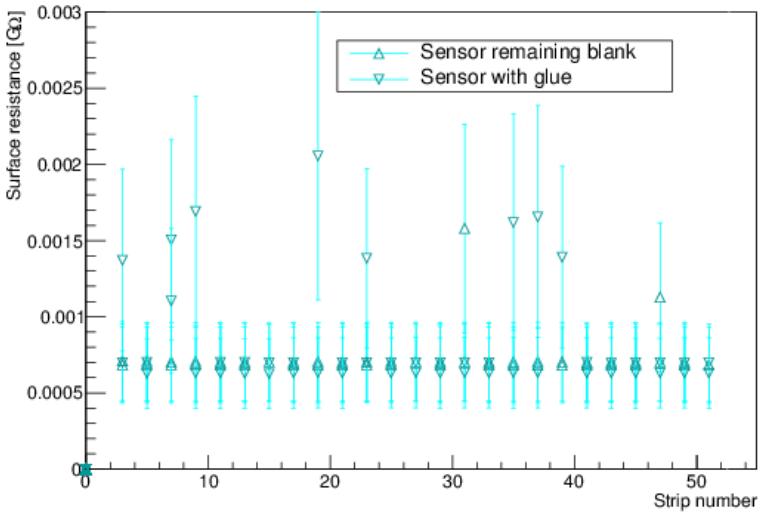

Figure 5.54: Surfaces resistances of ATLAS07 sensors after irradiation with 800 MeV protons. Blank sensors and sensors with glue showed similar results.

without glue.

5.10 Impact of Irradiation with Reactor Neutrons

Sensors irradiated with reactor neutrons showed similar leakage currents (about 45 µA measured at -700 V, see figure 5.55) as sensors irradiated with protons (about 39 µA measured at -700 V, see figure 5.37). While several sensors showed early breakdowns before irradiation, all sensors could be biased up to -700 V after irradiation. No differences were observed between sensors with and without glue.

After irradiation with reactor neutrons, sensors with and without glue did not show any differences in the measured bulk capacitance 5.56.

Inter-strip capacitances after neutron irradiation showed the same behaviour as FZ1 sensors after proton irradiation: blank sensors showed a lower capacitance (about 0.7 pF) than sensors with glue (about 0.8 pF), see figure 5.57. Similar to FZ1 sensors (with and without p-spray), FZ2 sensors with p-spray did not show an increased inter-strip capacitance due to the formation of a type inverted layer, as the p-spray counteracted the effect. Glue on the sensor surface thus acted as a dielectric between strips and led to an increased inter-strip capacitance.

As observed for proton irradiated sensors, neutron irradiation led to increased surface currents $\mathcal{O}(10^{-5}\,\mathrm{A})$ and reduced surface resistance $\mathcal{O}(10^{-4}\,\mathrm{G\Omega})$, see figure 5.58. Matching observations after proton irradiations, irradiation with reactor neutrons reduced surface resistances equally for sensors with and without glue. Again, the independence of the decrease from the presence

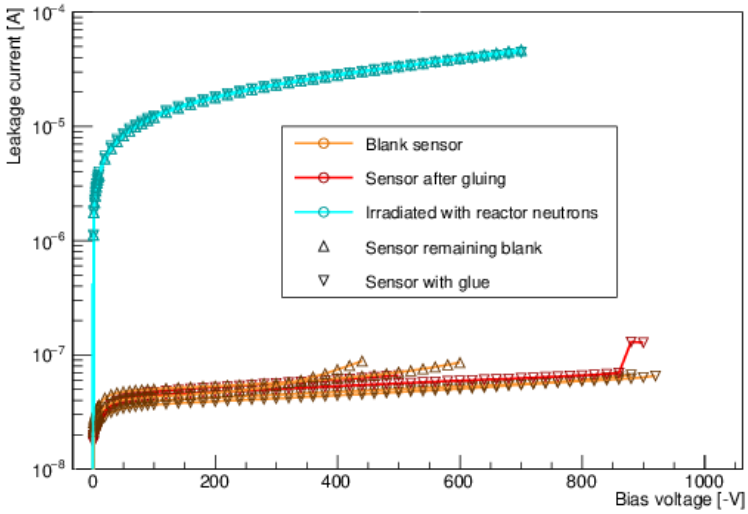

Figure 5.55: Leakage currents of ATLAS07 FZ2 sensors with p-spray after irradiation with reactor neutrons in comparison with leakage currents before and after gluing. Leakage currents of sensors with and without glue did not show any discrepancies after irradiation with reactor neutrons.

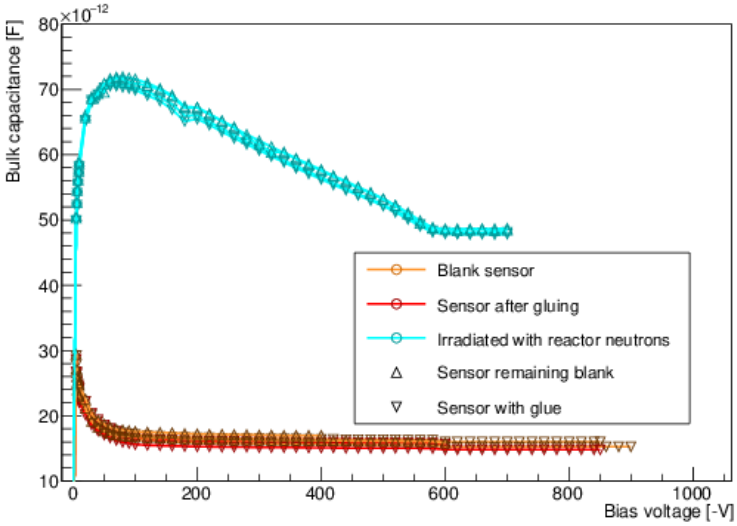

Figure 5.56: Bulk capacitance measurements of ATLAS07 FZ2 sensors with p-spray after irradiation with reactor neutrons, in comparison with measurements before and and after gluing. Bulk capacitances of sensors with and without glue did not show any differences after irradiation with reactor neutrons.

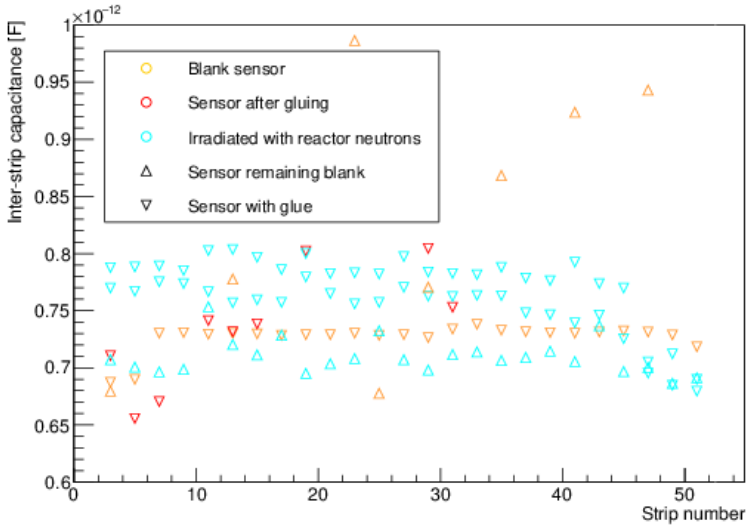

Figure 5.57: Inter-strip capacitances of ATLAS07 FZ2 sensors with p-spray after irradiation with reactor neutrons in comparison with sensor measurements before and after gluing. Sensors with glue show a higher inter-strip capacitance than sensors without glue after neutron irradiation.

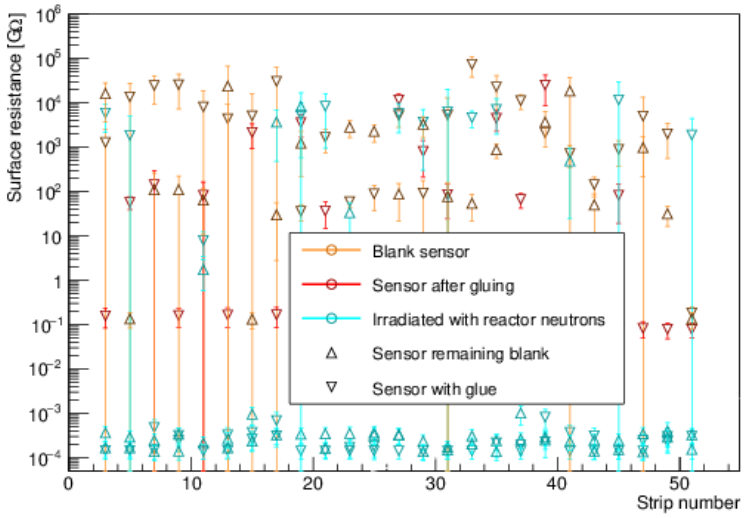

Figure 5.58: Surface resistances of ATLAS07 FZ2 sensors with p-spray after irradiation with reactor neutrons in comparison with surface resistances before and after gluing. Surface resistances after irradiation did not show discrepancies between sensors with and without glue.

of glue indicates a sensor effect and can be explained by a reaction of silicon oxide with oxygen during irradiation.

5.11 Conclusion of Probe Station Measurements

Probe station measurements showed that gluing affects several sensor characteristics.

Leakage currents of all sensors under investigation were higher after gluing, which corresponds to a higher noise. An increased fraction of sensors showed early or soft breakdowns, especially if glue covered the sensor bias ring, which meant several sensors did not fulfil the maximum current and minimum breakdown voltage requirements of ATLAS07 sensors after gluing. Both irradiation and temperature cycling eliminated early sensor breakdowns, with temperature cycling leading to an increased number of soft breakdowns, and increased the average leakage current. Only for sensors irradiated with 23 MeV protons, sensors with glue showed a tendency towards higher leakage currents than blank sensors, which disappeared after temperature cycling. Gluing was thus found to have a disadvantageous effect on sensors before irradiation, which was then restored to normal by sensor irradiations.

Bulk capacitances of sensors did show small changes after gluing, but no systematic increase or decrease for several sensors of the same type or glued with the same glue. Hence, the glues under investigation could not be associated with a systematic impact on sensor bulk capacitances or depletion voltages.

The absence of changes in both leakage currents and bulk capacitance throughout different treatments indicate that defects in the silicon bulk caused by atoms or molecules diffusing into the silicon are negligible, if at all present.

The impact of gluing on sensor inter-strip capacitances (about 0.7 pF on blank sensors) could not be quantified with certainty, as a faulty setup led to unreasonably high capacitance measurements. Values within a reasonable capacitance range showed an increase of up to a factor of 3, which agrees well with simulated results. Temperature cycling mostly reduced inter-strip capacitances of sensors with glue: except for outliers with inter-strip capacitances up to 1.3 pF, most sensors with glue showed values around 0.8 pF. The impact of irradiation on sensors with glue depended on the sensor type: sensors where the formation of a type inverted layer was compensated by either high resistivity material or a p-spray layer showed inter-strip capacitances of blank sensors comparable to unirradiated sensors. Sensors with glue showed higher inter-strip capacitances than blank sensors (up to 1.2 pF) after irradiation with 23 MeV protons. FZ2 sensors without p-spray, where a type-inverted layer led to an increased inter-strip capacitance, benefited from the presence of glue: sensors with glue showed an inter-strip capacitance up to 25 % lower than blank sensors. Temperature cycling of irradiated sensors led to a similar effect. Glue was thus found to increase the inter-strip capacitance of sensors by $\mathcal{O}(0.1\,\mathrm{pF})$ for sensors under realistic conditions and to decrease the inter-strip capacitance for sensors where the type inverted layer after irradiation had increased the inter-strip capacitance. A capacitance increase of about 0.1 pF for sensors with glue translates into an increased module noise $\mathcal{O}(10\,\mathrm{ENC})$ [2], which matches observations on module prototypes.

Gluing was found to reduce surface currents and showed a trend to improved surface resistances. While all subsequent treatments led to reduced surface resistances and increased surface currents

(most notably after irradiation), blank sensors showed similar changes as sensors with glue. Lowered surface resistances were thus dominated by sensor effects rather than glue. While surface resistances are not a standard parameter to evaluate the performance of silicon sensors, these measurements showed that glue did not become conductive during irradiation, or corrode the sensor surface directly or during temperature cycling and irradiation.

Probe station measurements thus found that gluing with the glues under investigation can lead to a significantly impaired sensor performance in the short term (early breakdowns), but causes only minor noise increases from higher leakage currents and inter-strip capacitances in the long term. Except for a dependence on the glue consistency, which affects how well the glue area can be controlled and thus the sensor performance, different glues showed similar results.

6 Sensor Studies in a Beta-Source Setup

The most important characteristic of a sensor used in particle tracking is its capability to collect charges generated by traversing particles (see section 6.1). The number of accumulated charges determines the signal registered in a sensor channel and is a defining variable of the overall signal-to-noise-ratio of a detector.

The fraction of actually collected charge with respect to the expected charge generated by a traversing particle is called charge collection efficiency (CCE). Assuming a sensor without defects, it can be predicted from theoretical considerations. It is reduced if the sensor accumulates defects, e.g. from radiation damage, and is thus a good indicator of the overall performance of a sensor. Hence, for all miniature sensors under investigation, the charge collection efficiency was measured to determine the impact of gluing on the sensor performance.

A beta source setup, where β-particles emitted by a β-source traverse a sensor, was used to generate charges in silicon sensors and measure their charge collection efficiencies.

6.1 Signal Generation of Charged Particles in Silicon Strip Sensors

Charged particles traversing matter lose energy due to interactions with atoms. By using tracking detector materials such as silicon strip sensors, designed to be able to read out the deposited energy from different segments, particle detectors are able to reconstruct tracks from the energy depositions along a particle's path.

6.1.1 Energy Deposition in Silicon Sensors

Depending on the kinetic energy of a particle, the dominating mechanism for energy loss in matter is either:

- energy transferred to atomic nuclei at low energies
- ionisation, i.e. an interaction with atoms' electrons
- radiation losses, i.e. the emission of photons at high energies

The average energy loss per path length, called stopping power, $\langle \frac{\mathrm{d}E}{\mathrm{d}x} \rangle$ of a particle can be calculated using the Bethe-Bloch-formula [110]:

$$-\left\langle \frac{\mathrm{d}E}{\mathrm{d}x} \right\rangle = K \cdot \frac{Z}{A} \cdot \rho \cdot \frac{z^2}{\beta^2} \left[\frac{1}{2} \cdot \ln \frac{2m_e c^2 \beta^2 \gamma^2 \cdot T_{\max}}{I^2} - \beta^2 - \frac{\delta}{2} - \frac{C(\beta\gamma, I)}{Z} \right], \tag{6.1}$$

where $\beta = \frac{\mathrm{v}}{c}$, with the particle velocity v and the speed of light c, and $\gamma = \frac{1}{\sqrt{1-\beta^2}}$, $K = 4\pi N_A r_e^2 m_e^2 c^2 \approx 0.307\,\mathrm{MeV} \cdot \mathrm{cm}^2/\mathrm{mol}$ with N_A the Avogadro-constant and $r_e = e^2/4\pi\epsilon_0 m_e c^2 \approx$

2.8 fm, corresponding to the classical electron radius. z and $\beta = \frac{v}{c}$ are charge and velocity of the incoming particle, Z and A are the atomic number and mass number of the traversed medium, I is the average energy required for the ionisation of an atom of the traversed medium, $T_{\max}$ is the maximum energy transferred to a shell electron in an interaction, δ and C/Z are phenomenological correction terms for high energies and low velocities, respectively.

Ionising interactions transfer enough energy to the shell electrons of an atom to move them from the valence band to the conduction band of a semiconductor material, so that the electrons can be collected and read out. The stopping power $\frac{dE}{dx}$ has a minimum (e.g. at $\beta \cdot \gamma \approx 3$ for muons), where a particle is minimally ionising (called a MIP). Estimates of the number of electrons produced in a detector volume use the stopping power of a MIP as a worst case estimate in order to ensure a sufficient signal-to-noise ratio for the full particle energy range under investigation.

The stopping power of a MIP in silicon is $3.9\,\mathrm{MeV{\cdot}cm^2/g}$ [38]. Using the density of silicon $\rho_{silicon} = 2.33\,\mathrm{g/cm^3}$, this can be converted to an energy deposition of $390\,\mathrm{eV/\mu m}$. The ionisation of a silicon atom, i.e. the creation of an electron-hole-pair, requires an energy of 3.6 eV, so that a MIP produces an average of 108 electron-hole-pairs per µm. The number of electron-hole-pairs actually produced by a traversing particle varies due to two major effects [111]:

- The overall energy deposition consists of a series of interactions with shell electrons, where both the number of interactions N as well as the energy transfer in each interaction δE show statistical fluctuations. The overall energy transfer $E = \sum_{i=1}^{N} \delta E$ is therefore described by a Poisson distribution.

- Central collisions of traversing particles with shell electrons lead to large energy transfers and the production of high-energy electrons called δ-electrons. The energy distribution of δ-electrons is proportional to $1/T^2$, where T is the kinetic energy of the incoming particle.

The production of δ-electrons causes the energy deposition distribution to show a tail towards higher energies, described by a Landau-Gauss-function (see figure 6.1). A key feature of the Landau-Gauss-function is its asymmetry, which makes its most probable value in this case about 30 % smaller than its average. For the production of electron-hole-pairs in silicon, an average energy deposition of $390\,\mathrm{eV/\mu m}$ and thereby creation of an average of 108 electron-hole-pairs per µm corresponds to most probable values of 76 electron-hole pairs per µm or $275\,\mathrm{eV/\mu m}$. The ATLAS07 sensors used in this study have a thickness of 320 ± 15 µm; the most probable number of electron-hole-pairs created by a traversing particle is thus approximately $24,000 \pm 1000$. For a given signal-to-noise-ratio required for readout, the most probable value defines the maximum allowed noise level of a sensor.

The ability of a sensor to collect the electrons or holes produced by a traversing particle is described by the charge collection efficiency (CCE), i.e. the most probable number of collected electrons or holes divided by the theoretical most probable value of produced electron-hole pairs. Hence, the charge collection efficiency is a good indicator of the functionality of a sensor and possible damages caused by external influences.

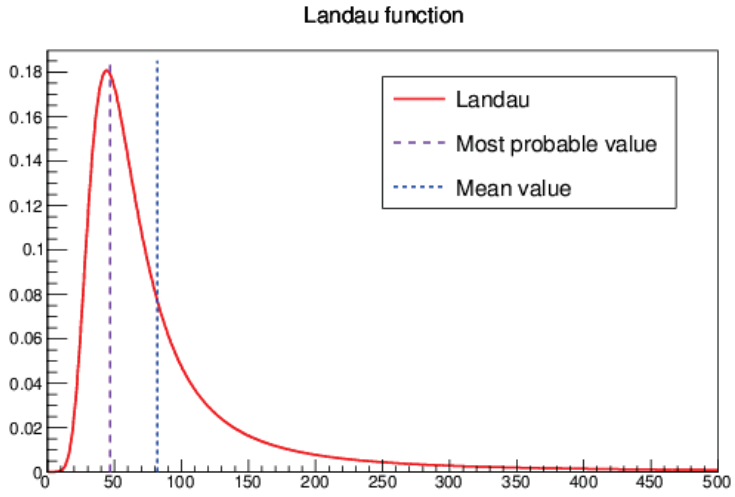

Figure 6.1: Example of a Landau function with mean and most probable value: the most probable value (47) is much smaller than the average (82.3).

6.1.2 Signal Collection in Silicon Strip Sensors

After electron-hole-pairs have been created by an ionising particle traversing a silicon sensor, they start to travel within the silicon according to the electric field produced by the applied bias voltage. ATLAS07 sensors were designed to collect electrons, because the higher mobility of electrons compared to the mobility of holes ($\mu_{\text{electrons}} = 1350\,\text{cm}^2/(\text{V}\cdot\text{s})$ compared to $\mu_{\text{holes}} = 450\,\text{cm}^2/(\text{V}\cdot\text{s})$ [38]) allows for a faster readout. By applying a negative voltage to the sensor backside and grounding the sensor surface, an electric field is built along which electrons travel to the n-type strip implants where they are read out.

The movement speed can be calculated from:

$$v_{\text{electrons}} = \mu_{\text{electrons}} \cdot E, \tag{6.2}$$

where $v_{\text{electrons}}$ and $\mu_{\text{electrons}}$ are the electrons speed and mobility and E is the electric field strength inside the sensor. For the sensors used in this study, the depletion voltage was found to be about -150 V, corresponding to a field strength of about 4.7 kV/cm for a sensor thickness of 320 µm. The electron velocity can thus be estimated to be about $6.3 \cdot 10^6$ cm/s, which, in a sensor thickness of 320 µm, corresponds to a drift time of about 5 ns.

Created charges are only collected from the depleted sensor volume, where they follow the electric field lines. For voltages below full depletion, the fully depleted sensor volume is smaller than the sensor thickness, leading to a smaller number of particles being collected. With increasing bias voltage, there is a linear increase of the depleted sensor volume and a corresponding increase of the collected charge and thus of the charge collection efficiency.

Defects in the sensor, e.g. disturbances in the electric field or bulk damages caused by irradiations (see section 3.3), reduce the ability of a sensor to collect charges efficiently, e.g. by traps which bind the created electrons and reduce the collected charge. The charge collection

efficiency hence directly measures the performance of a sensor at a given bias voltage and allows to assess the impact of different sensor treatments on its tracking behaviour.

6.2 Beta-Source Setup

A β-source setup allows to measure the charge collection efficiency of a sensor by reading out the charge deposited from β-particles traversing a sensor, which is operated under realistic detector conditions, i.e. depleted and cooled.

Figure 6.2 shows the schematic structure of the β-source setup used for measurements. A

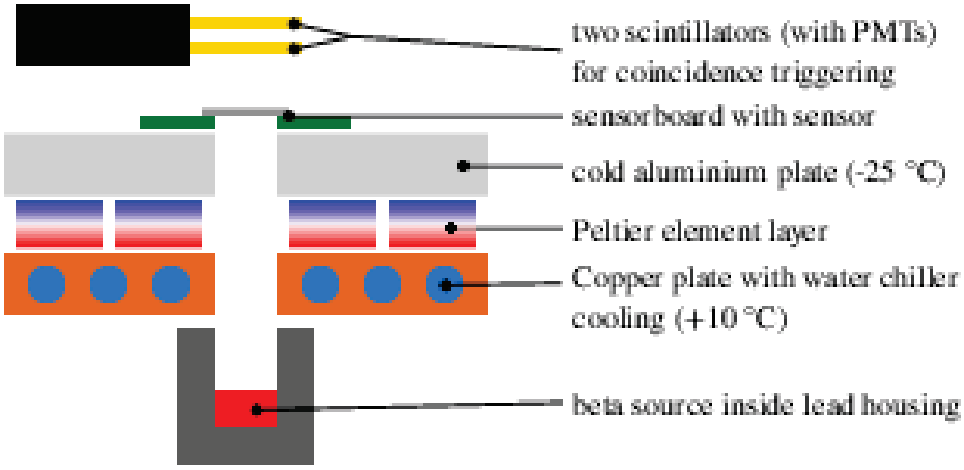

Figure 6.2: Schematic of the β-source setup used for charge collection efficiency measurements: the sensor under investigation is positioned between β-source and scintillators, connected to photo multipliers, used for triggering. Openings in all layers of the cooling setup ensure an unobstructed path of the β-particles to the sensor.

Sr^{90} β-source was used for these measurements, which emitted β-particles with energies of up to 2.3 MeV [112] and an activity of 185 ± 28 MBq. The source was secured inside a lead housing, whose opening also served as a collimator for the emitted particles. The source was placed below the sensor under investigation and two photo multipliers located on top of the sensor, which were used in coincidence to trigger data taking (see section 6.4).

The setup shown in figure 6.2 was located inside a box to shield sensors under investigation from light during measurements. Air-tight closures between box and lid allowed measurements at low temperatures, which required dry environments.

A cooling setup allowed to test sensors at realistic temperatures and to cool irradiated sensors down to operating temperatures of -20 °C. A three layer setup was used to reach the intended cooling temperatures:

- top layer: an aluminium plate heat spreader cooled down to -25 °C
- middle layer: 20 peltier elements [113] cooling the aluminium top layer, thermally connected to both top and bottom layer by thermal paste

- bottom layer: a copper plate kept at 10 °C by water from a chiller flowing through cooling lines to cool down the warm side of the peltier elements

Openings in the top and bottom layer were aligned with gaps between peltier elements, so that β-particles had a free path between emitting source and sensor, if both were aligned with the openings.

For sensor tests at low temperatures, the setup was flushed with either dry air or nitrogen to prevent condensation on the sensor surface.

A full description of the β-source setup can be found in [114].

6.3 Sensor Test Setup

In order to measure the charge collection efficiency of a sensor, each sensor strip was connected to a channel of an analogue readout chip on an ALiBaVa board [115]. Since these connections had to be made via wire bonds, which are sensitive to movements and vibrations, the sensor under investigation had to be mounted in a fixed position with respect to the readout board for both the wire bonding process and subsequent tests. An aluminium plate was designed to provide both optimal positioning of sensor and daughterboard for wire bonding and provide mechanical support during tests and transport.

Several sensors needed to be operated at -20 °C in order to compensate for their high leakage current after irradiation. The aluminium support was thus designed to have a large thermal contact area with the sensor to be cooled, while the readout board was mounted thermally insulated using plastic washers and screws. An example of an aluminium plate holding both sensorboard and readout board is shown in figure 6.3.

While data was read out using a standard ALiBaVa daughterboard and motherboard, a modified version of the sensorboard was used. The modified version accommodated specific requirements to measurements in both β-source and testbeam setups (see figure 6.4 for a comparison between the standard ALiBaVa sensorboard and the modified version used here):

- the openings in the board for particles being able to traverse the sensor without obstruction were widened to match the active area of ATLAS07 miniature sensors ($8 \times 8\,\mathrm{mm}^2$)
- sensor positions on the board were moved as close as possible towards the daughterboard to allow for direct wire bonding, eliminating the need for pitch adapters
- grounding pads, which were required to ground the top side of the sensor, were moved as close as safely possible to the sensor pads and increased in size to allow for easy wire bonding
- high voltage connectors were added to the board so that high voltage could be applied directly to the sensorboard instead of using the daughterboard
- high voltage safety protection was added to the sensorboards in order to allow bias voltages up to 1 kV

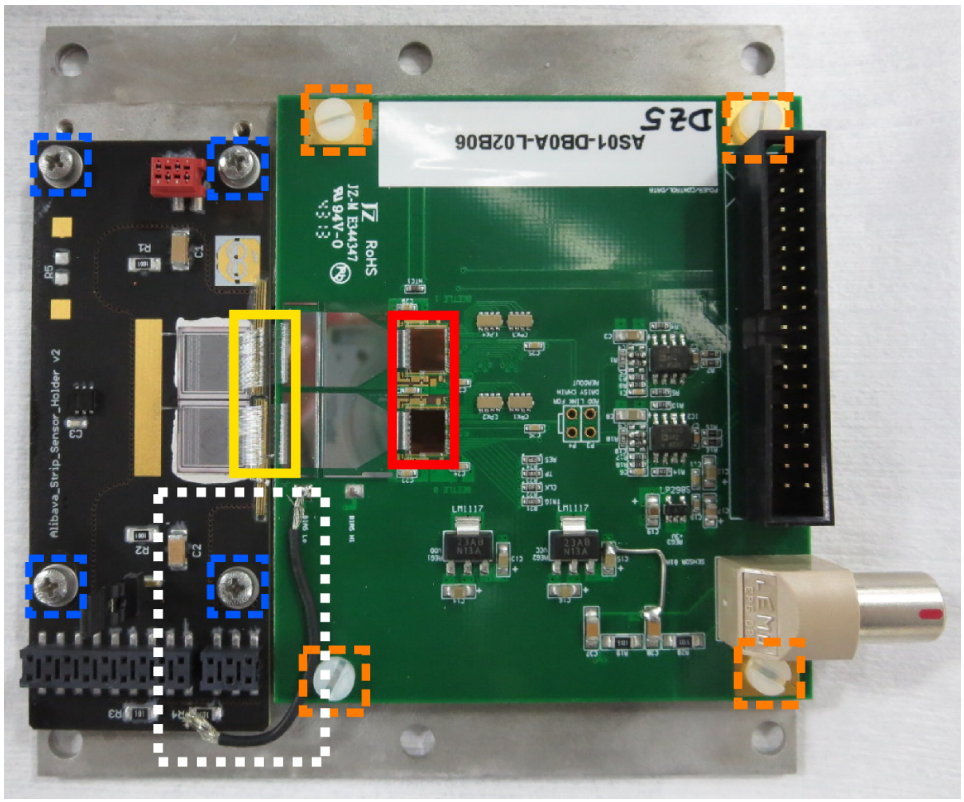

Figure 6.3: Aluminium plate with ALiBaVa daughterboard and sensorboard: in order to cool the sensors on the sensorboard (left side) to -20 °C, the sensorboard is thermally connected to the cooling plate below (metal screws are indicated by dashed blue lines). The ALiBaVa daughterboard (right side) is thermally insulated from the cooling plate by plastic screws and washers (dashed orange lines). The analogue readout chips (solid red lines) are connected to the sensors to be tested by wire bonds (solid yellow lines). A ground connection (dotted white line) between daughterboard and detector board has to be soldered to the respective pads.

- splitting the high voltage pads between the two sensor pads allowed to bias sensors individually - a jumper was added for the possibility to connect both pads if needed
- a temperature and humidity sensor was added to the board to monitor environmental conditions during testing

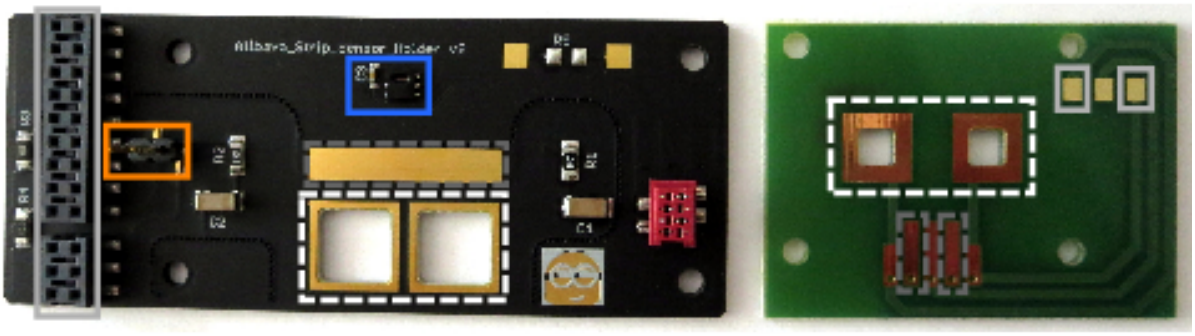

Figure 6.4: Modified ALiBaVa sensorboard and standard version in comparison: Sensor pads (dashed white boxes) were enlarged and moved closer together, ground pads (dashed grey boxes) were enlarged and repositioned closer to the sensor pads. High voltage connections (solid grey boxes) were changed from solder pads to plugs and both sensors could be biased together or separately using a jumper (orange box). A temperature and humidity sensor (blue box) was used to monitor environmental conditions on the board.

Each sensor was prepared for testing by using electrically conductive paint [116] to attach it permanently to the sensor pad of a sensorboard. Each sensorboard was cleaned in an ultrasonic bath using electrical grade cleaner [117] prior to being glued beneath a sensor. The sensorboard was then mounted on an aluminium cooling plate, using heat transfer paste to ensure a good thermal contact. Afterwards, the ground connection was soldered and wire bond connections between sensor and readout board were made.

6.4 Data Taking with an ALiBaVa System

The ALiBaVa system used for all charge collection studies here consists of two major components:

- daughterboard
  The daughterboard is a circuit board holding two readout chips called Beetle chips, an analogue readout chip used in the LHCb experiment at CERN [118]. Each Beetle chip has 128 readout channels, which are connected to the strips of a silicon sensor under investigation via wire bonds. Beetle chips work with a frequency of 40 MHz, allowing tests under conditions similar to those at LHC.
- motherboard
  A twisted pair cable is used to connect the daughterboard to a motherboard, which

converts the analogue signals read out by the Beetle chips into digital signals. Trigger inputs can be connected to LEMO sockets on the motherboard, which has an internal logic to trigger data taking.

The motherboard is connected to a computer via a USB cable, which allows data readout as well as real-time data monitoring using the ALiBaVa GUI.

6.4.1 Latency

Signal pulses from the beetle chips are read out using a time window smaller than the length of the pulse [119]. In order to get an accurate measurement of the deposited charge, the readout time window needs to be chosen such that it contains the maximum of the signal pulse. The ALiBaVa system allows to change the latency in steps of 25 ns while monitoring the average deposited charge per time bin (see figure 6.5a). This setting allows a coarse selection of a latency setting which moves the pulse maximum into the readout window. If the maximum is located at the edge of a readout window, the latency can be adjusted in smaller steps using a delay unit between trigger and ALiBaVa motherboard (see figure 6.5b), which moves the pulse maximum to the centre of the readout window (see figure 6.5c). Since the same setup and cabling was used for all sensor tests, the latency settings were not changed between measurements once an optimal setting had been determined.

6.4.2 Triggering

Data taking was triggered by two Bicron BC-408 scintillators [120], suitable for the detection of β-particles. Light from each scintillator was converted to a trigger signal by a R5900-03-M4 photo multiplier, operated at a voltage of -780 V [121]. Data taking was triggered if both photo multipliers registered a signal in coincidence.

The choice of latency and trigger settings was tested by collecting data for a sensor and monitoring data rate and hit map, i.e. the number of hits collected in each readout channel (see figure 6.6). A threshold was selected by starting from low photo multiplier operating thresholds, which corresponded to a high data taking rate, but a large fraction of fake hits caused by noise. The operating threshold was then increased until the efficiency reached a plateau.

Trigger thresholds for data taking were chosen to be -25 mV.

6.4.3 Calibration with Internal Calibration Function

The ALiBaVa system converts the analogue signal to ADC (**A**nalogue to **D**igital **C**onverter) counts, which vary between beetle chips. In order to compare results from sensors tested using different ALiBaVa daughterboards, ADC counts need to be translated back into deposited charge. The conversion factor between read out ADC counts and electrons (the gain) is determined using the internal ALiBaVa calibration function.

The calibration is performed using the internal calibration function of the system, which uses capacitors in the beetle chip to inject a defined charge into each readout channel, which is then read out. By increasing the injected charge in defined steps and relating the measured signals

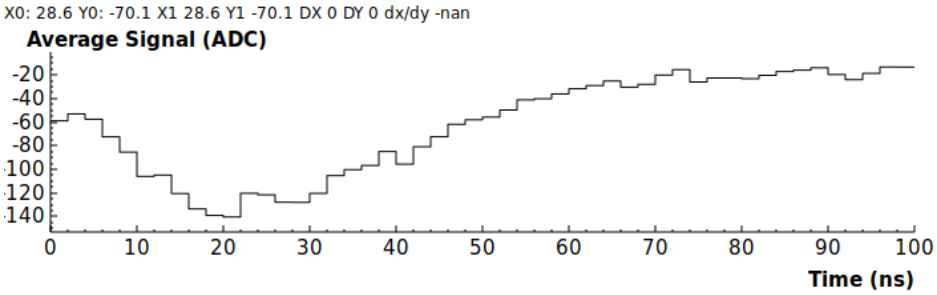

(a) Average signal read out per time bin showing the shape of the readout pulse: the extremum is located between 20 and 30 ns, i.e. in the readout time window, but situated at its edge.

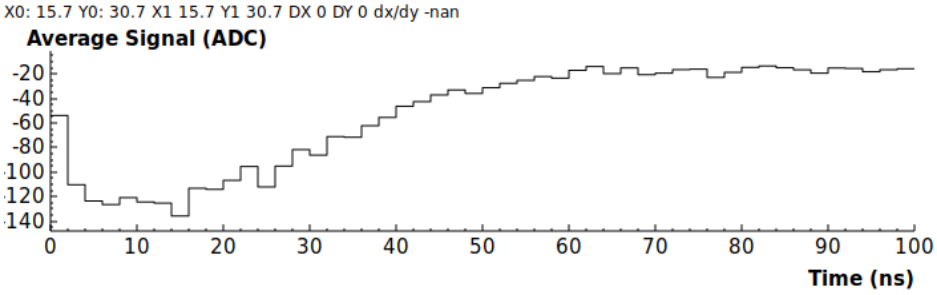

(b) Using a delay unit inserted between trigger and motherboard, the pulse extremum has been moved towards earlier time bins.

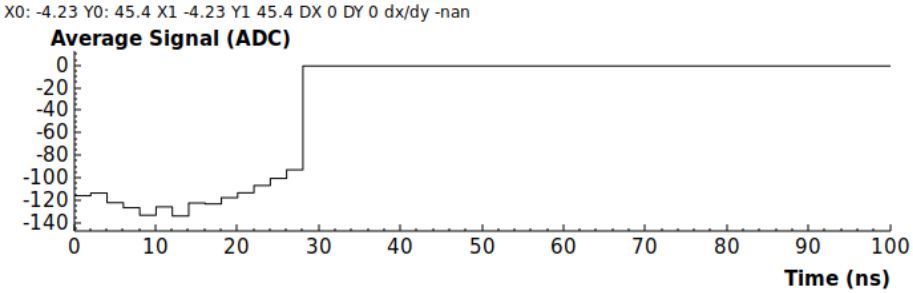

(c) Pulse shape as measured within the readout time window: the extremum of the signal pulse has been moved to the centre of the readout window, maximising the read out signal.

Figure 6.5: Choosing a latency setting for data readout with an ALiBaVa system using the time-resolved readout signal, averaged over 100,000 events: with the pulse shape being longer than the readout time window, the latency is chosen so that the maximum signal is contained in the ALiBaVa readout time window.

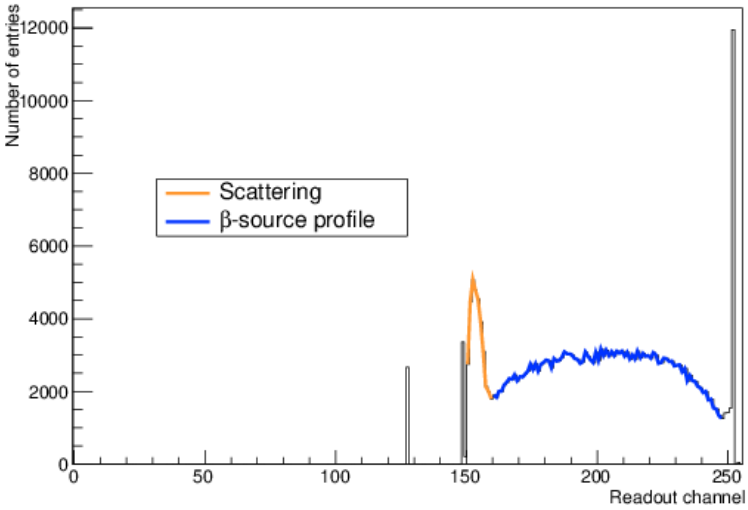

Figure 6.6: Hit map for a sensor in a β-source setup containing 300,000 hits: only one sensor was biased, hence hits were only collected by one beetle chip (channels > 128). Due to the circular opening in the cooling setup ($\varnothing = 8\,\mathrm{mm}$), strips in the sensor centre collected more hits than strips at the edges, leading to a curved shape of the hit map (blue line). Scattering at the edges of the openings led to an increased number of hits where the sensor was placed on top of the metal edges of the cooling setup (orange lines).

with the known charge, the gain can be determined from the linear increase of the measured signal as a function of injected charge.

The gain, i.e. the number of electrons corresponding to one ADC count, depends on the temperature of the beetle chip, which is affected by the temperatures of the aluminium support plate, the sensor and the cooling contacts between sensorboard, daughterboard and support plate. The beetle chip temperature during operation can thus not be predicted, but needs to be measured. Obtaining the gain of a beetle chip for an individual measurement thus requires a calibration prior to that measurement. Hence, each beetle chip was calibrated at multiple temperatures, so that the gain at any given temperature could be extrapolated from the measured data points (see figure 6.7).

While all channels on a beetle chip should have a similar gain at a given temperature, the analysis was set up to investigate sensor strips individually, which required knowledge about the gain of each channel. Hence, the calibration was set up to determine and extrapolate gain as a function of beetle chip temperature individually for each readout channel. Figure 6.7 shows an example of a calibration file. The gains calculated for each channel at different temperatures

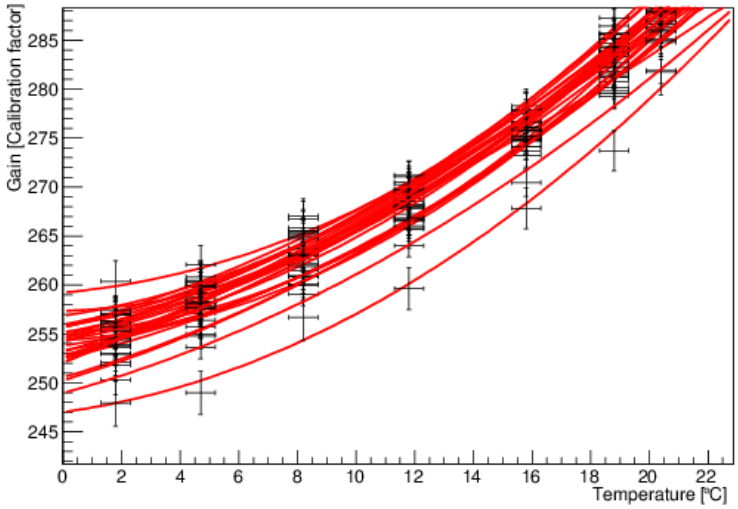

Figure 6.7: Example of a temperature-dependent calibration for all readout channels of one beetle chip: the ALiBaVa calibration function was performed at different sensor temperatures, translating into different beetle chip temperatures. For each channel, a cubic fit function was applied, so that gains could be determined at any given beetle chip temperature. Gains were found to be similar (within 3 %) for all channels on one beetle chip.

allowed to perform a cubic fit.

Applying the obtained gains to cluster charges measured for a fully depleted sensor showed that the determined gains were too high (see figure 6.8: while charges collected for a fully depleted sensor with a thickness of 320 µm are expected to have a most probable value of

about 24,300 electrons, an MPV of about 44,000 was found using the calculated gains. After

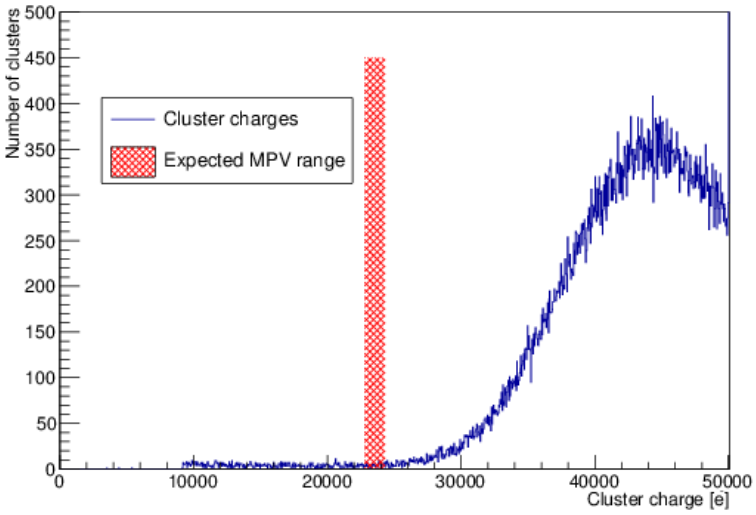

Figure 6.8: Measured cluster charge distribution for a fully depleted, unirradiated ATLAS07 sensor. The maximum of the reconstructed charge distribution was found to be much higher than the most probable value expected for a silicon sensor with a thickness of 320 µm.

investigating possible causes for the excess charge, it was found that the ALiBaVa firmware version used for measurements did not read out injected calibration charges correctly. Similar to a wrong latency setting (see section 6.4.1), a wrong ALiBaVa timing setting had led to an incomplete charge readout. A known injected charge was thus read out as a smaller value, leading to a higher gain.

For consistency of calibration and measurements, calibrations were not repeated with a different firmware version, but an alternative method was used for calibration (see below).

6.4.4 Calibration with Reference Sensors

An alternative method for the calibration of daughterboards relies on the consistency of charge collection in ATLAS07 sensors. By measuring the most probably cluster charge value for a fully depleted ATLAS07 sensor, the ADC counts corresponding to the number of electrons from 320 µm of silicon can be calculated. The charge was determined using the same procedure as for later measurements (see below).

The sensor temperature and, as a consequence, the beetle chip temperature were varied (see figure 6.9) and the gain was measured as a function of the beetle chip temperature. Gains were determined per beetle chip rather than per readout channel.

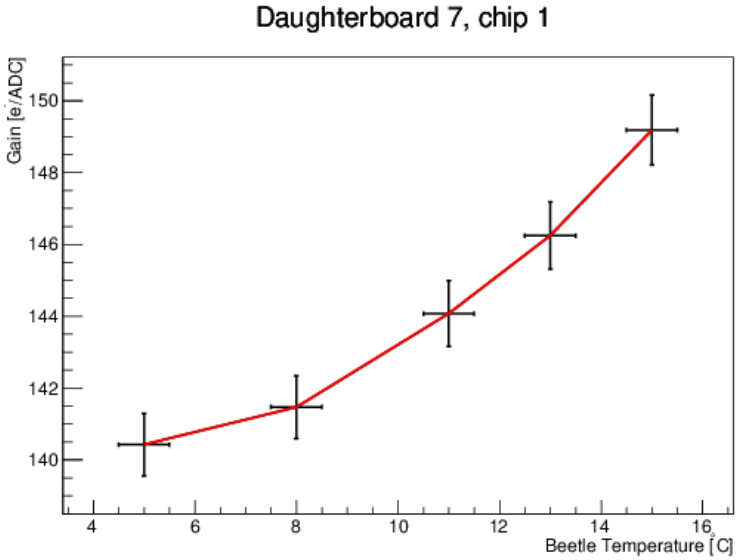

Figure 6.9: Gain of an ALiBaVa beetle chip using measured MPV for a fully depleted ATLAS07 sensor at different temperatures.

6.4.5 Pedestals

The ALiBaVa system reads out ADC counts with 10 bits, i.e. in a range from 0 to 1023. The beetle chip can be used with both n-in-p type sensors and p-in-n type sensors and thus needs to be able to read out both negative and positive charges. Hence, the base value of each readout channel is set to about 512 ADC (corresponding to no input charge). An input charge in a readout channel is added to the channel's base value: negative charges reduce the read out channel value with respect to its baseline value, positive charges increase the value.

An input charge is thus calculated with respect to the base value of each readout channel. Hence, the base value for each channel needs to be determined as accurately as possible.

For beetle chips on an ALiBaVa board, the base value is calculated from pedestal runs: without applying an input signal, all channels are read out repeatedly with an internally generated trigger at a frequency of about 700 Hz. By reading out the ADC count without charge repeatedly, the pedestal measurement allows to determine both the base value and the noise of each channel by performing a Gaussian fit of the obtained distribution (see figure 6.10).

Figure 6.11 shows base values and noise for an example pedestal measurement. The noise distribution showed that a beetle chip wire-bonded to a sensor shows a higher average noise than an unbonded beetle chip, which is expected, since the additional capacitance of sensor strips leads to increased noise (see section 5.3.3). Readout channels of a beetle chip partially connected to a sensor showed a higher noise in unbonded channels than in bonded channels due to a modification of grounding (see figure 6.4). While the grounding scheme ensured that the potential of a sensor bias ring did not fluctuate with respect to the reference of readout channels, unbonded channels did not compensate fluctuations of the bias ring potential, which were thus registered as noise. Since unbonded channels were not used at any part of the analysis,

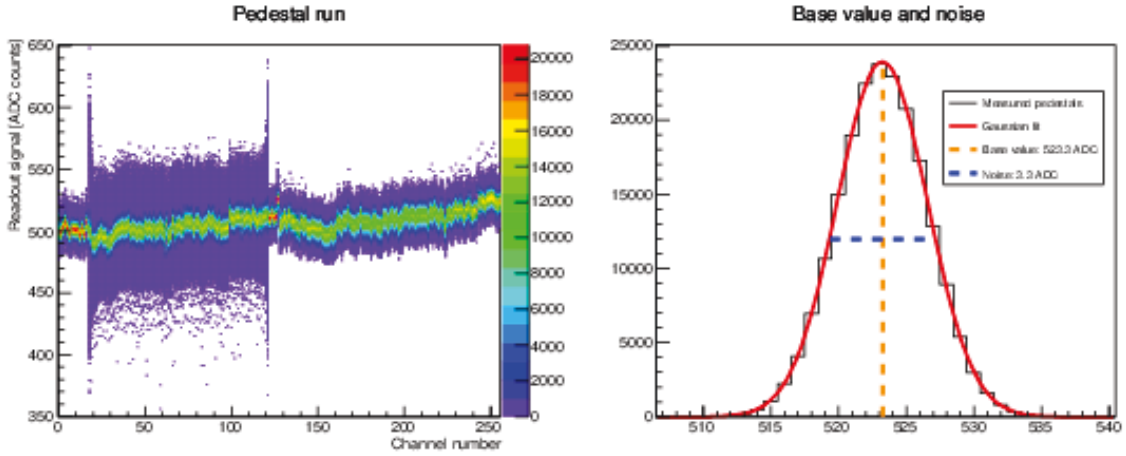

Figure 6.10: Pedestal scan with 200,000 events for all channels of two beetle chips and fitted results for an individual channel. The base value (mean of the Gaussian distribution) for all channels is around 500 ADC, but channels on a beetle chip connected to a sensor (0 to 127) show larger variations, i.e. noise, than channels on the unconnected beetle chip.

an increased noise in them did not have an impact on the measurement. Base values and noise were calculated for each pedestal scan were stored to be used for the data analysis of charge collection efficiency measurements (section 6.6). Since the noise depends on the environmental conditions of the sensor under investigation, pedestal scans had to be performed after each change of settings, e.g. applied bias voltage.

6.5 Testing Procedure

All scans were performed under measurement conditions as stable as possible in order to obtain comparable results for all sensors. The test procedure for all sensor tests is outlined below:

1. A sensor, mounted on a sensorboard and connected to a readout chip, was positioned above an opening in the cooling plates. High voltage connector, temperature readout and data readout cables were connected and tested. Afterwards, the β-source was positioned below the sensor and the scintillators were aligned with β-source and sensor. After all preparations requiring access to the sensor had been made, the lid was closed and sealed against light.

2. The setup was flushed with nitrogen (first measurements) or dry air (below 4 % humidity, later measurements), until the humidity was below 15 %, then the cooling process was started by powering the peltier elements. The voltage of each peltier element was increased up to 10 V (maximum: 12 V), while their warm side was cooled down by water at a temperature of 15 °C (first measurements) or 10 °C (later measurements). The humidity and dew point were monitored during cooling and cooling was stopped if the temperature

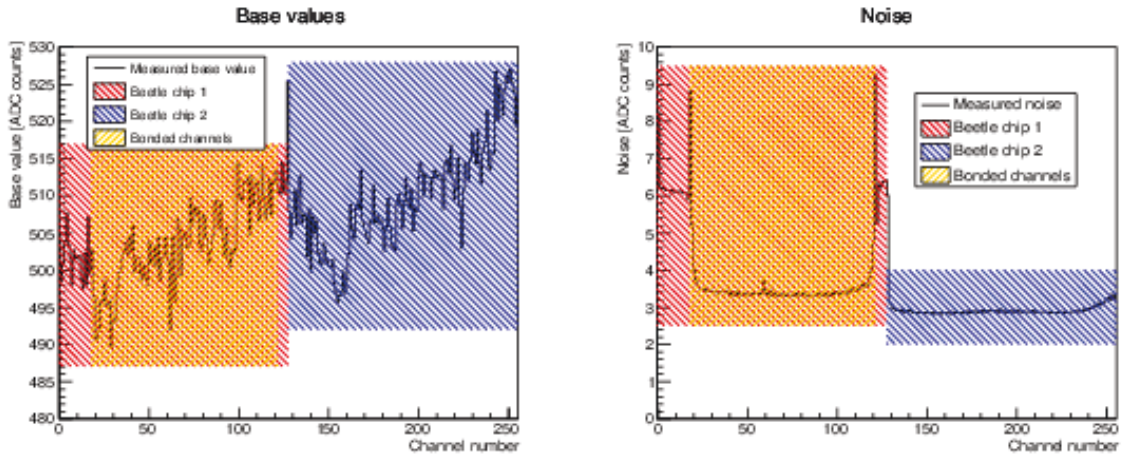

Figure 6.11: Base values and noise for all channels of two beetle chips, determined from pedestal scans, using 200,000 entries for each channel. Base values for channels on both beetle chips are similar (left), whereas a beetle chip connected to a sensor shows increased noise (right). Unbonded channels of a beetle chip partially connected to a sensor show a higher noise than bonded channels due to grounding.

was within 3 °C of the dew point, until the humidity had sufficiently decreased again. Measurements were started once the temperature had stabilised and the humidity was below 0.01 %.

3. High voltage was ramped up in steps of 10 V in order to find the maximum bias voltage a sensor could be tested at: up to -700 V for unirradiated sensors, up to -1000 V for irradiated sensors. For stable operation, the maximum leakage current was chosen to be 100 µA. If the leakage current exceeded 100 µA at the respective maximum bias voltage, the peltier voltage was increased in order to decrease the temperature. If the temperature did not decrease further, a maximum bias voltage with a leakage current below 100 µA was chosen.

4. Each sensor was tested at bias voltages in steps of 100 V from -100 V to -700 V (unirradiated sensors) or -200 V to -1000 V (irradiated sensors), where measurements at -300 V and -900 V were skipped due to time constraints. At each bias voltage, a pedestal scan with 200,000 events and a data scan with 500,000 events were taken.

The series of voltage changes, pedestal scans and data taking was automated using a python script which went through data taking for the full voltage range automatically. Since pedestal runs were started before each data run, pedestal runs had to be taken in the presence of the β-source. In order to verify the validity of that approach, results for pedestal runs with and without a β-source were compared (see figure 6.12). Pedestal scan results did not change when taken in the presence of a source, allowing fully automatised data taking.

After measurements had been performed for all voltages of interest, the temperature was

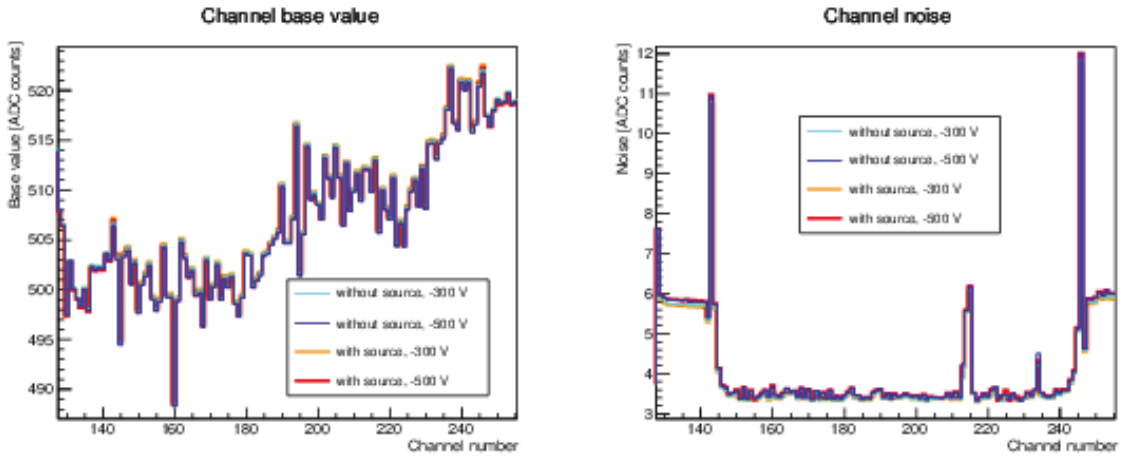

Figure 6.12: Base values and noise determined from pedestal scans at bias voltages of -300 V and -500 V with a β-source below the sensor and removed from it. Except for small changes in unbonded channels, the results were found to be independent of the presence of a source.

ramped back up until the β-source setup could be opened up without danger of condensation on the sensor. Between measurements, all sensors were stored in a freezer.

6.6 Data Analysis

Figure 6.13 shows a schematic overview of the steps performed for the analysis of ALiBaVa data from a β-source setup. Each analysis step is explained in detail below.

For each read out ALiBaVa event, the ADC counts registered by each readout channel were stored (raw data). In order to calculate the charge deposited by a traversing particle and ultimately the charge collection efficiency of a sensor, the C++ software framework ROOT [87] was used to perform the following analysis steps:

1. *Pedestal subtraction*
   For each event and readout channel, the registered signal was compared to the channel's base value and the difference was calculated. This subtraction levelled out channels with different base values, so that 0 fC input charge corresponded to 0 ADC counts for each channel (see figure 6.15).

2. *Common mode noise correction*
   Random fluctuations in the applied voltage lead to shifts in the channel base value, called common mode noise. These shifts lead to variations of the readout signal on top of the internal noise of each channel, effectively widening the distribution of read out ADC counts and thus making the calculated noise appear wider. Since voltage fluctuations affect all channels simultaneously, the resulting noise can be corrected for event by event. A systematic shift of the ADC count of all channels with respect to their average base

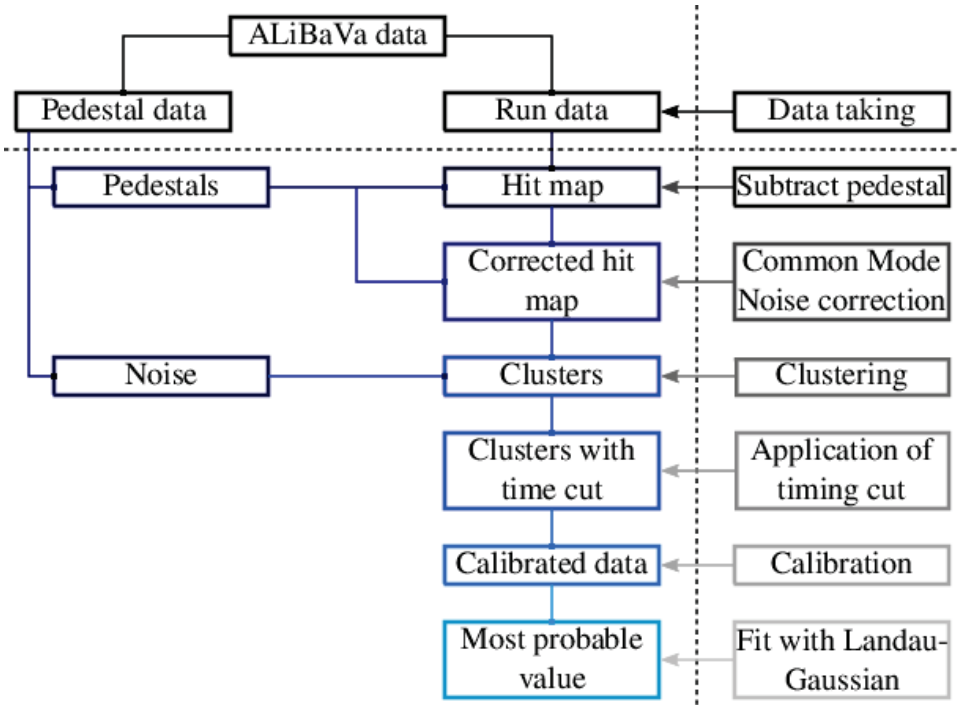

Figure 6.13: Schematic overview on an ALiBaVa data analysis routine: pedestal data and run data are stored separately and combined for data analysis. Up to the computation of the most probably value, each analysis step is performed on an event-by-event base.

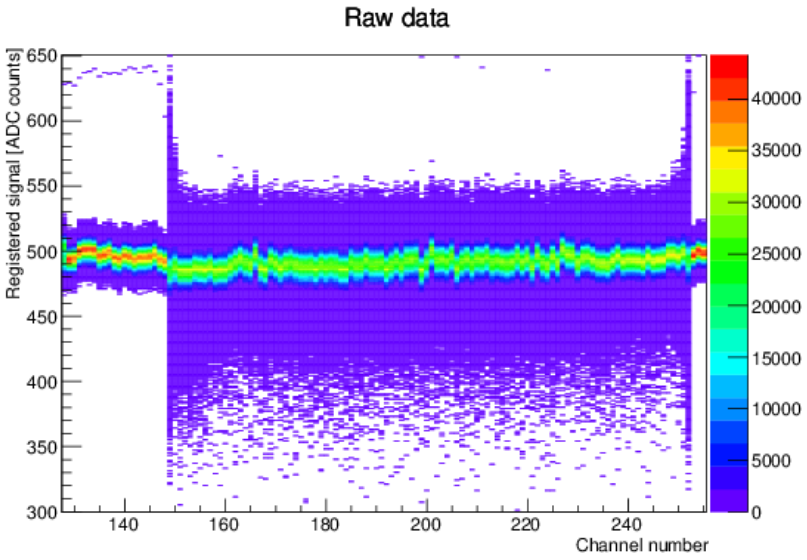

Figure 6.14: Raw data collected in 500,000 events for all readout channels of one beetle chip. During each event, the ADC count of each readout channel is read out, hence 500,000 entries are stored for each channel. Negative charges collected by the readout system are visible as entries extending further to lower ADC count values than to higher ADC count values.

value can be determined by calculating the average for the pedestal subtracted ADC counts of all channels for each event. The obtained offset per event is then corrected for in each channel, which reduces the width of the readout signal distribution (see figure 6.16).

3. *Clustering*
   After the signal corrections have been performed, each event was searched for clusters by comparing the corrected signal of each channel to its noise value σ:
   - a signal was considered a cluster seed if the signal exceeded the channel's noise by a factor of 5 (cluster seed cut, chosen in accordance with standard ALiBaVa analysis settings [119])
   - neighbouring channels were added to the cluster seed if their signal exceeded their noise by a factor of 3 (neighbour cluster cut)
   - the maximum number of channels allowed to be added to one cluster was limited to 5 (cluster cut)
   - the deposited charge of the cluster was calculated by adding up the signals of all channels associated with the cluster. Charges from all cluster seeds contained in one data run were then filled into a histogram (see figure 6.17).

4. *Calibration*
   In order to calculate the charge collection efficiency and compare results from different

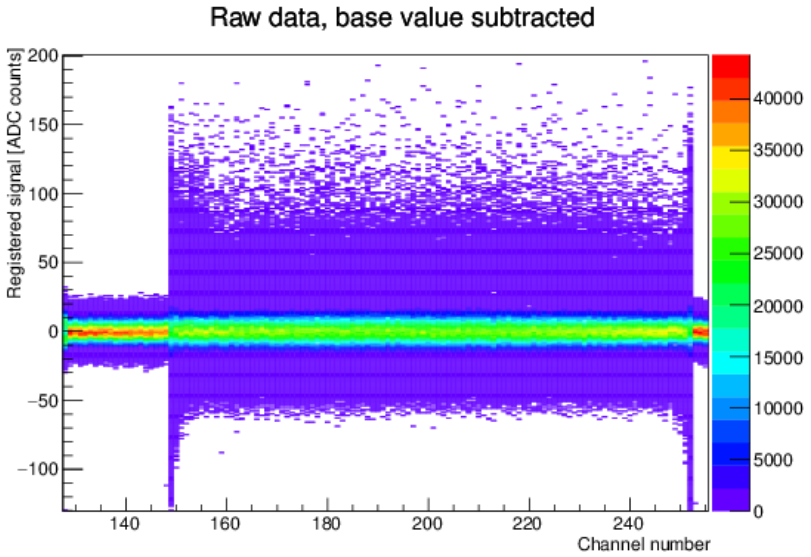

Figure 6.15: Raw data collected for a data run with 500,000 events, with base values of each readout channel subtracted from each registered ADC count. Wire-bonded channels can be seen to show an asymmetric distribution extending to high ADC counts, while unbonded channels show a broader, symmetric distribution. Maxima of all readout channels are centred around 0 ADC counts. Charges were multiplied with a factor of -1, so that reconstructed cluster charges were positive.

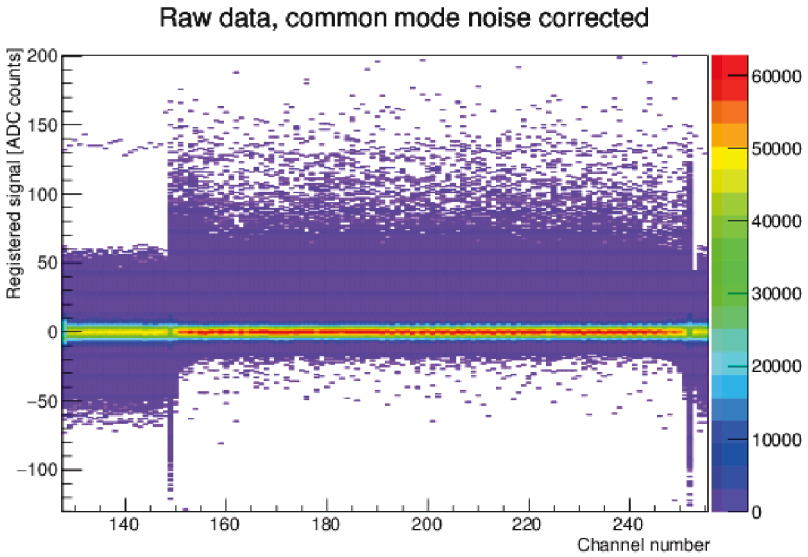

Figure 6.16: ALiBaVa raw data for 500,000 events after base value subtraction and common mode noise correction. The width of the background distribution, i.e. the distribution around readout signal = 0 ADC, has been decreased with respect to the signal before common mode noise correction.

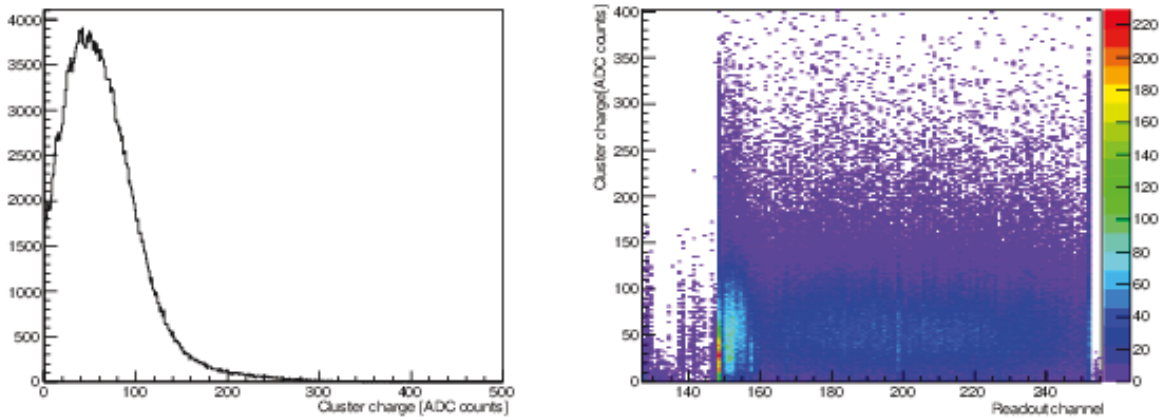

Figure 6.17: Cluster charges reconstructed from 500,000 events collected after clustering for a whole sensor (left) and individual sensor strips (right).

daughterboards, the cluster charge distributions calculated in ADC counts need to be converted to electron counts using the gain factors calculated from beetle chip calibrations (see section 6.4.3).

5. *Determining the most probable value*
   The most probable value of each cluster charge distribution is calculated by performing a Landau-Gauß-fit [122]. The uncertainty of the determined value is the uncertainty of the fit. Figure 6.18 shows an example of a Landau-Gauß-fit.

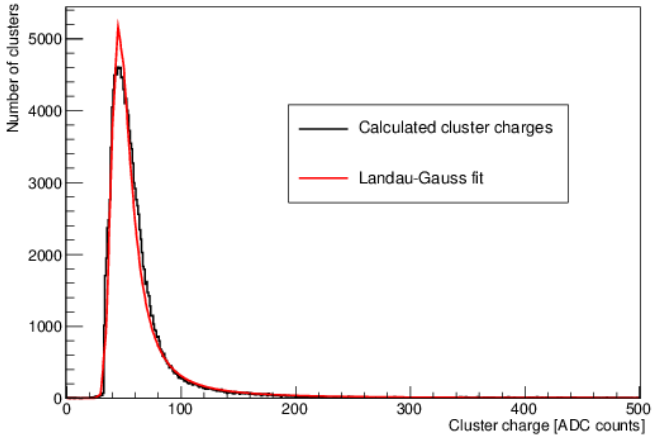

Figure 6.18: Example of a cluster charge distribution with a Landau-Gauß fit. The most probably value of the distribution corresponds to the collected charge (for the bias voltage applied during this scan).

6.6.1 Selection of a Time Cut

An additional cut is applied using timing information: signals from the ALiBaVa beetle chip have an approximately Gaussian shape with a fast increase and a slower decrease. In order to collect the actually deposited charge in a readout channel, the signal has to read out at a defined sampling point on the rising side of the pulse at 90 % of the signal maximum [118]. While small deviations from this optimal sampling point (see below) do not affect the reconstructed charge, large deviations lead to the calculation of a significantly reduced cluster charge.

In order to be able to judge the timing of an event, the time discrepancy between the input trigger and the 25 ns reference signal from the ALiBaVa motherboard is stored with the event information. The impact of the time discrepancy, called time to digital converter (TDC), can be illustrated by calculating the average input charge for all events with the same TDC (see figure 6.19). The reconstructed charge was found to depend significantly on the TDC bin, with a plateau of maximum charges over five time bins (7 ± 2 ns for the cabling and latency setting in use) and smaller charges for earlier and later time bins. The data analysis framework allowed to place requirements on the TDC associated with an event, requiring the selection of a reasonable

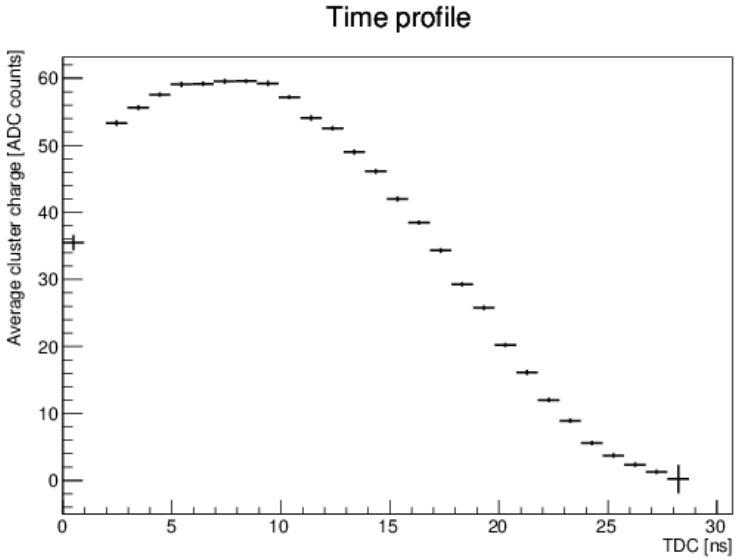

Figure 6.19: Time profile of 500,000 ALiBaVa events produced by averaging the input charge of all events with the same time discrepancy. The charge distribution shows a plateau over five time bins with lower reconstructed charges for both smaller and larger time discrepancies.

range of accepted TDC bins. Figure 6.20 shows a sensor's Landau-Gauß charge distributions obtained using different timing bin cuts. Comparing the Landau-Gauß created with different timing cuts shows several effects on the charge distribution:

- Distributions created using tight cuts around the charge collection plateau (time bins 5-10) show the same maximum of the distribution
- For larger ranges of timing cuts, the distribution's maximum shifts towards lower values due to the inclusion of lower charges
- Distributions containing large timing bin ranges develop a plateau at small collected charges, changing the shape of the distribution
- Tight cuts on the timing bin range reduce the number of events in the resulting distribution significantly

It should be noted that due to the random emission of β-particles from the source in use, raw data events are distributed randomly over all time bins. By restricting the range of a TDC cut to a subset of the available time range, the number of events available for analysis is reduced accordingly. The timing cut was thus selected to maximise both the calculated most probable value number of events available for data analysis (see figures 6.21a and 6.21b). Comparing the results of different timing bin cuts, a range of 2 to 13 was used for the analysis of all sensor measurements.

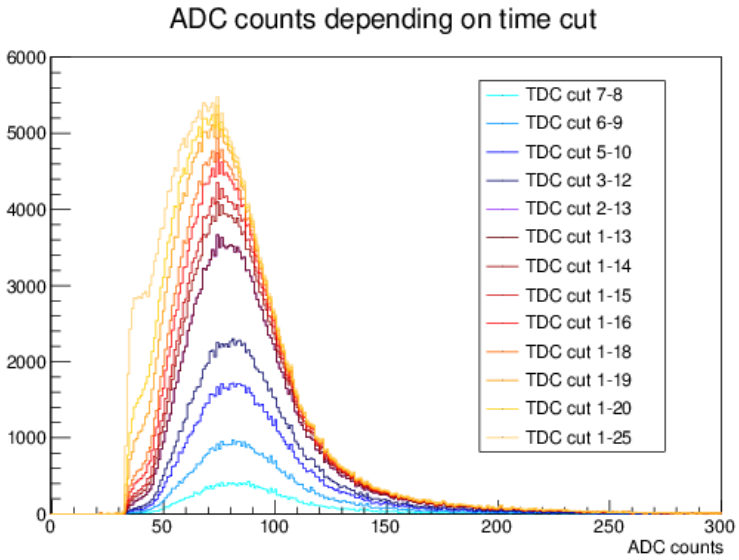

Figure 6.20: Landau-Gauß distributions for an irradiated sensor at a bias voltage of -600 V obtained using different cuts on the timing bin. Tight cuts around the time bins associated with the highest reconstructed charge (plateau at 5 to 10 time bins) show distributions with a higher most probable value than distributions with a looser time bin cut, but significantly reduced statistics.

Using these cuts and analysis steps, the most probable collected charge was calculated for both the whole sensor and each sensor strip individually for each applied bias voltage.

6.7 Results

The main criterion to compare different sensors was the charge collection efficiency. For each sensor under investigation, the most probable value was calculated for each applied bias voltage by performing a Landau-Gaussian fit (see section 6.6). The charge collection efficiency was calculated by dividing the MPV of the sensor under investigation by the known MPV for the used beetle chip and daughterboard. Since the gain of beetle chips is temperature dependent (see section 6.4.4), the beetle chip temperature during each measurement was determined by performing a fit of the measurement temperature (see figure 6.22). Three uncertainties had to be considered for the calculation of a charge collection efficiency:

- the uncertainty of the most probable value measured for a sensor under investigation, which was given by the width of the Landau-Gaussian fit function (about 0.5-1.0 %)
- the uncertainty of the calibration value, i.e. the most probable value measured for a reference sensor, which was also given by the width of the Landau-Gaussian distribution (about 1-2 %)

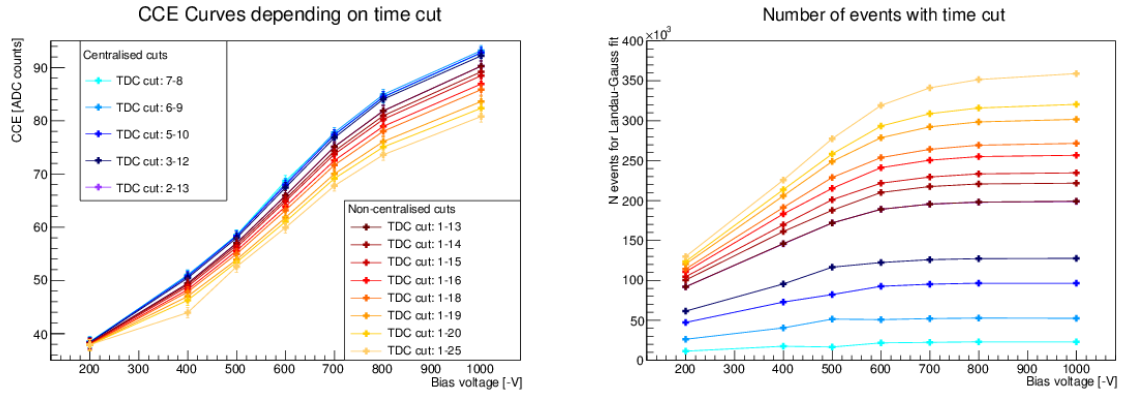

(a) Most probable value (MPV) of collected charge calculated using a Landau-Gauß fit. While for small bias voltages and cut ranges (up to 11 time bins), the resulting MPVs are comparable, larger cuts reduce the MPV.

(b) Number of events available for a Landau-Gauß fit depending on the time bin cut in use. Since events are distributed randomly over all time bins, reducing the allowed time bin range reduces the event number accordingly.

Figure 6.21: Most probable value of collected charge and number of events available for data analysis depending on the applied time bin range cut. While loosening the cut to above 11 timing bins leads to a reduction of the resulting MPV, each reduction of the allowed time range leads to a corresponding reduction of the available number of events.

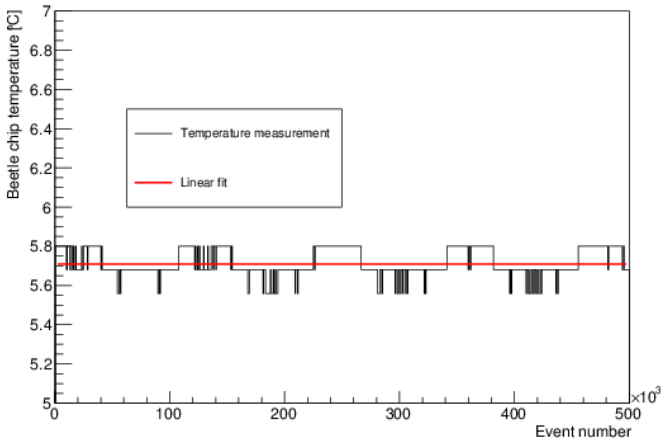

Figure 6.22: Beetle chip temperature read out during 500,000 ALiBaVa events. The measurement temperature is constant throughout the measurement and is well approximated by a linear fit.

- the uncertainty of the sensor thickness: since the number of produced electron-hole pairs is proportional to the sensor thickness (see section 6.1.1), the sensor thickness uncertainty translates directly into an uncertainty of collected charge. An uncertainty of 4 % (corresponding to the sensor thickness of $320 \pm 15\,\mu\text{m}$) was thus added to the measured MPV.

Contributions of all uncertainties were added quadratically and applied to each measured MPV.

An important requirement for the operation in the ATLAS detector is the signal-to-noise ratio (SNR) of a sensor. Since glue on sensor surfaces was found to affect sensor characteristics which are related to the sensor noise (see chapter 5), the SNR of a sensor could be reduced by a higher noise as well as by lower charge collection efficiency. For each sensor under investigation and bias voltage, the SNR was calculated using the MPV and the average noise, computed from the noise of all readout channels connected to a sensor strip. Since both noise and MPV were calculated in ADC counts, no calibration was required for the determination of the SNR. The uncertainty on the SNR was thus given by the width of the Landau-Gauss distribution of the charge and the standard deviation of the noise, added quadratically.

During the analysis of data taken in an electron beam using a sensor with glue, the presence of glue was found to lead to an increased average cluster size (see section 7.3). After this indication that glue had an impact on the cluster size, data taken in a β-source setup was used for an investigation of the cluster size as well. Cluster sizes were compared using the fraction of clusters with only 1 strip $N_{\text{cl,1s}}$ among all reconstructed clusters N_{cl}. Since each measurement had a number of cluster $\gg 1000$, the uncertainty of the fraction was calculated using $\sqrt{N_{\text{cl,1s}}}/N_{\text{cl}}$.

For each group of sensors under investigation, the MPV, SNR and fraction of 1-strip clusters were used to compare the performances of individual sensors.

6.7.1 Results for Blank Sensors

In order to study the behaviour of sensors after glue had been applied to their surface, two sensors were tested as reference samples. Due to the limited availability of sensors with sufficiently similar characteristics, several sensors with a BZ6 architecture (i.e. a strip pitch of 100 µm instead of 74.5 µm) had to be used for gluing tests. Initial measurements were thus performed for sensors with the nominal ATLAS strip pitch (74.5 µm) in comparison with BZ6 miniature sensors (strip pitch 100 µm). CCE and SNR in dependence of the applied bias voltage are shown in figures 6.23a and 6.23b. As expected for blank sensors without defects, both sensors show CCEs consistent with 100 % within uncertainties once the bias voltage reached the depletion voltage (200 V).

Both sensors showed similar fractions (about 94 %) of clusters with 1 strip (see figure 6.24). On ATLAS07 sensors, clusters with more than 1 strip can be assumed to be caused by particles passing through the transition region between adjacent strips. The produced charge is shared between both strips and is thus read out as a cluster with more than one strip. A small fraction of clusters with more than one responding strip thus matches the effect of charge sharing in transition regions between neighbouring strips.

Blank sensors were thus found to behave as expected.

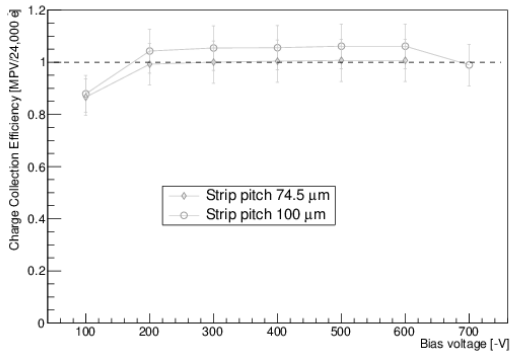

(a) Charge collection efficiency (CCE) of two blank ATLAS07 miniature sensors: both sensors have a CCE agreeing with 100 % within uncertainties.

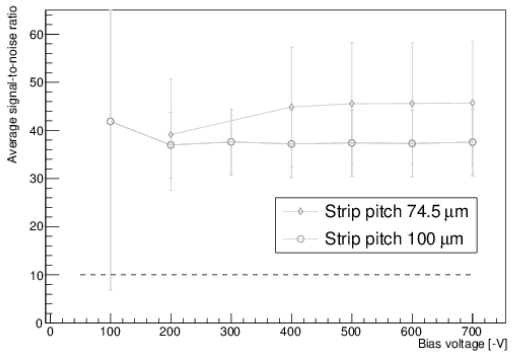

(b) Signal-to-noise ratios of two blank ATLAS07 miniature sensors: due to a higher noise, the BZ6 sensor has a lower SNR despite showing a larger CCE.

Figure 6.23: Charge Collection efficiency and signal-to-noise ratio of two blank ATLAS07 sensors: within uncertainties, both sensors have a CCE of 100 %. Both sensors show an SNR exceeding the required minimum for the ITk strip tracker of 10.

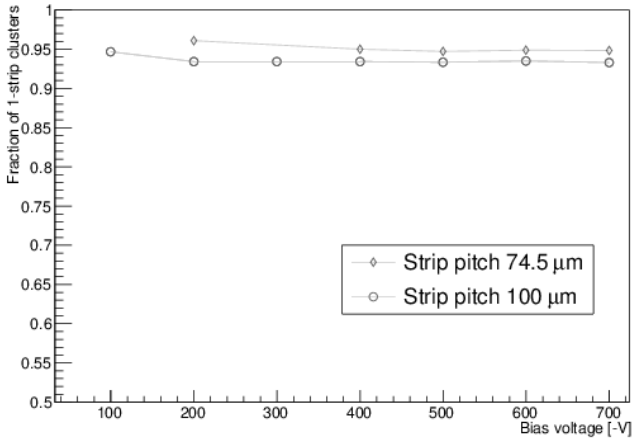

Figure 6.24: Fraction of 1-strip clusters in clusters on ATLAS07 miniature sensors: both sensors under investigation show a small discrepancy, which is expected due to different strip pitches.

6.7.2 Results for Sensors with Glue

For initial tests, sensors were covered with glue at their centre in order to identify glue which would lead to immediate sensor damage or breakdown. Since, at this point, Epolite FH-5313 had been successfully used for the construction of module prototypes, it was known not to cause immediate breakdowns and was thus not included in the initial tests.

Tests of sensors with glue showed distinct patterns in the obtained hit maps (see figure 6.25). While sensors without glue showed hit maps with most hits at the sensor centre (due to the

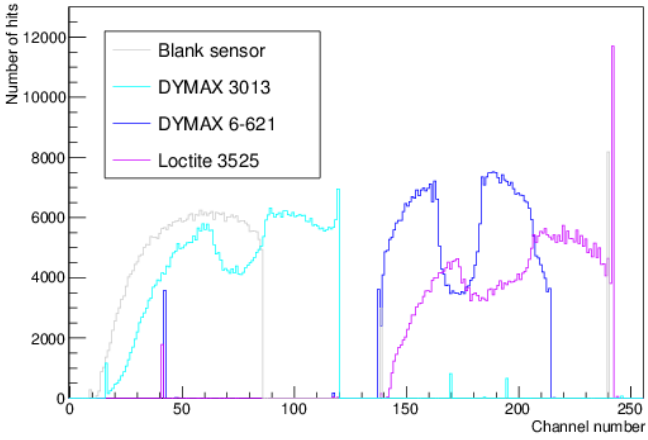

Figure 6.25: Hit maps of four fully depleted ATLAS07 sensors in a β-source setup. 500,000 events were taken for each sensor, with the number of registered hits depending on the position of the sensor with respect to the β-source. Sensors with glue at the centre show fewer hits in the centre due to particles being absorbed in the additional material.

circular shape of the opening below the sensor), sensors with glue showed fewer hits at the centre. A lower number of hits can be attributed to the presence of additional material in the particle path, which absorbs particles before they can reach the photo multipliers and trigger a readout. Thus hit maps show fewer hits for sensor strips partially covered by glue. It should be mentioned that this effect depends on the energy of traversing particles and is not relevant in particle physics detectors with particle energies $\gg 1\,\mathrm{MeV}$.

Sensors with glue covering only the central strips allowed to compare the behaviour of sensor strips with and without glue. Figure 6.26 shows the noise read out for different sensors. Sensor strips at the sensor centre, which were partially covered with glue, did not show a visibly higher noise than sensor strips without glue. Readout channels of beetle chips have a noise [118] of

$$ENC_E = 465.1\,[\mathrm{ENC}] + 45.22\,[\mathrm{ENC/pF}] \cdot C\,[\mathrm{pF}], \tag{6.3}$$

where C is the input capacitance of the attached detector. Compared to the nominal inter-strip capacitance of about 0.7 pF, an increase after gluing of $\mathcal{O}(0.1\,\mathrm{pF})$ (see section 5.5) is small compared to the beetle chip noise. The measured noise is thus not suitable to quantify the

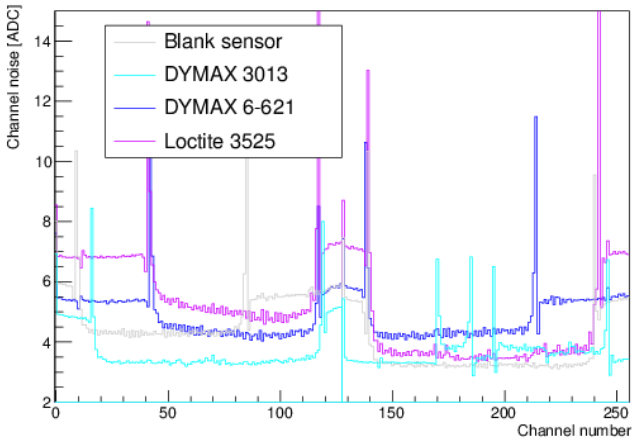

Figure 6.26: Noise of channels connected to sensors with glue covering the sensor centre. Sensor strips wire bonded to the readout system (two per glue type) are visible as areas with lower noise. Channels at the centre of a sensor do not show a higher noise than surrounding sensor strips. The variations seen for a sensor with DYMAX 3013 (cyan line, channels 128 to 256) are caused by a damaged beetle chip (see section 6.7.3.1).

noise increase after gluing, but does confirm that gluing does not lead to a large increase in capacitance and thus sensor noise.

Due to the limited availability of comparable miniature sensors, different sensor types (float zone 1 and 2, narrow and wide strip pitch) had to be used for this study. Results can thus not be directly compared for different sensors. Independent of the presence or type of glue on the sensor surface, all sensors were found to have a CCE compatible with 100 % (see figure 6.27a). The SNR was found to depend on the strip pitch, with a wider strip pitch resulting in a lower SNR, but was found to be above the required minimum value of 10 for all sensors with and without glue (see figure 6.27b).

Cluster sizes were found to be affected by the presence of glue (see figure 6.28). While sensors glued with DYMAX 6-621 showed similar cluster sizes as blank sensors, sensors with DYMAX 3013 and Loctite 3525 showed smaller fractions of 1-size clusters. It should be noted that sensors glued with DYMAX 6-621 were the only FZ1 sensors, which could potentially affect this measurement. Additionally, sensors glued with DYMAX 3013 and Loctite 3525 showed smaller 1-strip cluster fractions for sensors with a narrow pitch than for sensors with a wide pitch.

The CCE and SNR of sensors with glue was found comparable with sensors without glue within uncertainties, hence there was no indication of glues increasing the sensor noise or reducing the charge collection efficiency. Sensors with DYMAX 3013 and Loctite 3525 did show indications of the presence of glue leading to increased cluster sizes.

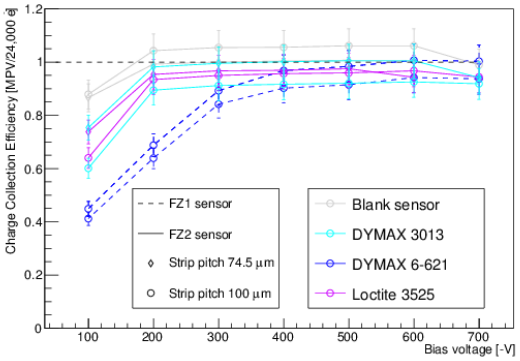

(a) CCE measured for different sensor types with and without glue. Within uncertainties, all sensors have a CCE of about 100 %. Depending on the float zone material, sensors reach depletion at different bias voltages.

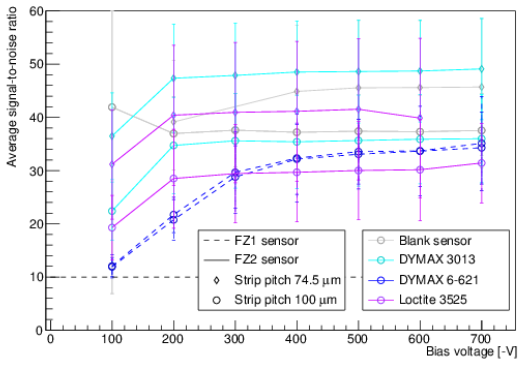

(b) SNR measured for different sensor types with and without glue. While all sensors have a signal-to-noise ratio above the required minimum (10), sensors with a wider strip pitch have lower SNR than sensors with a narrower strip pitch.

Figure 6.27: CCE and SNR for different ATLAS07 miniature sensor types with and without glue.

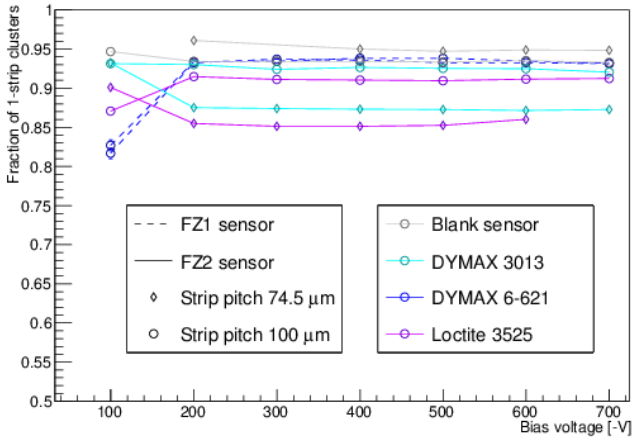

Figure 6.28: Fractions of 1-strip clusters for sensors with and without glue: sensors with Loctite 3525 and DYMAX 3013 showed fewer 1-strip clusters than blank sensors and sensors with DYMAX 6-621. Different from blank sensors, sensors with glue showed fewer 1-strip clusters for narrow strip pitches than for wide strip pitches.

6.7.3 Results for Sensors Irradiated with 23 MeV Protons or Neutrons

Sensors irradiated with 23 MeV protons (figure 6.29a) or neutrons (figure 6.29b) did show similar CCEs for sensors with and without glue. While the CCE of individual sensors show

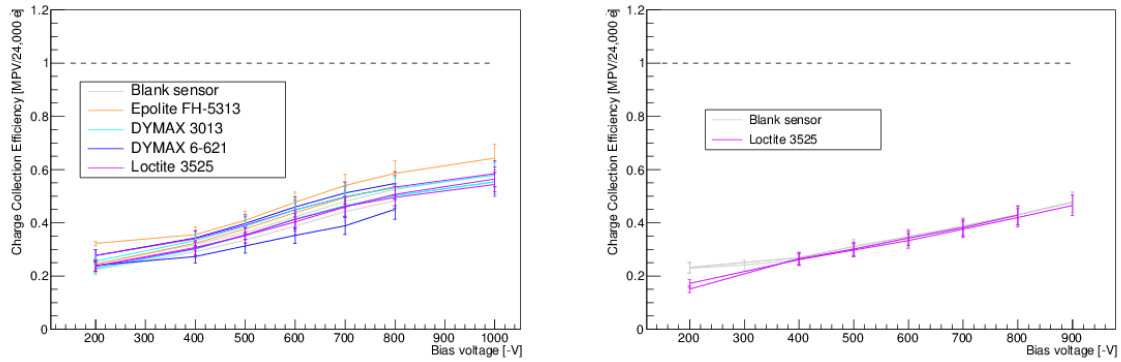

(a) CCE for sensors irradiated with 23 MeV protons at KIT

(b) CCE for sensors irradiated with reactor protons at JSI

Figure 6.29: CCE for irradiated ATLAS07 miniature sensors (FZ2, narrow pitch) with and without glue. CCEs show variations for different sensors, but no systematic differences between sensors with and without glue or individual glues. CCE at -1000 V could only be measured for sensors with sufficiently low leakage current (see section 6.7.3.1).

a spread exceeding the measurement uncertainty, the results were found consistent with the irradiation campaign performed with ATLAS12 and ATLAS07 sensors (see figure 6.30). Both the measurement CCE as well as the spread among individual measurements agree well with the observed results.

Similar to measured CCE, SNR of irradiated sensors with and without glue did not show any discrepancies exceeding the measurement uncertainty (see figures 6.31a and 6.31b). Sensors with all glues under investigation were thus found to fulfil the ITk strip tracker requirement of an SNR > 10 after irradiation.

A change was observed regarding cluster sizes: whereas before irradiation, sensors had shown different fractions of 1-strip clusters depending on the presence of glue, sensors after irradiation did not show notable differences (see figures 6.32a and 6.32b). Since irradiation affects both sensors and adhesives (see section 4.4), it was not possible to attribute the disappearance of a discrepancy between sensors with and without glue to either adhesive or sensors at this point.

With similar 1-strip cluster fractions, sensors with and without glue showed the same performance in CCE, SNR and cluster size after irradiations with protons or neutrons. Hence, gluing did lead neither to an increased sensor noise nor to a reduced charge collection efficiency after irradiation.

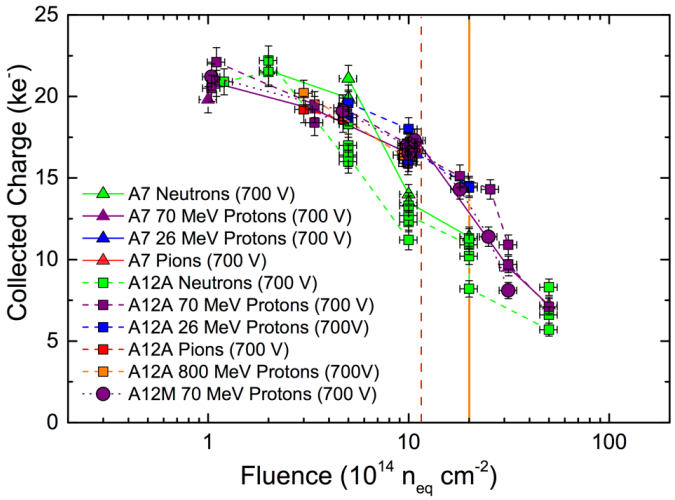

Figure 6.30: CCE measurements of ATLAS07 and ATLAS12 miniature sensors after irradiation with neutrons, protons and pions, from [2]. The orange line indicates the fluence used for the studies presented here.

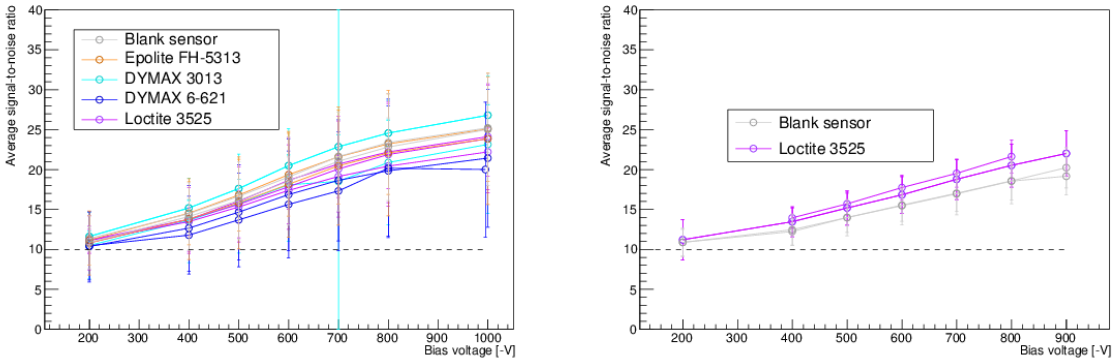

(a) SNR for sensors irradiated with 23 MeV protons at KIT

(b) SNR for sensors irradiated with reactor protons at JSI

Figure 6.31: SNR for ATLAS07 sensors (FZ2, narrow pitch) after irradiation. SNR for sensors with and without glues agreed within uncertainties and stayed above the required minimum SNR for bias voltages from 200 V.

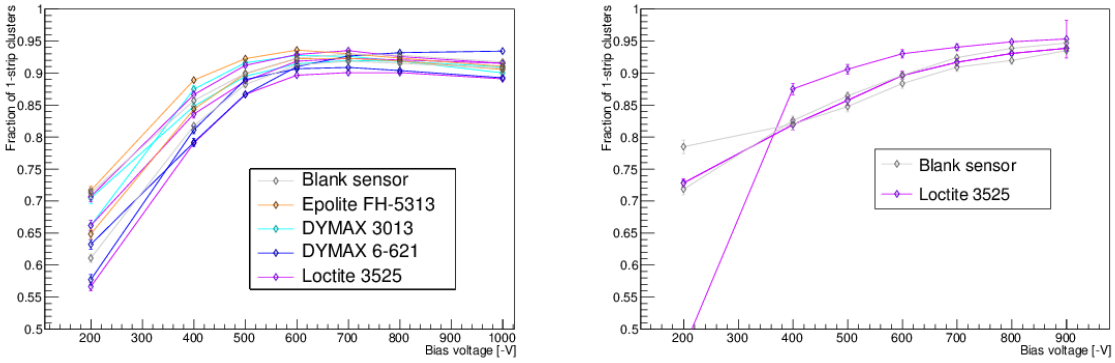

(a) Fraction of 1-strip clusters for sensors irradiated with 23 MeV protons at KIT

(b) Fraction of 1-strip clusters for sensors irradiated with reactor protons at JSI

Figure 6.32: Fraction of 1-strip clusters for ATLAS07 sensors (FZ2, narrow strip) after irradiation with 23 MeV protons or reactor neutrons. Proton irradiated sensors do not show any discrepancy between sensors with and without glue. Neutron irradiated sensors show an indication of different 1-strip cluster fractions for low bias voltage, which is reduced for high bias voltages, indicating that the effect is noise-related.

6.7.3.1 Current Runaway

During measurements in the β-source setup, individual sensors showed a sudden, exponential current increase if the following combination of circumstances was met:

- the tested sensor had a low resistivity bulk material (FZ2)
- the sensor had been irradiated to a fluence of $2 \cdot 10^{15}\,\mathrm{n_{eq}/cm^2}$
- bias voltage of -1000 V
- leakage current larger than 0.1 mA
- the measured sensor temperature was above -20 °C

Table 6.1 summarises the properties of all sensors the effect was observed for. It should be noted

Setup	Wafer	Architecture	Glue	Treatment
β-source setup	W154	BZ3	LOCTITE 3525	irradiated (n)
β-source setup	W154	BZ4D	-	irradiated (n)
β-source setup	W154	BZ2	LOCTITE 3525	irradiated (n)
testbeam	W148	BZ3	DYMAX 6-621	irradiated (p)
testbeam	W148	BZ4A	EPOLITE FH-5313	irradiated (p)

Table 6.1: Sensors for which current runaway was observed and selected characteristics.

that this list contains only sensors for which current runaway occurred accidentally, usually because the temperature increased unexpectedly above -20 °C. Due to permanent damages afterwards (see below), a current increase was not intentionally provoked for sensors.

If current runaway was observed, the bias voltage was reduced as quickly as possible and power to the peltier elements was increased in order to reduce the sensor temperature and overall leakage current. Once a sufficiently low temperature was reached (usually below -22 °C), the bias voltage was increased again and data taking was continued. Comparing results of a

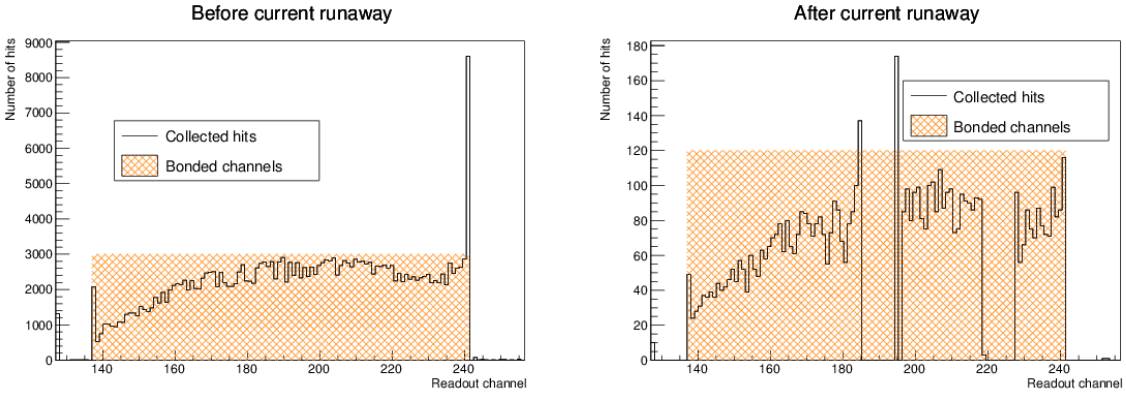

(a) Hit map of a neutron irradiated sensor, operated at -800 V, before current runaway

(b) Hit map of a neutron irradiated sensor, operated at -900 V, after current runaway

Figure 6.33: Hits on a neutron irradiated sensor before and after current runaway: while before the incident, each wire bonded channel registers hits, the hit map taken after the incident shows two gaps of channels not registering hits. Additionally, channels registering hits found fewer hits than before the incident.

sensor before and after a current runaway incident (see figures 6.33a and 6.33b), hit maps taken with the ALiBaVa system showed two gaps of about ten channels each where the ALiBaVa system did not read out any signal.

Searching for indications of damages to the ALiBaVa system revealed two effects:

- on the glass fan-outs with a pattern of metal traces to increase the strip pitch, several metal traces showed burned areas preventing any data readout (see figure 6.34a)
- bond pads on the front end part of the beetle chip with dead channels showed marks of burning (see figure 6.34b)

Both effects permanently damaged the daughterboard, explaining the occurrence of dead channels.

The cause was found during a visual inspection of the sensors in question under a laser microscope with high magnification: residue of the silver paint used to glue sensors on to the sensorboards was found on the sensor surface. Traces of silver were usually surrounded by burnt areas on the sensor (see figure 6.35), indicating previous high currents. Conductive residue on the sensor surface explains the current increase as well as localised damages on the readout chip.

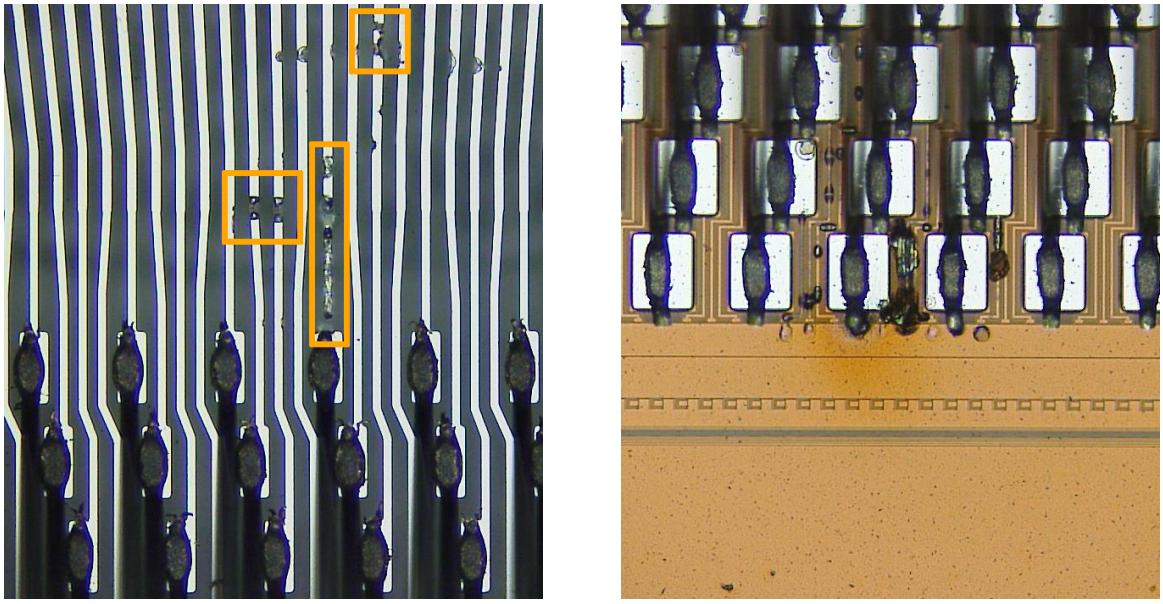

(a) Metal traces on glass pitch adapters showing burned areas interrupting the conducting path

(b) Bond pads on the front end area of an ALiBaVa beetle chip showing several burned areas

Figure 6.34: Indications of damages on an ALiBaVa daughterboard after the sensor connected to the readout chip experienced current runaway.

Positions of observed silver residue matched the positions of burnt channels on the ALiBaVa board and therefore strongly support the explanation.

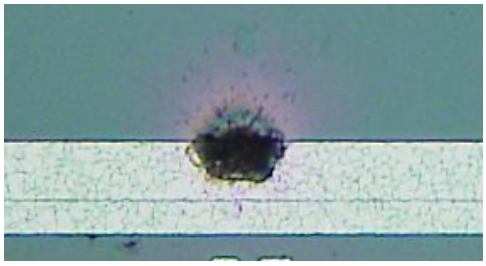

Figure 6.35: Residue of silver paint (diameter about 80 µm on the surface of an ATLAS mini sensor. The burnt area surrounding the silver paint indicates a previous high current.

The occurrence of residue on the sensor surface can be attributed to the necessity of re-attaching sensors to the sensorboard. While the design of sensorboards used in this thesis provided a larger window for particles to pass through the sensor, the resulting contact area between sensor and sensorboard was smaller than on standard boards. Most sensors were exposed to repeated cooling (for storage, tests in the β-source setup and the testbeam) and warming (e.g. during mounting) over the course of several months and in several cases, the glue layer failed. In order to re-attach a sensor to a sensorboard, left over traces of glue had to be removed and new glue had to be applied. While all work on sensors was performed under cleanroom conditions, the observed residue indicates that some silver paint dust had been transferred on to the sensors. It was found that all sensors which displayed current runaway had had to be re-attached to their respective sensorboard, further supporting the theory.

It was thus concluded that the occurrence of local currents, which were high enough to damaged attached readout electronics, was not an effect of sensor or glue on the sensor surface, but caused by handling. Therefore, sensors for which the effect had been observed, had to be excluded from further measurements on an ALiBaVa board in order to prevent further damages.

6.7.4 Results for Sensors after Temperature Cycling

Sensors after temperature cycling showed a similar behaviour as sensors after gluing: sensors with and without glue did not show any discrepancies in CCE (figure 6.36a) or SNR (figure 6.36b). It should be noted that one sensor (glued with DYMAX 3013) was damaged during probe station measurements and could not be fully depleted afterwards. It was thus excluded from the measurements. All remaining sensors showed CCE of $\geq 90\,\%$ and SNR > 40. Sensors with glue thus did not show an increased noise or reduced CCE compared to sensors without glue.

Similar to sensors after gluing, sensors after temperature cycling showed indications of increased cluster sizes for sensors with glue (see figure 6.37). Where fractions of 1-strip clusters had shown discrepancies of more than 5 % (among comparable sensor types) for sensors with and without glue (see figure 6.28), sensors after cycling showed significantly smaller discrepancies. Underlying effects causing this observation are discussed in section 6.8.

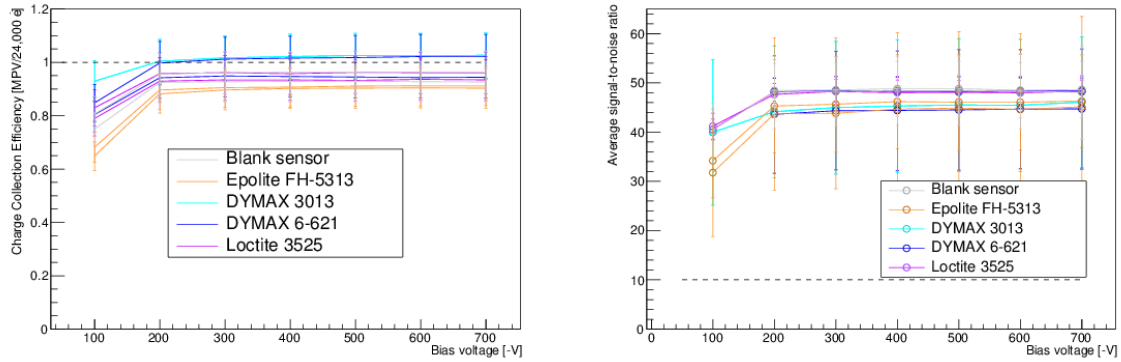

(a) CCE for sensors after 100 temperature cycles (b) SNR for sensors after 100 temperature cycles

Figure 6.36: CCE and SNR for ATLAS07 sensors (FZ2, narrow strip pitch) with and without glue. CCE for sensors with and without glue are comparable within uncertainties and at or above 90 %. SNR for all sensors agree within uncertainties and are well above the required minimum SNR of 10.

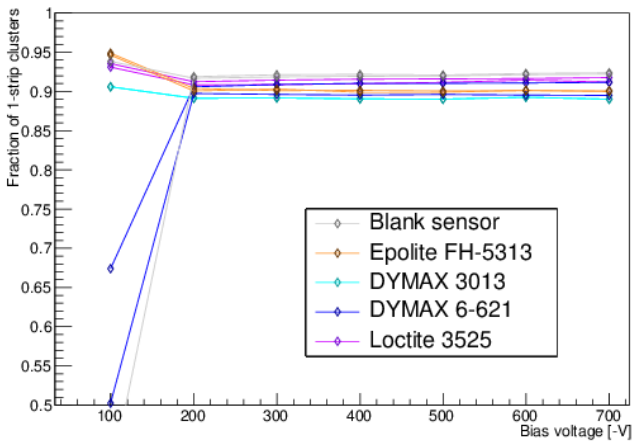

Figure 6.37: Fraction of 1-strip clusters for ATLAS07 sensors (FZ2, narrow strip pitch) with and without glue after 100 temperature cycles. Sensors with and without glue show a similar pattern as sensors after gluing, with blank sensors showing a higher fraction of 1-strip clusters than sensors with glue.

Although temperature cycling was found to decrease the discrepancy in cluster sizes between sensors with and without glue, the effect was still observed.

6.7.5 Results for Sensors after Irradiation with 23 MeV Protons and Temperature Cycling

A separate set of sensors, which was irradiated with 23 MeV protons and subjected to 100 temperature cycles afterwards, showed similar CCE (see figure 6.38a) and SNR (see figure 6.38b) as sensors only irradiated with 23 MeV protons. CCE and SNR were comparable (within

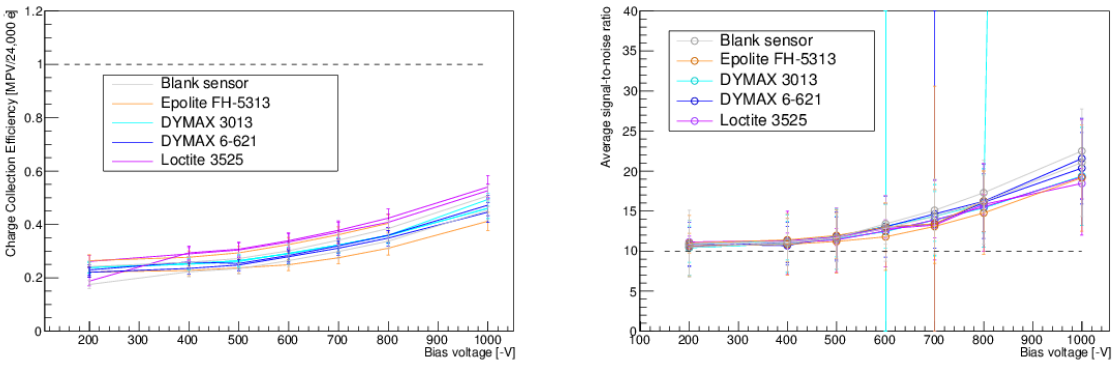

(a) CCE for sensors after proton irradiation and 100 temperature cycles

(b) SNR for sensors after proton irradiation and 100 temperature cycles

Figure 6.38: CCE and SNR for ATLAS07 sensors (FZ1, narrow strip pitch) with and without glue after proton irradiation and temperature cycling. CCE and SNR are comparable within uncertainties for sensors with and without glue.

uncertainties) for sensors with and without glue; the presence of an adhesive on the sensor surface thus did not lead to an increased sensor noise or reduced charge collection.

Cluster sizes on sensors that were both irradiated and exposed to temperature cycles were found to be increased compared to sensors after irradiation (see figure 6.39). While individual sensors show large discrepancies in measured fractions of 1-strip clusters, no dependence on the presence of glue on a sensor was found. The reduced fraction of 1-strip clusters, i.e. increased cluster size, matches probe station measurements of sensors after proton irradiation and temperature cycling (see section 5.8), which had found high inter-strip capacitances after irradiation and temperature cycles. Since elevated temperatures lead to a diffusion of bulk defects to the sensor surface, sensors can be assumed to accumulate defects at the surface after temperature cycling and irradiation. These accumulated defects result in an increased inter-strip capacitance, i.e. more coupling between adjacent sensor strips, and thus larger clusters.

Sensors subjected to both proton irradiation and temperature cycles did not show any dependence of the CCE or SNR on the presence of glue.

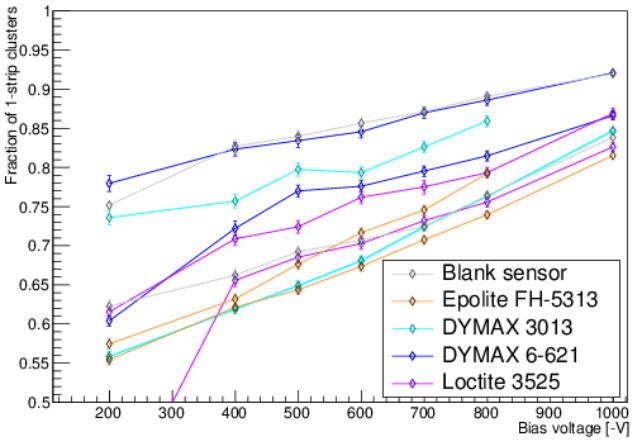

Figure 6.39: Fraction of 1-strip clusters for ATLAS07 sensors (FZ1, narrow strip pitch) with and without glue after proton irradiation and temperature cycling. Sensors with and without glue show similar fractions of 1-strip clusters.

6.7.6 Results for Sensors Irradiated with 800 MeV Protons

All β-source studies were performed 1 to 1.5 years after irradiations with 800 MeV protons had been conducted. Despite the cool-down time, the sensor activity was too high to allow abrasive treatments including wire bonding, so that the sensors could not be connected to a readout system. The charge collection efficiency could thus not be studied for these sensors.

6.8 Discussion of Results

Charge collection efficiency measurements were performed to assess the impact of glue on a sensor's ability to collect charge, i.e. effects on the silicon bulk. Since defects in the silicon bulk migrate, especially at elevated temperatures, bulk defects caused by glue can be assumed to affect the overall CCE of a sensor. However, effects caused by the presence of glue in a local sensor area, such as the accumulation of charge in the glue during irradiation, require the collection of charge directly in sensor areas covered by glue.

By testing a whole miniature sensor, of which about half was covered with glue and FR4, in a β-source setup, the measured CCE was assumed to be averaged over the full sensor area.

During measurements, sensors with glue and FR4 were found to have a lower data taking rate than blank sensors. Since approximately half of a mini sensor was covered by glue and FR4, the rate reduction was suspected to correspond to the sensor area with additional material that was covering the β-source (see figures 6.40b to 6.40e). Additional material was found to reduce the obtained hit rate in hit maps with glue at the sensor centre - the collected data can thus be assumed to be disproportionately from sensor areas not covered with glue.

Hence, if the addition of glue had a local impact on the sensor area directly below the glue that did not exist on the blank areas of the sensor, the measurements might not present an

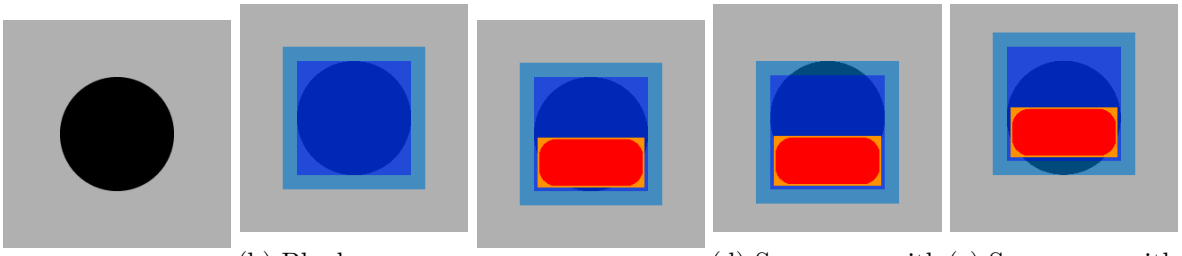

(a) Hole in cooling plate, without sensor, β-source below hole

(b) Blank sensor positioned over hole in cooling jig, rate about 330 Hz

(c) Sensor with glue and FR4 over hole in jig, rate about 140 Hz

(d) Sensor with glue and FR4 on hole, moved down, rate about 190 Hz

(e) Sensor with glue and FR4 on hole, moved up, rate about 100 Hz

Figure 6.40: Schematic of the possible impact of sensor positions on the data taking rate in a β-source setup: when a blank sensor (blue, active area indicated in dark blue) is positioned centred over the β-source, a much higher rate can be achieved than for sensors with additional material (glue (red) and FR4 (orange)). This indicates that the additional material blocks a significant fraction of the particles, so that a large fraction of events were collected for sensor areas without glue and FR4.

accurate image of the sensor performance. A comparative measurement was thus performed in an electron beam (see next chapter).

6.9 Conclusion of β-Source Setup Measurements

Measurements of charge collection efficiencies for sensors with and without glue did not show indications that the presence of glue on sensor surfaces affects their ability to collect charge. Several mechanisms of how a sensor could be impaired by glue had been considered as possibilities, all of which would have been detected by the presented measurements:

- the diffusion of atoms (such as carbon, oxygen or hydrogen, which are present in glue) into the silicon bulk, forming interstitials or Frenkel pairs (see figure 3.6), particularly after irradiation, which can break chemical bonds in glue molecules

- damage to the silicon bulk due to mechanical stress during temperature changes (particularly after irradiation when glue can be assumed to have a higher modulus of elasticity, see section 3.4.1)

- corrosion of the silicon bulk, such as the removal of individual silicon atoms, forming vacancies (particularly after temperature cycling which accelerates chemical reactions, see section 3.4.2)

Since bulk defects migrate through silicon, these effects can be assumed to be detectable in sensor areas which are not covered with glue as well as sensor areas covered with glue.

For all groups of sensors under investigation, the obtained charge collection efficiencies and signal-to-noise ratios agreed within uncertainties for sensors with and without glue. No indication of an impairment of the sensor performance by the presence of glue was found.

Differences in the sensor performance were only observed for unirradiated sensors, where average cluster sizes for sensors with glue were larger than for sensors without glue. Further, more detailed studies of this effect will be presented in chapters 7 and 8.

7 Sensor Performance Study in an Electron Beam

While measurements in a β-source setup indicated that there are differences in the performance of sensors with and without glue, signals of particles could not be unambiguously attributed to sensor areas with or without glue (see section 6.8).

Performing charge collection measurements in a testbeam with particle energies $\mathcal{O}$(GeV) provides a setup where data can be gathered for both sensor areas with and without glue. Additionally, the possibility of locating the position of a particle track on a sensor using a beam telescope (see section 7.1.1) allows to compare the performance of covered and uncovered sensor areas on the same sensor rather than comparing sensors with and without glue.

Hence, following the charge collection efficiency measurements described in the previous chapter, the performance of sensors with and without glue was also studied in an electron beam.

7.1 Testbeam

These sensor studies were conducted in testbeams generated by the DESY II electron synchrotron. Particles for testbeams are not directly extracted from DESY II, but generated via secondary interactions (see figure 7.1). By inserting a carbon fibre target into the synchrotron,

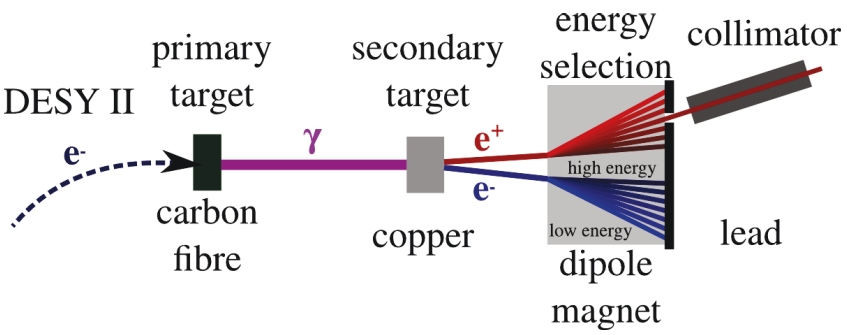

Figure 7.1: Testbeam generation at DESY II: A carbon fibre target in the electron or positron beam produces bremsstrahlung, which is converted into electron-positron-pairs using a secondary target. A dipole magnet selects particles of a specified energy, which reach the testbeam stand through a collimator.

a bremsstrahlung beam is generated. Secondary aluminium or copper targets with thicknesses of 1-5 mm inserted in the bremsstrahlung beam lead to the production of electron-positron-pairs. These particles then traverse a dipole magnet selecting electrons or positrons of a specific energy

to pass through a collimator into the testbeam hall. The particle energy (1-6 GeV) can be selected by changing the magnet current [123].

For theses studies, beam line 21 was used.

7.1.1 Beam Telescope

Electrons in the DESY-II testbeam have sufficient energy ($\mathcal{O}$(GeV)) to pass through more material, compared to β-particles, without significant energy loss. This allows the insertion of a beam telescope, consisting of several layers of pixel sensors, in the beam path around the sensor under investigation, so that the position of each particle track can be extrapolated with respect to the sensor. Figure 7.2 shows the schematic construction of a beam telescope. Each layer of

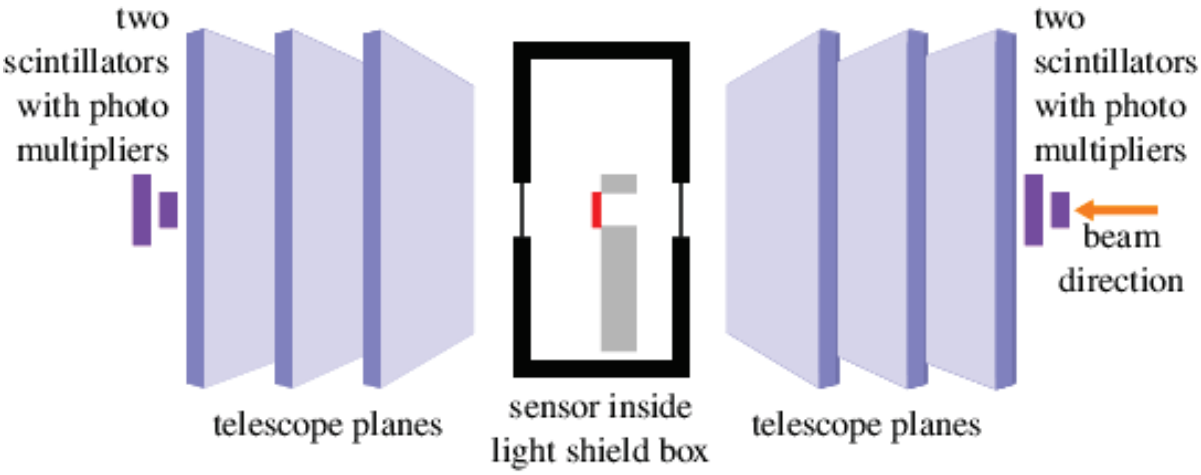

Figure 7.2: Schematic of a beam telescope as used in the testbeams presented here: A beam telescope consists of six layers of pixel sensors arranged in groups of three in front of and behind an object under investigation. Scintillators with photomultipliers (violet) both in front of the first and behind the last telescope plane allow to trigger on particles passing the telescope. A sensor (red) is mounted between the centre planes of a beam telescope inside a box, which acts as a light shield and allows temperature and humidity control.

the beam telescope consists of an aluminium frame holding a MIMOSA26 pixel sensor [124]. Each MIMOSA sensor has an active area of $21.1 \times 10.6\,\mathrm{mm}^2$ which holds 1152×576 pixels with a square size of $18.4 \times 18.4\,\mu\mathrm{m}^2$ each. For a high beam energy and low-material device under test (DUT), a track resolution of $\sigma = 2\,\mu\mathrm{m}$ can be achieved [125].

Scintillators with photomultipliers in front of the first telescope plane and behind the last telescope are used to trigger data taking. Each scintillator has an acceptance window of $1 \times 2\,\mathrm{cm}^2$, which matches the area of a MIMOSA26 sensor.

Data taking is triggered by the photomultipliers using a trigger logic unit (TLU) [126], which all four photo multipliers are connected to. If a trigger signal is detected in the photo multipliers, the TLU is triggered to read out all six telescope planes. In order to read out a sensor under

investigation in the same time frame as the telescope planes, it is connected to a channel of the TLU.

For the measurements presented here, the DATURA (DESY beam line 21) beam telescope was used. It was operated using a telescope threshold of 5, corresponding to a sensor efficiency of 99.6 % [125]. Only scintillators positioned to have their acceptance windows overlap with the active area of the MIMOSA sensors were used for triggering.

7.1.2 Setup for Sensor Tests in Electron Beam

Sensor testbeam studies were performed using an ALiBaVa readout system (see section 6.3), mounted on a copper cooling plate (see figure 7.3). Both the ALiBaVa daughterboard used for

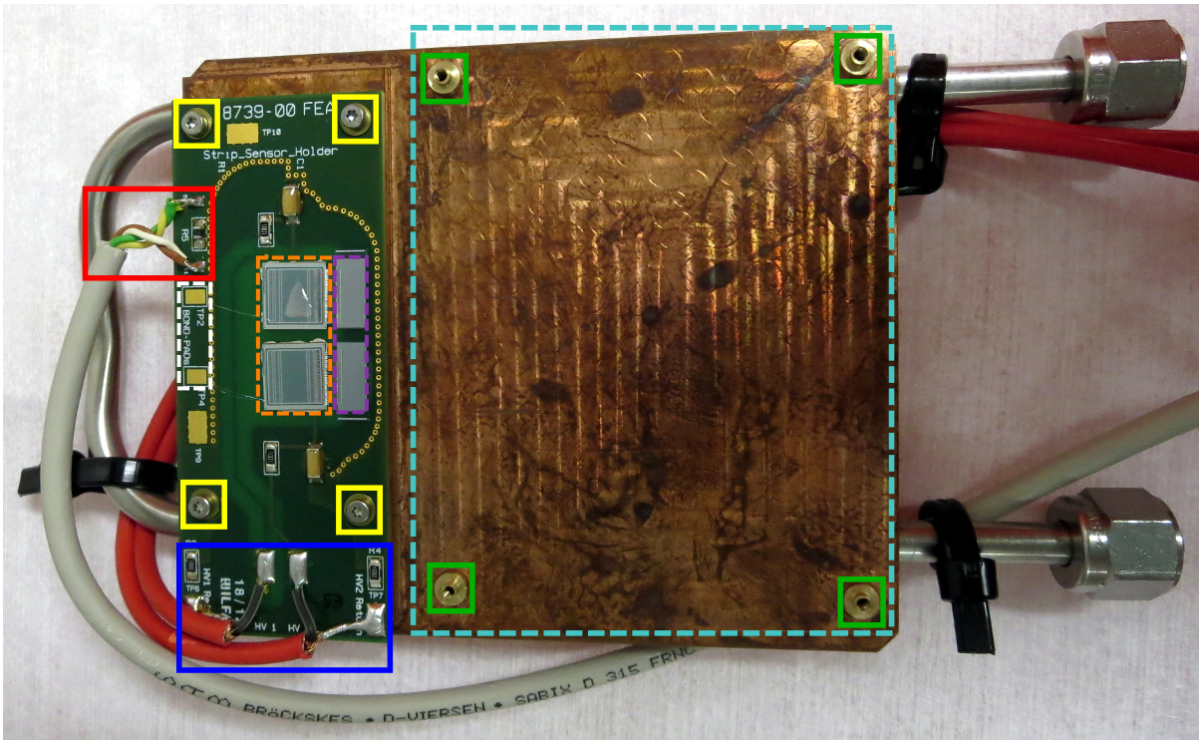

Figure 7.3: One-piece cooling setup for testbeam studies of unirradiated sensors: a metal pipe, connected to a chiller, is welded into a copper plate. An ALiBaVa daughterboard is mounted (indicated by dashed cyan line) on four brass rings (green lines) to provide electrical grounding while minimising thermal contact. The sensorboard is placed on a step of the cooling plate for maximal thermal contact and electrical grounding, using four metal screws (yellow lines). High voltage (blue rectangle) and temperature and humidity readout (red rectangle) are connected via soldered cables. Miniature sensors (indicated by orange rectangle) are connected to ground pads (white dashed line) and pitch adapters (dashed violet line) by wire bonds.

sensor readout and the sensorboard holding the miniature sensors were screwed directly onto

the copper plate cooled by a chiller. Unirradiated sensors were used in this study, requiring a cooling temperature of 10 °C. The cooling plate was mounted inside a plastic housing to minimise light exposure. Cooling tubes, high voltage cables, temperature and humidity readout and the ALiBaVa data readout cable were fed through the housing through holes in the plastic housing.

A detailed description of the setup used in this testbeam can be found in [127].

Two sensors were tested in comparison: one blank sensor and one sensor with the current baseline sensor glue FH-5313 (see figure 7.4). Glue was applied in a triangular shape in order to be able to compare sensor strips with different glue coverage. Sensors were operated fully

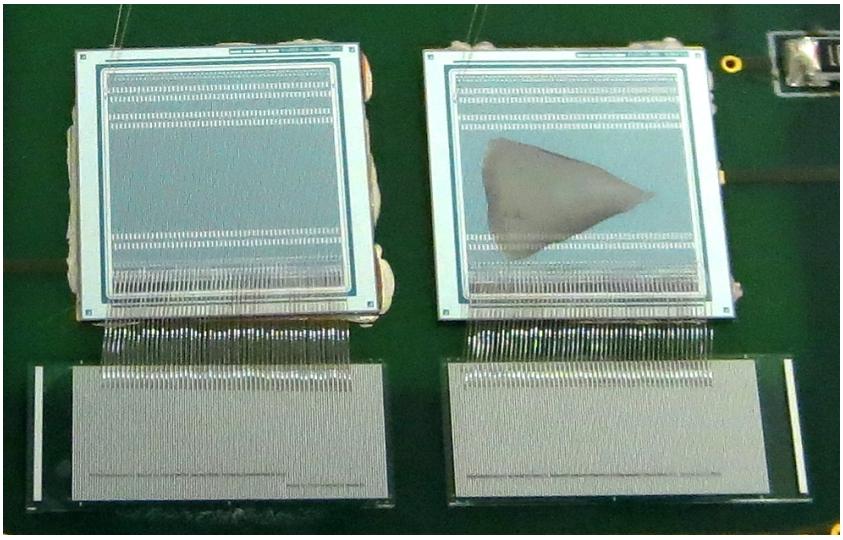

Figure 7.4: Sensors tested in electron beam: one sensor was tested without glue (left), one sensor with Epolite FH-5313 (right). Glue was applied in a triangular shape to study a range of glue coverages.

depleted at a bias voltage of -250 V.

7.1.3 Adjustment of Beam Position and Energy

When the setup had been mounted in the beam telescope, the latency was optimised first, then position and beam energy were adjusted for optimal data taking:

After a coarse alignment of the sensors in the beam by eye, xy-stages were used to move the position of the sensor with respect to the beam, where x was defined as the position perpendicular to the sensor strip orientation and y was defined parallel to the sensor strip orientation.

Collected hits from a particle beam were used to obtain an ALiBaVa hitmap showing the number of hits for each readout channel. As a first alignment step, the stage was moved in x-direction (perpendicular to the sensor strips), until the beam was centred.

A good position along the sensor strips was found by moving the stage in y-direction in small steps and measuring the hit efficiency at each given position. The hit efficiency, indicating the

percentage of triggered events where a hit was found by the ALiBaVa system, becomes maximal for a maximum overlap of the beam area with the active sensor area (see figure 7.5). All sensor

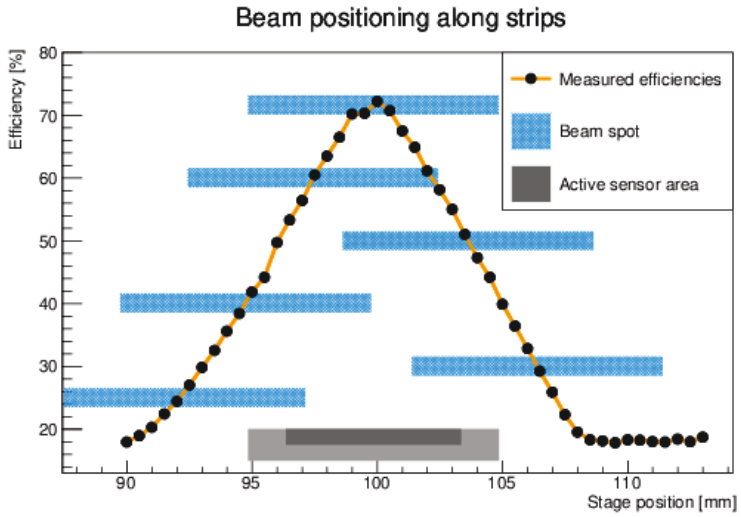

Figure 7.5: Hit efficiencies (number of triggered events for which a hit was registered in a sensor) depending on the position of the sensor (grey) with respect to the beam (blue). Each efficiency was obtained by collecting 20,000 events on two fully depleted sensors, beam energy 5.0 GeV. Since the beam size is larger than the active sensor area, the hit efficiency shows a plateau at the centre of the sensor.

tests were conducted at the y-position that was found to return the maximum hit efficiency.

Beam energies from 2 to 6 GeV were available for these studies, which could be selected in steps of 0.2 GeV by selecting the corresponding dipole magnet current. Particle rates peak at 2 GeV, corresponding to 3 to 8 kHz, depending on the secondary target [128]. The beam energy was chosen to

- be as high as possible in order to minimise scattering angles in telescope planes
- deliver a particle rate maximising the data acquisition rate
- deliver a particle rate low enough to minimise the fraction of events with multiple tracks per event

In order to find a compromise for these criteria, the readout time required for 20,000 events was measured for different beam energies (see figure 7.6). The beam energy selection shown here was taken at a later testbeam with different collimator settings, resulting in a different optimal beam energy. These measurements allowed to identify a beam energy of 4.6 GeV, where the particle rate was low enough to minimise the fraction of events with multiple tracks, while not reducing the data acquisition rate due to a low particle rate.

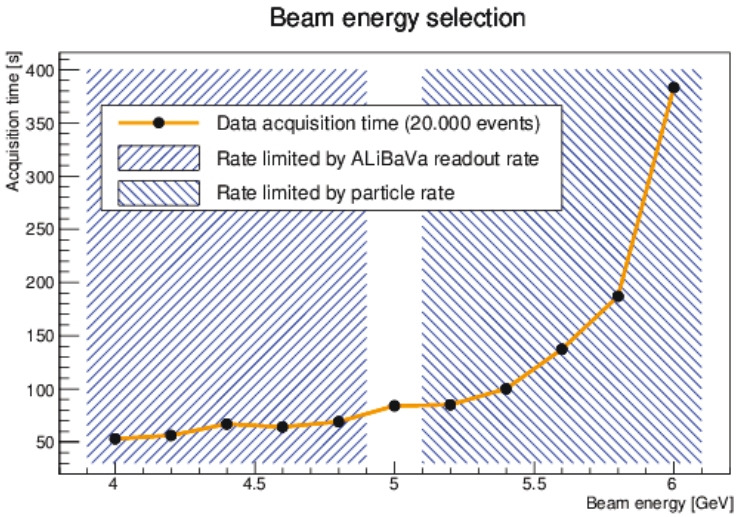

Figure 7.6: Acquisition times for 20,000 events for different beam energy settings. For beam energies below 5 GeV, the acquisition time is mostly flat, due to the limited readout speed of the ALiBaVa system. For beam energies above 5 GeV, the time increases significantly due to a low particle rate at high energies. Small variations in the measured acquisition times can be attributed to variations in the beam current, e.g. beam injections to the PETRA-III storage ring.

7.1.4 Data Taking

Data was read out using an ALiBaVa system as described in section 6.4: sensors were read out by beetle chips on an ALiBaVa daughterboard connected to a motherboard, which was read out by a laptop.

Data taking was triggered by photomultipliers mounted in front of the beam telescope. Their signal was fed into a trigger logic unit [126], which then sent a trigger to the ALiBaVa system. A busy signal from the ALiBaVa system was routed back to the trigger logic unit to prevent further data taking, limiting the overall data taking rate to about 300 Hz.

The ALiBaVa readout latency was optimised as described in section 6.4.1.

Sensors were tested at a temperature of 10 °C and a humidity < 0.01 %, monitored using a sensor on the sensorboard (see figure 6.4).

Data was taken in sequences of pedestal and data runs:

- initial pedestal run with 300,000 pedestal events
- 3 data runs with 500,000 events each
- final pedestal run with 300,000 pedestal events

The initial pedestal run was used for the analysis of subsequent data runs, the final pedestal run was used to ensure comparability throughout one data taking sequence.

Since this test was investigating sensor performances under conditions as expected in the detector, sensors were tested fully depleted without any voltage changes.

7.2 Data Reconstruction

Data from the testbeam was analysed in three main steps:

1. data taken with the ALiBaVa system was processed (see section 7.2.1)
2. telescope data was processed (see section 7.2.3)
3. using reconstructed ALiBaVa and telescope data, tracks were constructed (see section 7.2.4)

The full testbeam data analysis was performed using the EUtelescope framework [129] (version v-01-17-05) and the LCIO (Linear Collider I/O) software package and data format [130]. This data format was developed to contain all information associated to one event (identified by run number and time stamp) in different stages of reconstruction. Independent of the processing stage (raw data, clusters, hits, tracks etc.), LCIO provides a container format for all data associated with an event.

Figure 7.7 shows a schematic overview of the testbeam data analysis.

7.2.1 ALiBaVa Data Analysis

Data from the ALiBaVa system was analysed using a similar procedure as described in section 6.6 for the reconstruction of data taken in the β-source setup:

- analysis of pedestal data and computation of pedestal and noise for each readout channel
- subtraction of the pedestal value from the read out ADC count of each channel
- common mode noise correction on an event by event basis by subtracting the average input charge of all channels from each channel's read out signal

For event reconstruction, clustering cuts were chosen to be more loose than clustering cuts for the analysis of data from the β-source setup to reconstruct as many tracks as possible:

- seed cluster cut: signal-to-noise ratio of 3.5
- neighbour cluster cut: signal-to-noise ratio of 1.8
- maximum cluster size cut of 10

Tracks not fulfilling the standard cluster criteria were removed in a later data analysis step (see section 7.3).

For the analysis of data taken in a testbeam, an additional cross-talk correction was implemented. Cross-talk occurs due to a degradation of the square wave signal used to read out the charge of each channel. Because of the long readout cable in use (length of about 3 m), the signal read out from the n-th channel can become skewed, which leads to part of the signal

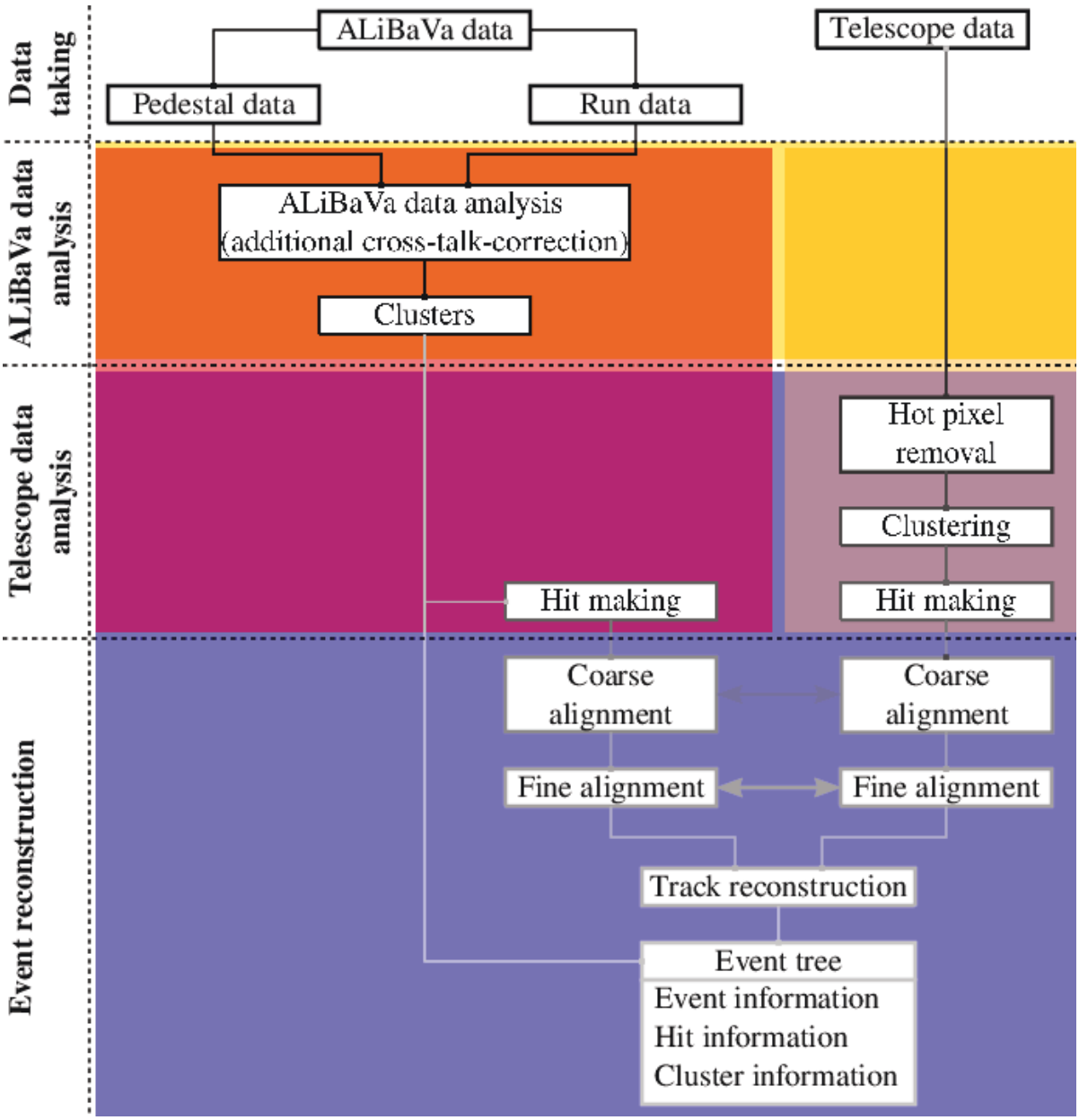

Figure 7.7: Schematic overview of the applied testbeam data analysis steps: for most of the analysis, ALiBaVa data and telescope data are processed separately, up to the alignment and track reconstruction step. Finally, ROOT event trees are built using the cluster charge and hit information.

from channel n being attributed to channel $n+1$ or $n-1$ [131]. Since this shift occurs only in one direction, it results in an asymmetric charge distribution in two-strip clusters. The charge division λ is calculated for each two-strip cluster:

$$\lambda = \frac{Q_{n+1}}{Q_{n+1} + Q_{n-1}}, \tag{7.1}$$

where Q_{n+1} and Q_{n-1} are the charges read out in the left and right strip of a two-strip cluster. An asymmetry of the resulting λ distribution is caused by cross-talk.

The effect is corrected for by calculating the average discrepancy of charge in strip $n+1$ and $n-1$ depending on the charge registered in strip n and subtracting the resulting shift from measured ADC counts. The corrected cluster charges for all events were stored with the event information.

7.2.2 Data Merging

During data taking, ALiBaVa events and telescope events were stored separately. Each event was associated with a time stamp and run number assigned by the trigger logic unit. In order to construct combined particle tracks from information of both DUT and telescope planes, ALiBaVa events need to be matched to telescope events using event time stamps and run numbers.

7.2.3 Telescope Data Processing

Telescope data processing is performed independently from the ALiBaVa data until both are used to reconstruct tracks combining hits in the telescope and hits on the sensor under investigation (see section 7.2.4). From raw entries in the different MIMOSA26 pixel sensor planes, the data is processed in a series of the following consecutive steps:

7.2.3.1 Hot Pixel Masking

Data was taken at a telescope sensor threshold set to be five times the pixel RMS noise, which maximises the data taking efficiency (99.6 %) [125]. At this threshold, each MIMOSA26 sensor plane was found to contain several hot pixels, i.e. cells which frequently register hits due to high noise. Figure 7.8 shows an example of a hit map containing hot pixels. Pixels with high noise (referred to as "hot" pixels) register hits more frequently than pixels only registering true hits from incoming particles. They can thus be identified from their increased occupancy: for each pixel cell, the average occupancy (hits/event) was calculated and pixel cells with an average occupancy > 0.01 were added to a database. Figure 7.9 shows part of the hot pixel mask created for the sensor plane events shown in figure 7.8. For all subsequent data processing steps using pixel entries, hot pixel masks stored in the database were used to ignore entries from pixel cells marked as "hot" pixels.

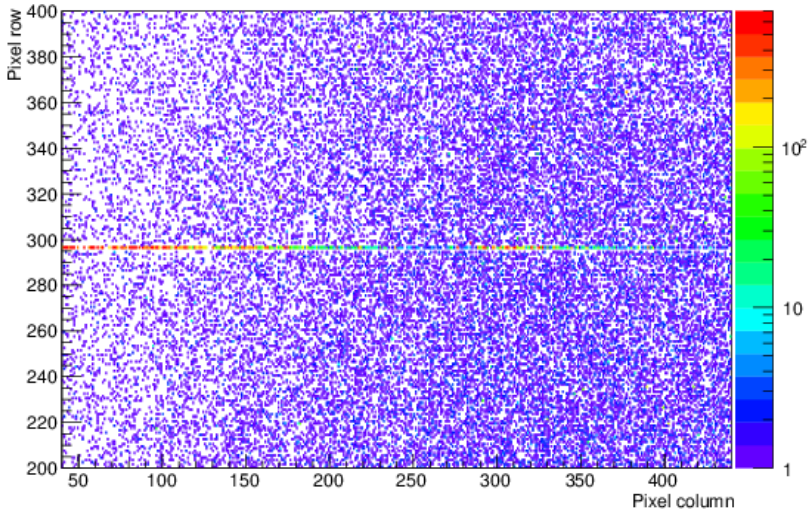

Figure 7.8: Hit map on sensor plane 2 from 100,000 telescope events using all sensor pixel entries (without hot pixel masking). The map shows a row of clusters corresponding to positions of noisy pixels visible as positions with increased hit frequency.

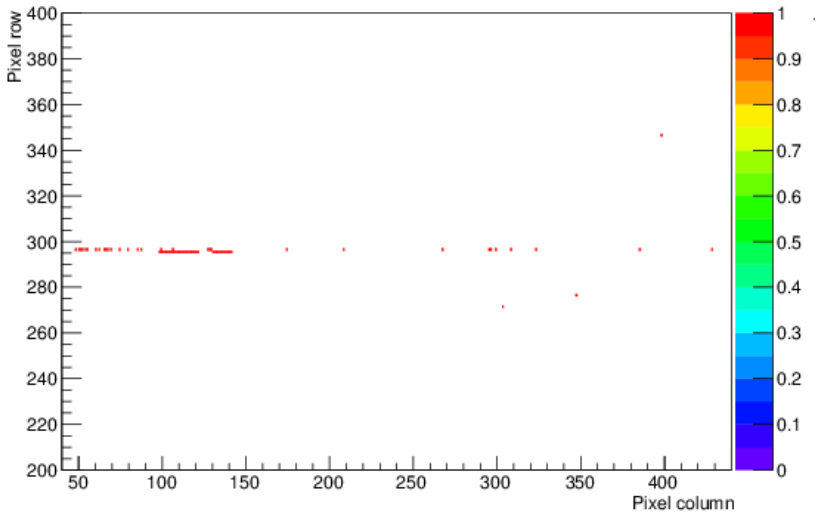

Figure 7.9: Detail of a hot pixel mask created for sensor plane 2 from 100,000 telescope events. Pixel cells were marked as hot if their occupancy was higher than 0.01 hits/event. Hits from hot pixels were ignored in subsequent processing steps.

7.2.3.2 Clustering and Hit Making

In the next step, entries in individual pixel cells are grouped together to form clusters: on an event-by-event base, each entry in a pixel cell in any telescope plane is searched for entries in adjacent cells. If existing, adjacent cells with hits are merged together to clusters until no further hits are found in any of the pixel cells surrounding the cluster. All clusters are stored in a cluster database and clusters with more than 3 cells contributing in x or y-direction are marked as bad. Figure 7.10 shows the distribution of cluster sizes in 100,000 events. Afterwards hits

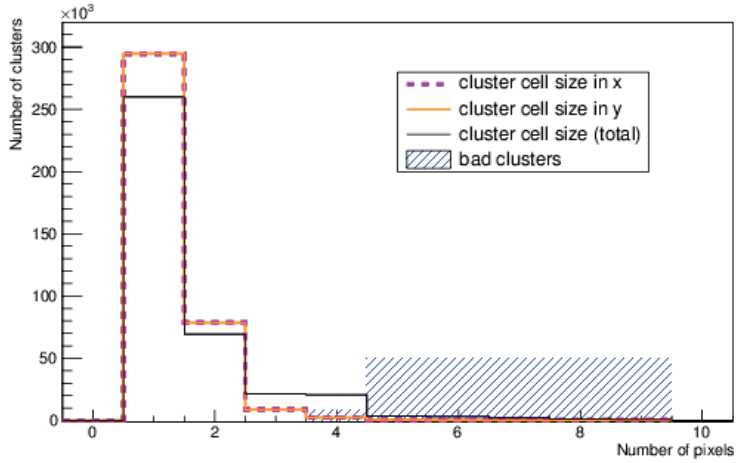

Figure 7.10: Sizes of clusters on telescope sensor plane 1 for 100,000 telescope events: as expected for the square MIMOSA-26 pixel cells, cluster size distributions in x and y overlap. Most clusters have widths of one or two cells and only a small number of clusters contain more than five cells in total. Clusters with more than 3 cells in either x or y are marked as bad.

are created from clusters by assigning a hit position and uncertainty to each cluster depending on its number of contributing cells, their positions and pattern.

All hits are then stored in a hit collection database.

7.2.3.3 Coarse Alignment (Correlation)

After clustering and hit making in telescope planes and DUT, the positions of all sensors with respect to each other need to be determined before particle tracks can be reconstructed.

The coordinate system used for testbeam reconstruction is chosen as follows:

- the z-axis is oriented along the beam with $z = 0\,\text{mm}$ on the surface of the telescope plane first traversed by the beam
- the x-axis is oriented horizontally (i.e. perpendicular to sensor strips in the setup used here) and perpendicular to the beam axis, with $x = 0\,\text{mm}$ at the first pixel (row 0, column 0) of the first telescope plane

- the y-axis is oriented vertically (i.e. parallel to sensor strips in the setup used here), with $y = 0\,\text{mm}$ at the first pixel (row 0, column 0) of the first telescope plane

Positioning information is collected in a gear file, which contains both the geometry information of each sensor plane (i.e. thickness, size and number of pixel columns and rows, where strip sensors are treated as pixel sensors with only one row in y) and a best guess for the positions of all sensors:

- positions in z (along the beam axis) are measured at the testbeam using a ruler and thus have an uncertainty of about $\pm 1\,\text{mm}$
- positions in x and y are assumed to be identical for all MIMOSA-26 sensor planes (assuming a well aligned beam telescope)
- rotation angles of all sensors are assumed to be $0\,^\circ$

A coarse improvement of the initial alignment is achieved by correlating the hit positions in different sensor planes (see figure 7.11). Since tracks are mostly straight lines through all telescope planes, offsets in the x and y positions of the same particle track in different telescope layers can be used for a coarse alignment. By relating these offsets to the position of the first telescope planes (used as reference plane), relative shifts of different telescope planes can be calculated (see figure 7.12). The displacement between pixel positions in x and y in different

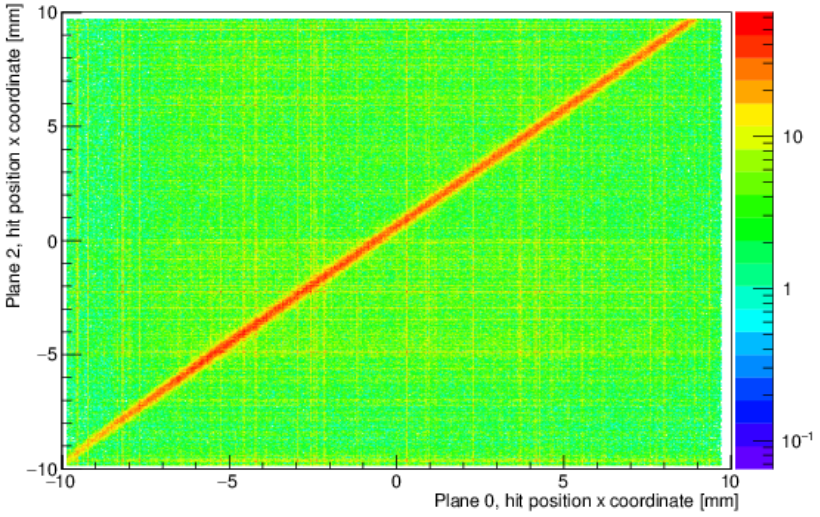

Figure 7.11: Comparing the x coordinates of hit positions on sensor planes 0 and 2 shows a visible correlation band, i.e. good correlation between both sensors. A grid of entries away from the correlation band indicates hits caused by pixels with a high noise.

telescope planes is then plotted for each sensor plane. The peak of the offset distribution is then used to correct the initially guessed telescope positions.

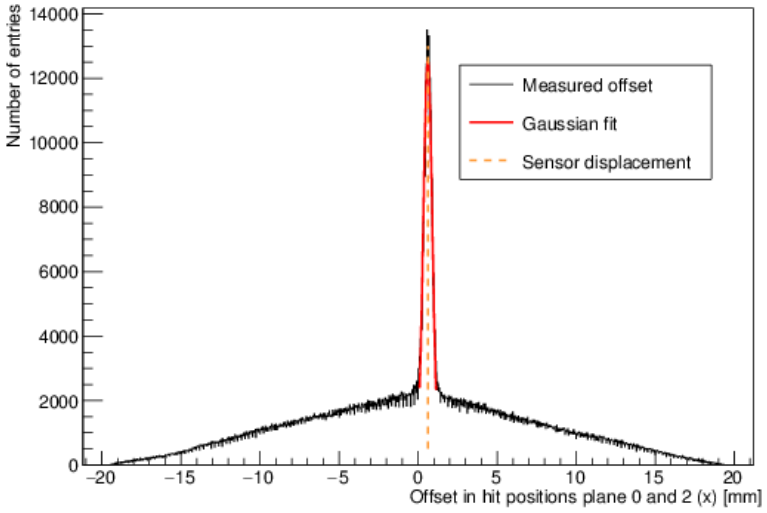

Figure 7.12: Offsets (i.e. difference of the x-coordinates) of the hits in telescope planes 0 and 2. The distribution shows a distinct peak from actual tracks as well as a broader distribution caused by noise. The centre of the peak provides a good assumption for the offset between telescope planes 0 and 2 in x (here: 0.62 mm).

7.2.3.4 Track finding

Hits are combined into tracks using the following procedure:

1. Doublet finding
   Hits in the first (last) three telescope planes are used by combining hits in telescope planes 0 and 2 (3 and 5). If hits are within ±1 mm in x and y (i.e. maximum total distance ±1.4 mm), they are combined to a doublet.

2. Triplet finding
   Doublets found in the first step are extrapolated through the telescope between the two planes used for the doublet search. If a hit in telescope plane 1 (4) can be found within ±0.02 mm (in x and y) of the extrapolated doublet path from planes 0 and 2 (3 and 5), a triplet is formed from hits in planes 0, 1 and 2 (3, 4 and 5).

3. Triplet matching
   Triplets from the first and last three telescope planes are extrapolated to the centre of the beam telescope and compared. If the extrapolated tracks from exactly two triplets intersect within ±0.02 mm in x and y and their slopes agree within ±0.1 rad in x and y, they are combined to a track through the whole telescope. If more than one triplet can be matched to another one in the same event, the event is rejected.

4. Track matching to DUT
   A track is matched to a sensor hit, if the extrapolated track position on the sensor falls

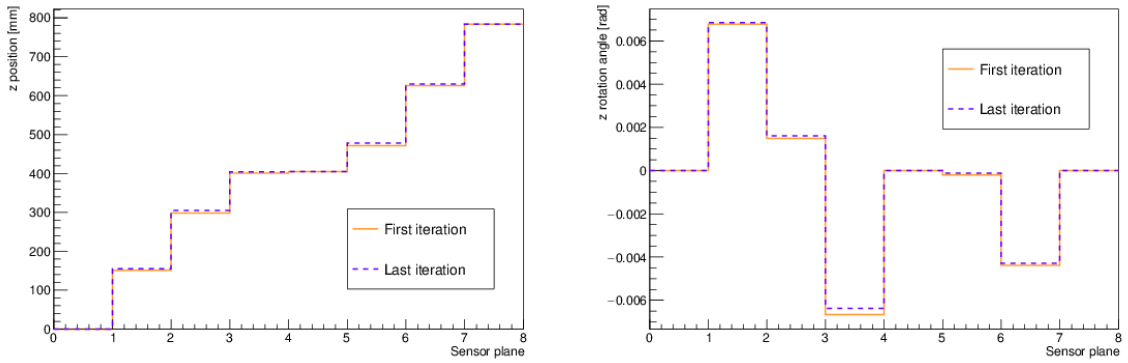

(a) z positions of telescope planes (sensors 0 to 2 and 5 to 7) and sensors under investigation (3 and 4) calculated from tracks created using a General Broken Lines algorithm.

(b) z rotation angles of telescope planes (sensors 0 to 2 and 5 to 7) and sensors under investigation (3 and 4) calculated from tracks created using a General Broken Lines algorithm.

Figure 7.13: z positions and z rotation angles of telescope planes and sensors under investigation, calculated from tracks in 10,000 events using a General Broken Lines algorithm. Rotation angles are largest for the sensor under investigation glued down by hand (sensor 3). z positions show small improvements between the first and last iteration.

within $\pm 0.15\,\mathrm{mm}$ of the sensor strip position in x, i.e. twice the strip pitch. Since strip sensors with only one row of strips were used, no criterion was applied on the position in y.

7.2.3.5 Fine Alignment

After the coarse alignment step, which uses only hit information, a fine alignment step was performed using 10,000 of the obtained particle tracks.

The reconstructed tracks are used to perform a fine alignment of telescope planes and DUT by calculating shifts in x, y and z as well as rotation angles for all sensor planes (see figures 7.13a and 7.13b). The alignment process was applied iteratively until the uncertainties of the alignment were larger than the computed corrections.

In order to judge the success of the alignment, two distributions were of main interest: $\chi^2/N_{\mathrm{d.o.f.}}$ of tracks and residuals of sensors (see figures 7.14a and 7.14b). Residuals on DUTs are computed by constructing the track without a hit on the sensor in question and extrapolating it to the sensor, where the residual is calculated from the theoretical and actual hit position. By omitting hits in the first and last sensor plane, the track length available for the extrapolation is reduced. The residuals for the first and last telescope plane are larger than for telescope planes in between, because for the latter tracks are extrapolated through planes in front of and behind the plane in question.

The alignment step and update of the gear file, which were repeated for each data run, conclude the analysis of telescope data.

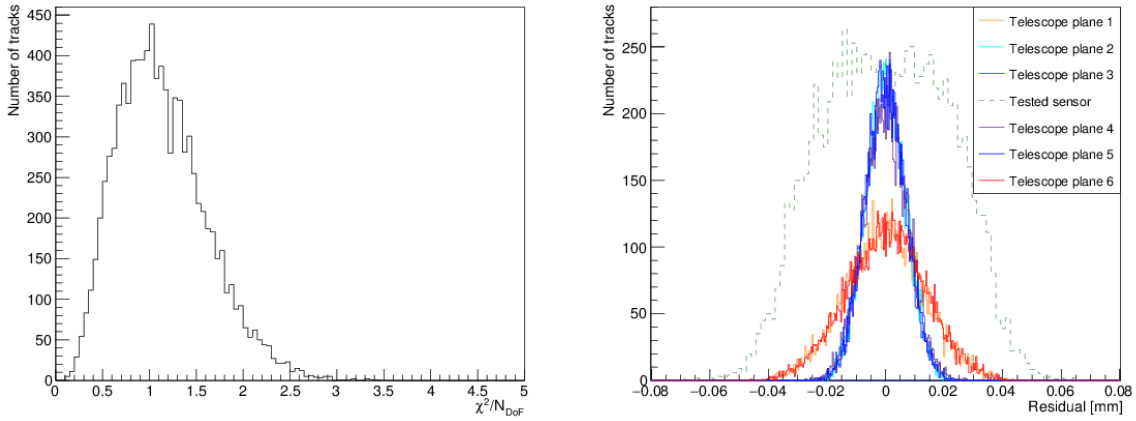

(a) Distribution of $\chi^2/N_{\text{d.o.f.}}$ for tracks from 100,000 events, added up from individual plane χ^2 contributions. The distribution is centred around 1, indicating a successful track reconstruction.

(b) Residuals of different sensors in a testbeam setup, calculated from tracks in 100,000 events. As expected, the strip sensor with a larger strip pitch has larger residuals than the pixel sensors.

Figure 7.14: $\chi 2/N_{\text{d.o.f.}}$ distribution and residuals indicating a successful alignment step.

7.2.4 Event Reconstruction

Using the obtained alignment information, all events in a data run were reconstructed and combined to a ROOT event tree [87] containing:

- event information
- track information (extrapolated position on the sensor under investigation)
- cluster information (responding channels and reconstructed charges)

These ROOT trees were used for subsequent data analysis.

7.3 Results

While clusters were reconstructed using looser cluster cuts (see section 7.2.1), in order to be considered for subsequent data analysis clusters had to pass the standard signal-to-noise ratio cuts (seed cluster cut SNR > 5 and neighbour cluster cut SNR > 3, noise as determined in pedestal scans).

After charge collection efficiencies of sensors with and without glue had not shown large discrepancies (see section 6.8), the track position information associated with a particle hit was used to calculate cluster charges in areas with and without glue. For these maps, average cluster properties were calculated in $50 \times 50\,\mu\text{m}^2$ bins in order to map the full sensor surface, covering areas with and without glue. Figure 7.15a shows a picture of the sensor partially covered with glue. Figure 7.15b shows a map of the average cluster charge. The sensor area was found to

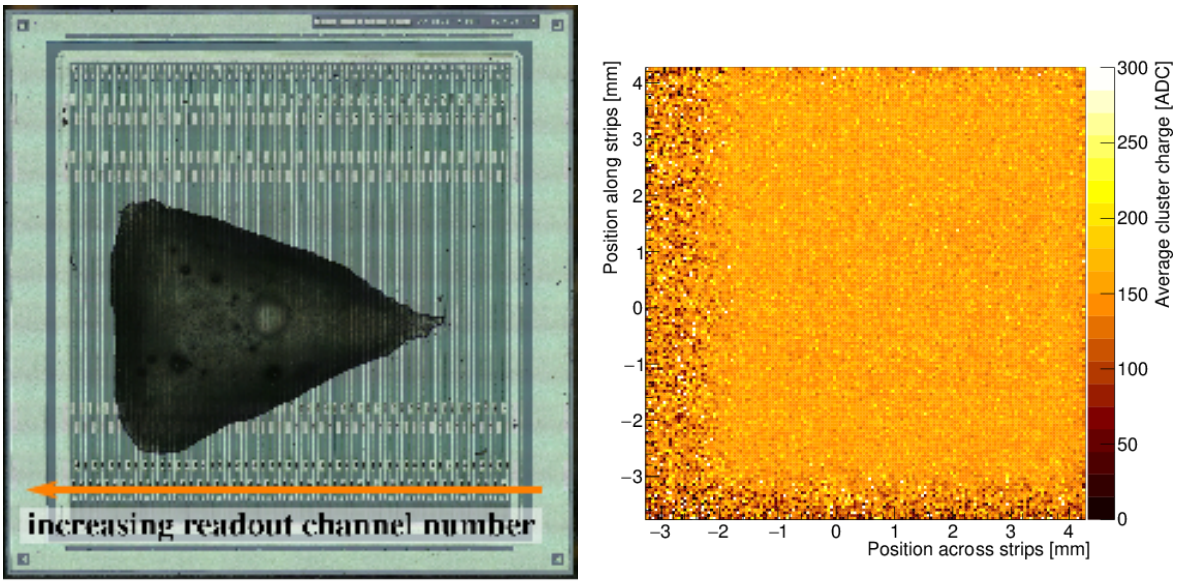

(a) ATLAS07 miniature sensor with Epolite FH-5313

(b) Cluster charge map of miniature sensor with glue

Figure 7.15: Average cluster charges reconstructed for different positions on an ATLAS07 miniature sensor did not show differences for sensor areas with and without glue. Due to the orientation of the sensor with respect to the telescope planes, maps are mirrored compared to the sensor image.

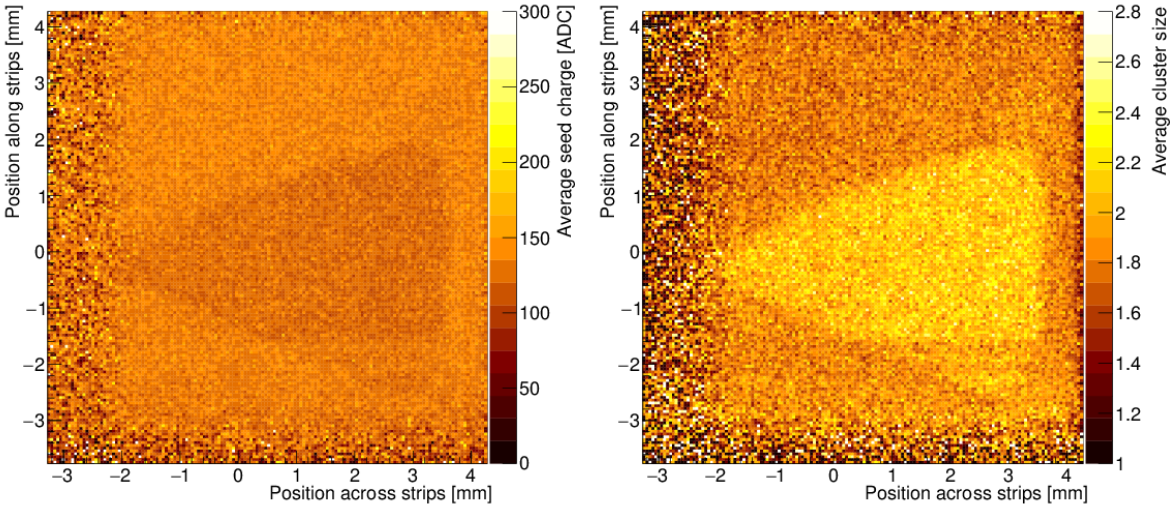

(a) Map of average seed cluster charges

(b) Map of average cluster sizes

Figure 7.16: Maps of cluster parameters reconstructed on an ATLAS07 miniature sensor: while the total cluster charge distribution is uniform (see figure 7.15), average cluster size and seed charge are different in sensors with and without glue.

show areas with large fluctuations at the bottom and left edge, which can be explained by the sensor mounting: since the opening in the sensorboard is smaller than the active sensor area and the sensor was not placed centred on the board, part of the active sensor area is blocked by the sensorboard. The larger amount of material leads to increased scattering and thus a lower fraction of reconstructed tracks, which results in lower statistics and thus larger fluctuations.

Areas with glue did become visible when different cluster characteristics were mapped: both average seed cluster charge (see figure 7.16a) and cluster size (see figure 7.16b) showed discrepancies between areas with and without glue. Areas with glue were found to have a lower seed charge and larger cluster sizes than blank sensor areas. Since the total cluster charge did not show differences between sensor areas with and without glue, these distributions indicate that seed charges were distributed over a larger width and thus more strips, but the total cluster charge was conserved.

The distributions of cluster sizes were compared for sensors with and without glue (see figures 7.17a and 7.17b). It was found that while the blank sensor had a larger fraction of 1-strip clusters than the sensor with glue, the distribution of 2-strip clusters was similar for both sensors. Fractions of clusters with three or more strips were larger for the sensor with glue, with fractions more than doubling in large regions of the charge distribution range. It should be noted that charges of a traversing particle being spread over more than two sensor strips is only expected for particles travelling more than the strip pitch while traversing the sensor volume, corresponding to an angle of about 14 °. A track angle of 14 ° is unlikely in the used electron beam and would lead to particles moving out of the window of MIMOSA sensors, making the

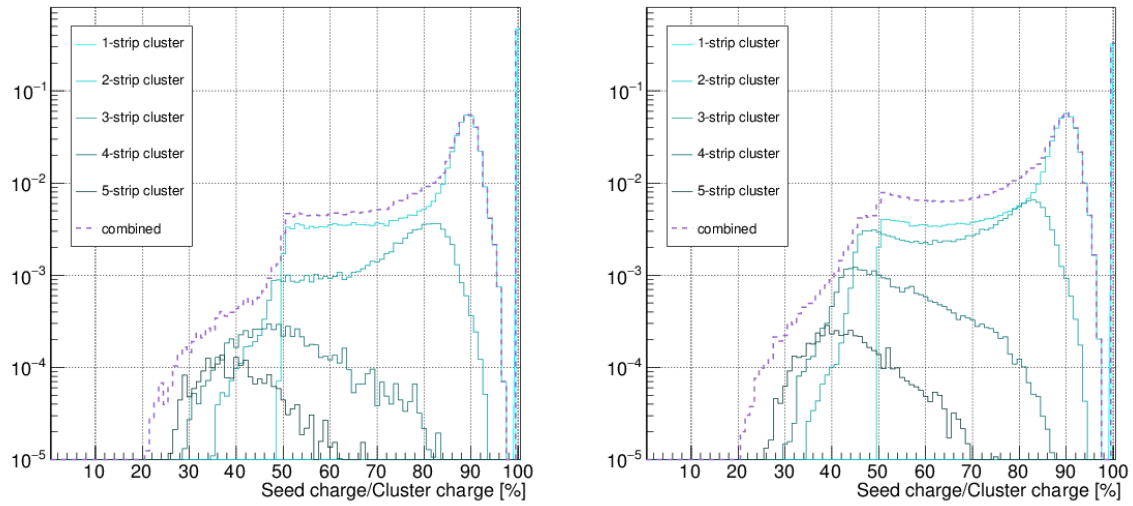

(a) Cluster distribution for a sensor partially covered with glue

(b) Cluster distribution for a blank ATLAS07 miniature sensor

Figure 7.17: Distribution of cluster sizes and fraction of the seed charge from the overall cluster charge. While the distribution of 2-strip clusters is similar for both sensors, cluster sizes with more than 2 strips occur more often on the sensor with glue.

existence of reconstructed tracks impossible (due to doublet selection criteria). Clusters with more than two strips are thus more likely to be caused by noise fluctuations than by charge being distributed over three or more strips. An increased number of larger clusters on sensors with glue thus indicates that the presence of glue on the sensor increases the likelihood of neighbour readout channels to see fluctuations above the $3\,\sigma$ signal-to-noise ratio.

Probe station measurements have shown that sensors with glue tend to have larger inter-strip capacitances than blank sensors (see section 5.5). Larger inter-strip capacitances increase charge sharing between adjacent strips, which would lead to increased cluster sizes and potentially reduce the seed charge. However, an increased inter-strip capacitance would be expected to affect a whole sensor strip independent of the hit position of a particle, whereas the effect was only observed locally where glue had been applied to the sensor. Allpix simulations [132] of the testbeam setup have shown that the amount of glue applied to the sensor surface would not be sufficient to produce enough scattering or secondary tracks to explain the increased cluster size [133].

A follow-up investigating possible causes for the observed increase in cluster sizes will be presented in the following chapter 8.

Comparing the maps of average seed charges and cluster sizes (see figures 7.16a and 7.16b) with the sensor layout (see figure 7.15a), it is interesting to note that bond pad areas are visible in maps of both average cluster size and seed charge. This observation supports an indication from a different measurement suggesting that the sensor behaviour in bond pad areas is different

from sensor areas without bond pads (see section 9.3.1). Measurements studying this effect will be presented in chapter 9.

7.4 Conclusion

Studies of sensors with and without glue in an electron beam have shown that the collected charge is independent of the presence of glue. Other cluster characteristics did show a dependence on the presence of glue: on average, cluster sizes were larger and cluster seed charges were lower.

It should be noted that, in the ATLAS ITk, sensors will be read out with a binary readout chip, which will be operated at a threshold corresponding to a signal-to-noise ration > 10. The increased cluster sizes observed using an analogue readout system with a much lower signal-to-noise ratio cut will thus not be observed in the detector.

Glue on sensor surfaces was thus found to affect cluster distributions on a sensor, but not its tracking performance.

8 Investigation of Charge Cluster Widening by Glue

Sensors with glue (unirradiated) had been found to produce larger cluster sizes than blank sensors both in β-source measurements (see section 6.7.2) and electron beam measurements (see section 7.3). Initially considered explanations were inconsistent with the results:

- Larger coupling between adjacent strips due to an increased inter-strip capacitance after gluing would lead to more charge sharing. But while unirradiated sensors with glue did show a cluster size increase, sensors with glue after irradiation, for which an increased inter-strip capacitance was also measured, did not show increased cluster sizes.

- Production of secondary particles diverging from the primary particle, leading to several particle tracks traversing the sensor and thus the readout of charge in a larger number of strips. Secondary particles could explain increased cluster sizes seen in an electron beam, where sensors were facing the beam (see figure 8.1a), but not in the used β-source setup, where sensors were not facing the β-source (see figure 8.1b). In the latter configuration, secondary particles would move away from the sensor and thus could not produce larger charge distributions (see figure 8.1).

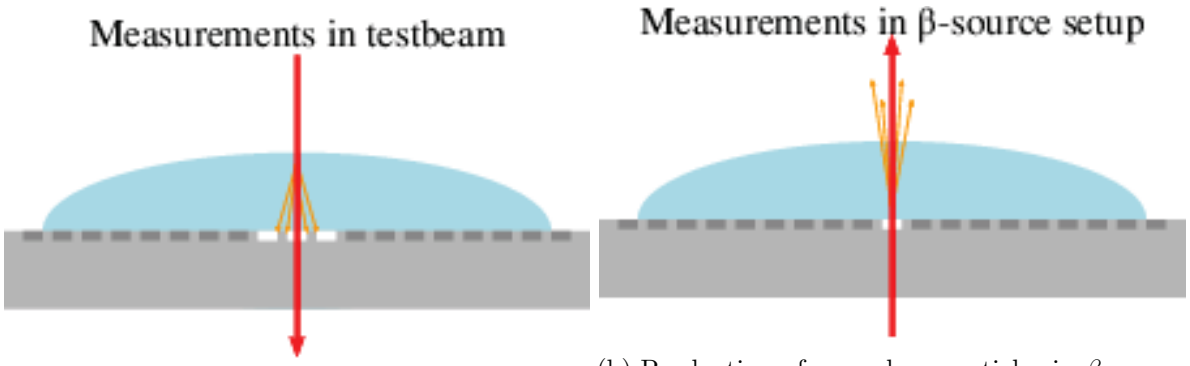

(a) Production of secondary particles at testbeam

(b) Production of secondary particles in β-source setup

Figure 8.1: Paths of electrons (red) through glue (blue) and sensor (grey) in a testbeam and a β-source setup (not to scale). While secondary particles (orange) produced in testbeam tests (left) could theoretically lead to larger clusters, the sensor orientation in the β-source setup (right) would not lead to larger cluster sizes caused by secondary particle tracks.

Testbeam studies had shown (see section 7.3) that glue affects the sensor performance only in sensor regions where glue is present, indicating a localised effect.

During the preparation of the sensor samples, glue was found to be fluorescent under UV light (see figure 8.2). If the energy of UV photons is sufficient to produce fluorescence in glue,

Figure 8.2: ATLAS07 miniature sensor with DYMAX 3013 glue exposed to UV light: the glue becomes fluorescent under UV light exposure.

passing electrons in both β-source and testbeam measurements can be expected to cause similar effects. Light emitted via fluorescence could match several observations:

- Light on the surface of a biased silicon sensor would result in a photo current, that would be registered as a signal. While the energy deposition from fluorescent light can be expected to be small enough to not affect the overall cluster charge, it could lead to neighbour channels' noise fluctuations exceeding a signal-to-noise ratio of 3 more frequently, thus explaining an increased cluster size.

- Fluorescence light does not have a preferred direction and would thus have the same effect independent of whether a sensor is facing electrons or pointing away from them.

- in bond pad regions, a larger fraction of the sensor surface is covered by aluminium due to the presence of bond pads (see section 2.3). Since metal reflects light and thus prevents it from causing photo currents within the sensor volume, the presence of bond pads would be expected to reduce a cluster size increase caused by light inducing a photo current.

- sensors with glue were found to have increased cluster sizes compared to sensors without glue before irradiation, but not after irradiation. Since glue was found to change during

irradiation and change in consistency and colour, it can be assumed to produce and transmit light from fluorescence different than glue before irradiation.

In order to investigate whether fluorescence in glue could cause a signal in a sensor, a specific measurement setup was designed.

The findings presented here were also published in [134].

8.1 Measurement Setup for Glue Fluorescence Studies

Sensor signals produced by fluorescence can be expected to be much smaller than signals produced by traversing particles. A measurement studying whether fluorescence can cause hits being registered in a sensor thus had to be set up to provoke fluorescence in a glue layer on top of a sensor without causing direct sensor hits.

The measurement was thus planned to be conducted by directing a beam inside the glue layer parallel to the sensor surface (see figure 8.3). For a beam to only point at glue without also

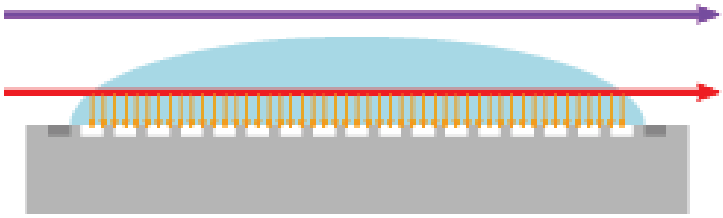

Figure 8.3: conceptual design to investigate signal production by fluorescence: by directing a beam into a glue layer parallel to the sensor surface (red line), fluorescence would produce light along the beam path, of which light reaching the sensor surface could cause sensor strips to register signals (white). This effect would occur only if the beam traverses the glue, not if it is positioned above the glue (violet line).

reaching the sensor and thus producing electron-hole-pairs, it has to have a sufficiently small beam diameter to be fully contained within the thickness of a glue layer. This requirement was met by a 15 keV X-ray beam provided by the Diamond Light Source, which can be focussed to a diameter $\mathcal{O}(\mu m)$ over a distance of more than 1 cm [135].

A measurement was thus set up, where a micro-focused X-ray beam was moved along the edge of a sensor and sensor signals were read out for each given beam position. By moving the beam above the sensor surface, it could be directed into the glue layer without also pointing at the sensor itself. Since the beam could not be visually aligned to be above the sensor surface, the sensor volume had to be found by mapping the area over which a sensor registered hits. 15 keV photons in silicon have an attenuation coefficient of $24.15\,\mathrm{cm}^{-1}$ [136], so that the intensity of an incoming beam is reduced by 51 % every 300 µm. This effect was used to divide the sensor under investigation into different measurement areas. Areas were defined with respect to a beam pointed at the sensor perpendicular to the strip orientation and parallel to the sensor surface (see figure 8.4):

Figure 8.4: Scheme of a fluorescence measurement of a strip sensor with glue (not so scale): a beam is pointed at the sensor perpendicular to sensor strips (dark grey). While strips at the sensor edge (yellow area) are expected to see hits while the beam is pointed at the sensor, photon absorption inside the silicon will prevent strips further away from the sensor edge from registering hits (violet area). Strips beneath glue (red area) are thus expected to see hits only when the beam is pointed at the glue and if fluorescence occurs.

- strips next to the sensor edge the beam was pointed at, which were expected to see hits while the beam was positioned on the sensor,
- strips in the centre of the sensor which were not expected to see hits from a beam, because of an exponential absorption of photons in the sensor volume,
- strips on the sensor side opposite of the incoming beam, which were covered with glue. Due to the absorption of photons from the beam in the sensor volume, these sensor strips were expected to see signals only from beam interactions with glue.

It should be noted that the sensor was positioned at an angle with respect to the incoming beam for a better understanding of the actual position of the beam on the sensor (see figure 8.5).

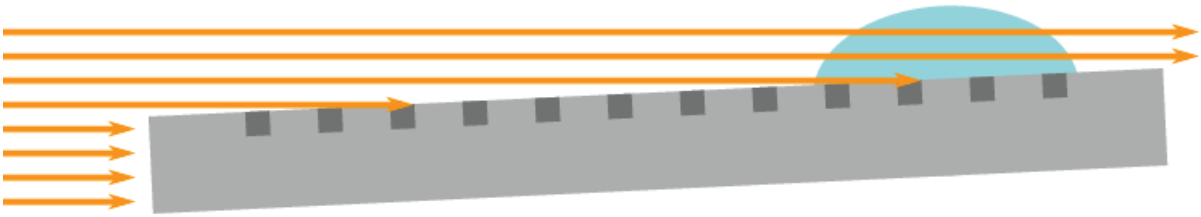

Figure 8.5: Scheme of fluorescence measurement on sensor showing the sensor rotation with respect to the incoming beam.

Measurements were performed using an ATLAS12 miniature sensor [137], which has the same sensor architecture as an ATLAS07 sensor with BZ3 architecture (see section 3.1) and was thus considered comparable enough. Since the active sensor area on all sensors is surrounded by several protective rings (see section 2.3), there is a distance of about 1.1 mm between the sensor edge and the first sensor strip. A 15 keV X-ray beam thus loses about 94 % intensity before reaching the first sensor strip. In order to reduce these intensity losses by absorption, sensors were diced slimmer by removing part of the active edge (see figure 8.6). Dicing was performed at the University of Glasgow using a diamond saw. Only 24 hours of beam time were available

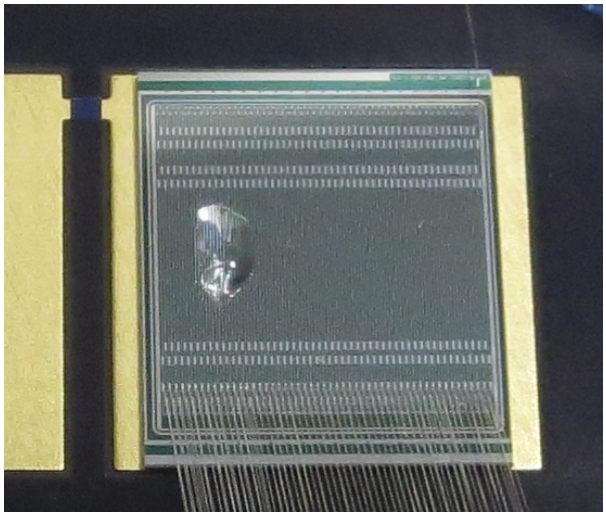

Figure 8.6: Sensor prepared for fluorescence measurements: sensor edges parallel to sensor strips were diced slimmer to reduce beam intensity loss inside the sensor. Glue was applied only to strips that did not register direct hits from a beam pointed at the sensor from the right side.

for fluorescence measurements, which were not sufficient to study the impact of all glues under investigation. Since only one glue could be tested, DYMAX 3013 was chosen for this study, as it showed the most fluorescence under UV light and the largest cluster size increase seen in β-source measurements and thus provided a worst case estimate. Glue was applied on the centre of 20 sensor strips up to a height measured to be up to 120 µm in a laser microscope.

Removing part of the active edge of the sensor led to both an increased leakage current and an early breakdown at a bias voltage of -200 V. The sensor was thus operated at a bias voltage of -150 V and hence under-depleted (full depletion of ATLAS12 sensors occurs between -350 and -400 V [36]). In order to reduce the leakage current during the measurement, the sensor was cooled down to -20 °C.

Sensor testbeam studies were conducted using an ALiBaVa readout system (see section 6.4). A sensorboard holding a sensor under investigation and a daughterboard were mounted on an aluminium plate as described in section 6.3.

Sufficient cooling of the sensors under investigation was achieved by mounting the detector boards on an aluminium plate cooled by Peltier elements. The warm side of the Peltier elements was thermally connected to an aluminium block, cooled through internal tubes attached to a chiller. The aluminium top plate holding detector board and daughterboard was positioned on the support plate with peltier elements using plastic screws. Figure 8.7 shows the thermal setup. The sensor was protected from light and electromagnetic fields by placing the setup in an aluminium box. Cables for high voltage, temperature and humidity, the data cable as well as tubes for gaseous nitrogen and chiller fluids connecting ALiBaVa daughterboard and motherboard were laid through dedicated feedthroughs in the box. In order to avoid the beam losing more intensity while traversing the wall of the aluminium box, openings were milled into

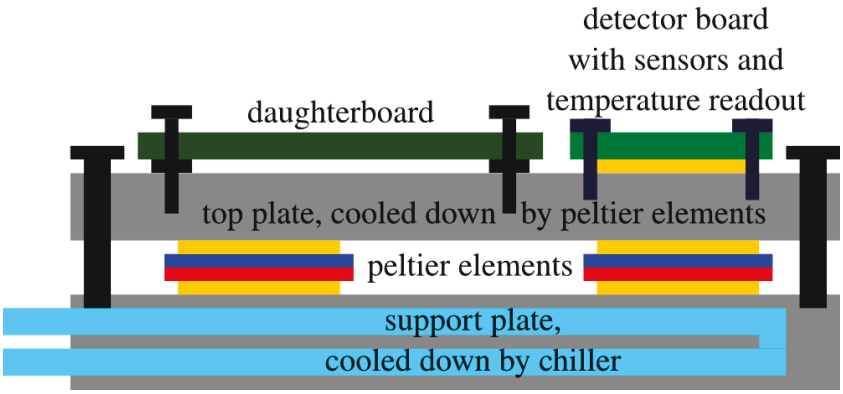

Figure 8.7: Schematic of the cooling setup used for sensor testbeam studies, heights not to scale. An aluminium support plate connected to a chiller is used to cool down peltier elements, sandwiched support plate, top plate and layers of thermally conductive pads. The top plate holds an ALiBaVa readout board, thermally insulated by plastic screws and plastic washers, and a detector board. Sensors on the detector board are thermally connected to the cooled top plate by thermally conductive paste and metal screws. The top plate is mounted on the base plate using plastic screws to avoid a thermal contact.

the walls of the aluminium box at the sensor position.

A new version of sensorboards was designed for this measurement (see figure 8.8): while the temperature sensor and HV filter on the version used for β-source setup measurements were positioned next to the sensor, they were moved to allow an unobstructed beam path to the sensor edge. Since the X-ray beam was not required to pass through the sensorboard, openings behind the sensors were no longer required and the sensors were placed on full gold pads to improve their cooling contact.

During the measurement, the box holding both sensorboard and ALiBaVa daughterboard was placed on an xy-stage with micrometer precision to allow precise movements between measurements.

8.2 Performed Scans for Glue Fluorescence Studies

X-ray photons at the Diamond Light Source arrive in intervals of 2 ns (corresponding to 900 bunches distributed over a synchrotron length of 562 m) at a frequency of 500 MHz [138]). The use of a composite refractive lens for a monochromatic beam reduced the photon flux to $1.2 \cdot 10^8\,\mathrm{s}^{-1}\mathrm{mm}^{-2}$, measured for the applied beam configuration using a calibrated diode with an uncertainty of $\pm 20\,\%$. This flux corresponds to 1.2 ± 0.2 photons arriving within 10 ns. Using a probability of each photon to react within a 300 µm detector volume of 51.5 % (see above) and the sampling rate of 25 ns of the ALiBaVa readout system, the probability for 0, 1, 2 or 3 photons to react with the sensor within a random 25 ns readout window can thus be estimated to be 24.2, 36.5, 25 and 10.6 % with an average number of 1.36 ± 0.34 photons per event.

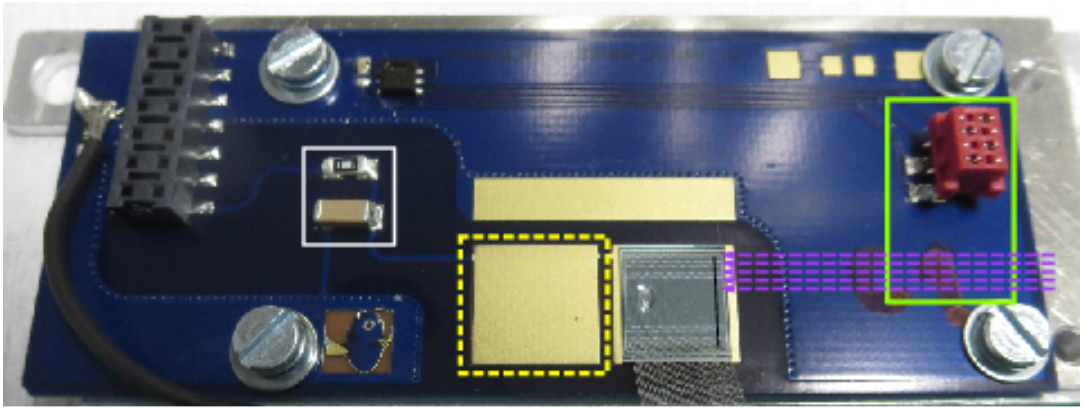

Figure 8.8: Sensorboard designed for fluorescence measurements using an ALiBaVa readout system: Openings in the sensorboard were closed for better support and cooling contact (yellow area), a second HV filter (white area) was removed and a temperature readout connector moved (green area) for an unobstructed beam path for a beam pointed at the sensor (indicated by violet lines) perpendicular to the sensor strip orientation (black).

Since X-ray photons arrived in random intervals and it was not possible to trigger on arriving photons, data was taken continuously using the ALiBaVa pedestal mode. Different from data taking with triggering information, data in pedestal mode is read out without consideration of timing information, so that the readout window can not be restricted to the signal peak and charge information is thus not reliable.

Data analysis is independent of the data taking mode and was performed as described in section 6.6:

- subtraction of pedestal data taken without beam
- common mode noise correction
- hit making

Different from previous data taking (see section 6.6), data was not clustered and only hits were counted.

At the photon energy used for these measurements, X-ray photons in silicon react mostly via photoelectric absorption [139]: they are fully absorbed by an electron of a silicon atom, which afterwards has an energy of 15 keV and produces electron-hole-pairs in the depleted silicon. The input charge created by one 15 keV photon can thus be estimated to be:

$$\frac{15\,\text{keV}[\text{photon energy}]}{3.6\,\text{eV}[\text{energy per electron-hole-pair production}]} = 4.167\,\text{electron-hole-pairs} \tag{8.1}$$

per absorbed photon. For the measurement temperature and ALiBaVa daughterboard in use, 4,167 electrons correspond to a most probable value of about 29 ADC. A high channel input

noise was measured during the measurement (see below) of up to 17 ADC, which was attributed to insufficient shielding. The high noise and low input charge required a modification of the seed cut, which determined whether a read out charge was considered a hit or not. For this measurement, the signal-to-noise ratio cut thus had to be reduced to 1. The ALiBaVa data analysis was performed as explained in section 6.6.

Scans were performed by moving the beam along the 300 µm sensor edge and 200 µm above in steps of 50 µm with 200,000 events being taken at each beam position.

The height range covering the sensor volume was found by visually aligning the beam using a positioning laser and performing a scan over a distance of 1.7 mm in steps of 0.1 mm (see figure 8.9). Hits were seen inside the sensor volume at beam positions of -0.5 and -0.6 mm as

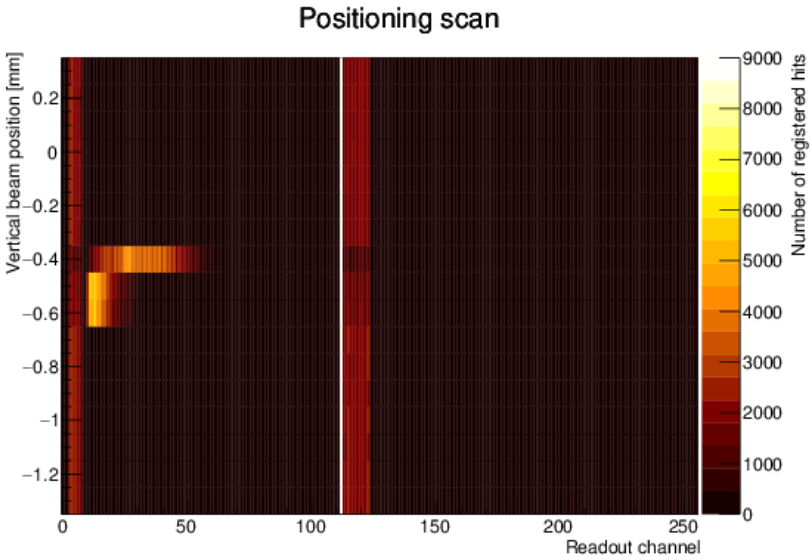

Figure 8.9: Hit map recorded in positioning scan for fluorescence measurements: the first bonded channels (beginning at channel 10) show hits for beam positions -0.6 mm and -0.5 mm, showing the expected decrease towards higher channel numbers. At a beam position of -0.4 mm the beam points at the sensor surface, leading to hits being registered in about 50 readout channels. Unbonded channels next to bonded channels have a high noise, leading to hits being registered over the full scan range (e.g. channels around 120).

well as hits on the sensor surface at beam position -0.4 mm. The scan was thus set up to cover beam positions of a height range from -0.75 to -0.25 mm in steps of 25 µm. After completing a scan over the full sensor height, the beam was moved along the strip in steps of 200 µm in order to study sensor regions both with and without glue.

The initial scan showed a notable pattern of readout channels alternately collecting more and fewer hits (see figure 8.9, most notably in hits on the sensor surface). This observation was matched by the readout channel noise distribution (see figure 8.10). A similar effect had been studied for detector modules with similar wire bonding patterns, where it was found

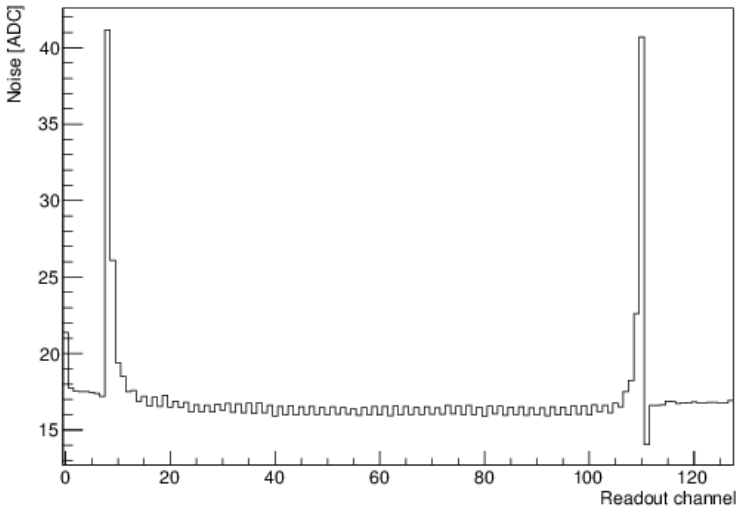

Figure 8.10: Noise of readout channels in an ALiBaVa setup used for fluorescence measurements. Channels connected to a sensor (from about 10 to 110) show alternately higher and lower noise. At the border between bonded and unbonded readout channels, noise peaks are registered due to the modified grounding scheme of the sensorboards in use (see section 6.4.5).

that wire bonds arranged in two layers lead to a higher noise in channels connected to the top layer of wire bonds [140]. Since top layer channels are known to be more likely to see signals from surrounding electromagnetic fields, more hits in the corresponding readout channels are expected as a result.

8.3 Results of Glue Fluorescence Scans

A detailed scan at the same sensor position used for the positioning scan allowed to identify different sensor regions. Figure 8.11 shows hits registered for beam positions within the sensor volume. As expected, channels at the sensor edge closest to the beam show the highest number of hits. Due to absorption, the incoming photon flux decreases exponentially within the sensor, leading to an exponential decrease of registered hits. The attenuation coefficient determined from an exponential fit is $21.4 \pm 0.2\,\mathrm{cm}^{-1}$, which is reasonably close to the nominal value of $24.15\,\mathrm{cm}^{-1}$ [136].

The sensor surface area was located by comparing hit patterns: within the sensor volume, hits showed a exponential decrease towards higher channel numbers (see figure 8.11a), whereas on the sensor surface, the maximum of registered hits was shifted towards higher channel numbers. Figure 8.12 shows a hit map for beam positions on the sensor surface. Assuming that channels directly pointed at by the beam see the maximum number of hits for a given beam position, the sensor surface can be mapped by locating the beam position returning the highest number

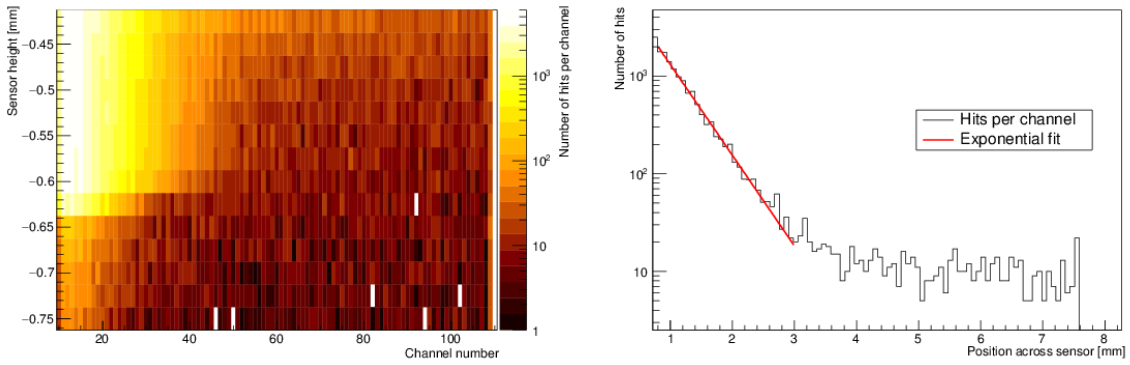

(a) Hit map for beam positions below the sensor surface

(b) Exponential decrease of photons within the sensor volume

Figure 8.11: Hits registered within the sensor volume from a beam pointing at the sensor edge. The hit map (left) shows hits within the depleted sensor volume, with a lower hit rate in the undepleted sensor volume. For a given beam position, an exponential decay of photons within silicon leads to a corresponding exponential decrease of registered hits (right).

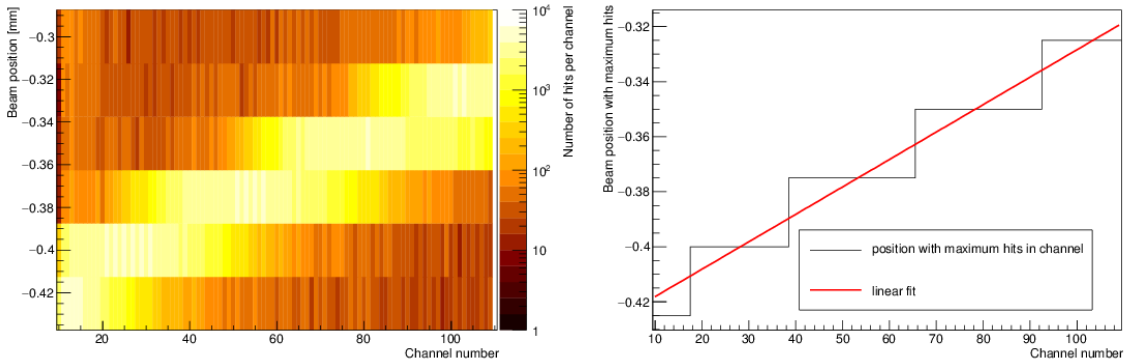

(a) Hit map for beam positions pointing at the sensor surface, for an example beam position at $x = -10.8\,\text{mm}$

(b) Beam positions with maximum hit number for each sensor channel for an example beam position at $x = -12\,\text{mm}$

Figure 8.12: Hits registered from an X-ray beam pointed at the surface of a tilted sensor (left). By finding the beam position resulting in the most hits read out in each channel (left), the tilt angle of the sensor could be determined by applying a linear fit.

of hits in a given channel. By fitting positions with maximum hit numbers (see figure 8.12b), the tilt angle of the sensor was calculated to be $0.76 \pm 0.16\,^{\circ}$. This angle agrees well with the mechanically set angle of $0.5\,^{\circ}$ considering the unknown flatness of the used xy-stages and jig are taken into account.

After identifying the location of the sensor with respect to the beam, the obtained hit maps were compared for indications of fluorescence (see figures 8.13a-8.13d). It was found that channels did register hits when the beam was pointed at glue located on top of the corresponding sensor strip. While, due to noise fluctuations, several sensor strips showed hits while the beam was positioned above their surface, sensor strips with glue registered systematically more hits.

The effect was visualised by calculating the average number of hits read out by each channel for all beam positions above the surface of that channel (see figure 8.14a). Mapping hits above the sensor surface showed that, where glue is present, a sensor registered additional hits. In general, the number of hits registered for beam positions above the sensor surface was small compared to the number of hits registered when the beam was directed at the sensor.

Two additional observations should be mentioned: for beam positions above the sensor surface, channels at the sensor edge registered more hits than higher channel numbers (see figure 8.15a). Similar to hits within the sensor volume, the number of hits decreased towards higher channel numbers. Beam positions on or below the sensor surface resulted in more hits registered by channels below glue (see figure 8.15b). Both effects can be explained by a contamination of the beam: for a beam energy of 15 keV, the third harmonic contamination occurs at 45 keV with a lower intensity than the primary beam [141]. While the 15 keV beam is micro-focused where the sensor is mounted, the focus point of 45 keV photons is at a larger distance and 45 keV photons have a radius of about 550 µm at the position of the sensor. A large 45 keV beam with low intensity matches the observed hit map patterns (see figures 8.15c and 8.15d). 45 keV photons have a lower attenuation coefficient than 15 keV photons ($1.33\,\mathrm{cm}^{-1}$ compared to $24.15\,\mathrm{cm}^{-1}$)) and are thus absorbed later in silicon. Due to the unknown intensity of 45 keV photons in the beam, their contribution to registered hits is unknown.

Comparing cluster charges for different positions of the beam with respect to the sensor surface shows similar charge distributions (see figure 8.16) for beam positions inside and below the depleted sensor volume, on the sensor surface and inside glue. Hits produced from beam hits inside the undepleted and depleted sensor volume are expected to have different cluster charges, but did show similar cluster charge distributions differing mainly in number of registered hits. Hits on and above the sensor surface show maxima at lower cluster charges, but due to an unknown contribution of 45 keV hits inside the depleted sensor volume, the charge distribution is not representative of charges from fluorescence. Hence, this study does not allow a quantitative analysis of input charge added from fluorescence in glue.

It should be noted that the mechanism resulting in additional sensor hits below glue is not fully understood. Pictures from a raspberry pi camera, which was mounted in an opening of the testbeam box directly facing the sensor under investigation, did not show any indication of visible light being produced. It is thus unlikely that 15 keV produced visible light as observed under exposure to UV light. It is considered more likely that the additional input signal was caused by X-ray fluorescence, where an X-ray photon excites an electron on an inner orbital of an atom and electrons on outer orbitals move to inner orbitals to fill the produced gap. During

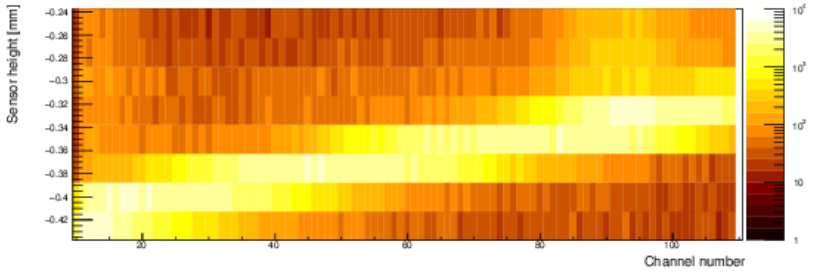

(a) Hit map for first beam position along the sensor strip ($x = -12\,\text{mm}$)

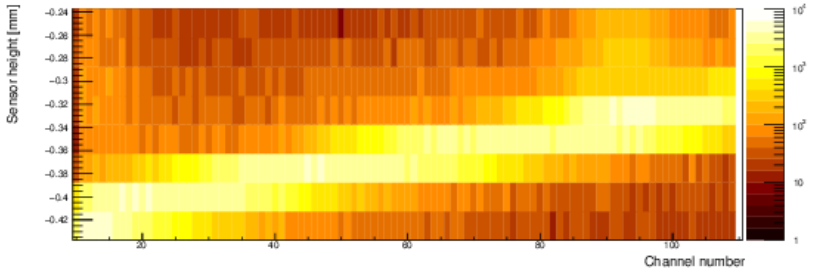

(b) Hit map for second beam position along the sensor strip ($x = -11.8\,\text{mm}$)

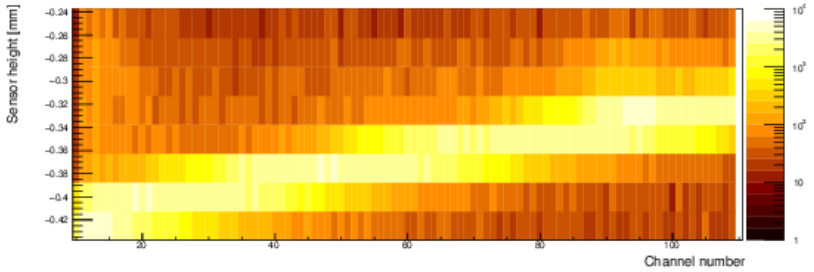

(c) Hit map for third beam position along the sensor strip ($x = -11.6\,\text{mm}$)

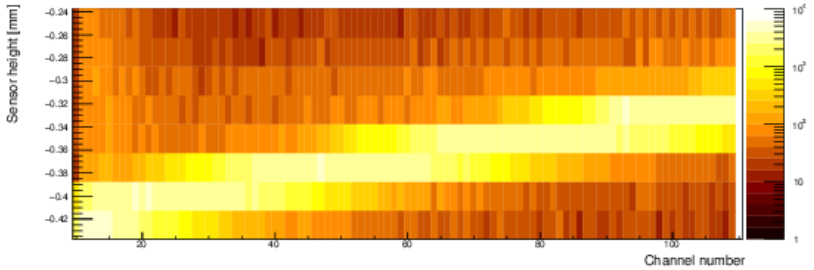

(d) Hit map for fourth beam position along the sensor strip ($x = -11.4\,\text{mm}$)

Figure 8.13: Hit maps for different beam positions along sensor strips: at the first and second beam position (figures 8.13a and 8.13b), channels between 80 and 110 (position of glue dot) see hits at beam positions above the sensor surface (above -0.3 mm). Hit maps further along the sensor strips (figures 8.13c and 8.13d) do not show comparable hit patterns above the sensor surface.

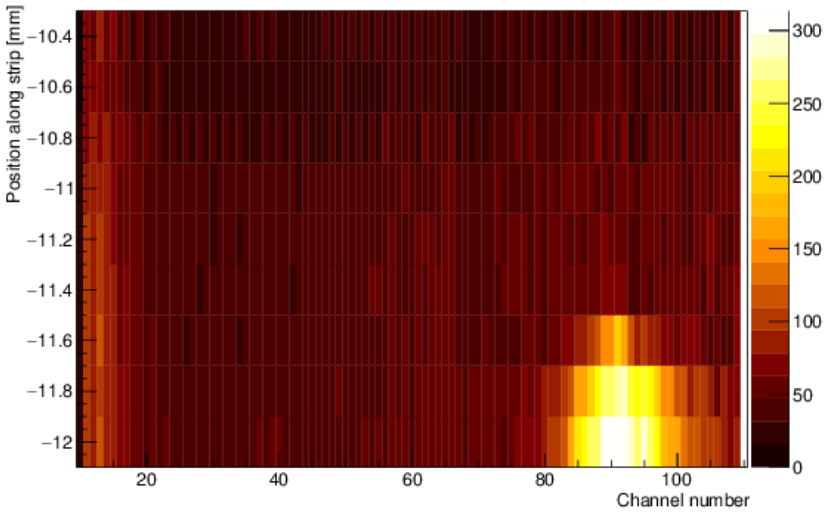

(a) Average number of hits per channel and beam position along sensor strips, averaged over all beam heights above the sensor surface

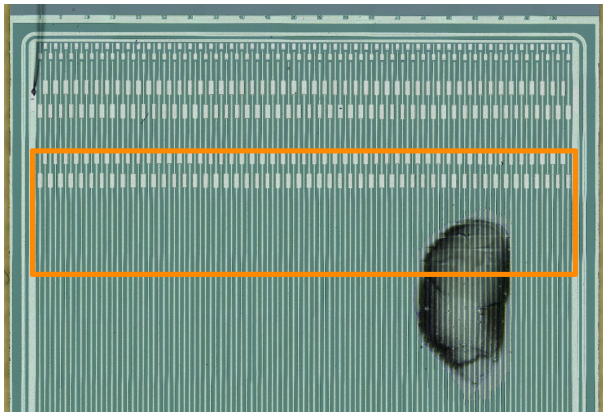

(b) Approximate sensor surface area corresponding to the obtained hit map in figure 8.14a

Figure 8.14: Hit map parallel to the sensor surface showing sensor hits registered for beam positions above the sensor surface. Hits on the sensor surface (see figure 8.14a) match the location of glue on the sensor (see figure 8.14b). The sensor image has been mirrored for better comparability with the hit map.

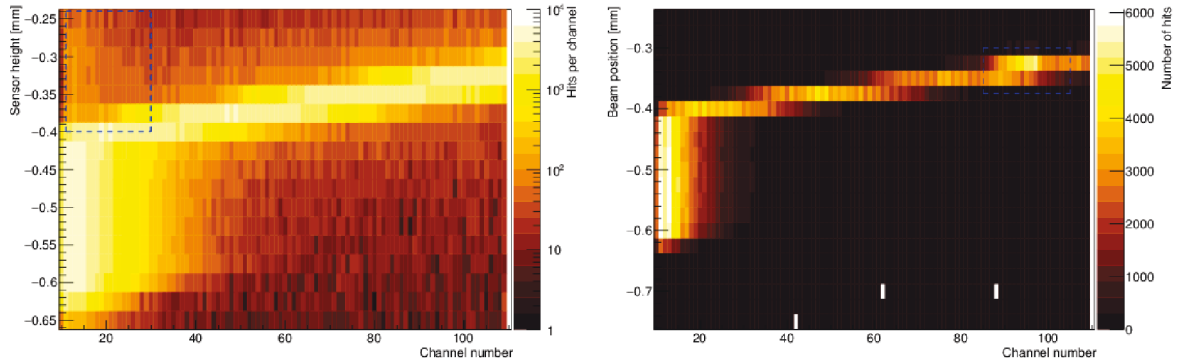

(a) Hit map for a sensor: channels at the sensor edge show higher numbers of hits (dashed blue line) if the beam is positioned above the sensor surface

(b) Hit map for a sensor: channels below a glue dot show higher numbers of hits (dashed blue line) if the beam is positioned below the sensor surface

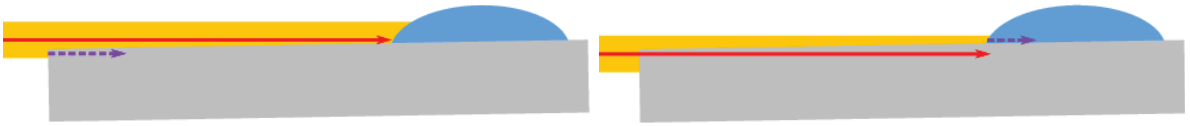

(c) A wide beam (orange) surrounding the monochromatic beam (red) can lead to hits in strips at the sensor edge (violet) if the beam is positioned above the sensor surface

(d) A wide beam (orange) surrounding the monochromatic beam (red) can lead to additional hits (violet) in strips below glue if the beam is positioned below the sensor surface

Figure 8.15: Illustration how a wide beam background affects the hit map of a sensor: independent of the beam position, the beam halo leads to additional hits in strips at the sensor edge as well as strips below a glue dot.

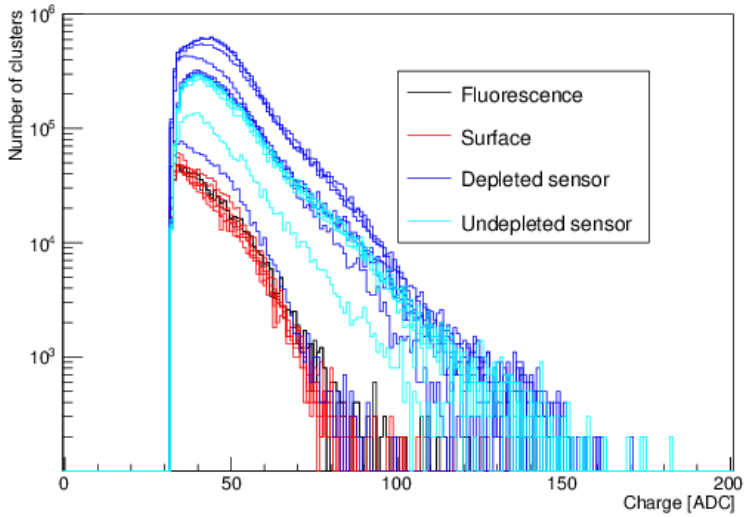

Figure 8.16: Charge distributions of clusters for different beam positions, categorised according to the beam position with respect to the sensor. Hits within the sensor volume show similar distributions, differing in number of clusters depending on the sensor depletion depth. Clusters from surface and fluorescence hits show charge distributions shifted to lower cluster charges.

this process, photons with an energy corresponding to the potential difference between both orbitals are emitted. X-ray fluorescence matches the effects observed in previous measurements:

- The emitted light does not have a preferred direction, hits would thus be registered independent of the orientation of the beam with respect to the sensor, as seen in β-source setup measurements and testbeam measurements (see section 7.3).
- Emitted light is registered as an input signal if it reaches the silicon surface, but, depending on its wave length, could be reflected by metal surfaces, such as bond pads. The presence of bond pads would thus counteract the effect of cluster size increases due to photons emitted in glue, as observed for the bond pad area of a miniature sensor with glue in a testbeam (see section 7.3).
- After irradiation, sensors with glue did not show increased cluster sizes. Since irradiation has been found to change the chemical composition of glue (see section 4.3), the production and transmission of photons in irradiated glue can be assumed to differ from unirradiated glue.

The measurement thus confirmed that emissions from glue have sufficient energy to be registered as hits in sensors.

An additional observation was made for hit maps parallel to the sensor surface (see figure 8.17 as an example). Whereas all previous hit maps were found to have alternately more and fewer

hits due to two rows of wire bonds (see section 8.1), hits for two beam positions showed a pattern of more hits in odd numbered channels (at $x = -10.4\,\text{mm}$) and more hits in even numbered channels (at $x = -10.8\,\text{mm}$), see figure 8.17. The beam position corresponding to

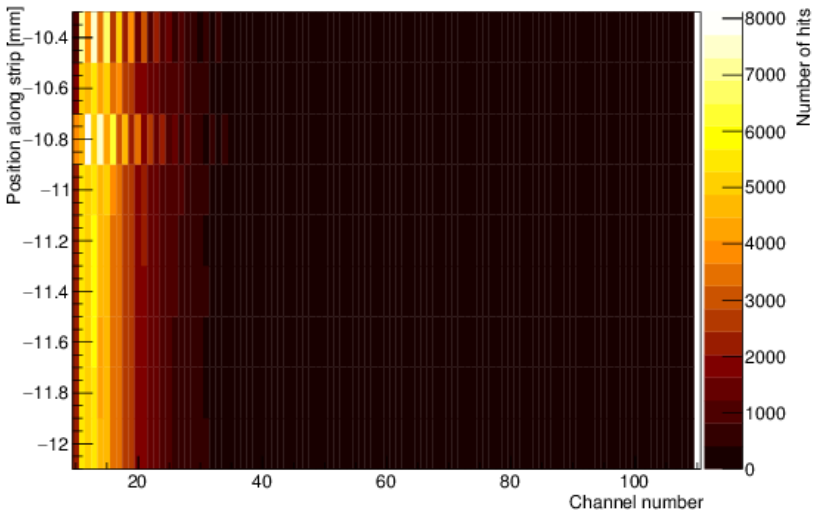

Figure 8.17: Hit map in a plane parallel to the sensor surface for a beam position pointing at the depleted sensor volume. For two beam positions along sensor strips, channels show more hits in even numbered channels (at -10.4 mm) and more hits in odd numbered channels (at -10.8 mm). The position and distance between measurement rows matches the positions of bond pads in the scanned area (see figure 8.14b).

these patterns match the positions of bond pads on the sensor. Given the length of a bond pad (200 µm), the chosen step size along sensor strips (200 µm) suggest that each beam position showing an unusual pattern matches the position of one row of bond pads. Numbers of collected hits thus suggested again that the presence of bond pads affects charge collection in a sensor. A detailed study investigating the sensor performance around bond pads will be presented in the next chapter.

8.4 Conclusions

A micro-focused X-ray beam was used to study whether radiation traversing glue could cause emissions registered as signals by a sensor. The measurement confirmed that a sensor registers hits if no charge is deposited by a direct beam. In setups with a beam pointed perpendicular at a sensor, the same effect could lead to additional hits in sensor strips next to the strip traversed by a particle and thus increase cluster sizes. Increased cluster sizes below glue on a sensor observed in electron beam tests (see section 7.3) can thus be attributed to radiation causing photon emissions from glue.

The measurement was not suited to determine the mechanism leading to photon emissions.

It should be mentioned that the cluster size increase found using an analogue readout system is not indicative of the performance of a detector module: the signal-to-noise ratio used for this data analysis is low compared to the threshold required to register a hit in a binary readout system (see section 9.2.1). Preliminary measurements of a prototype module in an electron beam showed a cluster size increase of 2 % in sensor regions with glue compared to sensor regions without glue [142].

9 Studying the Impact of Local Sensor Geometries in Testbeams

The silicon strip sensors investigated in these studies are treated as homogeneous area inside the bias ring. Each sensor strip is assumed to collect electrons over a width corresponding to the strip pitch along the whole strip implant. However, strip implants are not homogeneous throughout their length due to the necessity to attach wire bonds to sensor strips. Investigations into the homogeneity of silicon sensor strips were performed in X-ray and electron beam measurements in 2015 and 2016. The findings summarised here were also published in [135] and [143].

9.1 Geometrical Inhomogeneity of Silicon Sensors Strips

Wire bonds are needed to electrically connect each sensor strip to an ASIC readout channel (see section 2.2.3), requiring the addition of electrically conductive bond pads to the aluminium layer on top of each strip implant. The dimensions of these bond pads are defined by wire bonding necessities:

- a single bond foot (the area over which a wire bond is connected to a bond pad) has a width and length of up to $35 \times 120\,\mu m^2$ (see figure 9.1)
- a typical wire bonding wedge used for this application has a width of about $80\,\mu m$
- in case of wire bonding failures, further wire bonding attempts can be necessary, requiring a bond pad length sufficient to accommodate several bond feet

Based on these requirements, the bond pads were chosen to have an approximately rectangular shape of about $56 \times 200\,\mu m^2$, i.e. close to the strip pitch ($74.5\,\mu m/75.5\,\mu m$ for ATLAS07 and ATLAS12/ATLAS17 sensors, respectively).

With a strip pitch of $74.5\,\mu m$ and a bond pad width of $56\,\mu m$, the sensor can not accommodate bond pads on each sensor strip. Therefore bond pads are arranged in two rows, alternately on odd and even sensor strips (see figure 9.2). Below bond pads, the width of the strip implant is increased to cover the full bond pad area. P-stop implants, which for most of the length of strips are straight and at the centre between two neighbour sensor strip implants, are arranged around these bond pads, leading to varying distances depending on the position along the strip.

Since the sensor architecture in these areas is different from the standard sensor layout, a possible impact on the sensor performance was investigated.

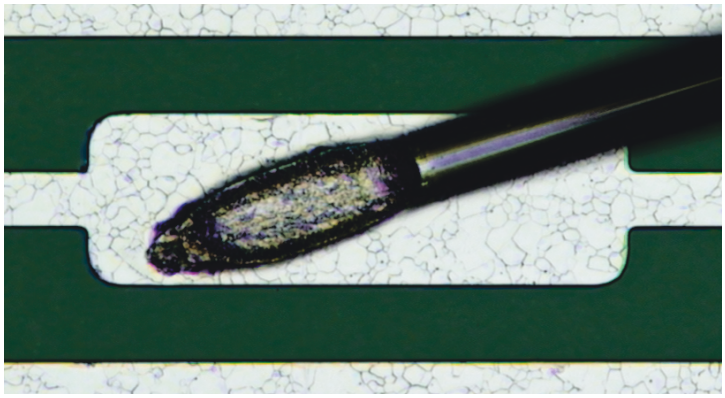

Figure 9.1: Laser microscope image of a wire bond foot on an aluminium bond pad on a dummy silicon sensor, from [143]. The bond wire (diameter 25 µm) is pressed down and thereby welded on to the bond pad, increasing its width on the bond pad to about 35 µm. The length of the wire bond footprint is about 120 µm. The bond foot is not aligned parallel to the bond pad orientation, requiring the bond pad to be wider than the expected width of the wire bond foot. The bond pad is longer than the bond foot to allow repeated wire bonding attempts, i.e. more than one bond foot on the same bond pad.

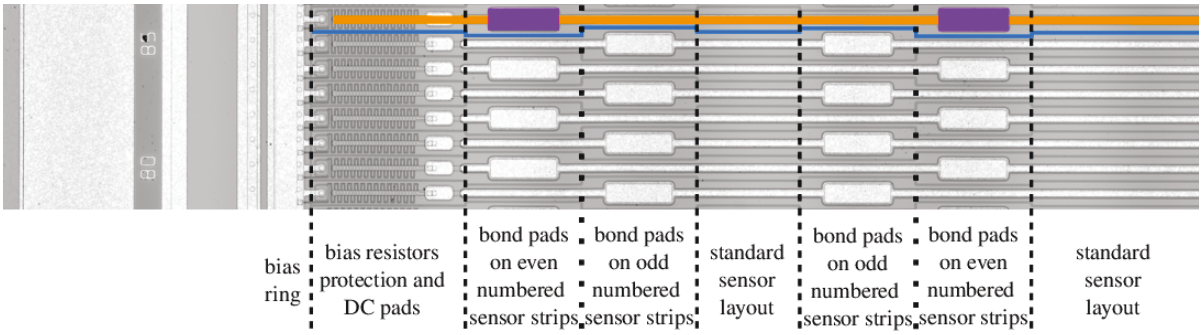

Figure 9.2: Laser microscope image of a miniature sensor showing bias ring, bias resistors and sensor strips (orange) with bond pads (violet), electrically separated by p-stop implants (blue). One complete row of bond pads, comprised of one row of bond pads on even numbered sensor strips and one row of bond pads on odd numbered strips, stretches over a length of 700 µm. Image from [143].

	Barrel module	End-cap module
Sensors	two ATLAS12 miniature sensors, $1 \times 1\,\mathrm{cm}^2$ with 104 strips each, strip pitch 74.5 µm	two trapezoidal sensors, about $3 \times 4\,\mathrm{cm}^2$ each) with 768 strips, arranged in two rows, each, strip pitch increasing with trapezoid shape
Hybrid	barrel hybrid, designed for ten ABC130 ASICs arranged in one row	end-cap hybrid, designed for twelve ABCN250 ASICs, arranged in two rows of six ASICs each
ASICs	three ABC130 ASICs	twelve ABCN250 ASICs

Table 9.1: Components of modules used for X-ray beam tests: ABC130 components were available in small quantities for barrel module geometry. For the end-cap module, only ABCN250 components were available.

9.2 Initial X-ray Beam Measurements

First measurements [135] were conducted at the Diamond Light Source using a micro-focused X-ray beam with a photon energy of 15 keV. Two silicon strip sensor modules, constructed to be as similar as possible to modules to be used in the ATLAS Inner Tracker with the components available at the time of construction (see table 9.1), were investigated. Since insufficient ABC130 ASICs were available for the construction of a full barrel module at the time, two miniature sensors, each requiring one readout chip, were wire-bonded to a barrel hybrid. An end-cap type sensor was studied using a full module prototype with ABCN250 ASICs [62]. With an X-ray beam size of 2.6×1.3 µm, significantly smaller than strip pitch (74.5 µm) and implant width (16 µm), the small beam diameter allowed to resolve a strip's response at different positions across its width.

9.2.1 Signal Readout in X-ray Beam Measurements

Both the ABCN250 and ABC130 ASICs used in these studies are binary readout chips, registering a hit if a collected charge surpassed a preset threshold instead of reading out the collected charge itself. Appropriate thresholds were chosen by performing threshold scans using the ASIC's internal calibration circuits: known charges were fed into all ASIC readout channels and, for increasing thresholds, each channel was repeatedly read out. For an ideal binary readout chip, the resulting distribution is expected to be a step function: low thresholds lead to each readout trigger returning a hit, high thresholds lead to no hits, with a step at the threshold corresponding to the chosen input charge. Due to noise in each readout channel, the step function is smeared and becomes an S-curve. By measuring the fraction of registered hits depending on the applied threshold, i.e. the S-curve, for all module channels, their characteristics can be extrapolated:

- Vt50
  the threshold at which a channel finds hits for 50 % of readout triggers after a certain charge was injected

- Noise
  the internal noise of each ASIC channel, which can lead both to false hits being registered and actual hits not being registered

While the noise is mostly independent of the injected input charge (in a range of 0.5-1.5 fC) and could be conservatively estimated to be 600 ENC, the Vt50 threshold increases with the injected input charge as expected.

As explained in section 8.2, 15 keV photons in silicon transfer their energy to an electron, which then produces 4,167 electron-hole pairs, corresponding to an input charge of 0.67 fC.

In order to select an appropriate threshold for the intended studies, Vt50 thresholds were determined for a range of input charges including the expected input charge of 0.67 fC (see figures 9.3a and 9.3b).

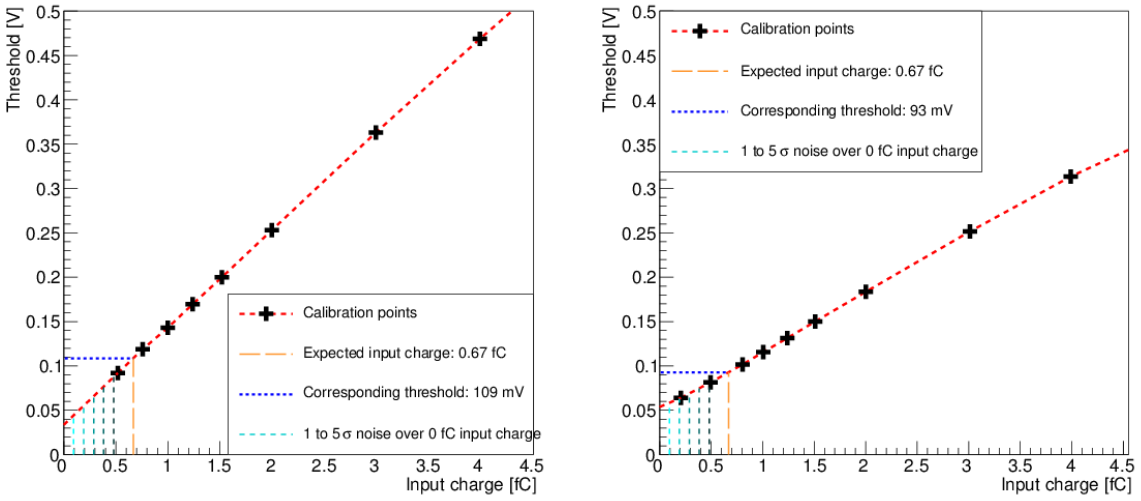

(a) Vt50 threshold depending on input charge, measured for end-cap module

(b) Vt50 threshold depending on input charge, measured for barrel module

Figure 9.3: Threshold settings corresponding to different input charges, determined by internal calibration circuits of the devices under test (red lines), from [135]. Due to internal noise of the ASIC, an input charge of 0 fC corresponds to threshold levels of 30/40 mV for the ABCN250/ABC130 device. Each data point (black markers) represents an average of the input channels of one ASIC.

9.3 Sensor Scans Performed Using an X-ray Beam

For this study, the beam was pointed at a sensor position and a fixed number of readout triggers were sent to each ASIC channel and the number of hits per channel were read out.

As explained in section 8.2, 15 keV X-ray photons from the Diamond Light Source arrive at random multiples of 2 ns. For this measurement, a photon flux of $1 \cdot 10^8 \pm 20\,\%$ was measured,

corresponding to an average of 1.0 ± 0.2 photon in 10 ns. Within a 25 ns readout window, an average of 1.34 ± 0.27 photons can be estimated to react within the detector volume.

After data had been collected for all readout triggers, the stage holding a module was moved by one step across the sensor strips and the readout process was repeated. Table 9.2 summarises the scan parameters for both modules under investigation. Readout thresholds were chosen to

	Barrel module	End-cap module
Vt50 at 0 fC (input charge), [mV]	52	33
Vt50 at 600 ENC ($1\,\sigma$ noise), [mV]	57	44
Vt50 at 1800 ENC ($3\,\sigma$ noise), [mV]	69	66
Vt50 at 3000 ENC ($5\,\sigma$ noise), [mV]	80	87
Vt50 at 0.67 fC (input charge), [mV]	93	109
Readout threshold, [mV]	84	99
Strip pitch, [µm]	74.5	103
Scan step size, [µm]	5	10
Scan width, [µm]	210	190
Triggers per threshold	10,000	3,500

Table 9.2: Overview of scanning parameters for threshold scans across sensor strips: due to a higher number of hits per trigger, fewer triggers and a larger step size were sufficient for the end-cap module.

be below the Vt50 threshold corresponding to the expected input charge in order to maximise the number of hits. Simultaneously, the readout threshold was chosen to be higher than the Vt50 threshold corresponding to 0 fC input charge plus $5\,\sigma$ channel noise in order to minimise fake hits from noise.

9.3.1 Results from 1-dimensional Sensor Scan with an X-ray Beam

For each beam position, a hit map was obtained, which counts the number of hits found in each channel. Figure 9.4 shows an example hit map from the barrel module scan.

In order to study which area of a sensor strip responded for a given beam position, the number of hits for a given threshold and the readout channels under investigation was compared for each beam position. Figures 9.5a and 9.5b show the responses from three adjacent channels over the scanned area. It was found that, for the end-cap module, all channels under investigation collected a consistent number of hits over a scan width corresponding to the expected strip width. In contrast, a similar comparison obtained for the barrel module was found to show uneven responsive areas for the channels under investigation: channels 652 and 654 responded over areas which were wider than the strip pitch. The intermediate channel, 653, responded over a smaller area than the strip pitch. After initially assuming a defective sensor strip, it was found that while the sensor response did not match the expected sensor architecture, it did agree with the sensor layout around bond pads (see figure 9.5b, where strip pitch and bond pad positions are indicated). The miniature sensors used for the construction of the barrel module

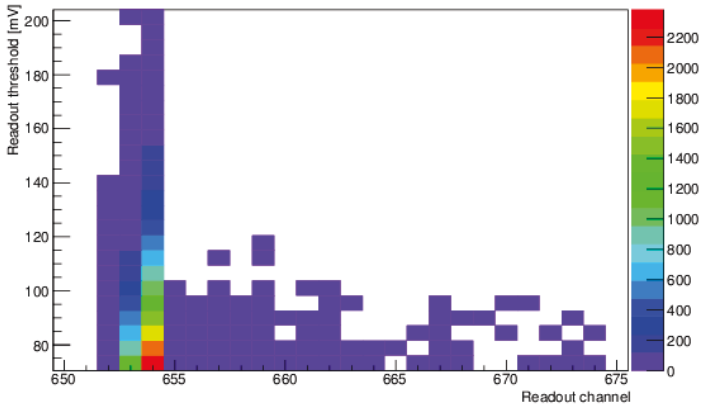

Figure 9.4: Example hit map from an X-ray scan of a barrel module showing only a selection of readout channels. Each horizontal line of entries was obtained by sending 10,000 readout triggers and counting all hits above the preset threshold. The mainly responding channel is channel 654, with channel 653 showing fewer hits, indicating that the beam was pointed at channel 654, close to channel 653.

under investigation have four rows of bond pads, accounting for 2.8 mm of the active sensor area of about 7 mm, making the bond pads a likely position for the scan. The test suggested that sensors show uneven responses in bond pad regions.

Two further studies were conducted in order to investigate the sensor strip response in bond pad regions.

9.4 Studies of Sensor Geometry Using Electrons

Initial indications of bond pads affecting sensor hits were observed exclusively in X-ray beams, where charge is deposited over a short distance of up to 30 µm [143]. In order to investigate if the same effect occurs for a sensor operated under realistic conditions, data collected for an ATLAS07 sensor in an electron beam (see section 7.1.2) was used.

While the resolution of the obtained data was not sufficient to see any width variations along an individual strip, variations became visible by combining the hits collected for odd and even numbered strips. Figure 9.6 shows the resulting hit maps obtained for one ATLAS07 sensor miniature. The number of recorded particle hits per sensor position showed that the presence of bond pads leads to a statistical effect on the number of recorded hits: sensor strips with bond pads show an increased number of hits in the bond pad area, while sensor strips without bond pads show fewer hits in the same area. Since the overall number of hits (i.e. the combined hits from odd and even numbered channels) is approximately constant over the whole sensor area, an increased/decreased number of hits indicates hits were collected over a larger/smaller sensor area. Figure 9.7 shows a projection of the number of collected hits in order to attempt a quantification of the effect. After the previous testbeam results had indicated that bond

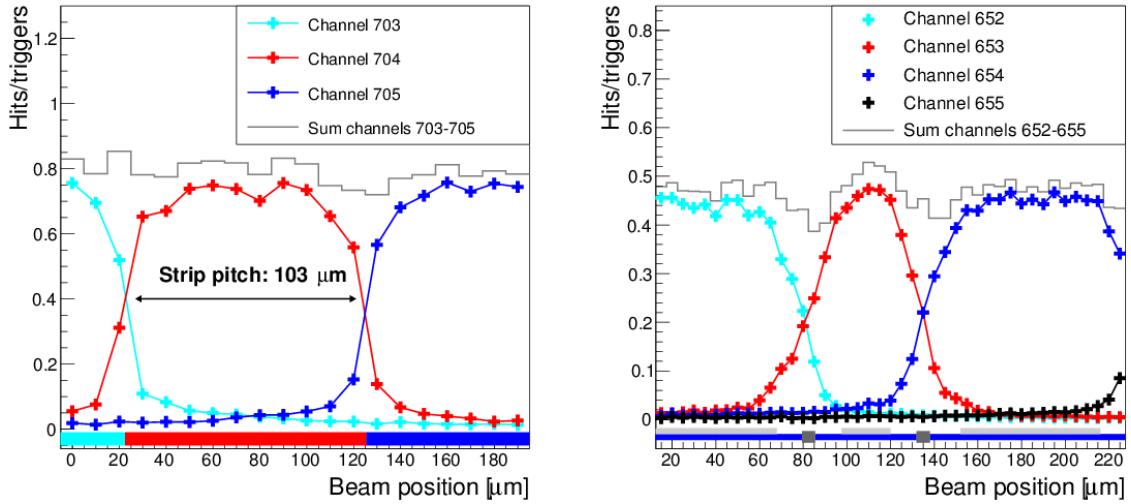

(a) End-cap module sensor scan: individual and combined hit rates from three adjacent strips for a scan across three strips (cyan, red and blue), showing the individual hit rates at a threshold of 99 mV, selected to be between Vt50 corresponding to the expected input charge (109 mV) and Vt50 for $5\,\sigma$ over 0 fC input charge, 87 mV. The collected hit rates for the three channels fit both the positions of the strips and the sensor strip pitch well. This sensor does not have p-stop implants.

(b) ABC130 module sensor scan: individual and combined hit rates from four adjacent channels at a threshold of 84 mV, selected to be between Vt50 corresponding to the expected input charge (93 mV) and Vt50 for $5\,\sigma$ over 0 fC input charge, 80 mV. At the bottom, the probable sensor geometry is shown: silicon (blue), aluminium layer (light grey) and p-stops (dark grey). The hit rates can be seen to agree well with the expected locations of p-stops and sensor strips.

Figure 9.5: Hit rates from several adjacent channels for an end-cap module and a barrel module. Due to different versions of readout chips used on both modules and different numbers of triggers applied during the scan, the hit rates from both devices can not be directly compared. Figures from [135].

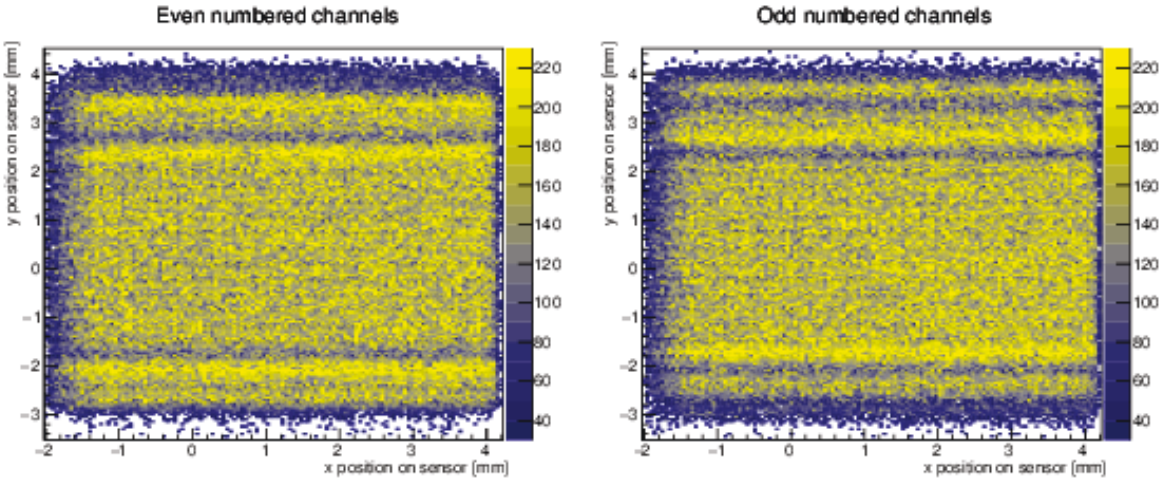

Figure 9.6: Positions of particle hits on an ATLAS07 miniature sensor for 6 million events. The sensor strip implants are oriented parallel to the y-axis. The left plot shows the hit map of only even numbered sensor strips, the right plot shows the hits collected only by odd numbered strips. Areas with fewer hits are paired with areas with more hits, matching the positions of bond pad rows consisting of one row of bond pads for even numbered channels and one row of bond pads for odd numbered channels each. Figure from [143].

pads might lead to different widths over which a sensor strip responds, the findings from this testbeam showed a similar effect: the presence of a bond pad on a sensor strip results in this strip collecting hits over a larger area than intended. This effect leads to an average difference of up to 30 % in number of collected clusters in bond pad regions compared to sensor regions without bond pads.

The effect was made more visible by dividing the sensor area in a grid with bin sizes of $14.9 \times 149\,\mu m^2$ and finding the sensor channel collecting the most hits for any given position. Figure 9.8a shows the resulting resulting response map for an ATLAS07 miniature sensor in comparison with its bond pad layout 9.8b. The hit map confirms that the modified sensor architecture in bond pad areas affects the area over which a sensor strip responds: a sensor strip responds in a wider area around a sensor bond pad, while neighbour sensor strips respond over a smaller area. The effect of sensor strips responding over smaller or wider areas than expected could not be unambiguously attributed to either the presence of bond pads or modified p-stop positions, given the maximum resolution achieved in the setup.

9.5 Sensor Layout Considerations

The ATLAS12 sensor [137] is divided in four strip segments, where each segment has a length of $\approx 2.5\,cm$ and five rows of bond pads. Each row, consisting of bond pads on odd and even numbered sensor strips, accounts for $700\,\mu m$ of modified p-stop positions of which bond pads

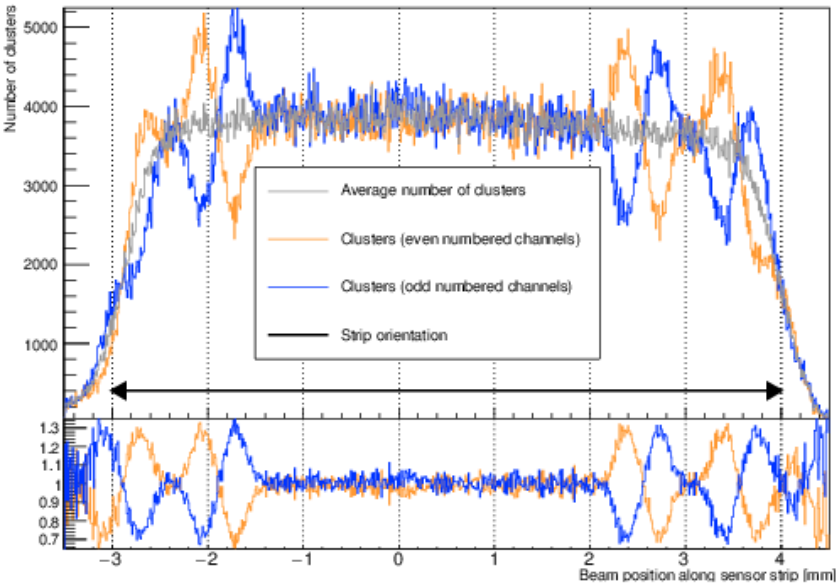

Figure 9.7: 6 million hits collected on an ATLAS07 miniature sensor, projected on the sensor axis parallel to the strip implants. Separating the clusters according to the highest responding channel (odd/even) shows regions where the number of clusters in odd/even channels deviates from the average by up to 30 %. Figure from [143].

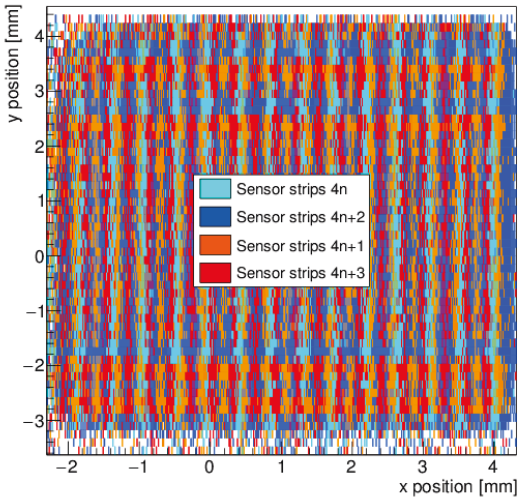

(a) ATLAS07 miniature sensor map showing the mainly responding sensor for a given position on the sensor: orange and red bins represent odd numbered channels, cyan and blue bins represent even numbered channels.

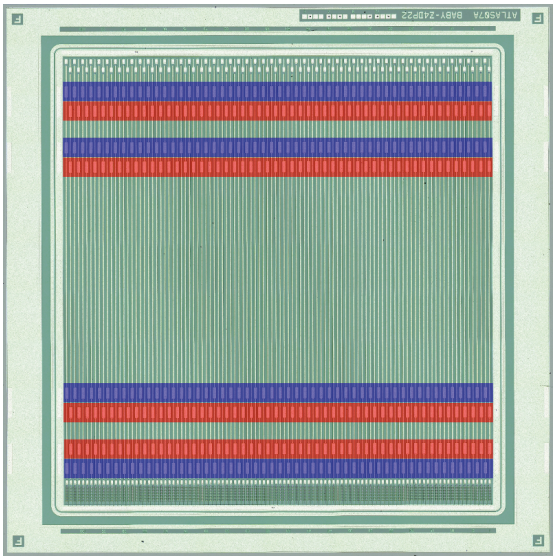

(b) ATLAS07 miniature sensor in the same orientation as used in the testbeam. Bond pads of odd and even numbered channels are coloured red and blue, with a total of eight rows of bond pads on the miniature sensor.

Figure 9.8: Sensor hit map in comparison with the sensor layout: the size of the hitmap has been scaled to approximately match the active area of the miniature sensor. The hit map shows that in several areas of the sensor the mainly responding channels are almost exclusively odd or even. The positions of these areas match the bond pad rows indicated on the sensor layout. It can be seen that the pattern of bond pad rows (alternating on even and odd channels in the sensor top half, even-odd-odd-even in the bottom half) is also found in the pattern of mainly responding channels, indicating that the effect found in the hit map is caused by the array of bond pad rows on the sensor. Figures from [143].

make up 400 µm. With overall dimensions of $9.75 \times 9.75\,\mathrm{cm}^2$, five rows of bond pads on each of the four strip segments lead to a total of 14 mm (14.4 %) of modified p-stops and 8 mm (8.2 %) of bond pads on one sensor strip. In these areas, charge collection differs from the expected standard sensor behaviour and thus particle tracking can be affected. Depending on the main contributor to the variations (modified p-stop positions or bond pads), a modification of the sensor layout could be contemplated:

- if bond pads were found to affect the responding area of a sensor strip, the number of bond pad rows on the sensor could be reduced
- if modified p-stop positions were found to define the area over which a strip responds, the sensor architecture could be modified (using optimised p-stop positions or a sensor architecture with p-spray).

In each case, the implementation of a track reconstruction algorithm including position information associated with the sensitive sensor regions could counteract a negative impact on particle tracking. In order to identify the element defining of a sensor strip's responding area, a further study using high positioning precision was performed.

9.6 Detailed 2D-mapping in an X-ray Beam

In order to investigate the impact of p-stops and bond pads on the charge collecting area of a sensor strip, a new measurement was set up using a micro-focused X-ray beam ($2 \times 3\,\mu\mathrm{m}^2$). A sensor area containing the following sensor regions was chosen (see figure 9.9):

- equidistant p-stops
- modified p-stop positions
- modified p-stop positions around bond pads

By using a beam size much smaller than the structures under investigation, differences in collected hits for different sensor areas could be resolved.

9.6.1 Setup for 2D Sensor Scans Using an X-ray Beam

For this study, two ATLAS07 BZ3 sensor (see section 3.1) were used, as the same sensor architecture is used for ATLAS12 sensors [137]. The effect was studied for two devices in comparison:

- one non-irradiated sensor, attached to an ABC130 readout chip, using the same setup as described in section 9.2
- one irradiated sensor (irradiated with reactor neutrons to $2 \cdot 10^{15}\,\mathrm{n_{eq}/cm^2}$, connected to an ALiBaVa readout system, using the same testbeam setup as described in section 8.1

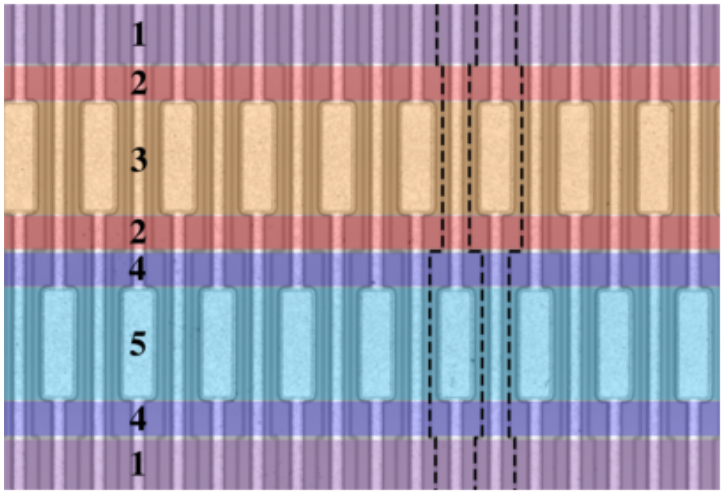

Figure 9.9: Laser microscope image of bond pad rows on sensor showing the different sensor architectures around bond pads. P-stops are visible as dark lines between strip implants with aluminium tops and bond pads. The nominal sensor layout with equidistant p-stops is coloured violet (1). Bond pads on odd (light blue, 5) and even (orange, 3) numbered strips are surrounded by p-stops (dashed black lines). Between bond pads and nominal sensor layout, a transition region (red (2)/dark blue (4)) can be seen, where p-stops are not equidistant, but no bond pads are present. Figure from [143].

	x-direction (across sensor strips), [µm]	y-direction (along sensor strips), [µm]
bond pad	60	200
modified p-stops		
around bond pads	52	350
between bond pads	97	350
scanning step	15	60
scanning length	210	1300

Table 9.3: Parameters of a grid scan over the bond pad area of an ATLAS07 sensor: step sizes were chosen to be smaller than sensor architecture features.

If p-stops were defining the area over which a sensor strip responds, their effect can be expected to be increased by irradiation [144]. Hence, two sensors of the same architecture, one irradiated and one unirradiated, were tested. Due to the high irradiation level of the irradiated ATLAS07 sensor, the depletion voltage exceeded the possible bias voltage range of up to -1000 V and could not be determined from measurements. The sensor was thus operated under-depleted at a reverse bias voltage of -1000 V and at a temperature of -20 °C. The non-irradiated ATLAS12 sensor was operated over-depleted at a bias voltage of -360 V (nominal full depletion voltage -300 V [137]).

While the different readout systems connected to the two sensors required different modes of data taking concerning triggers and numbers of collected hits, the geometrical parameters of scans on both sensors were chosen to be identical (see table 9.3). The scan length was chosen to ensure that one strip was entirely covered, including the presumably widest area around its bond pad. Step sizes were chosen to ensure that at least one point of the scanning grid would fall into each of the sensor architectures of interest, in particular the region were p-stops were not equidistant, but no bond pads were present.

For the irradiated sensor read out by an ALiBaVa system, 100,000 events were collected for each position of the beam on the sensor. Here, clusters in the ALiBaVa system were reconstructed using channels with a signal lying $1\,\sigma$ above the determined noise level. Maximal one neighbouring cluster was added if its signal exceeds $1\,\sigma$ over the noise level. These thresholds had to be set lower than usual because of the generally lower charge deposited by the X-ray photons and to be sensitive to small signals and small differences between signals. The clustering was restricted to the area hit by the beam (5 strips in total) in order to suppress the creation of random clusters from noise elsewhere in the sensor.

For the non-irradiated sensor attached to an ABC130 readout chip, a threshold scan was performed for thresholds ranging from 62 mV to 152 mV (see figure 9.10, where 10,000 triggers per threshold were collected.

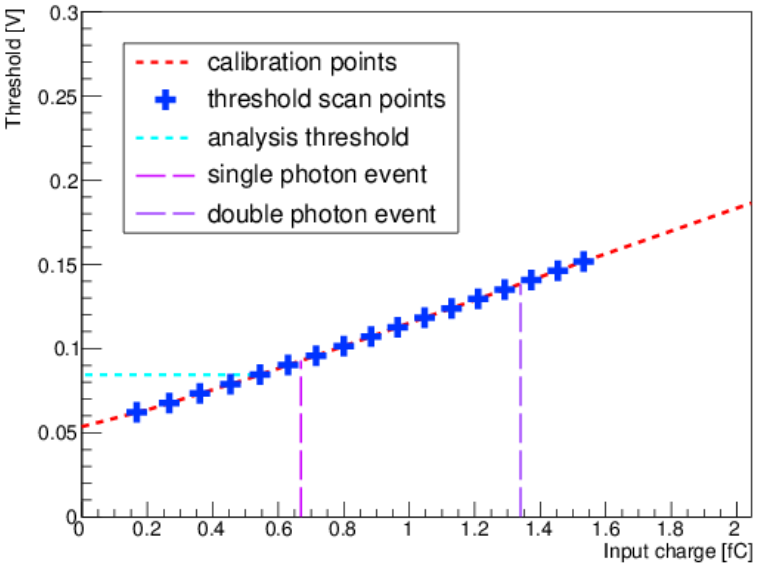

Figure 9.10: Thresholds and input charges for the device under investigation: the thresholds corresponding to any given input charge were calculated using internal calibration circuits of the readout chips. The threshold corresponding to the expected input charge of a 15 keV electron, 0.67 fC, was found to correspond to a threshold of 93 mV. For data taking, a lower readout threshold of 85 mV was chosen. Figure from [143].

9.6.2 Results of 2D Sensor Scans Using an X-ray Beam

For each sensor strip covered in the scan, the number of collected hits for each beam position was plotted to map its responding area. Figure 9.11 shows the scanned sensor area and the corresponding hit maps. The results show that the width over which a sensor strip responds, does depend on the sensor architecture at that position: the presence of bond pads increases the area over which a sensor responds, with the number of hits collected by neighbour strips being decreased accordingly.

In order to investigate the impact of p-stop positions on the responding sensor area, sensor areas without bond pads, but non-uniform p-stop positions were studied. Similar to the map shown in figure 9.8a, the number of hits collected in each channel were compared for each bin, showing the mainly responding channel for each beam position. Figure 9.12 shows the resulting sensor map. It was found that the area over which a strip mainly responds is not defined by the p-stop shape. Instead, the strip sensors responding over wider or narrower areas can be attributed mainly to the presence of bond pads, with the impact of the p-stop position being negligible.

Irradiation influences the electric field of the sensor and thus the responding area of each sensor strip [145]. The results obtained for a non-irradiated sensor were compared to a similar scan performed on an ATLAS07 sensor irradiated to a fluence of $2 \cdot 10^{15}$ 1 MeV neutrons/cm^2 using reactor neutrons. This corresponds to twice the full HL-LHC dose expected in the ATLAS ITk strip detector. Figure 9.13 shows the hit maps obtained from individual sensor strips of an irradiated sensor. Due to limited available beam time, the scanned area on the irradiated sensor was smaller than the area scanned on the non-irradiated sensor. While scan steps had been chosen to contain at least one row of scanned points within the area of modified p-stops without bond pads, the initial beam position was found to lead to scan points being located mostly in areas at least partially covered by bond pads or mixed with standard p-stop positions. Only one row of scan points (located below the bottom bond pad row, see figure 9.13) was contained entirely within a region of modified p-stops only where the collected hits can be seen to show only minor changes for standard and altered p-stop positions. Analogous to the findings for a non-irradiated sensor, hit maps for an irradiated sensor hence indicated that changes in the number of collected hits are mostly caused by the presence of bond pads, with altered p-stop positions having only a minor impact.

It should be noted that the number of photons passing through the sensor for each beam position was found to vary over time, translating into different numbers of hits being collected. Figure 9.13 shows a visible discrepancy in collected hits between two areas on the hit map, with the transition being marked by one bin showing significantly fewer entries than the surrounding positions. Comparing the timestamps of each beam position with the beam current, changes over time were found to match the variations observed in the numbers of collected hits. Figure 9.14 shows the measured beam current over time. The hit map entry with the low number of entries was found to correspond to a beam loss, leading to a low number of photons and registered hits. After restarting, the beam current was higher than before and slowly decreasing, translating into fewer hits collected by the sensor. The higher beam intensity after restart led to the number of corresponding hits increasing by 25 %, with the subsequent 22 %-beam intensity decrease (see figure 9.14) translating into hit numbers decreasing by 11 %. While the changes of the beam

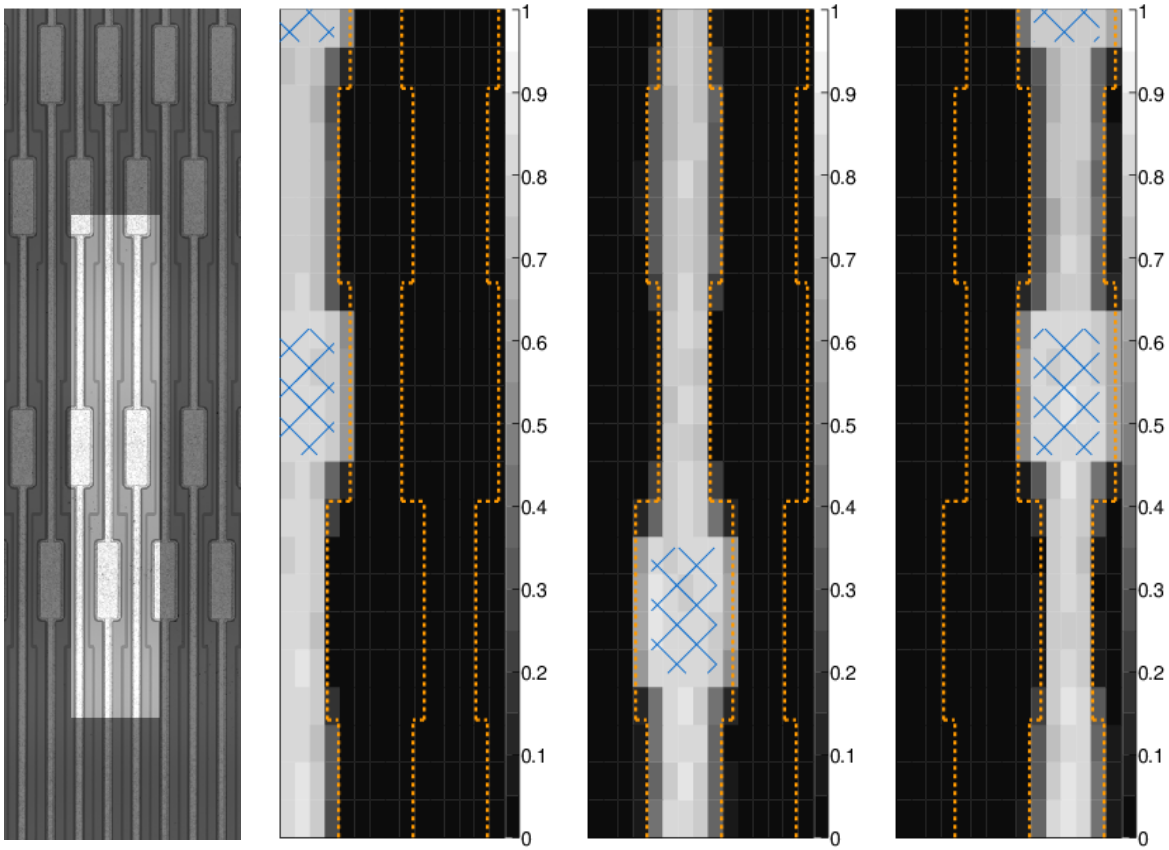

Figure 9.11: Approximate sensor area (highlighted) covered in X-ray beam scan and resulting three hit maps. Each plot shows the hits collected by one readout channel for the same scan area of $1.26 \times 0.21\,\mathrm{mm}^2$, divided by the maximum number of hits per bin in the map. Positions of p-stops (dashed orange lines) and bond pads (blue shaded areas), determined from fits of collected hit distributions are indicated on the hit maps. Figures from [143]

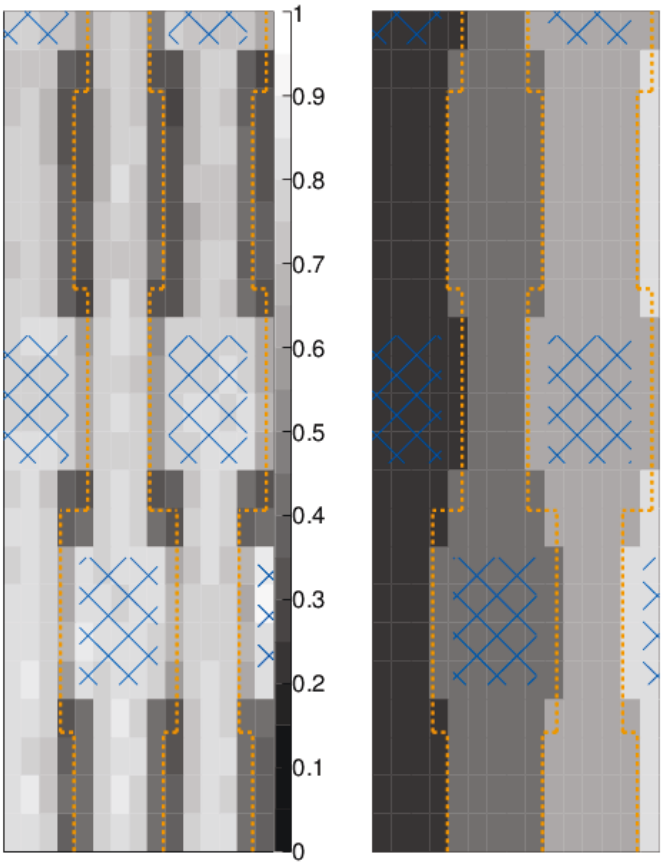

(a) (b)

Figure 9.12: (a) combined hits relative to the maximum number of hits per bin from four adjacent sensor strips over a $1.26 \times 0.21\,\mathrm{mm}^2$ area of a sensor bond pad region. Combined hits from neighbour channels show that, around bond pads, the number of collected hits is higher than in the standard sensor area without bond pads. Charge sharing between adjacent strips leads to fewer hits being collected by the binary readout system and a less efficient region between strips. (b) Mapping the channel with the highest number of collected hits for each beam position shows that the area over which a sensor strip responds does not follow the shape of a p-stop: sensor strips show similar responses in areas with equidistant and unevenly spaced p-stops. Figures from [143].

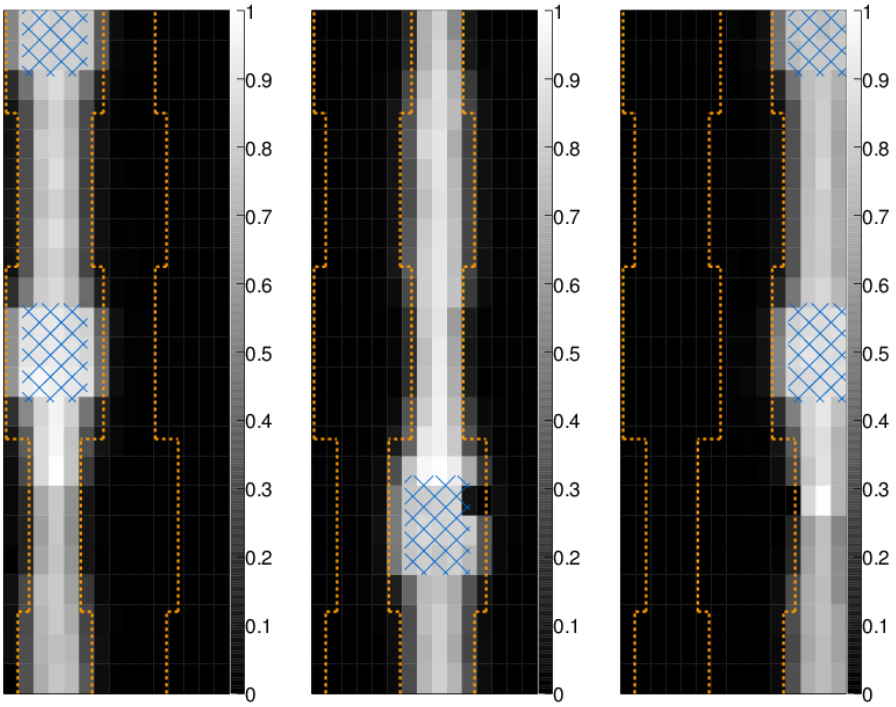

Figure 9.13: Hit maps for three sensor strips over an area of $1.32 \times 0.21\,\mathrm{mm}^2$ in steps of $60 \times 15\,\mu\mathrm{m}^2$. Hit numbers are shown relative to the maximum number of hits collected for one sensor strip. Positions of sensor features (p-stops (dashed orange lines) and bond pads (shaded blue areas) were determined from hit distributions and are shown on the maps. While the responding areas of individual strips are larger around bond pads, no difference could be observed between areas with equidistant p-stops and unevenly spaced p-stops.

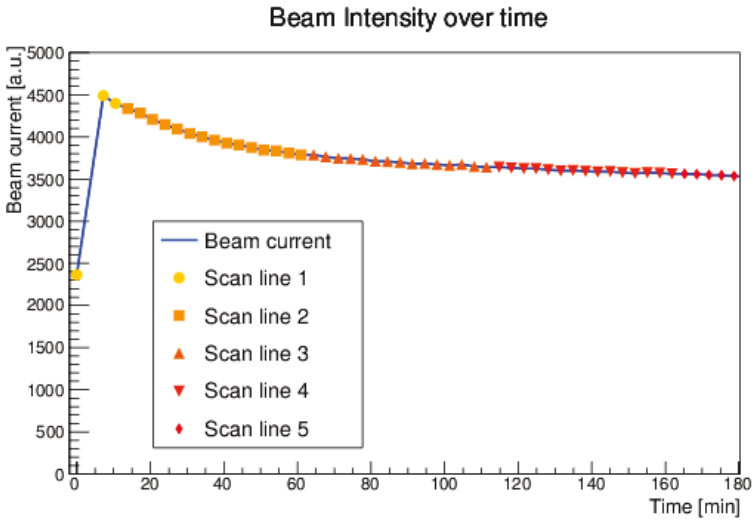

Figure 9.14: Synchrotron beam line current measured after a restart as a function of time. Markers represent one beam position of the scan grid, with one scan line consisting of 15 scan points across the sensor strips.

current complicate absolute statements about collected hits and efficiency, the variations were small enough to allow for the comparison of responding sensor areas.

9.7 Comparison of Sensor Maps with Simulations

The observed charge collection behaviour of the sensors was compared to 2D TCAD simulations of ATLAS07/ATLAS12 sensor architectures 9.15. Layout modifications matching the different sensor regions showed that the position of p-stops around strip implants has only a minor impact on the electric field inside a sensor (see figures 9.15a and 9.15b), matching the observations found in testbeam measurements.

Areas between strip implants show a lower electric field strength than areas below strip implants, which agrees with the hit maps obtained in testbeams showing fewer hits being collected at the edges of a strip than in its centre. The presence of a wider implant and bond pad (see figure 9.15c) was found to extend the region of higher electric field strength further towards the edges of a strip, leading to a more homogeneous field around the implant. A larger area of high field strength can be assumed to lead to better charge collection in the corresponding sensor region. The simulations agreed well with the wider areas of collected charge below bond pads and minor impact of p-stop positions observed in testbeams. After irradiation, local defects disturb the electric field of a sensor [146], reducing the overall charge collecting behaviour, particularly at the less efficient edges of sensor strips. Similar to the behaviour observed for a non-irradiated sensor, the wider implant and added bond pads in bond regions were found to increase the increase the charge collecting area of a sensor strip towards its edges. A similar effect has been observed in TCT measurements of irradiated sensors [147].

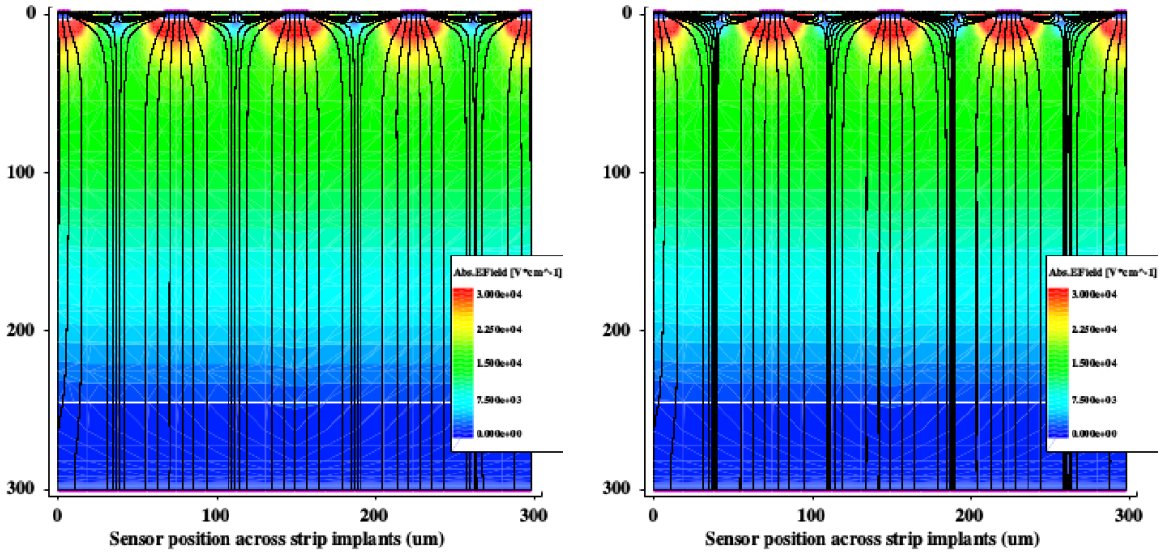

(a) Simulation of the standard sensor layout with equidistant p-stop positions

(b) Simulation of the sensor layout with altered p-stop positions

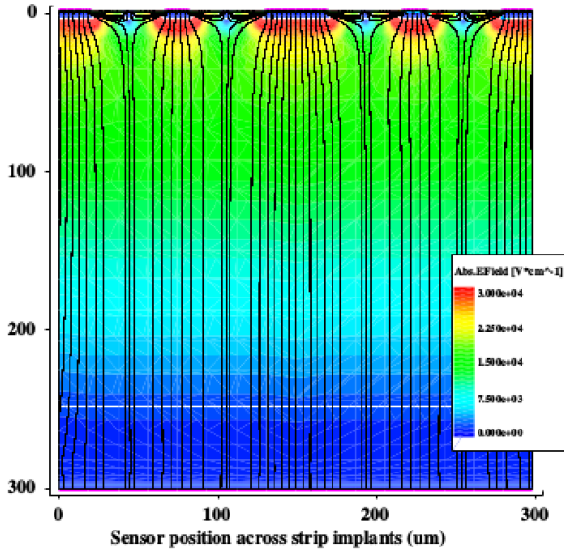

(c) Simulation of the sensor layout with bond pads and altered p-stop positions

Figure 9.15: 2D TCAD simulation of the electric field and its streamlines of a silicon strip sensor. The simulated cross-section of the sensor shows a width and thickness of 300 µm. A reverse bias of -300 V is applied at the back side of the sensor at 300 µm. The simulations are done for a resistivity of 2.5 kΩ·cm, to study the effect of different widths of the metal contact and strip implant, and the effect of different p-stop positions. Figures from [143].

The altered sensor architecture in bond pad regions can thus be assumed to have a similar beneficial effect on the electric field of an irradiated sensor as simulated for a non-irradiated sensor.

9.7.1 Conclusion of Sensor Geometry Studies

Studies of the bond pad regions of silicon strip sensors with high spatial resolution have confirmed that on ATLAS07 and ATLAS12 sensors, strips respond over a larger width when bond pads are present. It was found that the strip response can be attributed mainly to the geometry of bond pads and the underlying implant, with the impact of p-stop positions being much smaller. Similar effects were observed in 2D TCAD simulations of comparable layout alterations. Bond pads were found to increase the local width over which a sensor strip collects hits from 74.5 µm to $\approx$ 95 µm and reduce the responding width of adjacent strips to $\approx$ 54 µm, leading to corresponding variations in the numbers of collected clusters.

Sensor strips collecting charges over a larger width around bond pads corresponds to sensor hits deviating from the expected sensor strip position: in detector simulations, all sensor strips are expected to respond over a rectangular area with the width of the strip pitch. Around bond pads, a sensor strip will respond at a position, where the detector simulation would foresee its neighbour strip to respond, effectively shifting the responding readout channel by ± 1. For high momentum tracks, this shift was suspected to lead to charge mis-reconstruction: for a straight track, a shifted sensor strip could be falsely reconstructed as a wrong charge leading to a bent track. A follow-up study investigated the impact of bond pads on charge reconstruction by randomly shifting a percentage of sensor channels with hits by ± 1 and comparing results for reconstructed and simulated tracks. The study did not find a significant discrepancy between mis-reconstructed charges for tracks with and without randomly shifted hits, which were about 0.02 % in both cases [148]. A discrepancy was however observed in reconstructed track parameters: random shifts were found to reduce the resolution for e.g. track momentum, angle and impact parameter. The extent to which the presence of bond pads affected the area in which a sensor strip responded, had not been fully understood at the time of the study. Hence, the probability of random shifts assumed in this study was overestimated.

In order to minimise the occurrence of shifted hits, the layout of future ATLAS strip sensors was modified as a result of the findings:

- since a small impact of p-stop positions on the responding area of sensor strips could not be fully excluded, p-stop positions were modified: the area of unevenly spaced p-stops was minimised by arranging p-stops closely around bond pads (see figure 9.16b)
- the number of bond pad rows was reduced to eliminate extra bond pads: where e.g. previous barrel sensor layouts had four bond pad segments per strip (one segment consists of four rows of bond pads: two for odd and two for even numbered strips), future barrel sensors are designed to have two bond pad segments consisting of only one row of bond pad for odd and even numbered strips each.

The impact of bond pads on the sensor response was thus discovered early enough to minimise its impact on the sensor tracking performance.

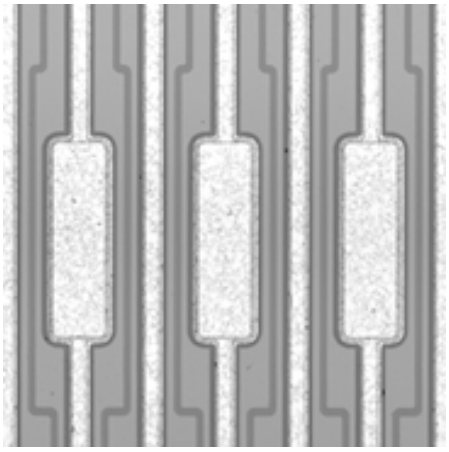

(a) Sensor layout around bond pads on ATLAS07 sensor

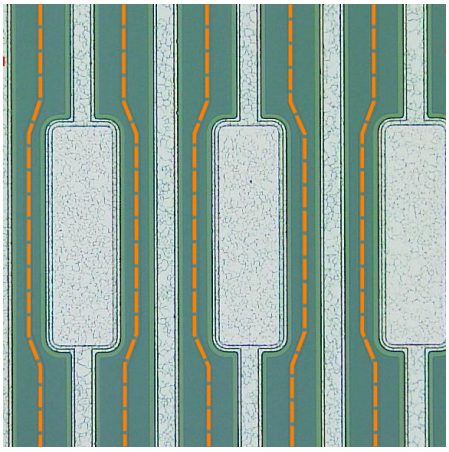

(b) Sensor layout around bond pads on ATLAS R0 miniature sensor

Figure 9.16: Bond pad layouts on ATLAS07 and R0 miniature sensors: silicon strip sensors were designed to minimise areas with unevenly spaced p-stops after modified sensor areas were found to impact tracking. Bond pad geometries were not modified.

10 Conclusion

This thesis investigated how silicon strip sensors are affected by the presence of adhesives on their surface.

Sets of sensors with similar characteristics were used as test structures. Adhesives were applied to their surface in a process approximating future strip module build methods. Subsequently, these sensors were subjected to treatments designed to emulate conditions expected in the future ATLAS ITk strip tracker: temperature cycles between -20 °C and +50 °C and irradiations to fluences of $2 \cdot 10^{15}\,\mathrm{n_{eq}/cm^2}$ with protons and neutrons. ATLAS07 miniature sensors were tested in combination with four adhesives: the baseline glue for module construction (Epolite FH-5313) in comparison with three UV cure glues with different viscosities (DYMAX 3013, DYMAX 6-621 and Loctite 3525).

In order to study the impact of irradiation on the performance of sensors with glue, effects of irradiation in the glue itself were evaluated first. Three standard analysis methods for polymer materials were tested for applicability. Among the tested methods, gas chromatography in combination with mass spectrometry was found to be able to identify chemical changes caused by irradiation. The adhesives under investigation showed two effects to different extents: molecule fragments being broken off from larger molecules and unconnected or weakly connected molecules forming chemical bonds with other molecules. The chosen method allowed to quantify different radiation effects and provided a measure of radiation hardness for adhesives.

In order to assess changes of the electrical characteristics of a sensor after the application of glue to its surface, probe station measurements were conducted. Measurements were focused on the inter-strip capacitance as the dominant contributor to the sensor noise as well as bulk capacitance and leakage current, which are indicators of changes in the sensor bulk.

The leakage current was found to be affected by the presence of glue: sensors with glue showed increased leakage currents and a higher likelihood for early breakdowns. Early breakdowns were found to be improved by thermal cycling. Irradiations of sensors showed a similar effect on the sensor performance, allowing to fully cure early breakdowns. The presence of glue on sensor surfaces was found to increase inter-strip capacitances, corresponding to a minor increase of the sensor noise. Probe station measurements thus showed adverse effects caused by the presence of glue on sensor surfaces. These effects were improved by thermal cycling and mostly cured by irradiation.

No impact on the sensor charge collection efficiency, measured using a β-source setup, was found for any of the adhesives under investigation. A difference was observed for the average cluster sizes of sensors with and without glue: for sensors (partially) covered with glue, larger cluster sizes were observed. The same effect was observed after thermal cycling. After irradiations, no difference in cluster size was observed - sensors with glue behaved identically to sensors without glue.

Tests in an electron beam confirmed that the presence of glue on a sensor leads to a locally higher average cluster size. A follow-up measurement with a micro-focused X-ray beam pointed at the edge of a sensor partially covered with glue showed that the exposure of glue to an X-ray beam generates photons. Increased cluster sizes on sensors with glue could be attributed to the detection of photons generated inside the glue layer.

A previously unobserved effect was discovered during sensor tests in electron and X-ray beam tests: observations showed inhomogeneous charge collection in bond pad areas. In comparison with TCAD simulations, subsequent studies found varying widths of the strip implant and aluminium top layer to cause changes of the electric field inside a sensor, which led to correspondingly inhomogeneous charge collection.

In summary, changes of the sensor performance caused by the presence of glue were found to be small and to require analogue readout systems for detection. At the foreseen operating threshold for the ITk strip tracker, the impact of gluing on the sensor performance is negligible. In addition, the environmental conditions expected in the ITk were found to mitigate adverse effects of adhesives on silicon strip sensors.

These findings confirm that the use of all considered adhesives on the active area of silicon strip sensors meets all requirements for the targeted ten year operation period of the HL-LHC.

Bibliography

[1] The ATLAS Collaboration. The ATLAS Experiment at the CERN Large Hadron Collider. *Journal of Instrumentation*, 3(08):S08003, 2008.

[2] The ATLAS Collaboration. Technical Design Report for the ATLAS Inner Tracker Strip Detector. Technical Report CERN-LHCC-2017-005. ATLAS-TDR-025, CERN, Geneva, 04 2017.

[3] The ATLAS Collaboration. The Barrel Modules of the ATLAS SemiConductor Tracker. Technical Report ATL-INDET-PUB-2006-005. ATL-COM-INDET-2006-009, CERN, Geneva, 07 2006.

[4] S Haywood, L Rossi, R Nickerson, and A Romaniouk. *ATLAS inner detector: Technical Design Report, 2*. Technical Design Report ATLAS. CERN, Geneva, 1997.

[5] The ATLAS Collaboration. Letter of Intent for the Phase-II Upgrade of the ATLAS Experiment. Technical Report CERN-LHCC-2012-022. LHCC-I-023, CERN, Geneva, 12 2012.

[6] Keithley Instruments Inc. *Model 6485 Picoammeter, Model 6487 Picoammeter/Voltage Source User's Manual*, Rev. B edition, 1 2003.

[7] Lyndon Evans and Philip Bryant. LHC Machine. *Journal of Instrumentation*, 3(08):S08001, 2008.

[8] The ALICE Collaboration. The ALICE experiment at the CERN LHC. *Journal of Instrumentation*, 3(08):S08002, 2008.

[9] The CMS Collaboration. The CMS experiment at the CERN LHC. *Journal of Instrumentation*, 3(08):S08004, 2008.

[10] The LHCb Collaboration. The LHCb Detector at the LHC. *Journal of Instrumentation*, 3(08):S08005, 2008.

[11] The ATLAS Collaboration. Precision measurement and interpretation of inclusive W^+, W^- and Z/γ^* production cross sections with the ATLAS detector. *Eur. Phys. J. C*, 77(CERN-EP-2016-272. 6):367. 97 p, 12 2016.

[12] The ATLAS Collaboration. Evidence for single top-quark production in the s-channel in proton–proton collisions at $\sqrt{s} = 8$ TeV with the ATLAS detector using the Matrix Element Method. *Phys. Lett. B*, 756(arXiv:1511.05980. CERN-PH-EP-2015-286):228–246. 16 p, 11 2015.

[13] The ATLAS Collaboration. Observation of a new particle in the search for the Standard Model Higgs boson with the ATLAS detector at the LHC. *Phys. Lett. B*, 716(CERN-PH-EP-2012-218):1–29. 39 p, 08 2012.

[14] The ATLAS Collaboration. Search for new phenomena in events containing a same-flavour opposite-sign dilepton pair, jets, and large missing transverse momentum in $\sqrt{s} = 13$ TeV pp collisions with the ATLAS detector. *Eur. Phys. J. C*, 77(CERN-EP-2016-260. 3):144. 46 p, 11 2016.

[15] de Florian, Daniel and Mazzitelli, Javier. Higgs Boson Pair Production at Next-to-Next-to-Leading Order in QCD. *Phys. Rev. Lett.*, 111:201801, 11 2013.

[16] Matthew J. Dolan, Christoph Englert, and Michael Spannowsky. Higgs self-coupling measurements at the LHC. *Journal of High Energy Physics*, 2012(10):112, 2012.

[17] The ATLAS Collaboration. Physics at a High-Luminosity LHC with ATLAS. Technical Report ATL-PHYS-PUB-2012-001, CERN, Geneva, 08 2012.

[18] The ATLAS Collaboration. Search for flavour-changing neutral current top quark decays $t \to Hq$ in pp collisions at $\sqrt{s} = 8$ TeV with the ATLAS detector. *The European Physical Journal C*, 76(1):12, 2016.

[19] Christopher T. Hill. Topcolor assisted technicolor. *Physics Letters B*, 345(4):483 – 489, 1995.

[20] Robert M. Harris and Supriya Jain. Cross sections for leptophobic topcolor Z' decaying to top-antitop. *The European Physical Journal C*, 72(7):2072, 2012.

[21] Search for heavy particles decaying to pairs of highly-boosted top quarks using lepton-plus-jets events in proton–proton collisions at $\sqrt{s} = 13$ TeV with the ATLAS detector. Technical Report ATLAS-CONF-2016-014, CERN, Geneva, 03 2016.

[22] The ATLAS Collaboration. *ATLAS inner detector: Technical Design Report, 1.* Technical Design Report ATLAS. CERN, Geneva, 1997.

[23] The ATLAS Collaboration. *ATLAS liquid-argon calorimeter: Technical Design Report.* Technical Design Report ATLAS. CERN, Geneva, 1996.

[24] The ATLAS Collaboration. *ATLAS tile calorimeter: Technical Design Report.* Technical Design Report ATLAS. CERN, Geneva, 1996.

[25] The ATLAS Collaboration. *ATLAS muon spectrometer: Technical Design Report.* Technical Design Report ATLAS. CERN, Geneva, 1997.

[26] The ATLAS Collaboration. *ATLAS magnet system: Technical Design Report, 1.* Technical Design Report ATLAS. CERN, Geneva, 1997.

[27] The ATLAS Collaboration. *ATLAS level-1 trigger: Technical Design Report.* Technical Design Report ATLAS. CERN, Geneva, 1998.

[28] Peter Jenni, Marzio Nessi, Markus Nordberg, and Kenway Smith. *ATLAS high-level trigger, data-acquisition and controls: Technical Design Report*. Technical Design Report ATLAS. CERN, Geneva, 2003.

[29] M Capeans et al. ATLAS Insertable B-Layer Technical Design Report. Technical Report CERN-LHCC-2010-013. ATLAS-TDR-19, 09 2010.

[30] Letter of Intent for the Phase-I Upgrade of the ATLAS Experiment. Technical Report CERN-LHCC-2011-012. LHCC-I-020, CERN, Geneva, 11 2011.

[31] T Kawamoto, S Vlachos, L Pontecorvo, J Dubbert, G Mikenberg, P Iengo, C Dallapiccola, C Amelung, L Levinson, R Richter, and D Lellouch. New Small Wheel Technical Design Report. Technical Report CERN-LHCC-2013-006. ATLAS-TDR-020, 06 2013.

[32] M Shochet, L Tompkins, V Cavaliere, P Giannetti, A Annovi, and G Volpi. Fast TracKer (FTK) Technical Design Report. Technical Report CERN-LHCC-2013-007. ATLAS-TDR-021, 06 2013.

[33] M (CERN) Aleksa, W (Pittsburgh) Cleland, Y (Tokyo) Enari, M (Victoria) Fincke-Keeler, L (CERN) Hervas, F (BNL) Lanni, S (Oregon) Majewski, C (Victoria) Marino, and I (LAPP) Wingerter-Seez. ATLAS Liquid Argon Calorimeter Phase-I Upgrade Technical Design Report. Technical Report CERN-LHCC-2013-017. ATLAS-TDR-022, 09 2013. Final version presented to December 2013 LHCC.

[34] The ATLAS Collaboration. Technical Design Report for the Phase-I Upgrade of the ATLAS TDAQ System. Technical Report CERN-LHCC-2013-018. ATLAS-TDR-023, 09 2013. Final version presented to December 2013 LHCC.

[35] The ATLAS Collaboration. ATLAS Phase-II Upgrade Scoping Document. Technical Report CERN-LHCC-2015-020. LHCC-G-166, CERN, Geneva, 09 2015.

[36] Marcela Mikestikova et al. Study of surface properties of ATLAS12 strip sensors and their radiation resistance. *Nuclear Instruments and Methods in Physics Research Section A: Accelerators, Spectrometers, Detectors and Associated Equipment*, 831:197 – 206, 2016. Proceedings of the 10th International Hiroshima Symposium on the Development and Application of Semiconductor Tracking Detectors.

[37] K. Hara, N. Hamasaki, Y. Takahashi, S. Mitsui, Y. Ikegami, Y. Takubo, S. Terada, and Y. Unno. Design of Punch-Through Protection of Silicon Microstrip Detector against Accelerator Beam Splash. *Physics Procedia*, 37:838 – 843, 2012. Proceedings of the 2nd International Conference on Technology and Instrumentation in Particle Physics (TIPP 2011).

[38] Frank Hartmann. *Evolution of Silicon Sensor Technology in Particle Physics*. Springer, 2009.

[39] Y. Unno et al. Development of n-on-p silicon sensors for very high radiation environments. *Nuclear Instruments and Methods in Physics Research Section A: Accelerators, Spectrometers, Detectors and Associated Equipment*, 636(1, Supplement):S24 – S30, 2011. 7th International Hiroshima Symposium on the Development and Application of Semiconductor Tracking Detectors.

[40] Hunter, Rob and Keller, John and Koffas, Thomas and Mikestikova, Marcela and Soldevila, Urmila and Wizemann, Felix. ATLAS12EC R0 Test Results. ITk Sensor Meeting, 06 2017.

[41] Martin Stegler. Measurements of the mechanical strength of silicon strip sensors in a four-point bender. private communication, 2017.

[42] Mercedes Minano. Radiation Hard Silicon Strips Detectors for the sLHC. Poster for ANIMMA, 6 2009.

[43] Anthony Affolder. Result of Surface Glue on HPK Sensors. Talk at ATLAS Tracker Upgrade Workshop, 11 2008.

[44] The ATLAS Collaboration. The barrel modules of the ATLAS semiconductor tracker. *Nuclear Instruments and Methods in Physics Research Section A: Accelerators, Spectrometers, Detectors and Associated Equipment*, 568(2):642 – 671, 2006.

[45] L. Poley and others. Alternative glues for the production of ATLAS silicon strip modules for the Phase-II upgrade of the ATLAS Inner Detector. *Journal of Instrumentation*, 11(05):P05017, 2016.

[46] DYMAX. 3013 Product Data Sheet. Technical report, DYMAX, 2015.

[47] DYMAX. 6-621 Series Product Data Sheet. Technical report, DYMAX, 2011.

[48] Henkel. LOCTITE AA 3525 Technical Data Sheet. Technical report, Henkel, 9 2014.

[49] Luise Poley. ATLAS silicon detector upgrade: process optimisation and adhesive studies. Master's thesis, Humboldt-Universität zu Berlin, 12 2013.

[50] H.B. Fuller. Epolite FH-5313 technical data sheet. Technical report, H.B. Fuller Company, 4 2003.

[51] Liv Wiik. Glue Study: Hybrid on Sensor. talk at ATLAS meeting, 11 2011.

[52] Biozym Scientific GmbH, Postfach, D-31833 Hess, Oldendorf. *Nichiryo LE.* data sheet.

[53] Edison Opto Corporation. *Federal 3535 UV & IR Series Datasheet*, 2013.

[54] J Lindhard and V Nielsen. Nuclear collisions and ionisation fluctuations in charged particle detectors. Vol: 2, 10 1962.

[55] Michael Moll. *Radiation damage in silicon particle detectors: Microscopic defects and macroscopic properties.* PhD thesis, Hamburg U., 1999.

[56] M. Huhtinen. Simulation of non-ionising energy loss and defect formation in silicon. *Nucl. Instrum. Meth.*, A491:194–215, 2002.

[57] Riccardo Mori et al. Long term performance stability of silicon sensors. 796, 03 2015.

[58] Alexander Dierlamm. Irradiations in Karlsruhe. talk at 16th RD50 Workshop, 6 2010.

[59] Konstantin Toms and others. Annealing Effects on Depletion Voltage and Capacitance of Float Zone and Magnetic Czochralski Silicon Diodes After 800 MeV Proton Exposure. talk at 17th RD50 Workshop, 11 2010.

[60] I. Mandic et al. Bulk damage in DMILL npn bipolar transistors caused by thermal neutrons versus protons and fast neutrons. *IEEE Transactions on Nuclear Science*, 51(4):1752–1758, 8 2004.

[61] Elsa Reichmanis et al. *Radiation Effects on Polymeric Materials*, chapter 1.

[62] S. Kuehn et al. Prototyping of hybrids and modules for the forward silicon strip tracking detector for the ATLAS Phase-II upgrade. *Journal of Instrumentation*, 12(05):P05015, 2017.

[63] C.I.F. FR4 Data Sheet. Technical report, Farnell, 9 2016.

[64] DuPont. DEC Kapton summary of properties. Technical report, DuPont, 10 2016.

[65] H. Walter et al. Bestimmung der Querkontraktionszahl von Polymeren mittels Grauwertkorrelationsanalyse. In *Polymerwerkstoffe 2002, Tagungsband*, pages 260–263, Halle, 9 2002.

[66] Trace Laboratories-East. Test report. 03 2006.

[67] H. Cease et al. Measurement of mechanical properties of three epoxy adhesives at cryogenic temperatures for CCD construction. 2006.

[68] Philip S. Turner. Thermal-Expansion Stresses in Reinforced Plastics. *Journal of Research of the National Bureau of Standards*, 37(4):239–250, 6 1946.

[69] Autar K. Kaw. *Mechanics of Composite Materials*. Tayler and Francis Group, LLC, 2006.

[70] Ralf Bürgel. *Festigkeitslehre und Werkstoffmechanik*. Vieweg+Teubner Verlag, 1 edition, 2005.

[71] Guillermo Hamity. Stencil (Hybrid to Sensor) Design. talk in UK ATLAS Upgrade WP3 meeting, 10 2016.

[72] Arnold F. Holleman and Egon Wiberg. *Lehrbuch der anorganischen Chemie*. de Gruyter, 1995.

[73] *Installations- und Betiebsanleitung: Temperatur- und Klimaprüfschränke Serie WTL und WKL*, 04 2009.

[74] Keyence. 3D Laser Scanning Microscope VK-X100K/X200K Series. Technical report, Keyence Corporation, 2012.

[75] National Institutes of Standards and Technology. stopping-power and range tables for protons. online programme.

[76] Radiation background studies for the Phase II inner tracker upgrade. Technical Report ATL-UPGRADE-PUB-2014-003, CERN, Geneva, 9 2014.

[77] Martin Bonnet. *Kunststofftechnik: Grundlagen, Verarbeitung, Werkstoffauswahl und Fallbeispiele*. Springer Vieweg, 3rd edition edition, 2016.

[78] Igor V. Chernushevich and Alexander V. Loboda and Bruce A. Thomson. An introduction to quadrupole-time-of-flight mass spectrometry. *Journal of Mass Spectrometry*, 36(8):849–865, 8 2001.

[79] Bernd Trathnigg. *Size-Exclusion Chromatography of Polymers*. John Wiley & Sons, Ltd, 2006.

[80] Lakshmi HimaBindu M.R, Angala Parameswari S, and Gopinath C. A Review on GC-MS and Method Development and Validation. *International Journal of Pharmaceutical Quality Assurance*, 4(3):42–51, 2013.

[81] Todd F. Wheeler, John R. Heim, Maria R. LaTorre, and A. Blair Janes. Mass Spectral Characterization of p-Nonylphenol Isomers Using High-Resolution Capillary GC-MS. *Journal of Chromatographic Science*, 35:19–30, 1 1997.

[82] DYMAX. 3013 Material Safety Data Sheet. Technical report, DYMAX, 2012.

[83] DYMAX. 6-621 Material Safety Data Sheet. Technical report, DYMAX, 2011.

[84] Henkel. 3525 Material Safety Data Sheet. Technical report, Henkel, 2012.

[85] H.B. Fuller Company. FH5313 Material Safety Data Sheet. Technical report, H.B. Fuller Company, 2003.

[86] The Dow Chemical Company. D.E.H. 29 Epoxy Curing Agent Material Safety Data Sheet. Technical report, The Dow Chemical Company, 2004.

[87] R. Brun and F. Rademakers. ROOT: An object oriented data analysis framework. *Nucl. Instrum. Meth.*, A389:81–86, 1997.

[88] Neufingerl, F. *Chemie. 1. Allgemeine und anorganische Chemie*. Jugend und Volk, 2009.

[89] Cole Helling, Luise Poley, et al. Study of n-on-p sensors breakdown in presence of dielectrics placed on top surface. to be published in a special issue of "Nuclear Instrumentations and Methods in Physics Research, Section A", 2018.

[90] Cascade Microtech Inc. *PA200 Semi-Automatic Probe Systems - User Guide*, 2010.

[91] Keithley Instruments Inc. *Model 2400 Series SourceMeter User's Manual*, Rev. G edition, 5 2002.

[92] Agilent Technologies Deutschland GmbH. *Agilent E4981A 120 Hz/1 kHz/1 MHz Capacitance Meter - User Manual*, 12 2008.

[93] Matthias Bergholz. *Manual for the DESY Zeuthen measurement software MeasureSoft*. DESY, 1.01 edition, 2013.

[94] Matthias Bergholz. *Vergleich relevanter Parameter von Multipixelsensoren für Spurdetektoren nach Bestrahlung mit hohen Proton- und Neutronflüssen*. PhD thesis, Technische Universität Cottbus, 2015.

[95] Kazunori Matsuda, Katuhisa Suzuki, Kazuhisa Yamamura, and Yozo Kanda. Nonlinear piezoresistance effects in silicon. *Journal of Applied Physics*, 73(4):1838–1847, 1993.

[96] D. Campbell, A. Chilingarov, and T. Sloan. Frequency and temperature dependence of the depletion voltage from CV measurements for irradiated Si detectors. *Nuclear Instruments and Methods in Physics Research Section A: Accelerators, Spectrometers, Detectors and Associated Equipment*, 492(3):402 – 410, 2002.

[97] Serway, R.A. and Gordon, J.R. *Principles of Physics*. Number v. 2 in Principles of Physics. Saunders College Pub., 1998.

[98] Lee, S.J.J. and Sundararajan, N. *Microfabrication for Microfluidics*. Artech House integrated microsystems series. Artech House, 2010.

[99] C. M. Lei et al. Adhesive Testing for the BTeV Pixel Detector, 2005. FERMILAB-TM-2339-E.

[100] S. C. Sun and J. D. Plummer. Electron mobility in inversion and accumulation layers on thermally oxidized silicon surfaces. *IEEE Transactions on Electron Devices*, 27(8):1497–1508, 8 1980.

[101] J. Suzuki, K. Hara, and Y. Unno. Hot electron imaging by IR camera. talk at ATLAS ITk sensor meeting, 6 2016.

[102] Goran Kovačević and Branko Pivac. Structure, defects, and strain in silicon-silicon oxide interfaces. *Journal of Applied Physics*, 115(043531-1), 2014.

[103] M. Ullán et al. Embedded pitch adapters: A high-yield interconnection solution for strip sensors. *Nuclear Instruments and Methods in Physics Research Section A: Accelerators, Spectrometers, Detectors and Associated Equipment*, 831:221 – 228, 2016. Proceedings of the 10th International "Hiroshima" Symposium on the Development and Application of Semiconductor Tracking Detectors.

[104] Celeste Fleta et al. Interstrip Properties of Highly Segmented Double Metal Strip Sensors. poster at IEEE NSS/MIC RTSD 2016, 10 2016.

[105] Craig Sawyer. private communication.

[106] Vitaliy Fadeyev. private communication.

[107] M. Schreuder et al. Encapsulated white-light CdSe nanocrystals as nanophosphors for solid-state lighting. *Journal of Materials Chemistry*, 18:970–975, 1 2008.

[108] Luise Poley. Klebstoffe für den Bau des ATLAS Silizium-Streifen-Detektors: Untersuchung des Einflusses von Bestrahlung auf Härtungseigenschaften. talk at DPG spring meeting, 3 2015.

[109] *Analytical Techniques for Semiconductor Materials and Process Characterization 6*, volume 25, Pennington, New Jersey, USA, 2009. The Electrochemical Society.

[110] C. Patrignani et al. Review of Particle Physics. *Chin. Phys.*, C40(10):100001, 2016.

[111] Kolanoski, Hermann and Wermes, Norbert. *Teilchendetektoren - Grundlagen und Anwendungen*. Springer Spektrum, 2016.

[112] Lund University. Table of Isotopes decay data, 10 2014.

[113] Hebei I.T. (Shanghai) Co., Ltd. *Thermoelectric Cooler TEC1-12706*, 2.03 edition.

[114] Christian Ritschel. Measurements on a mini sensor for the ATLAS strip detector upgrade with a newly setup beta radiation test stand. Master's thesis, Humboldt-Universität zu Berlin, 11 2015.

[115] ALiBaVa systems. *ALiBaVa GUI*.

[116] Ted Pella, Inc. *Safety Data Sheet Product Leitsilber 200 Conductive Paint*, 6 2015.

[117] Electrolube. *Electronic and General Purpose Cleaning Technical Data Sheet SWAJ Safewash Jigwash*, 1 edition, 10 2013.

[118] Löchner, S and Schmelling, M. The Beetle Reference Manual - chip version 1.3, 1.4 and 1.5. Technical Report CERN-LHCb-2005-105, CERN, Geneva, 11 2006.

[119] Michel Walz. Charakterisierung von planaren Siliziumstreifendetektoren zum Einsatz am LHC-Upgrade. Master's thesis, Albert-Ludwigs-Universität Freiburg im Breisgau, 12 2010.

[120] Saint-Gobain Industrial Ceramics, Inc. *BC-400/BC-404/BC-408/BC-412/BC-416 Premium Plastic Scintillators*, 4 1998.

[121] Laetitia Adkins. Characterisation of reference detectors for TAXI. DESY Summer Student Report, 9 2014.

[122] L. Landau. On the energy loss of fast particles by ionization. *J. Phys.(USSR)*, 8:201–205, 1944.

[123] Ties Behnke et al. Test Beams at DESY. Technical Report EUDET-Memo-2007-11, Deutsches Elektronen-Synchrotron, 11 2007.

[124] J. Baudot et al. First test results of MIMOSA-26, a fast CMOS sensor with integrated zero suppression and digitized output. In *2009 IEEE Nuclear Science Symposium Conference Record (NSS/MIC)*, pages 1169–1173, 10 2009.

[125] Hendrik Jansen et al. Performance of the EUDET-type beam telescopes. *EPJ Techn Instrum*, 3(1):7, 2016.

[126] David Cussans. Description of the JRA1 Trigger Logic Unit (TLU), v0.2c, 9 2009. EUDET-Memo-2009-4.

[127] Eda Yildirim. *Measurement of the Lorentz Angle in irradiated ATLAS HL-LHC Silicon Micro-Strip Sensors at the DESY Test Beam.* PhD thesis, Universität Hamburg, 2016.

[128] DESY. DESY II Description & Status. web page, 12 2017.

[129] Igor Rubinskiy. EUTelescope. Offline track reconstruction and DUT analysis software. Technical report, DESY, 12 2010.

[130] F Gaede, T Behnke, N Graf, and T Johnson. LCIO - A persistency framework for linear collider simulation studies. Technical Report physics/0306114, DESY, Hamburg, 6 2003.

[131] The LHCb Collaboration. Studies of pre-prototype sensors for the UT Upgrade project. Technical Report LHCb-PUB-2015-006. CERN-LHCb-PUB-2015-006, CERN, Geneva, 03 2015.

[132] M. Benoit, J. Idarraga, and S. Arfaoui. The AllPix simulation framework, 3 2015.

[133] Edoardo Rossi. private communication.

[134] Dennis Sperlich, Luise Poley, et al. Signals from fluorescent materials on the surface of silicon micro-strip sensors. In *Nuclear Instrumentations and Methods in Physics Research, Section A (NIMA).* to be published in 2018.

[135] Luise Poley et al. Characterisation of strip silicon detectors for the ATLAS Phase-II Upgrade with a micro-focused X-ray beam. *Journal of Instrumentation*, 11(07):P07023, 2016.

[136] NIST. X-ray Mass Attenuation coefficients.

[137] Y. Unno et al. Development of n+-in-p large-area silicon microstrip sensors for very high radiation environments – ATLAS12 design and initial results. *Nuclear Instruments and Methods in Physics Research Section A: Accelerators, Spectrometers, Detectors and Associated Equipment*, 765:80 – 90, 2014. HSTD-9 2013 - Proceedings of the 9th International Hiroshima Symposium on Development and Application of Semiconductor Tracking DetectorsInternational Conference Center, Hiroshima, Japan, 2 - 5 September 2013.

[138] Yu. S. Chernousko et al. The timing system for Diamond Light Source. *Conf. Proc.*, C060626:3182–3184, 2006. [,3182(2006)].

[139] Stefaan Tavernier. *Experimental Techniques in Nuclear and Particle Physics*. Springer-Verlag Berlin Heidelberg, 2010.

[140] Konrad Albrecht. Untersuchung des Einflusses elektromagnetischer Wechselfelder auf das Rauschverhalten eines Siliziumstreifendetektor-Moduls, 2015. BA thesis: Humboldt-Universität zu Berlin.

[141] Ian Pape. private communication.

[142] Andrew Blue et al. Testbeam evaluation of heavily irradiated silicon strip modules for ATLAS Phase - II Strip Tracker Upgrade. 11th International "Hiroshima" Symposium on the Development and Application of Semiconductor Tracking Detectors, 12 2017.

[143] L. Poley et al. Investigations into the impact of locally modified sensor architectures on the detection efficiency of silicon micro-strip sensors. *Journal of Instrumentation*, 12(07):P07006, 2017.

[144] Y. Unno. ATLAS ITk sensor meeting.

[145] I. Pintilie, G. Lindstroem, A. Junkes, and E. Fretwurst. Radiation-induced point- and cluster-related defects with strong impact on damage properties of silicon detectors. *Nuclear Instruments & Methods in Physics Research Section A: Accelerators Spectrometers Detectors and Associated Equipment*, 611:52–68, 11 2009.

[146] Urmila Soldevila. Radiation-hard silicon for HL-LHC trackers. *Journal of Instrumentation*, 6, 12 2011.

[147] I Mandić et al. TCT measurements of irradiated strip detectors with a focused laser beam. *Journal of Instrumentation*, 8(04):P04016, 2013.

[148] Kunlin Ran. Study on Simulation of ATLAS ITK Strips. Technical report, DESY, 9 2016. summer student report.

Acknowledgements

Irradiations presented in this thesis were performed at Karlsruhe Institute of Technology (KIT) and Jožef Stefan Institute (JSI) and I want to thank Dr. Alexander Dierlamm, Felix Bögelspacher and Dr. Vladimir Cindro for their their advice and fast and reliable handling of sensor irradiations. This work was supported by the Project for Enabling Technologies for Silicon Microstrip Tracking Detectors at the HL-LHC (PETTL). This project has received funding from the European Union's Horizon 2020 Research and Innovation programme under Grant Agreement no. 654168.

The measurements leading to these results have been performed at the Testbeam Facility at DESY Hamburg (Germany), a member of the Helmholtz Association (HGF). I want to thank the testbeam coordinators and telescope support, Dr. Marcel Stanitzki and Dr. Jan Dreyling-Eschweiler in particular, for their help and support during the testbeam.

This project received funding from the Helmholtz CAS Joint Research Grant HCRJ-300 "Novel Technologies for the New ATLAS Silicon Micro-Strip Detector at the High Luminosity LHC".

Many thanks Diamond Light Source for access to beamline B16 (proposals MT13500 and MT11639), which contributed to the results presented here. I would like to thank personnel of the B16 beam, especially Kawal Sawhney, Ian Pape, Oliver Fox and Andy Malandain for providing advice, support and maintenance during the experiment.

This document was prepared by Luise Poley as a result of the use of facilities of the U.S. Department of Energy (DOE), which are managed by Los Alamos National Security, LLC (LANS) acting under Contract No DE-AC52-06NA25396. Neither LANS, DOE, the U.S. Government, nor any person acting on their behalf: (a) make any warranty or representation, express or implied, with respect to the information contained in this document; or (b) assume any liabilities with respect to the use of, or damages resulting from the use of any information contained in the document.

I've had a lot of support during my PhD time and while it is unfortunately impossible for me to mention every single person who deserves it, but I would like to thank a few selected people without whom it would have been a lot more difficult.

I want to thank my family for helping me to get this far and supporting me all along the way and especially my husband for tolerating me during the final year.

Thanks to all of my amazing friends who stuck with me and supported me during the writeup.

And thanks to my student mentor Philip, without whom I would not have made it that far.

A big thank you to all the people at the ITk strip tracker project, who have helped me so much over the past years:

Thanks to the ATLAS strip sensor community for allowing me to use the last reserve of ATLAS07 miniature sensors as well as helping me with measurements and data analysis, especially to Bart, Marcela, Miguel, Celeste and Vitaliy.

Thanks to the RAL group - Bruce, Craig, Jens, Peter and Stephanie - and Matt for allowing us to loot their labs for testbeam setups and helping with the setups, which would never have worked that well without the particular magic of ITSdaq.

Thanks to Andy for introducing me to the art of testbeaming: I had not been at a testbeam until May 2015 and by the end of 2016, I had been to nine of which I had run six myself. I'm still not sure how that happened, but thanks for teaching me.

Thanks to the Liverpool group, especially Tim and Peter, for the great time I had during my authorship qualification task and for giving me a topic to go back to between spending hours, days and weeks readjusting probe station needles for cooled tests of irradiated sensors. And to Lingxin for her TCAD simulations.

A special thanks to my colleagues at DESY:

thanks to our radiation officers Martin and Anne - sorry for irradiating so much stuff.

thanks to Eda and Artur for helping us to set up our first testbeam, so that we did not have to start all over again - it's hard to grasp the amount of time we were spared by Eda's knowledge and experience in my first testbeam

thanks to Martin for helping out with wire bonding - sorry for the glue and the carbon particles and the aceton and the triple use of bond pads.

thanks to everyone who volunteered to help with testbeam shifts: Haider, Laura, Kristin, Dennis and Martin - without you, I could not have done it.

I was very lucky to have colleagues to learn from, to work with and to rely on: thanks to Martin, who taugh me to test sensors in a probe station and how to find out why it didn't work, thanks to Dennis for saving us from sitting at the testbeam or the betasetup all night and generally helping to make sure stuff worked. thanks to Laura for jumping in whenever help was needed, and especially to Kristin, who, despite her full schedule and her even fuller to-do-list, always found time to sit down with me, teach me how to do things and spend all this time on getting things to work.

And thanks to Ingo, who was simply the best supervisor I could have asked for.

And of course I want to thank Klaus for making sure I didn't forget to apply for an extension, lose my account or mess up otherwise - and for generally making sure I eventually handed in my thesis.

Finally I want and have to thank my proofreaders - especially Kristin and Jens - for voluntarily spending so much of their time on helping me.

,